Coupled Theoretical and Experimental Methods to Characterize Heterogeneous, Anisotropic, Nonlinear Materials: Application to Cardiovascular Tissues

A DISSERTATION
SUBMITTED TO THE FACULTY OF THE GRADUATE SCHOOL
OF THE UNIVERSITY OF MINNESOTA
BY

Colleen M. Witzenburg

IN PARTIAL FULFILLMENT OF THE REQUIREMENTS
FOR THE DEGREE OF
DOCTOR OF PHILOSOPHY

Victor H. Barocas, Adviser

October 2014

© Colleen M. Witzenburg October 2014

Acknowledgments

First, I would like to thank my thesis advisor, Dr. Victor H. Barocas, who has been an amazing mentor and teacher over the past five years. I am grateful for his patience in working with me while I learned the concepts and techniques necessary to complete my research and his commitment to ensuring that I gained both the scientific and professional skills necessary to pursue a career in academia. I cannot thank him enough for his unwavering support and encouragement through the many ups and downs of graduate school. In particular, I am incredibly grateful for the flexibility he showed me in my third year of graduate school when he allowed me to work remotely so I could live with my husband and continue my graduate studies.

I would also like to thank all the members of the Barocas group, past and present, who have contributed to this work. Dr. Ramesh Raghupathy created the Generalized Anisotropic Inverse Mechanics method as well as the image correlation technique upon which many of the methods and techniques presented herein rely. I would like to thank him for providing technical guidance as well as a strong foundation for this work. He has been incredibly insightful and helpful in overcoming roadblocks and was always willing to take the time to answer my questions. While an undergraduate student in the lab, Sarah Vanderheiden performed many of the rat heart ventricle experiments presented in this thesis and I appreciate her diligence and care when handling and testing these samples. I would also like to thank Rohit Dhume who was instrumental in the computational implementation of automatic segmentation scheme and who has taken on the task of modeling aortic failure using my structurally inspired networks. I want to thank Sachin Shah, Faisal Hadi, and Julia Quindlen who have also all contributed to the modeling efforts of the ascending aortic failure problem. I am also pleased to welcome Chris Korenczuk to the group and excited he will be taking over the project. In addition, I want to acknowledge both the technical and professional guidance of Drs. Spencer Lake and Hallie Wagner. Dr. Lake provided excellent advice and guidance on the academic career

trajectory. Dr. Wagner acted as a superb sounding board for all of my scientific notions; taking her personal time to read and comment on my thesis. I really appreciate all of the technical discussions and brainstorming sessions we shared. Again, I want to thank all the members of the lab group with whom I have worked over the past few years. I have been very fortunate to work with such an incredible group of people.

I would also like to thank my wonderful family. I want to thank my parents, Michael and Kay, for their boundless love, support, and encouragement. I cannot express how much it means to me to have you in my corner. I also greatly appreciate the support and encouragement of my wonderful sister, Kate, and her family. My sister has always been a great inspiration in my life and is someone I continually strive to emulate. I also want to thank my good friend Rachel with whom I have shared many of the trials and tribulations of graduate school. Lastly and most importantly, I want to thank my amazing husband who is the love of my life and my best friend. He is my rock and I could not have done any of this without his love, support, and patience.

Abstract

The Generalized Anisotropic Inverse Mechanics (GAIM) method is able to provide general tissue characteristics in terms of stiffness, anisotropy strength, and preferred orientation. It allows for the computational dissection of samples, capturing regional differences within a single sample nondestructively. However, the linear assumption implicit in GAIM limited its utility, particularly in the case of cardiovascular soft tissues, which exhibit markedly nonlinear behavior when operating at physiologic strain levels. Therefore, GAIM was extended to consider large-deformation kinematics, a nonlinear closed-form structural model of planar fibrous tissue mechanics was utilized to describe the nonlinear behavior of a cardiovascular soft tissue (rat ventricle wall), and the partitioning method utilized by GAIM was replaced with a more robust partitioning scheme. Then, GAIM was applied in a stepwise fashion (NGAIM) in order to capture the full nonlinear kinetics of cardiovascular soft tissues. Finally, experiments characterizing the three-dimensional loading and failure of healthy porcine ascending aorta were discussed.

The work presented in this thesis marks the development and use of novel theoretical and experimental approaches for the analysis of complex cardiovascular soft tissues. An analysis method was developed, NGAIM, that can be applied to examine regional mechanical differences in planar, nonlinear, anisotropic, heterogeneous, tissue samples from all over the body which yields full-field stress. Finally, a partnering was proposed which exploits the characterization capacity of NGAIM with the predictive capacity of the multiscale model to create full three-dimensional simulations of cardiovascular soft tissue behavior.

Table of Contents

List of Tables

List of Figures

Chapter 1: Introduction

1.1 Cardiovascular System

The primary role of the heart is to pump blood, a fundamentally mechanical process. The cardiovascular system is responsible for maintaining blood flow such that nutrients (e.g. oxygen, glucose, amino acids, fatty acids, and water) and waste (e.g. carbon dioxide, urea, creatinine, heat) can be transported to and from the body's tissues and organs, Figure 1.1. The ventricular walls expand and contract over 2.5 billion times during the

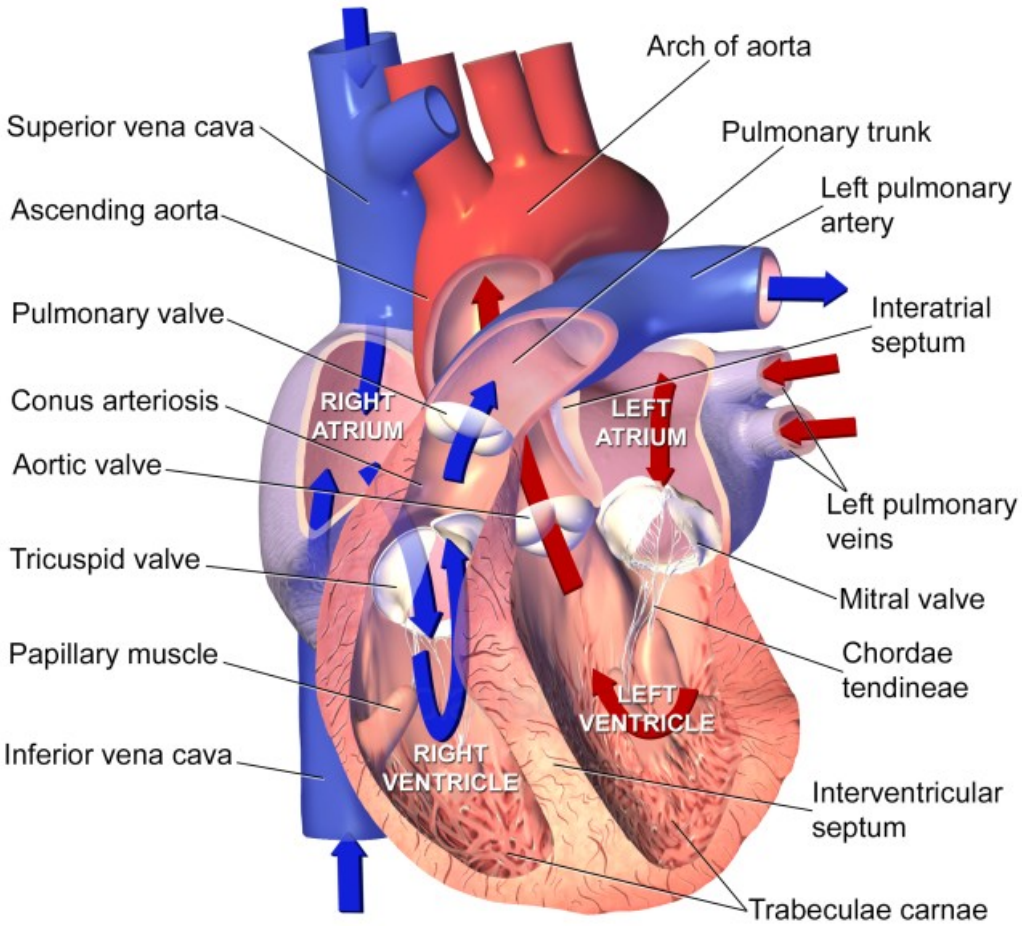

Figure 1.1: Schematic showing an anterior sectioned view of the heart with the blood flow indicated and the chambers labeled. [1]

average human lifespan [2]. The right atrium receives deoxygenated blood from the body through the superior and inferior venae cavae. The deoxygenated blood enters the right ventricle (RV) through the tricuspid valve, and the RV pumps it through the pulmonary valve, pulmonary trunk, and pulmonary arteries and into the lungs. Four pulmonary veins return oxygenated blood to the left atrium. The oxygenated bloods flows through the mitral valve into the left ventricle (LV), which pumps it through the aortic valve and the aorta to the body. In this work we focus on both the mechanics of ventricular tissue and that of the ascending aorta.

1.1.1 The Ventricular Walls

The ventricular walls form the chambers within the heart responsible for collecting and expelling blood. Figure 1.2 shows the cardiac cycle for the left ventricle. The entire cycle occurs in ~ 0.7 seconds. At the end of diastole, both the atrium and ventricle are relaxed, the mitral valve is open (atrial pressure > ventricular pressure), and the aortic valve is closed (ventricular pressure < aortic pressure). Contraction of the ventricles, systole, is initiated by almost synchronous electrical excitation. As the ventricle contracts, ventricular pressure rises very rapidly, quickly exceeding atrial pressure and causing the closure of the mitral valve, thus preventing backflow of blood into the atrium. The ventricle undergoes isovolumetric contraction until the ventricular pressure surpasses the aortic pressure (afterload) and the aortic valve opens. Ejection begins, and aortic pressure rises along with ventricular pressure. The majority of the cardiac output occurs within the first quarter of the ejection phase, before the peak in pressure. As the force of ventricular contraction diminishes, there is a deceleration of the ejecting blood, and when the ventricular pressure falls below the aortic pressure the aortic valve closes. Diastole begins with the closure of the aortic valve and isovolumetric ventricular relaxation. As the ventricle relaxes, pressure decreases, and when ventricular pressure dips below atrial pressure, the mitral valve opens. Venous blood, which has been accumulating in the atrium since the closure of the mitral valve, flows quickly into the ventricle. The vast majority of filling occurs in the first quarter of diastole when the rate of blood flow is

enhanced by diastolic suction, recoil of the relaxing myocardium from its contracted systolic configuration. The pressure and volume curves for the right ventricular cardiac cycle are similar. However, the right ventricle operates at lower pressure than the left ventricle (maximum systolic pressure is ~ 5.3 times lower). Additionally, the pulmonary arterial pressure is much lower than the aortic pressure, causing the pulmonic valve to open prior to and close after the aortic valve.

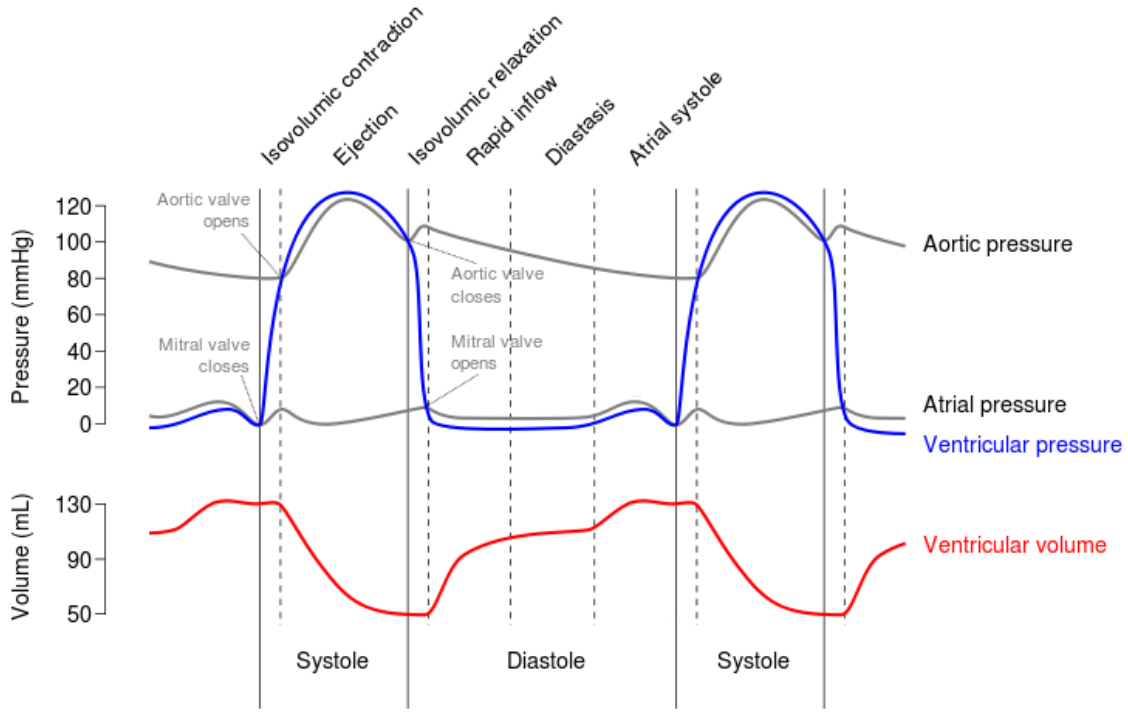

Figure 1.2: Left ventricular pressure and volume during the cardiac cycle. [3]

Aging, injury, and disease can all cause significant changes in the heart's performance. For example, myocardial infarction (heart attack) is a common cause of ventricular dysfunction. Each year, approximately one million Americans experience a new or recurrent myocardial infarction, and about 60% of patients survive [4,5]. The myocardium does not extract oxygen from the blood within the atria and ventricles but is supplied with oxygen-rich blood through the coronary arteries. The buildup of plaque within the coronary arteries restricts blood flow, and severe restriction can cause myocardial infarction. The percentage of survivors is increasing due to earlier and more

effective intervention aided by both education and technology [6–12], but heart attack survivors have life-long damage to their ventricular tissue.

Following infarction, the ischemic myocardium loses its ability to generate systolic force and contribute to ejection. The lost myocardium is replaced not with muscle but with scar tissue, additional extracellular matrix (ECM). In healthy myocardium, the ECM provides the structural network that supports cardiomyocytes, helps translate their individual contractions into organized tissue-scale contraction during systole, and prevents overstretching or tearing during diastole. Although it is the death of cardiomyocytes that characterizes a myocardial infarction, infarction causes the remaining myocardium to modify the heart's ECM, and therefore its passive mechanical properties, in an effort to retain pumping function. ECM deposition is a local phenomenon, and new ECM often forms with different alignment, composition, and mechanical properties from those of the original matrix [13]. The more widespread the damage, the higher likelihood of progressive negative remodeling leading to ventricular dilation, a lowered ejection fraction, and/or reduced diastolic filling, common symptoms of heart failure. Once heart failure symptoms present, the 5-year mortality rate is almost 50% [14].

Consequently, various treatments have been developed to revive, regenerate, and/or replace infarcted tissue. While intervention techniques, such as reperfusion therapy [6], have proven effective, they must be applied within minutes of symptom onset, which severely limits their practicality. Stem cell therapy is associated with reduction in infarct scar size and improvements in left ventricular function and can be applied days after infarction [15], but issues surrounding stem cell therapy, such as cell type, dosing, and timing, remain open [15–17]. In the future, tissue-engineered cardiac patches could be used to replace infarct tissue altogether. Current patch technology [18,19] generally involves seeding cardiac cells (or stem cells) within a porous three-dimensional scaffold. Scaffolds, usually made of a degradable polymer, are meant to provide structural support until replaced by the cells own secreted extracellular matrix. While patches have shown promise in small-animal models, their efficacy has not been documented in large animals

or humans [18] and they typically require invasive surgical techniques. A better understanding of the regional mechanical behavior of diseased ventricle would aide in the development of a bioartificial myocardium substitute and new infarct treatments.

1.1.2 The Ascending Aorta

The aorta is the main trunk in the series of vessels that transport oxygenated blood to the body. The aorta is divided into two sections: the thoracic aorta, which runs from the heart to the diaphragm, and the abdominal aorta, which runs from the diaphragm to the aortic bifurcation site (where the aortic splits to form the two iliac arteries). The aorta is a long vessel, with the thoracic aorta measuring about 35 cm long [20]. The thoracic aorta is subdivided further into the ascending aorta, aortic arch, and descending aorta, Figure 1.3. In general, branches from the ascending aorta (the two coronary arteries) supply blood to the heart, branches from the aortic arch (the innominate, left common carotid, and left subclavian arteries) supply blood to the head, neck, and arms, and branches from the descending aorta (the visceral - pericardial, bronchial, esophageal, mediastinal - and the parietal - intercostal, subcostal , superior phrenic arteries), supply blood to the chest.

Later in this thesis, there will be considerable study of the ascending aorta. Though it is only about 5 cm in length [20,21], (15% of the total length of the thoracic aorta), about 60% of all thoracic aortic aneurysms involve the ascending aorta [22]. The ascending aorta supports tremendous hemodynamic loading; expanding (~ 11% area change [23]) under the systolic pressure and elastically recoiling during diastole, augmenting the forward flow of blood and coronary perfusion [2]. An ascending thoracic aortic aneurysm (aTAA) is a gross expansion of the section of aorta nearest to the heart that tends to develop over a period of years. Blunt trauma, connective tissue disorders (i.e. Marfan's syndrome), congenital deformities (e.g. bicuspid aortic valve), medial degeneration, and advanced age (> 70 years) are all associated with higher risk of aTAA [22]. Aneurysm dissection and rupture (resulting in imminent death) are the primary risks associated with TAA. Dissection and rupture occur when the remodeled tissue is no longer able to

withstand the stresses generated by the arterial pressure. A tear forms in the intimal layer of the aorta and blood streams through this tear into the media, causing the medial layers to separate forming a false lumen. The false lumen may compromise blood flow to the body by blocking the true lumen and/or diverting and slowing blood flow. In addition, the false lumen is vulnerable to both thrombus formation (due to sluggish blood flow, irregular geometry, and inflammation) and rupture (due to reduced wall thickness and asymmetric loading). Unfortunately, surgical repair of an aTAA, by removing the aneurysm and replacing it with a synthetic tube graft, also involves considerable risk. Statistically, death from rupture becomes more likely than death during surgery at an aTAA diameter over 5.5 cm, setting the current interventional guidelines [22,24]. Aortic rupture remains a mysterious phenomenon, however, occurring in a significant number of patients with smaller aneurysms [22,25] while many patients with aTAA diameters above 5.5 cm do not experience aortic dissection or rupture. A better understanding of the aneurysmic tissue's mechanics and structure would improve surgical decision making.

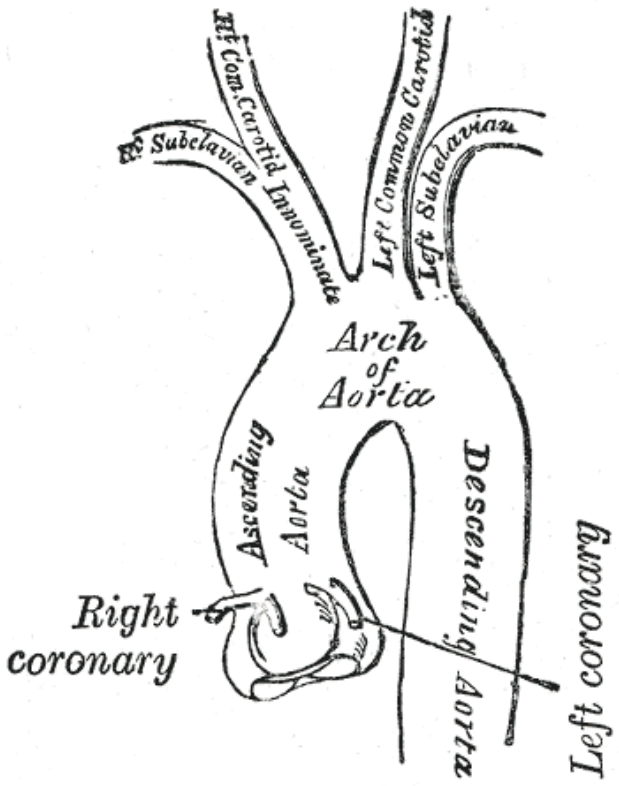

Figure 1.3: Schematic showing the location of the ascending aorta. It is distal to the aortic valve and ends at the aortic arch (branch point for the innominate, left common carotid, and left subclavian arteries). [21]

1.2 Cardiovascular Soft Tissues: General Characteristics

The purpose of a constitutive model to describe the mechanical response of a material under a variety of physically meaningful loading configurations. Cardiovascular soft tissues (aorta, ventricular wall, heart valve leaflet, etc.) are fundamental to the load-bearing capacity of the cardiovascular system. The intrinsic complexity of cardiovascular soft tissues; however, presents a tremendous challenge in constitutive modeling. The ECM transmits force throughout the tissue endowing it with structural stability and load carrying capacity. The ECM is often [26] described as a fiber-reinforced composite: with a fibrous network of proteins (e.g. collagen, elastin, fibronectin, laminin, etc.) embedded in a amorphous mixture of glycosaminoglycans and extracellular water. The mechanical behavior of a cardiovascular soft tissue depends strongly on both the composition and organization of its ECM, which in turn depends upon the anatomical and physiological demands of the body. The complexity of the ECM, combined with the complexity of the cells in the tissue, leads to characteristics that present a challenge to the constitutive modeler: anisotropy, heterogeneity, nonlinearity, and viscoelasticity. These features are described in the subsequent paragraphs.

1.2.1 Anisotropy

The structural constituents of a cardiovascular tissue's ECM typically have specific orientations and concentrations particular to the anatomy and physiology of the tissue. For example, the collagen fiber bundles within the medial layer of elastic arteries, like the aorta, have been well documented to be circumferentially oriented [27,28]. The myocardium is structured from sheets of locally parallel muscle fibers embedded in an extracellular matrix (composed mainly of collagen types I and III). The angle of the fibers changes continuously through the myocardium [29], but the average transmural fiber orientation of both ventricles is the circumferential direction.

The composition and organization of the ECM of cardiovascular soft tissues has been interrogated in various ways. The fibrous constituents themselves can be viewed using a scanning electron microscope [27,30]. Histology and light microscopy are standard practice in the local determination of the orientation and proportions of the ECM constituents [27,31,32]. Both polarized light [33] and small angle light scattering [34] have been utilized to quantify collagen fiber orientation and anisotropy strength. Diffusion tensor magnetic resonance imaging [35,36] allows for the three-dimensional fiber structure of a tissue to be measured nondestructively. The composition of the ECM is also often quantified through chemical assays [37].

The structural anisotropy exhibited by many cardiovascular soft tissues is widely accepted to be the cause of their strong mechanical anisotropy. For example, when a sample is extended along the direction of the fibers, it exhibits a much larger stress than when extended the same distance in the cross-fiber direction. It has been well established that arterial wall is anisotropic with respect to the unloaded configuration with the circumferential direction stiffer than the axial [38]. For example, Doyle and Dobrin [39] performed inflation experiments on canine carotid arteries measuring Cauchy stress under equibiaxial extension. From the stresses measured they determined that the carotid artery is stiffer in the circumferential direction than in the axial direction. A prominent paper by Patel and Fry [40] is an excellent example of the quantification of mechanical anisotropy in canine arteries. They performed inflation-elongation experiments on segments of canine aorta and carotid arteries at various pressures and extension loads and measured the rotation of the lower end of the vessel. They concluded from their strain measurements that arteries are cylindrically orthotropic (i.e. they are symmetric with respect to the radial, circumferential, and axial directions). Equibiaxial extension tests on myocardial tissue taken from both the right [41] and left ventricles [42] indicate higher stiffness in the fiber direction as compared to the cross fiber direction, particularly for the right ventricle. Yin and colleagues studied the mechanical behavior of the endocardium and epicardium as well. They found anisotropic behavior for both canine [43] and bovine [44] epicardium with the ratio of Cauchy membrane stress strongly favoring the

circumferential direction over the apex-to-base direction for both the right and left ventricle. A similar anisotropic response was observed in bovine endocardium [44], with larger stresses in the circumferential direction during equibiaxial extension.

1.2.2 Heterogeneity

Both the direction and degree of fiber alignment as well as the presence and proportions of the ECM constituents vary locally within cardiovascular tissues, causing regional differences in both anisotropy and stiffness. For example, when an artery branches (i.e. bifurcates), such as at the aortic arch where the brachiocephalic, left common carotid, and left subclavian arteries begin, the microstructure no longer has circumferential alignment as the vessel no longer has a circular cross section. Rowe et al. [33] found the tissue at the branch points of cerebral arteries to be tendon-like with a higher concentration of collagen, greater thickness, and a markedly stronger alignment (in the direction of the apical ridge) than that seen in straight cylindrical arteries. Delfino [45], who focused on the human carotid artery, performed one of the most complete studies on branch points. His results agree that the bifurcation point is highly collagenous, thick, and strongly aligned and go further into a full 3D analysis of the stress-strain response. He characterized the principal stress at various cross section locations along the bifurcation showing that both the mechanical anisotropy and stiffness of the tissue change with location. The proportions of the ECM components within elastic arteries has also been shown to vary with distance from the heart. Collagen-to-elastin ratios in the aorta vary from below one near the heart to above one in regions far from the heart [46,47]. A extensively studied cardiovascular soft tissue with regionally varying fibrous alignment is the aortic valve leaflet. There is great interest in using it to develop replacement valves for the treatment of aortic valve disease. Quantitative polarized light imaging reveals commissure-to-commissure fiber alignment throughout the aortic valve leaflet [48]. Billiar and Sacks [49] performed specialized biaxial testing elucidating the local structure-strain relationship of the tissue. One final example of heterogeneity is that of the heart itself. During systole and diastole there are considerable regional differences in the

sequence, size, and extent of myocardial deformations [50]. Though systolic shortening and diastolic lengthening generally increase in magnitude from base to apex the ventricle walls also experience large shear strains during both systole and diastole. Demer and Yin [51] studied regional differences in the mechanical behavior of the ventricle by excising samples from both the anterior and posterior LV free wall and the basal and apical halves. They biaxially tested samples, identifying the fiber and cross-fiber directions visually, and showed that samples taken closer to the base of the heart had a more anisotropic stress-strain response than those taken closer to the apex. When studying the mechanical properties of the right ventricle, Sacks and Chuong [41] found the tissue excised from the conus region to exhibit more anisotropy than that from the sinus region, although both were stiffer along the average fiber direction than the cross-fiber direction. Omens et al. [52] showed that the ventricular myocardium has a complex, non-uniform distribution of residual stress and strain. Their results suggest that there is regional heterogeneity in LV myocardial mechanical properties both transmurally and in the apex-base direction. Ghaemi et al. [53] completed displacement controlled biaxial testing on samples from four different regions of the bovine heart (the interventricular septum, LV free wall, RV free wall, and apex) to characterize regional mechanical differences. Their results showed that the mechanical behavior of samples from all four regions was similar (nonlinear with higher stiffnesses in the cross-fiber rather than the fiber direction) and that the LV free wall and interventricular septum were significantly stiffer overall than the RF free wall and apex. Finally, Zhang et al. [36] show beautiful DTMRI images detailing the complex wrapping of the fibrous layers of the ventricle challenging even the simplifying nature of symmetry assumptions.

The heterogeneous nature of tissues becomes particularly evident in instances of disease of damage. For instance, the aortic wall thins and weakens nonuniformly during aneurysm, and variation has been reported [54–56] between the lesser and greater curvatures of the aortic arch. Catastrophic failure of the aorta occurs when a section of the wall is no longer able to withstand the stresses generated by the arterial pressure and dissects or ruptures. Once dissection begins both the fluid dynamics within the vessel and

mechanical stresses within the vessel wall suffer from drastic local changes. Another example is the aortic valve. Aortic valve disorder in both native [57] and bioartificial [58] valves can range from mild thickening to severe calcification of leaflets. It is characterized by dramatic disruptions in the fiber architecture of the leaflet, irregular dystrophic calcification and lipid deposition, and leaflet disfigurement [57,58]. Calcification causes pronounced stiffening in the affected region relative to the rest of the valve damaging the leaflet nonuniformly and causing deterioration in function, often allowing regurgitation and pathologic flow. Finally, myocardial infarction is an example of severe damage to the ventricle. Restriction of coronary blood flow causes a portion of the ventricle to die which is then replaced with scar tissue and remodels in a dynamic temporal process [59]. Scars tend to be stiffer and to vary in anisotropy from the surrounding healthy myocardium, creating a gradient in the wall properties. The scar is sensitive not just to local changes in the ECM but also to the local stress-strain environment as it is coupled with the adjacent healthy myocardium [13]. Fomovsky et al. [60] studied the regional mechanics of scars in both small and large animal models considering anisotropy in both the structure and mechanical behavior of the scar, concluding that conflicting reports of anisotropic preference were due to scar geometry and location.

1.2.3 Nonlinearity

In addition to the strong anisotropy often exhibited by cardiovascular soft tissues in their stress-strain response there is also often marked nonlinearity. Mechanical testing (biaxial extension, inflation, etc.) results for epicardium [43], myocardium [2,61], healing myocardial infarction [59], aortic valve leaflet [49], and ascending thoracic aorta [62] all reveal nonlinear behavior. The tissue is initially very compliant, but as the strain is increased, it becomes much stiffer. Nonlinearity in the mechanical response becomes increasing pronounced as the strain level imposed on the tissue is increased. Large strain levels (upwards of 30%) are of most interest, as physiologically cardiovascular tissues operate at large strains [63], so the nonlinearity of the response is extremely important.

1.2.4 Viscoelasticity

Cardiovascular tissues also exhibit hysteresis during cyclic loading, which is indicative of viscoelastic behavior. Preconditioning, cyclically stretching the tissue prior to obtaining results, is used to minimize hysteresis such that the tissue exhibits negligible changes in its loading and unloading curves. Cyclic loading is physiologically reasonable for both the ventricle and aorta as they experience cyclic loading *in vivo*. Once preconditioning has been performed, the tissue can be treated as pseudo-elastic. The stress-strain relationship is now well defined and repeatable, and one can treat the material as one elastic material in loading, and another elastic material in unloading. The usefulness of pseudo-elasticity is increased by the circumstance that most cardiovascular soft tissues, including ventricular and aortic tissue, exhibit behavior that is essentially independent of strain rate [2,50]. Fung reports that an increase as large as 1000 fold in strain rate causes between only a 1 and 2 fold increase in stress for most soft tissues [64]. Ghaemi et al. [53], biaxially tested bovine myocardial samples from four different regions of the heart using a variety of different biaxial protocols and strain rates and observed no change in either the fiber or cross-fiber behavior with strain rate.

The complex structure and mechanical behavior of cardiovascular tissues make formulating an appropriate constitutive relation difficult. Most often, constitutive relations are obtained by determining the general characteristics of the tissue, establishing an appropriate theoretical framework, identifying a specific functional form of the relation, and fitting the material parameters to experimental data [2,26,65–67]. There are many prominent strain energy functions (reviewed in [2,64,68,69]) that are utilized to describe the mechanical behavior of cardiovascular tissues. Fung-type relations, which are exponential in terms of the Green strain, and neo-Hookean relations, which rely on the first invariant of Green's deformation tensor, have been modified to account for material symmetry. The Mooney-Rivlin model describes material behavior over a broader range of strains and includes both the first and second invariant of Green's deformation tensor. The Ogden model expresses the material behavior in terms of a

summation of a weighted exponential form of the principal stretch. Humphrey compares the use of various models to describe the mechanical behavior of cardiovascular tissues extensively [2]. For example, Humphrey compares the results from strain energy relations determined by Chuong and Fung [70], von Maltzahn [71], and Takamizawa and Hayashi [72] by applying them to same data from the planar biaxial deformation of an artery. The various functions not only determine different stiffnesses for the tissue, but they also differ in directionality: the Chuong and Fung relation characterizes it as anisotropic with circumferential preference, the Takamizawa and Hayashi relation characterizes it as isotropic, and the von Maltzahn relation characterizes it as anisotropic with axial preference. This result reinforces the idea that even widely used constitutive relations, which are successful in describing material behavior, are limited to a range of relevant deformations and may not have adequate predictive capabilities to be applied in alternate loading configurations. This concern leads to the notion of the direct inverse problem: instead of selecting a strain energy function and fitting the material parameters to experimental data, use experimental data directly to determine a strain energy function.

1.3 Direct Inverse Problems: Literature Review

Inverse problems involve determination of inputs from observed outputs, in contrast to forward problems, in which outputs are determined from knowledge of inputs. In order to illustrate this difference a simple example of a spring under load will be used in which the force, f, within the spring is related to the spring's change in length, x, by the spring constant, k, such that $f = kx$. Then, the problem is defined as follows:

- In the *forward problem* both spring constant and the imposed displacement are known; i.e. a spring of known material is being deformed by a known distance, x, and the corresponding force, f, is determined.
- In the *inverse problem* only the imposed displacement and the resultant force are known; i.e. a spring of unknown material (and thus unknown k) is deformed by a distance, x, the corresponding reaction force, f, is measured.

- If the inverse problem is approached *indirectly*, this is typically through an iterative application of the forward problem. In the spring case, a guess is made for the spring constant, k, and a force, f_k, for the given displacement, x, is calculated and compared to the measured force, f. Then, k is altered, and the process is repeated until the difference between f_k and f is minimized.
- An alternative approach is the *direct* approach. In the direct approach the value of k is calculated right from the given displacement and measured force; in the spring example the force is divided by its corresponding displacement to obtain a value of k.

It is clear from even this simple example that each approach has advantages and pitfalls. The forward problem is well-posed: a solution exists, the solution is unique, the solution is smooth (i.e. an alteration in the applied displacement produces a predictable variation the reaction force). The forward problem also requires knowledge about the material which often, especially in the case of complex soft tissues, does not exist. In general, the main advantage of the inverse problem is that it allows for the study of the unknown, requiring only general assumptions about the overall behavior of the material (i.e. linearity in the spring example). Pitfalls of the indirect inverse problem include uniqueness (more than one solution may minimize difference between the theoretical and experimental value), sensitivity (the initial guess utilized for the unknown material constants may drive the fit to a particular solution), and parameter number (the consideration of anisotropy and inhomogeneity within the context of a nonlinear constitutive model increase both the number of parameters to be optimized as well as the number necessary iterations, making it quite expensive computationally). The direct inverse problem is much more efficient and is not dependent on any sort of initial guess, however it is very susceptible to noise and there is no implicit error measurement to quantify goodness of fit. One effective approach to reduce the effects of noise in both forms of the inverse problem, direct and indirect, is to collect multiple data points so as to make the problem over-determined. In the case of the simple spring example this might

mean measuring the force within the spring for ten different displacements (instead of one) and calculating the sum of squared error between the measured and predicted forces for all points (indirect inverse problem) or averaging the calculated spring constant over the full data set (direct inverse problem). In either case, over-constraining the system reduces the susceptibility of the inverse method to noise and increases its predictive capacity.

In the context of a cardiovascular soft tissues, the problem is more complex since the behavior is anisotropic, heterogeneous, and nonlinear (as discussed in the previous section) but the essential problem is the same: the goal is to characterize the mechanical behavior of the material such that the description is applicable to various physiologically relevant loading situations. The objective of the indirect problem is to match the full-field displacement predicted by the pre-determined strain energy equation to that of the experiment by altering the values of the constants within the constitutive law while satisfying the force balance and strain compatibility equations with the given boundary conditions (both traction and displacement). For the direct inverse problem, the objective changes in that the full-field displacement and boundary conditions (both traction and displacement) are used to solve for the constants of the constitutive law by satisfying the force balance and strain compatibility equations. Inverse methods have been applied to cardiovascular soft tissues in a variety of loading modalities.

1.3.1 Indentation

The most widespread use of the static inverse approach applied to soft tissues has been elastography, in which strain images are formed using external compression under static conditions (reviewed by [73–75]). Indentation has been applied to cardiovascular soft tissues to determine heterogeneity through its controlled and repeated application. Most elastographic methods assume linearity (infinitesimal deformation) and isotropy, but a few have been modified to account for the anisotropic, nonlinear behavior strongly exhibited by cardiovascular soft tissues. For example, the heterogeneous nature of the

developing embryonic chick heart has been studied extensively by Taber and colleagues through the coupling of nanoindentation to determine regional stiffness [76,77] and strain tracking of the myocardial surface to determine regional anisotropy [78]. Nonlinearity is considered implicitly in Taber's definition of transverse stiffness, but the addition of anisotropy is through external coupling. Utilizing atomic force microscopy, Costa and Yin [79] investigated the effects of indenter geometry, nonlinear material behavior, and large deformations on soft tissues in a local manner, gathering in-depth information regarding tissue heterogeneity, but failed to include anisotropy in their analysis. While also limited by the assumption of isotropy, the nonlinear inverse elasticity method of Oberai, Barbone, and colleagues [80–83] is perhaps the most compelling in the measurement of heterogeneity. In their study of breast cancer tumors [83], the size, shape, and location of regions within a tissue sample with varying shear moduli were identified with the exceptional clarity. Cox et al. [84], developed an indentation method capable of capturing anisotropy by combining force and deformation gradient data (captured through an inverted confocal microscope). They utilized repeated indentation to quantify the inhomogeneous nature of heart valve leaflet [85], which they coupled with an inverse finite element analysis using a mixed numerical approach to determine local material properties. Nonlinearity was incorporated using a constitutive framework developed by Holzapfel et al. [86]. Chai et al. [87,88] further utilized the methods of Cox to characterize the heterogeneous properties of atherosclerotic plaques, focusing on the drastic differences in the material properties of the various plaque components using a sophisticated inverse finite element analysis method. Other approaches for extracting anisotropic material properties during indentation involve the use of simultaneous indentation and stretch [89] and the use of an indenter with asymmetric geometry [90]. Nonlinearity is typically incorporated numerically, but has also been incorporated analytically as per Humphrey et al. [91]. While indentation is attractive as it can be applied to a tissue specimen locally in a controlled repeatable manner it is less relevant to in-vivo function than other loading modalities.

1.3.2 Inflation

Inflation is also a common modality for the study of inverse mechanics in soft tissues and of blood vessels in particular, as it considers the tissue in a natural loading configuration. Seshaiyer & Humphrey [92] address nonlinearity and anisotropy in their inverse finite element method through the selection of a hyperelastic constitutive equation and manage heterogeneity through the use of homogeneous subdomains, which allow for the estimation of the material properties locally from boundary and inner displacements. The method was utilized successfully in the quantification of the material properties of the lens capsule [93] but was limited to small regions of interest within the tissue and has yet to be applied to the full-field vessel inflation data captured using their advanced experimental technique [94]. Kroon and Holzapfel [67,95] proposed a method for the estimation of the nonlinear elastic properties of anisotropic membranes during inflation for application in cerebral and aortic aneurysm with particular emphasis on the determination of the anisotropy distribution within the material. Their extended method allowed for alternative geometries, the full continuous distribution of material parameters, and was optimized for numerical efficiency but lacked the advanced strain energy function necessary to capture anisotropy [96]. A pointwise identification method for the determination of heterogeneous, nonlinear properties of cerebral aneurysms was, proposed [97], validated [98], and applied to patient specific geometries [99] by Lu and Zhao. Anisotropy was introduced into the model per the method of Kroon and Holzapfel [67,95] allowing for the full characterization of actual aneurysms. Inflation is also often coupled with axial extension in the study of blood vessel mechanics. Einstein and colleagues modeled the pressurization and axial stretch of blood vessels [100] and the inflation of heart valve leaflet [101] using an inverse approach based on successive response surface methodology. The nonlinear, anisotropic inverse approach was able to capture tissue behavior well in both studies; because it could be solved in parallel convergence was achieved rapidly, but it assumed homogeneity along the tissue's surface. In the first study [100], the wall itself was represented as a layered structure, accounting for some transmural differences in properties, but layer thickness and number were

imposed a priori. Kyriacou et al. [102–104] developed an inverse finite element method for the characterization of nonlinear hyperelastic membranes and applied it in both symmetric and asymmetric inflation. While their unique loading apparatus developed both equibiaxial and strip biaxial like strains, shear strain was not achieved. Their investigation into anisotropy was limited, considering only biases in the circumferential and meridonional directions, and homogeneity was assumed along the length of the vessel. A major drawback of inflation is the inability to impose variable strain fields and in particular to shear the tissue. One exception is a unique experimental system capable of imposing torsion described by Humphrey et al. [105], which has not yet led to a new constitutive model or inverse approach [106].

1.3.3 Extension and Shear

The fundamental goal in constitutive modeling is to predict the mechanical response of the material under a variety of physically meaningful loading configurations. In order to ensure that predictions are meaningful, the model itself must be built from data from multiple loading modalities. Planar extension allows for the investigation of the multiaxial behavior of the tissue and the introduction of shear. Cardiovascular soft tissues however, like many soft tissues, have an inelastic response, exhibiting hysteresis in the loading and unloading stress-strain behavior. If material behavior from multiple loading configurations is to be combined properly, some form of preconditioning must be applied such that pseudo-elasticity can be reasonably applied. Nielsen and colleagues [107,108] built a one-of-a-kind multiaxial tester to capture the mechanical behavior of anisotropic, heterogeneous tissues and verified their deformation measurement technique on both an inhomogeneous rubber membrane and sheep diaphragm. In other work by Nielsen [109,110], multiple loading configurations encompassing both indentation and shear were used to investigate the properties of skin. A Tong and Fung relation was fit to the data (errors ranging from ~ 13 to 22%), but the heterogeneous nature of the tissue was not investigated. Flynn et al. [111] present an elegant inverse method to determine anisotropic, nonlinear properties of planar soft tissues subjected to a variety of biaxial

loading conditions which encompass both tension and shear. They utilize the tangent stiffness along with an incremental force-displacement approach to capture the nonlinear behavior of the tissue. The main drawback of Flynn's approach is the need to test multiple specimens from different physical locations to investigate heterogeneity.

Table 1.1 summarizes the capabilities of the methods discussed herein as well as their use of a direct or indirect method and the type of applied load. Cox et al. [84,85,112] have created one of the most comprehensive inverse models for indentation (considering heterogeneity, anisotropy, and nonlinearity), but, in the context of heart valve leaflet, indentation is an unsuitable loading modality. A sophisticated inverse analysis of inflation, a more physiologically relevant loading modality, is provided by Seshaiyer and Humphrey [92], who quantified material properties locally through the use of discrete homogenous subdomains but imposed a distribution of anisotropic material properties. Holzapfel and Kroon [67] developed an alternative inverse approach to inflation including the capacity to describe spatially varying anisotropy but did not address asymmetric loading or geometry. Finally, the work of Flynn et al. [111] brings together the ability to test the material under many physically relevant loading modalities (including shear) with the capacity to quantify material properties for anisotropic, nonlinear materials. The main drawback of Flynn's technique is its inability to handle heterogeneous materials. Regional characterization relies on cutting small homogeneous samples from an intact specimen and mechanically testing each individually.

Although the inverse techniques discussed in this section have proven successful in many cases, the Generalized Anisotropic Inverse Mechanics (GAIM) method (discussed in the next section) addresses gaps in current combined capability. The GAIM method is capable of (1) handling anisotropic materials, (2) computationally segmenting a heterogeneous material into homogeneous subregions (without a priori knowledge of partition location or size), (3) analyzing behavior from many physiologically relevant loading modalities, and (4) performing without the high computational cost associated with repeated forward solutions. In addition, it is one of the main goals of this thesis to

apply GAIM such that it can address the full nonlinear behavior of the material, not just providing metrics describing the regional stiffness and anisotropy of the tissue but solving for its full-field stress and full-field strain energy.

Table 1.1: Summary of different prominent inverse methods including loading modality, direct or indirect nature, and material characteristics.

Method	Inverse Method	Loading Mode	Material Characteristics Considered		
			Anisotropy	Heterogeneity	Nonlinearity
Force-Displacement and Surface Displacement Method of Taber and colleagues [76,77]	Direct	Indentation	In part	✓	✓
Finite Element Model of Costa and Yin [79]	Direct	Indentation		✓	✓
Nonlinear Inverse Elasticity Method of Oberai, Barbone, and colleagues [80–83]	Indirect	Indentation		✓	✓
Mixed Numerical Experimental Method of Cox et al. [84,85,112]	Indirect	Indentation	✓	✓	✓
Subdomain Inverse Finite Element Method of Seshaiyer and Humphrey [92]	Indirect	Inflation	✓	✓	✓
Inverse Finite Element method for Saccular Cerebral Aneurysms by Kroon and Holzapfel [67,95]	Indirect	Inflation	✓	✓	✓
Pointwise Identification Method of Lu and Zhao [97–99]	Direct	Inflation	In part	✓	✓
Inverse Approach Based on Successive Response Surface Methodology of Einstein and colleagues [100,101]	Indirect	Inflation	✓		✓
Inverse Finite Element Method of Kyriacou et al. [102–104]	Indirect	Inflation	In part		✓
Multiaxial Analysis using Tong and Fung model of Nielsen and colleagues [109,110]	Indirect	Indentation, Extension, and Shear	In part		✓
Finite Element Based Method Using Incremental Force-Displacement of Flynn et al. [111]	Direct	Biaxial Extension and Shear	✓		✓
GAIM Method of Raghupathy and Barocas [113]	Direct	Biaxial Extension and Shear	✓	✓	

1.4 Review of Generalized Anisotropic Inverse Mechanics Method

The Generalized Anisotropic Inverse Mechanics (GAIM) method was created by Raghupathy and Barocas [113] to quantify the mechanical behavior of inhomogeneous, anisotropic tissues. As in Seshaiyer & Humphrey [92], heterogeneity is managed by segmenting the sample domain into many homogeneous subdomains, assumed to have uniform properties. However, GAIM is applied not to a series of inflation or indentation tests but to an extensive biaxial extension protocol designed to place every point in the sample under both tension and shear.

The GAIM method requires a paradigm switch in the way we think about biaxial testing. Traditional biaxial experimental testing focuses on homogeneous loading. Connecting the tissue to the machine causes strong heterogeneous deformation near attachment points. Traditional biaxial testing utilizes Saint-Venant's principle and focuses on creating a homogeneous strain field in the central region of the tissue, from which all measurements are then taken [114]. GAIM requires a rich data set of force strain measurements at every location within the material in order to accurately determine parameter estimates. It parses the tissue into homogenous subdomains and in order to distinguish material characteristics, unique information about each subdomain is required. Therefore heterogeneous strain fields and slightly asymmetric sample geometry are desirable. One drawback to this technique is that in order to generate a sufficiently rich set of deformations within each partition that one can solve for the six components of its general linear elasticity tensor, many biaxial protocols are necessary. All possible permutations of extensions are explored [115], leading to the application of 15 separate biaxial protocols to a single specimen. Shear is induced in the sample through asymmetric stretches, allowing a more complete set of experimental strains to be spanned. In GAIM, the equations are combined and solved in a least-squares sense assuming that the material does not change significantly throughout testing. As explained in Chapter 2, a final equibiaxial extension was added to the original GAIM protocol to ensure that the sample's response did not change as a result of this extensive testing.

As for all other inverse methods, GAIM requires certain constraints. The tissue is considered a linear elastic material at static equilibrium and is described by

$$\sigma_{ij,j} = \left(C_{ijkl}\varepsilon_{kl}\right)_{,j} = 0 \tag{1.1}$$

where C is the symmetric fourth-order elasticity tensor, σ is the Cauchy stress, and ε is the linearized strain, $\varepsilon_{kl} = \frac{1}{2}(u_{k,l}+u_{l,k})$ [113,115]. Using the Galerkin finite element method and assuming that C is constant over each element, the problem is restated in terms of a global linear equation

$$M\mathrm{C} = \mathcal{F} \tag{1.2}$$

where C is a column vector specifying the C_{ijkl} parameters of all elements, $\mathcal{F}$ is a column vector of the nodal forces (tractions and reactions), and M is a matrix consisting of the terms that remain when the material parameter terms are factored out, i.e. a combination of the Galerkin basis functions and linearized strain. Every node within the global nodal force balance, equation 1.2, has one equation for each spatial dimension.

A finite element mesh is created to describe the sample domain and then is segmented automatically into homogeneous partitions to manage heterogeneity across the sample surface. All mesh elements within a single partition are assumed to have the same material parameters, i.e. the same elasticity tensor. Least-squares is used to solve the resulting overdetermined liner system

$$\mathrm{C} = (M^T M)^{-1}(M^T \mathcal{F}) \tag{1.3}$$

In the original GAIM method as proposed and validated by Raghupathy [113,116] partitions are determined by probing various choices of homogenous subdomains starting from the gripped boundary. A partition is accepted and its elements are removed from the unsolved element set only if the evaluated parameters result in a residual force norm that is smaller than the preset tolerance.

$$\|\mathcal{F} - M\mathrm{C}\|_2 < tolerance \tag{1.4}$$

This process advances inward towards the center of the sample on the reduced domain with resultant forces from the solved partitions. It continues until no unassigned elements

remain, and the model's performance is evaluated using 95% confidence intervals on all components of $\mathbf{C}$ for each partition. A new partitioning scheme that relies solely on the sample's deformation field is presented in Chapter 4. The new scheme better captures the heterogeneous structure of the tissue analogs studied in [116] as well as the heterogeneous nature of both simulated soft tissue samples and aortic plaque and supraspinatus tendon.

From the six components of the elasticity tensor, the strain eigentensors and the Kelvin moduli associated with each partition are determined. Appendix A details the calculation of the Kelvin moduli. The largest Kelvin modulus is used as a measurement of the stiffness of the tissue because it is related to a stretch in the direction of average anisotropy orientation [36]. The eigenvectors corresponding to the largest Kelvin modulus can be normalized and then projected back to form a strain eigentensor from which the preferred orientation and anisotropy strength are determined. The mechanical characteristics of the entire tissue sample domain are represented by an alignment and stiffness map. The alignment map shows the anisotropy index and preferred orientation for each partition and the stiffness map shows the maximum Kelvin Modulus for each partition. In addition to stiffness and alignment, the degree of tissue heterogeneity can be quantified by calculating the spatial standard deviations, denoted μ (so as not to be confused with stress), of the largest Kelvin modulus, the preferred stiffness direction, and the anisotropy index in each sample.

There is one main drawback in the use of GAIM: it assumes linearity. Cardiovascular soft tissues exhibit markedly nonlinear stress-stretch behavior. Initially, they are quite compliant, but they become much stiffer as stretch increases. In the case of cardiovascular tissues, the presumption of linearity is particularly troublesome since the tissue operates at large strains (~ 30%) physiologically. This work attempts to correct that deficiency without sacrificing the tremendous efficiency advantage of the linear model. First, GAIM is extended to consider large-deformation kinematics of ventricle wall, Chapter 2. Then, a nonlinear closed-form structural model of planar fibrous tissue

mechanics (NSFM) is utilized to describe the nonlinear behavior of rat ventricle wall, Chapter 3. The fitted NSFM model will be used to simulate biaxial extensions of heterogeneous cardiovascular soft tissues. The original partitioning method utilized by GAIM is replaced with a more robust partitioning scheme in Chapter 4. Then, GAIM is applied in a piecewise fashion in order to capture the full nonlinear kinetics of cardiovascular soft tissues in Chapter 5. Finally, experiments characterizing the three-dimensional loading and failure of healthy porcine ascending aorta will be described in Chapter 6. Proposals for multiscale microstructural models (MSM) will also be discussed. We will conclude with a discussion of the incorporation of GAIM's power to characterize planar nonlinear, heterogeneous tissues with the unique ability of the MSM to simulate failure, a fundamentally local phenomenon, Chapter 7.

Chapter 2: Extension of the Generalized Anisotropic Inverse Mechanics Model to Include Nonlinear Kinematics and Application to Rat Right Ventricle

This work was a part of the paper:
Mechanical Changes in the Rat Right Ventricle with Decellularization
Journal of Biomechanics, 2012, 45 (5)
Witzenburg, C.M., Raghupathy, R., Kren, S.M., Taylor, D.A., and Barocas, V.H.

2.1 Motivation of Research

The GAIM method was applied to soft tissue analogs [116] that were created such that they were both isotropic, polydimethylsiloxane (PDMS), and anisotropic, collagen tissue equivalents (TE). In addition, both homogeneous and heterogeneous samples were created in terms of stiffness, PDMS, and anisotropy, collagen TE. The largest Kelvin modulus, preferred stiffness direction, and anisotropy index were determined for each region of each sample. Results matched the material properties determined experimentally both structurally (quantitative polarized light imaging for collagen TE) and mechanically (Young's modulus calculation from uniaxial extension) well. The goal of the work in this chapter was to apply GAIM to full-field deformation and force measurements made on cardiovascular tissue specimens, in this case right rat heart ventricles. Since all cardiovascular soft tissues, including rat heart ventricle, are highly deformable, GAIM was modified to account for large-deformation kinematics, i.e. the infinitesimal strain was replaced by the Green strain and the stress balance was restated in terms of the 2nd Piola-Kirchoff Stress rather than the Cauchy stress. In addition to the extension of GAIM, it was the goal of this work to determine the mechanical consequences of the removal of the cellular content of the ventricle by perfusion decellularization. There was concern that since the decellularizing agent is not applied uniformly by perfusion, local changes in tissue anisotropy and/or stiffness could arise.

The stiffness, anisotropy, and heterogeneity of freshly dissected (control) and perfusion-decellularized rat right ventricles were compared using the extended GAIM method. Cruciform tissue samples were speckled and then tested under a series of different biaxial loading configurations with simultaneous force measurement on all four arms and displacement mapping via digital image correlation. Based on the displacement and force data, the sample was segmented into piecewise homogeneous partitions. Tissue stiffness and anisotropy were characterized for each partition using a large-deformation extension of the general linear elastic model. The perfusion-decellularized tissue had significantly higher stiffness than the control, suggesting that the cellular contribution to stiffness, at least under the conditions used, was relatively small. Neither anisotropy nor heterogeneity (measured by the partition standard deviation of the modulus and anisotropy) varied significantly between control and decellularized samples. Therefore, we concluded that although decellularization produces quantitative differences in modulus, decellularized tissue can provide a useful model of the native tissue extracellular matrix and further, that the large-deformation extension of the GAIM method can be used to quantify regional variation in stiffness and anisotropy of cardiovascular soft tissues.

2.2 Introduction

A bioartificial heart is a possible alternative to transplantation or a mechanical left ventricular assist device. Whole-organ perfusion-decellularization has been established as a potential tool to produce an intact three-dimensional scaffold for bioartificial hearts [117–119]. Separating the cells from the extracellular matrix also provides the opportunity to study cardiac wall mechanics in a simplified system, and attribute myocardial tissue properties to the respective cellular/extracellular constituents. For instance, localized matrix injury or scarring that occurs in myocardial infarction [35,59] could be studied on the extracellular matrix with decellularized tissue.

Previous studies of healthy and/or infarcted myocardium have focused on constitutive modeling of small samples cut from different locations to assess heterogeneity while assuming homogeneity in each sample (e.g. [41,120]). Assessing heterogeneity by means of multiple samples is impossible, however, if the entire tissue is too small. For example, the ventricle of the Sprague-Dawley (SD) rat, a popular choice for myocardial decellularization experiments [117], is only about 10mm across and not amenable to assessment of heterogeneity with samples cut from different locations. Although indentation could be applied regionally (as discussed in Chapter 1), it is less relevant to in vivo function. An experiment in which heterogeneous properties could be extracted from a single sample during biaxial loading would be far more valuable.

The GAIM method [113,116] enables study of heterogeneous, anisotropic tissues, like the ventricle, by dissecting small samples computationally rather than physically. GAIM directly solves the finite element representation of the stress balance in the tissue for the unknown components of the two-dimensional general linear elasticity tensor. Heterogeneity within the sample is managed by partitioning the sample into many subdomains, each assumed to have uniform properties. In this study, we utilized multiple biaxial tests and an extended version of GAIM to determine the mechanical properties of freshly dissected (control) and decellularized right ventricles from SD rats. We focused on the right ventricle due to the prohibitively large thicknesses of control left ventricle samples.

Two hypotheses were tested. First, since the extracellular matrix, particularly collagen, plays a large role in tissue mechanical behavior [121], and since decellularization reduces tissue volume considerably with negligible collagen loss [117], we hypothesized that *decellularized samples would have larger stiffness values for the right ventricle as measured by our methods*. We expected this increase in stiffness to be proportional to the thickness reduction, as observed previously [117]. Second, based on minimal changes in the collagen structure following decellularization, we hypothesized that *decellularized samples would not exhibit a change in degree of mechanical anisotropy or heterogeneity*.

2.3 Methods

2.3.1 Sample Preparation

Whole cadaveric rat hearts were removed from ten adult female SD rats (9–13 weeks) for testing. All experiments were performed in accordance with US Animal Welfare Act and

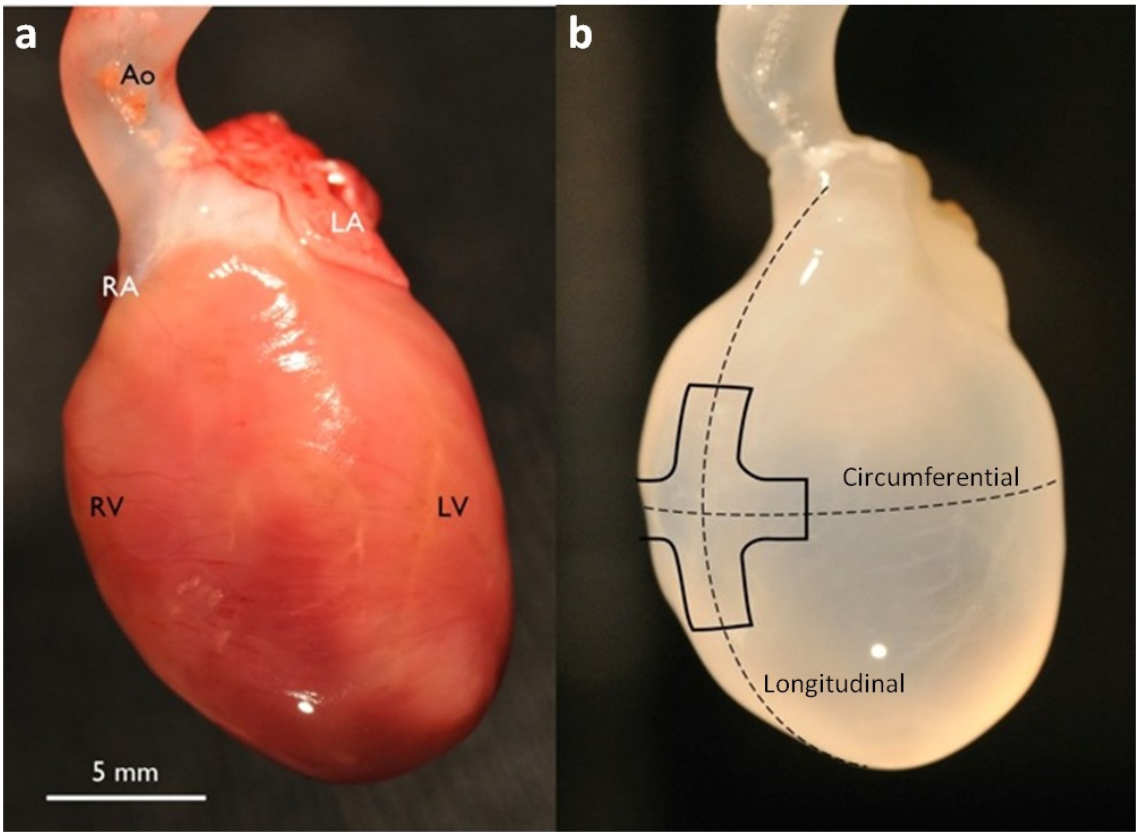

Figure 2.1: Sample geometry. (a) Rat heart during decellularization. Labels indicate aorta (Ao), right atrium (RA), left atrium (LA), right ventricle (RV), and left ventricle (LV). (b) Sketch of sample geometry overlaid on fully decellularized rat heart, showing the circumferential and longitudinal directions.

were approved by the Institutional Animal Care and Use Committee at the University of Minnesota. Five hearts underwent perfusion decellularization prior to ventricle dissection and five immediately underwent ventricle dissection (control). One sample from each group was discarded due to damage during experimentation; therefore, four samples from each group were analyzed. Measurements of live rat body weight prior to dissection

showed no significant difference (p = 0.28) between groups. Unless otherwise stated, all p-values reported in this chapter refer to unpaired two-tailed t-tests.

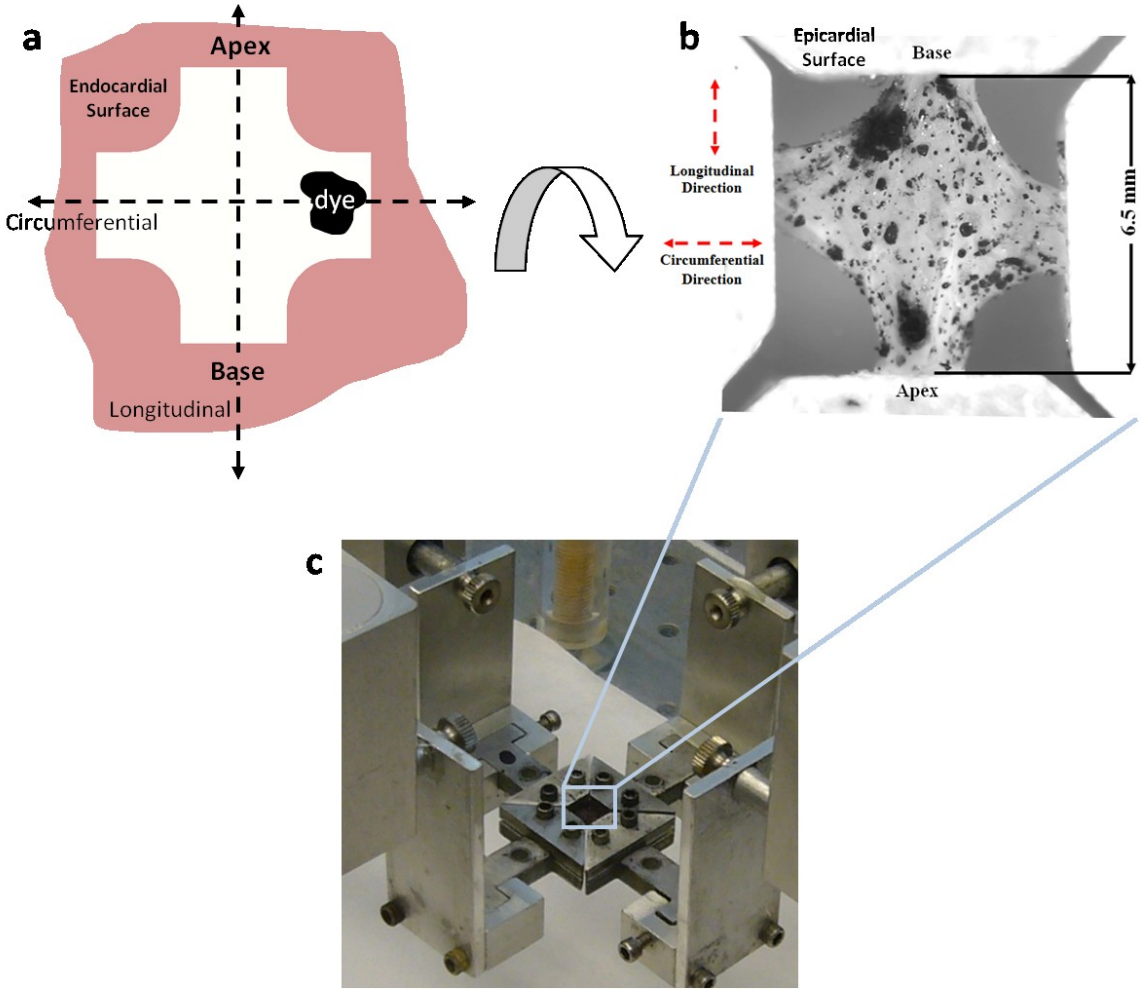

Figure 2.2: Sample dissection and clamping. (a) Schematic showing the anatomical position of the tissue during punching. (b) Epicardial surface of a representative decellularized right rat ventricle after clamping and speckling. (c) Clamping configuration during biaxial testing. The sample is submerged in 1% phosphate buffered saline at room temperature.

For decellularization, hearts were placed in a modified Langendorff apparatus and perfused through the coronary arteries with 1% sodium dodecyl sulfate (SDS) in water for 20 h, as described previously [117]. Each heart was then perfused with 60 ml deionized water, 60 ml 1% Triton-X100 in water, and 60 ml additional deionized water to flush the detergent. The hearts were then perfused with 500 ml phosphate buffered saline (PBS) in 5 aliquots, leaving only decellularized matrix behind. Figure 2.1 shows a rat

heart during decellularization and depicts where samples were cut from the right ventricle. Sample geometry is shown in Figure 2.1b.

The right ventricle was dissected from each heart and laid flat. A punch was used to cut each sample into a cruciform shape for biaxial testing. Anatomical orientation was marked on the endocardial surface as shown in Figure 2.2a. Samples were stored in 1% PBS at 4°C when not undergoing biaxial testing or thickness measurement. Sample thickness was measured by laser micrometer 5 min after removal from PBS.

2.3.2 Biaxial Testing

Samples were tested within 48 h of dissection. Verhoeff's stain was used to texture the epicardial surface for optical strain tracking (Figure 2.2b). The textured sample was attached to an Instron biaxial tester with four 5 N load cells via a custom rig that allowed easy sample mounting and immersion in 1% PBS at room temperature for the duration of testing (Figure 2.2c).

A series of biaxial protocols was applied to each sample. First, a slight preload, ~ 0.01 N, was applied to each cruciform arm. The grip forces were zeroed with respect to the preload. The sample was preconditioned with nine equibiaxial extensions; each of the four arms was extended 0.75 mm. Each loading and unloading cycle lasted 10 s. After preconditioning, fifteen separate displacement-controlled biaxial experimental extensions were performed (Figure 2.3). Unlike traditional mechanical tests, which are designed to maximize homogeneity of the strain field, our protocol was designed to produce many heterogeneous strain fields and to vary that heterogeneity over different tests. Heterogeneous, variable strain fields are necessary to provide detailed deformation data for GAIM, and using numerous fields improves the accuracy of parameters. An additional equibiaxial extension was performed at the end of testing to confirm that minimal damage had occurred during the experiment. During testing, images of the epicardial surface of the tissue and the forces at each grip were recorded.

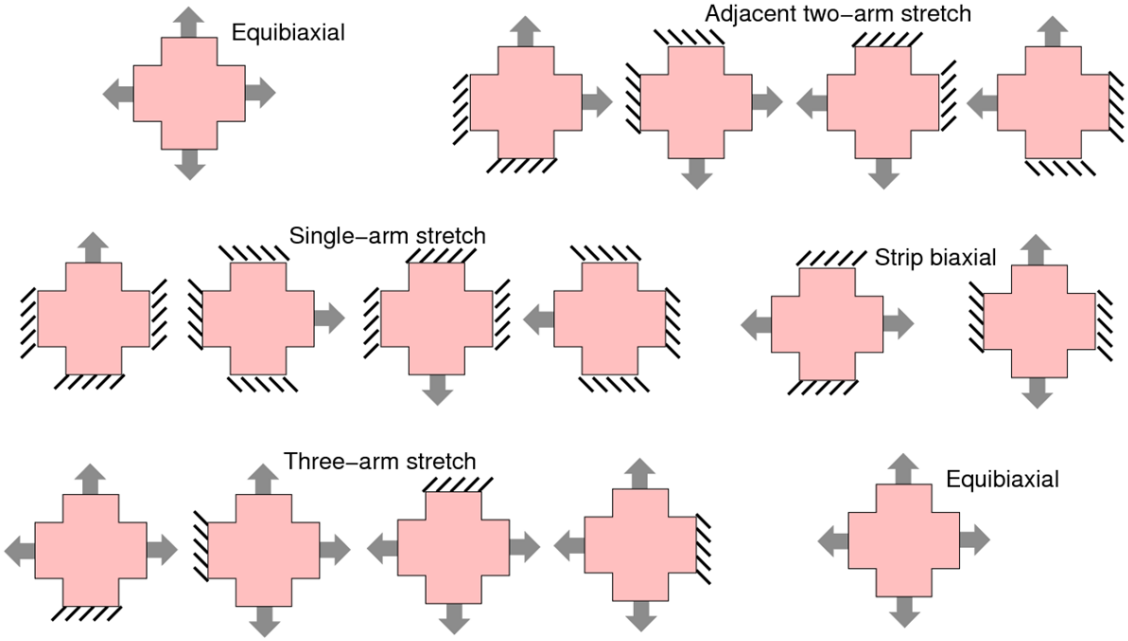

Figure 2.3: Protocol used for the biaxial testing of each sample. Dashed lines indicate fixed arms. Equibiaxial: each arm moved 0.75 mm. Adjacent two-arm stretch: extended arms moved 1.0 mm. Single–arm stretch: extended arm moved 1.0 mm. Strip biaxial: extended arms moved 0.75 mm. Three-arm stretch: middle extended arm moved 1.0 mm, other extended arms moved 0.75 mm.

2.3.3 Image Analysis and Strain Tracking

Digital video of ventricle deformation was obtained at 24 fps, 1080p HD resolution, and spatial resolution of ~ 96 pixels/mm. The video was synchronized and downsampled to construct grayscale image sequences corresponding to the loading curves of each test. The image at the end of preconditioning was used as the reference configuration. The tissue boundary was sketched on top of the reference image in Abaqus™, and meshed with quadrilateral elements. Successive pairs of images were correlated to track the movement of the mesh nodes throughout the loading sequence. This image correlation method was developed by Raghupathy [115] and used successfully in [116]. Displacement fields were constructed from movement of locations corresponding to the mesh nodes and smoothed to reduce noise. Green strains were computed from cumulative displacement fields by standard finite element theory for bilinear quadrilateral elements. We estimated the accuracy of our displacement calculations by digitally deforming the image of Figure 2.2b and comparing the displacements obtained from image correlation

with analytical values. Displacements were accurate to ± 0.06 pixels and the strains to ± 0.0026 (95% CI).

2.3.4 Generalized Anisotropic Inverse Mechanics (GAIM)

Regional mechanical properties were determined by an extension of our GAIM method [113,116]. The method, presented in more detail in our previous work, involves solving the direct inverse problem for a general linear elastic solid. That is, given the displacement data and forces on the sample grips, the method uses finite elements to solve the linear elastic stress balance $\left(C_{ijkl}\varepsilon_{kl}\right)_{,j} = 0$ for the components of C. The domain is partitioned into regions, over each of which C is taken to be a constant. The partitions are optimized so as to minimize error in the force balance while maintaining tight confidence intervals on the components of C [113]. All experiments within the protocol are evaluated concurrently to produce a large, overdetermined system of linear equations for C.

For highly deformable tissues such as myocardium, a formulation that accounted for large-deformation kinematics but maintained the generality, anisotropy, and linearity of the regression problem from our previous work was desired. We modified our original form to

$$S_{ij} = K_{ijkl}E_{kl} \qquad 2.1$$

where S is the 2nd Piola-Kirchhoff stress, E the Green strain, and K is an elasticity tensor analogous to C in linear elasticity and has the same major and minor symmetries. The stress balance is

$$\left(F_{mi}S_{ij}\right)_{,j} = \left(F_{mi}K_{ijkl}E_{kl}\right)_{,j} = 0 \qquad 2.2$$

where F is the deformation tensor, and differentiation is with respect to the undeformed coordinates. Equation 2.2, although nonlinear in the displacements, is linear with respect to the components of K, so the problem can be treated with linear regression theory [113]. Thus, the nonlinear kinematics are incorporated into the analysis, but the fitting

problem remains linear. Appendix B details the changes to the inverse matrix formulation.

In our earlier work, the tensor C was used to identify the major features of the tissue. Specifically, the eigentensors of C represent principal states of stress and strain [122,123], and the corresponding eigenvalues (Kelvin moduli) provide measures of material stiffness. We have found [116] that the largest Kelvin modulus is a useful measure and was comparable to Young's modulus for polydimethylsiloxane. A second important measure comes from the eigenvectors of the eigentensor corresponding to the largest Kelvin modulus. These eigenvectors describe the anisotropy of the material, with the direction corresponding to the larger eigenvalue aligning with the tissue preferred stiffness direction in theoretical studies [113], on a simple fiber model [124], and in experiments on cell-compacted collagen gels [116].

In this chapter, we computed large-deformation analogs of the Kelvin moduli (henceforth simply ''Kelvin moduli'' for brevity) and corresponding principal directions that give the preferred stiffness direction (θ) per a procedure analogous to that presented in Appendix A. In addition, the eigenvalues of the principal eigentensor of K, λ_1 and λ_2, were converted into an anisotropy index (r), indicating strength of the alignment. It varies from 0 for an isotropic sample to 1 for a perfectly aligned sample:

$$r = \frac{|\lambda_1| - |\lambda_2|}{|\lambda_1| + |\lambda_2|} \tag{2.3}$$

In addition to stiffness and alignment, we quantified tissue heterogeneity by calculating the standard deviation of each variable over all partitions within the center of the sample. That is, each partition was treated as an independent measurement, and the standard deviation was calculated. We refer to this value as the ''partition standard deviation'' to avoid confusion with measures of sample-to-sample variability.

2.4 Results

Right ventricle wall thickness was 2138 ± 527 μm (mean ± 95%CI) for controls and 381 ± 157 μm for the decellularization group ($p < 10^{-4}$). The drastic difference is stiffness was expected since cellular material comprises much of the tissue volume. When the first and final equibiaxial protocol strain maps were compared they showed extremely similar patterns and values. Figure 2.4 shows the full-field strain and load data for the first and final equibiaxial protocols for an alternative representative sample. There was no significant difference between the protocols in peak force for any arm of any sample ($p > 0.1$ for all samples, paired two-tailed t-test).

Loading behavior for the representative sample of decellularized tissue (Figure 2.2b) is shown in Figure 2.5. Figure 2.5b and c highlight a displacement-controlled equibiaxial test and single-arm extension test. For equibiaxial loading, the circumferential arms, right and left, had higher loads than the longitudinal arms, top and bottom. Shear forces were responsible for the discrepancy in force between opposite arms. The single-arm extension involved displacement of the right arm, as indicated by large forces on that arm and the reduced response of the left arm. Forces on the top and bottom arms were small in comparison.

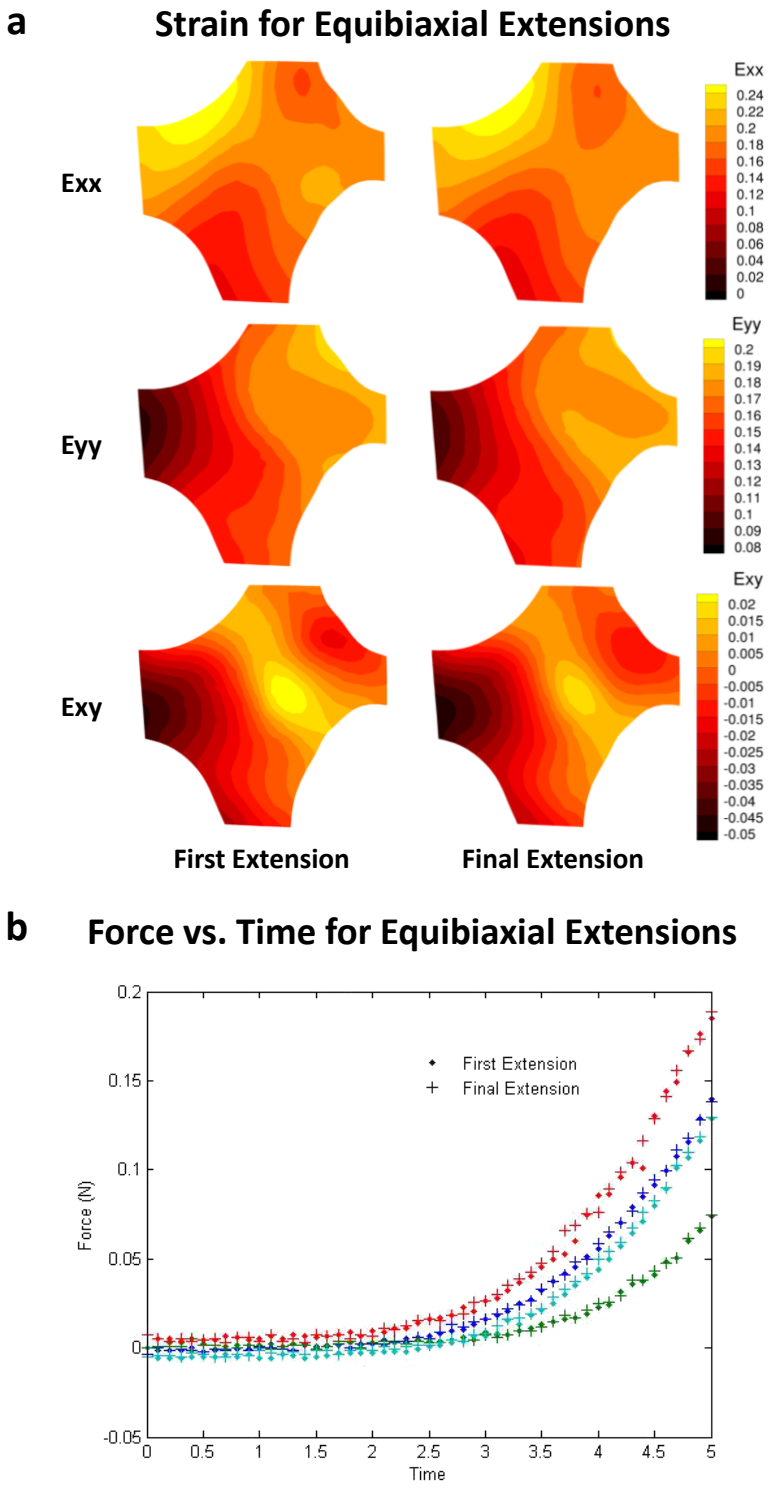

Figure 2.4: Representative (a) strain and (b) load data for an alternative sample. (a) The strain fields for the first and final experimental protocols are strikingly similar in both magnitude and pattern for normal strains as well as shear. (b) There is also a minimal change in the loading curves for the four arms of the test machine.

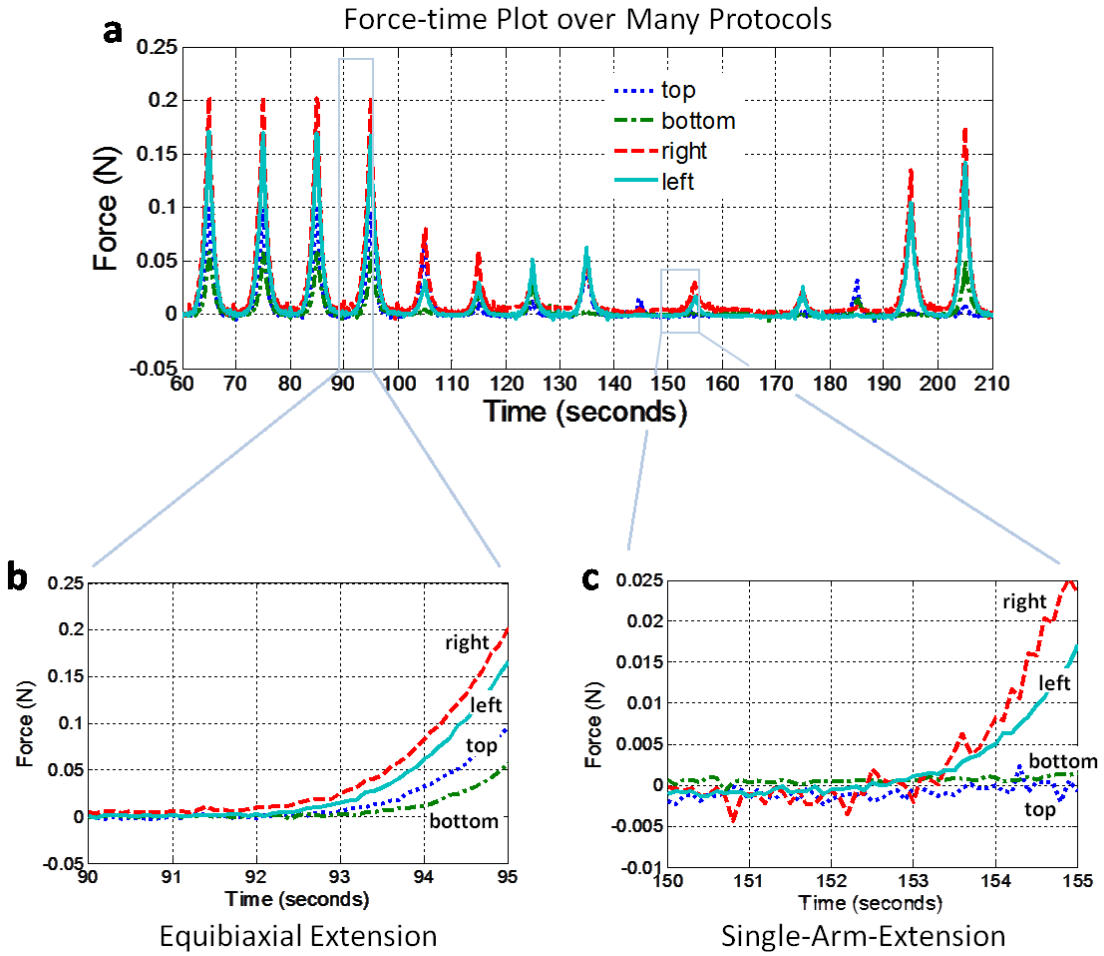

Figure 2.5: Representative load data for the decellularized sample shown in Figure 2.2b. (a) Three of nine preconditioning cycles are shown followed by the equibiaxial protocol, four adjacent two-arm extension protocols, four single-arm extension protocols, two strip biaxial protocols and one three-arm extension protocol. Other protocols not shown. (b) During equibiaxial loading, significant forces were generated in all four arms, with higher forces in the circumferential (left–right) direction because of tissue anisotropy. (c) When only the right arm was displaced, all forces were much smaller, and circumferential forces were much larger than longitudinal forces.

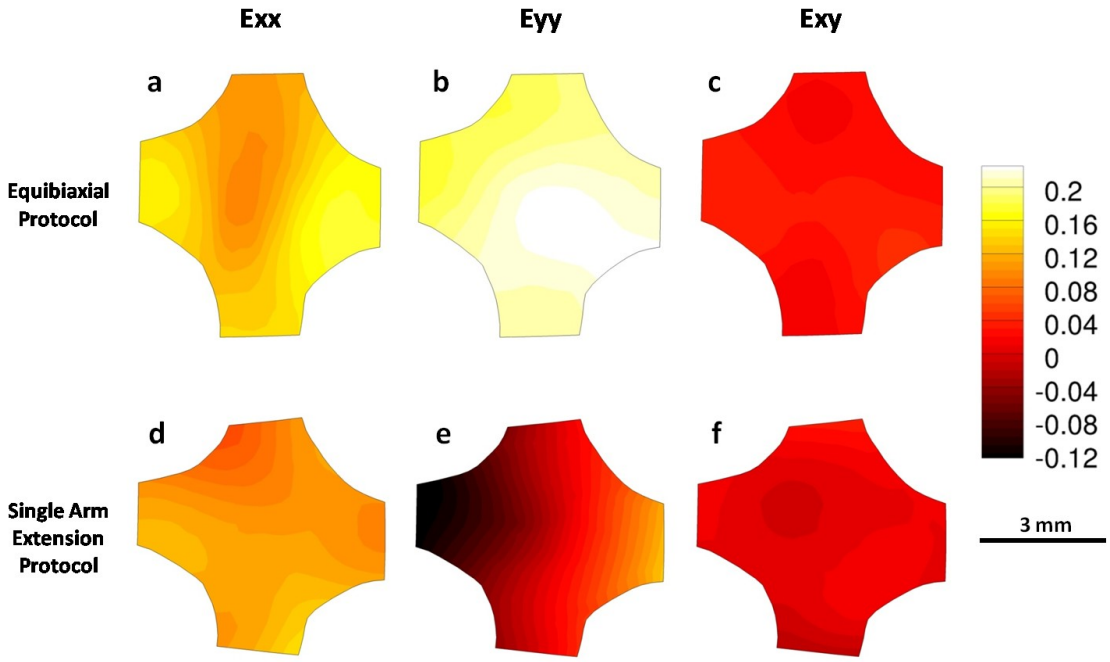

Figure 2.6: Representative strain results for the decellularized sample shown in Figure 2.2b. Strains are overlaid on the deformed sample shape at maximum deformation. During equibiaxial loading (a, b), the vertical strain (E_{yy}) was larger than the horizontal strain (E_{xx}) in the central region of the sample. During single-arm loading (d, e), E_{xx} was larger in the central region of the sample. Also, there was a gradient in the central region of the sample in the map for E_{yy}. In both cases, there was relatively little shear strain (c, f).

For the same sample, the Green strains - E_{xx}, E_{yy} and E_{xy} - at peak displacement for both equibiaxial and single-arm extension tests are shown in Figure 2.6. For the equibiaxial test, strain was larger in the vertical direction than in the horizontal direction in the central region of the sample. This effect was reversed for the single-arm extension test. Also, E_{yy} showed a strong horizontal gradient across the central region of the sample for the single arm extension (Figure 2.6e). Thus, as desired, strain fields were heterogeneous and the strain differed within the same region of the sample from one protocol to another. For both tests, however, there was relatively little shear strain.

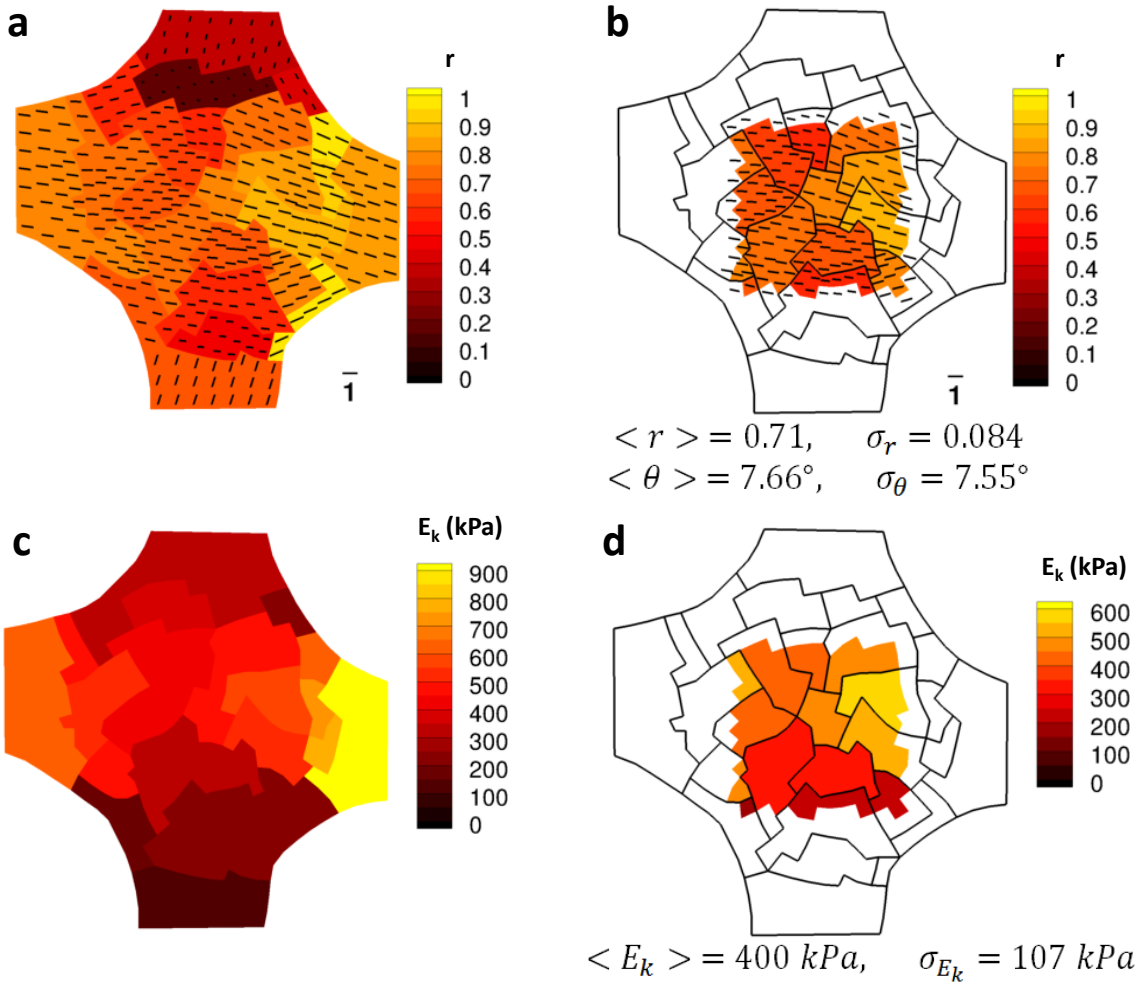

Figure 2.7: Representative alignment and stiffness results from GAIM for the decellularized sample shown in Figure 2.2b. Results are overlaid on the undeformed shape. For the alignment maps (a, b), the color shows the anisotropy index, and the vectors indicate the preferred stiffness direction, with vector lengths corresponding to the anisotropy index. For the stiffness maps (c, d) the contour shows the maximum Kelvin modulus. (a) Alignment map shows roughly uniform alignment in the center of the sample. (b) There was strong circumferential alignment in the central region of the tissue, $< r >= \mathbf{0.71}$, with low partition standard deviation $\sigma_r = 0.084$, and $< \theta >= \mathbf{7.66°}$, with a low partition standard deviation of $\sigma_\theta = 7.55^0$. Black blocks indicate partition domain. (c) Stiffness map shows roughly uniform E_k in the center of the sample. (d) The average value of the maximum Kelvin modulus within the central region of the sample, $< E_k >= 400\ kPa$, and the partition standard deviation, $\sigma_{E_k} = 107\ kPa$. Black blocks indicate partition domain.

Alignment and stiffness maps were calculated for each sample using the extended GAIM method. Figure 2.7 shows maps for the sample pictured in Figure 2.2b. The arms of the sample present as artificially aligned in the pull direction as a result of our inability to measure transverse forces on the grips and minimal transverse displacement in the arms.

However, the central region of the sample is well-specified, so our analysis focuses only on the central region (Figure 2.7b, d).

Figure 2.7a shows strong circumferential (i.e., left–right) alignment in the central region. The average value of the anisotropy index within the central region (Figure 2.7b) was 0.71, indicating strong anisotropy (roughly five times stiffer in the preferred, i.e. circumferential, direction). The partition standard deviation for the anisotropy index was low, 0.084. The average value for the preferred stiffness direction within the central region was 7.66° from the horizontal, and its partition standard deviation was 7.55°. Figure 2.7c shows the maximum Kelvin modulus within each region. The average value of the maximum Kelvin modulus within the central region (Figure 2.7d) was 400 kPa, and its partition standard deviation was 107 kPa.

Figure 2.8 summarizes the GAIM results for this study. Figure 2.8a–c show the average values of maximum Kelvin modulus, $< E_k >$, anisotropy index, $< r >$, and preferred stiffness direction, $< \theta >$, over the central region. There was significant difference between $< E_k >$ for the control and decellularized groups (p = 0.0003), indicating that the central region of the decellularized tissue was stiffer than that of the control. However, there was no significant difference between $< r >$ or $< \theta >$ for the control and decellularized groups (p = 0.06, p = 0.31), indicating no change in strength or direction of anisotropy. All samples were stiffer in the circumferential than the longitudinal direction.

Figure 2.8d-f show the normalized partition standard deviations of the maximum Kelvin modulus, $\sigma_{E_k}/< E_k >$, anisotropy index, $\sigma_r/< r >$, and preferred stiffness direction, $\sigma_\theta/< \theta >$, over the central region. These values were used to quantify the degree of heterogeneity of the parameters. For all three measures of heterogeneity (associated with stiffness, degree of anisotropy, and preferred direction) the control and decellularized samples gave statistically indistinguishable results (p = 0.22, 0.76, 0.11), indicating no significant change in heterogeneity between the decellularized and control groups.

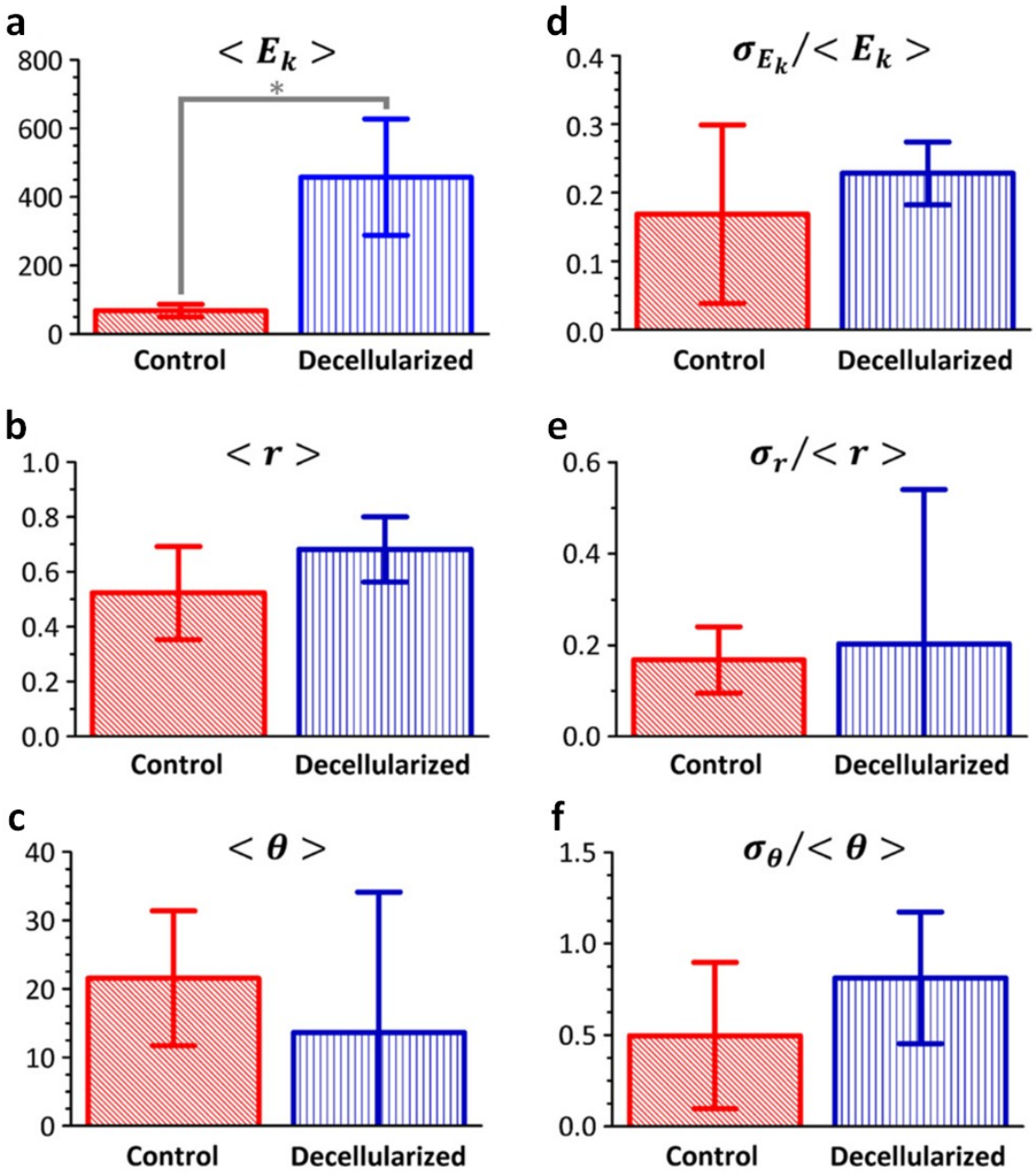

Figure 2.8: Stiffness, alignment and direction results for full study. (a) There was a significant difference between the control and decellularized groups in $< E_k >$, which indicates overall stiffening of the tissue with decellularization. Units of $< E_k >$ are kPa. (b, c) No significant difference in $< r_k >$ or $< \theta >$ was found between the control and decellularized samples, indicating minimal change in anisotropy. Units of $< \theta >$ are degrees and $< r >$ is unitless. (d, e, f) No significant difference was found between the normalized partition standard deviation of the maximum Kelvin modulus, anisotropy index or preferred stiffness direction. This indicates that the effect of decellularization is roughly uniform. All plots show mean ± 95% CI, $n = 4$.

2.5 Discussion

The major technical advance of this work was introduction of a nonlinear kinematic framework to the GAIM technique. The new formulation, which relates the second Piola-Kirchhoff stress to the Green strain linearly, maintains the efficiency of a linear regression model (i.e., the model is linear in the coefficients) but is suitable to large deformations often experienced by soft tissues. By doing so, we extended the potential applicability of the method to a wider range of soft tissue applications. The generalized model is not sufficient to capture many soft tissue behaviors, including the large toe region followed by a sharp rise in stiffness, but it provides a qualitative estimate of the material properties and, most importantly, an assessment of material anisotropy in different regions of an intact sample.

The major conclusions of this work as to the tissues tested were as follows: (1) The stiffness of right ventricular tissue, as measured by the average of the largest Kelvin modulus over the sample's center, increased by a factor of 6.7 with decellularization. This change was consistent with densification of the tissue (average 5.6-fold reduction in thickness) and was similar to that reported by others for decellularized cardiac tissue [117,125]. Although other factors (e.g., chemical interactions between decellularizing agents and the extracellular matrix) could be important, we attribute the slightly larger increase in stiffness than decrease in thickness to structural changes, specifically rotation of collagen fibers into the plane of testing. (2) The mechanical anisotropy of the tissue, which we have shown previously [116] to correlate to structural anisotropy, was largely unchanged by the decellularization process. (3) Finally, a key goal of this work was to assess tissue heterogeneity. We found that the spatial variation in tissue properties (stiffness, degree of anisotropy, and preferred stiffness direction) over the central region of the sample was largely unchanged by the decellularization process. Based on these three observations, we conclude that decellularized tissue can be used as a model for studying mechanical changes to the extracellular matrix in the heart. The decellularized model is particularly attractive for studies of rat left ventricle, which is sufficiently thick

(~ 4 mm) relative to the other tissue dimensions (~ 10 mm) that planar biaxial tests would be of questionable validity. In the decellularized sample, the thickness is 5–10% of the in-plane dimensions, making the assumptions underlying planar biaxial tests much more acceptable. Of course, the decellularized model does not allow for the study of the cells, but the combination of the decellularized system and GAIM analysis could allow assessment of mechanical consequences of ventricular remodeling (e.g., scar formation) without isolation of the remodeled tissue. Another potential advantage of the decellularized model is that, by virtue of being thinner, it would be less prone to artifacts from the flattening prior to planar biaxial tests.

The significant anisotropy of the right ventricular tissue is consistent with previous work [117] showing that both control and decellularized left ventricle were stiffer in the circumferential than longitudinal direction in equibiaxial tests and with previous studies of right ventricular properties (e.g. [53]). Ott et al. [117] performed biaxial tests on samples cut from cadaveric vs. decellularized left ventricle. Decellularized samples had significantly larger tangent moduli than their intact cadaveric counterparts. When adjusted for thickness, the significant difference in tangent moduli vanished, similar to our observations. Ott did not attempt to assess differences in anisotropy or heterogeneity. Figure 11 of Ghaemi et al. [53] appears to have a ratio of about 10:1 in stress between the two directions at 20% equibiaxial strain of bovine right ventricular wall. The Ghaemi study used hooks rather than clamps, but a 10:1 stress ratio would correspond to a very large value of r in our analysis, roughly 0.8 (the exact value would depend on the results of non-equibiaxial tests). Our calculated value of $< r > = 0.52$ for the cadaveric right ventricle samples is much lower. This difference is most likely due to our use of full-thickness samples in comparison with the use of samples extracted from the mid-one-third section of the heart by Ghaemi.

Although the decellularized tissue model is a simpler than the intact tissue, there remain questions to be considered. Variation in fiber orientation through the thickness of the myocardium (along with any contribution from the epicardium and endocardium) is

particularly important. The fiber angle changes continuously transmurally through the myocardium, with the average through-thickness fiber orientation of both ventricles in the circumferential direction. In addition, both the endocardium and the epicardium exhibit higher stiffness in the circumferential direction [43,44]. Due to the whole-organ perfusion-decellularization technique used we could not excise tissue from the midwall, as is standard for biaxial testing of ventricular tissue, for the decellularized sample group. Therefore, we tested full thickness samples from both groups, and our results must be considered as mean through-thickness descriptions. In our planar analysis, we assumed that the displacement was uniform through the tissue thickness, a reasonable but not necessarily correct assumption; further work is underway to track motion through the thickness as well as on the epicardial surface. Again, the properties calculated in this study must be seen as a transmural average of the properties of the decellularized tissue since there is no way to assess contribution from different layers.

To summarize, the current work has demonstrated that, in the right ventricle, decellularized tissue can provide a useful model of the native tissue extracellular matrix. Decellularization causes an increase in the metric describing stiffness, but when adjusted for the thickness decrease this effect is greatly reduced. There was no significant change in anisotropy or heterogeneity. A natural next step would be to apply the methods to the left ventricle (which is similar, [2,126]), where scarring and remodeling are of great interest. The GAIM technique is able to assess property variation within a tissue analog [116] and, with the improved kinematic framework developed herein, it can be applied to more complex problems of ventricular tissue mechanical characterization, especially in small-animal models, for which it may be difficult if not impossible to isolate a homogeneous sample of sufficient size for biaxial testing.

Chapter 3: Utilizing the Closed-Form Nonlinear Structural Model of Planar Fibrous Tissue Mechanics to Describe Rat Ventricle

3.1 Motivation of Research

GAIM was modified to account for large-deformation kinematics, but this modification still uses a linear relation to describe the material; essentially ignoring the nonlinear kinetics. In order to develop and validate a model including nonlinear kinetics, *in situ* experiments were necessary. In this study, we fit a closed-form nonlinear structural fiber model (NSFM) of planar tissue mechanics to biaxial behavior of decellularized rat ventricular tissue.

3.2 Introduction

Fundamental differences exist in the size and performance of male and female hearts. Even after adjustments for height and body surface area, the left ventricle of a healthy male is larger in both volume and mass [127]. Differences also exist in contractile performance between papillary muscle from male and female rats, with male rats showing slower responses in both isometric and isotonic tests [128]. It is less clear, however, whether the underlying structure or mechanical properties vary between the sexes as well. Of particular interest is the extracellular matrix (ECM) of the ventricular wall, which provides structural stability to the heart, and can be isolated by perfusion decellularization [117]. The objective of this study was to test perfusion decellularized rat left ventricular tissue biaxially to determine whether its mechanical characteristics vary with sex.

3.3 Methods

3.3.1 Sample Preparation

Whole rat hearts were removed from eleven male and eight female adult Sprague-Dawley (SD) rats (9-13 weeks). All experiments were performed in accordance with US Animal Welfare Act and were approved by the Institutional Animal Care and Use Committee at the University of Minnesota. Hearts were placed in a modified Langendorff apparatus and perfusion decellularized, as described previously [117]. The left ventricle was dissected from each heart and laid flat. A punch was used to cut each sample into a cruciform shape for biaxial testing and anatomical orientation was marked on the endocardial surface. Figure 3.1a shows a rat heart following decellularization and depicts where samples were cut from the left ventricle. Samples were stored in 1% PBS at 4°C when not undergoing biaxial testing or thickness measurement. Sample thickness was measured by laser micrometer 5 min after removal from PBS.

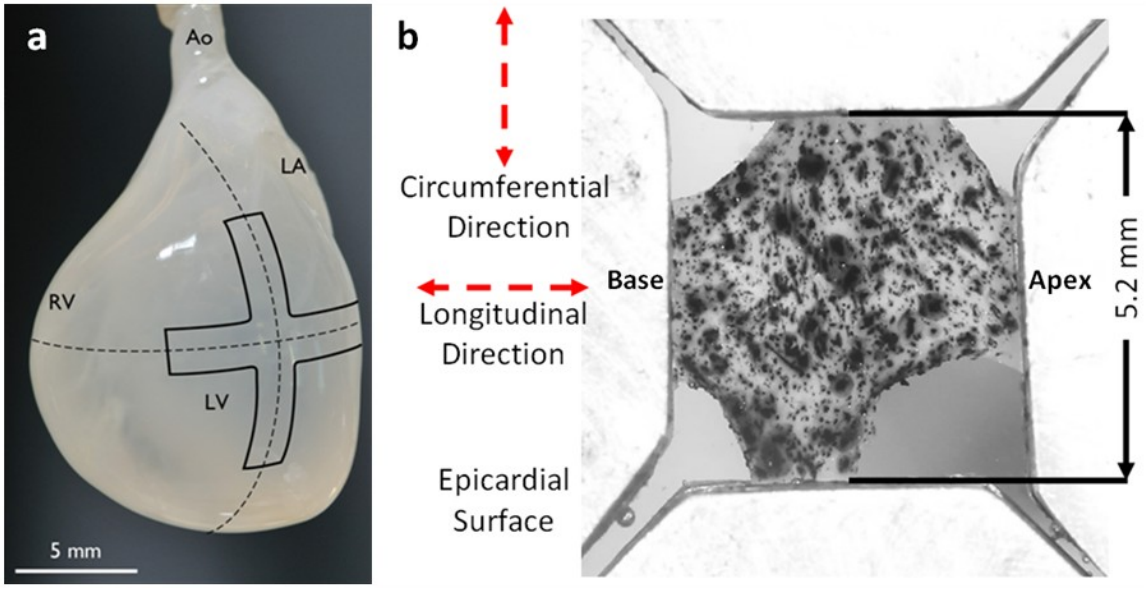

Figure 3.1: (a) Sketch of sample geometry on a fully decellularized rat heart. (b) Epicardial surface of a male decellularized left rat ventricle after clamping and speckling.

3.3.2 Biaxial Testing

Samples were tested within 48 h of dissection. The epicardial surface of each sample was textured for optical strain tracking using Verhoeff's stain, Figure 3.1b. The textured sample was attached to an Instron biaxial tester with four 5 N load cells via a custom rig that allowed easy sample mounting and immersion in 1% PBS at room temperature for the duration of testing. First, a slight preload, ~ 0.01 N, was applied to each cruciform arm and the grip forces were zeroed with respect to the preload. The sample was preconditioned with nine equibiaxial extensions; each of the four arms was extended 0.75 mm. Then, a series of displacement-controlled biaxial extensions were performed per our previous study [129]. Only three extensions were used in the analysis: equibiaxial, vertical strip biaxial and horizontal strip biaxial. At the end of testing, a final equibiaxial extension was performed to confirm minimal damage had occurred. During testing, the forces at each grip were recorded and deformation was captured with digital video at 24 fps, 1080p HD resolution, and spatial resolution of ~ 88 pixels/mm. Displacement fields showing the movement of the sample surface were generated using digital image correlation [115,129].

3.3.3 Closed-Form Nonlinear Structural Fiber Model of Planar Tissue Mechanics (NSFM)

A nonlinear fiber model was selected to fit the data due to its basis in fiber structure and physically meaningful parameters [124]. Briefly, it considers contributions from a population of fibers in which the constituents are assumed to deform affinely and stresses are assumed to be additive. The fiber population is represented by a bidirectional von Mises distribution,

$$f(\theta;\kappa,\mu) = \frac{1}{\pi I_0(\kappa)} \exp\{\kappa \cos[2(\theta-\mu)]\}, \qquad \theta \in [0,\pi) \tag{3.1}$$

where κ signifies the degree of anisotropy, and μ is the preferred fiber direction. The constitutive equation for the fiber is an exponential form based on the Green strain,

$$S_f = A\{\exp[B(\lambda_f^2 - 1)] - 1\} \quad 3.2$$

where λ_f is the fiber stretch for a fiber aligned with angle θ and S_f is the second Piola-Kirchoff stress in the fiber. The constants A and B capture the overall stiffness and nonlinearity of the fiber response, respectively. If A increases, the fiber is stiffer at all strain levels, and if B increases, the fiber stress-strain response becomes more nonlinear. The overall stress within the tissue is the sum of all the fiber stresses.

The fitting parameters (A, B, κ and μ) were determined using a nonlinear simplex search, fminsearch, in Matlab. The full-field displacement and boundary forces of the three protocols were considered. Initial guesses were based on equibiaxial force data. Displacement of clamped sample boundaries was prescribed, but all interior nodes and free-edge edges were fit.

3.4 Results

There was not a significant difference in rat body weight, heart weight, or decellularized heart weight between the age-matched male and female rats, (p = 0.24, 0.13, 0.90). Prior to decellularization the difference in heart-to-body weight ratio was significant at the 90% but not at the 95% level, with females having a higher ratio (p = 0.09). Following decellularization this difference disappeared (p = 0.51), as shown in Figure 3.2.

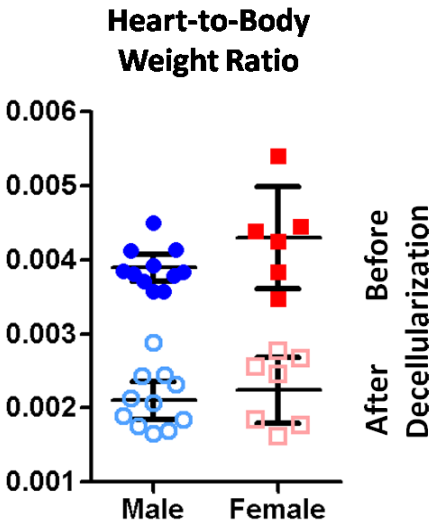

Figure 3.2: Heart-to-body weight ratio of male and female rats.

When comparing the first and final equibiaxial protocol, each sample's strain maps exhibited similar values and patterns, and no arm showed a percent deviation of more

than 8.1% in force. Figure 3.a-c shows loading behavior for a representative sample, pictured in Figure 3.1b. For equibiaxial loading, the circumferential (vertical) arms had higher loads than the longitudinal (horizontal) arms. Also, when the strip biaxial extensions were compared, the tissue had a larger response to the vertical extension. The discrepancy in force between opposite arms was due to shear forces. The model slightly underestimated tissue response in equibiaxial loading, but fit both horizontal and vertical strip biaxial extensions well. The displacement maps for the sample show both experimental tracking and model fit at maximum displacement, Figure 3.d-f. For all three extensions the model matched the data well.

The fiber parameters were fit using both the force and displacement data from the three protocols for each sample, assuming homogeneity. For the sample pictured in Figure 3.1b the best-fit model parameters were: $A = 2.98\ kPa$, $B = 11.1$, $\kappa = 2.36$ and $\mu = 22.5°$. For the representative sample (pictured in Figure 3.1b), B was large, indicating a high degree of nonlinearity, and A was small, indicating low overall tissue stiffness. Thus, at low strains the tissue was very extensible, and at high strains it rapidly became stiff. It is difficult to decouple A and B when comparing across sample groups as high levels of stiffness and nonlinearity both contribute to a large stress response. Therefore, when comparing across sample groups the fiber stress, S_f, is determined using the model fit A and B for a both a low (1.05) and high fiber stretch (1.20). For the representative sample $S_f = 6.3$ kPa and $S_f = 390.9$ kPa for low and high fiber stretch, respectively. A two-way ANOVA was performed to study the effects of both gender (male vs. female) and ventricle location (right vs. left) on fiber stress for both low and high fiber stretch, and the results are shown in Figure 3.4a and b. The two-way ANOVA showed no significant effect of gender on fiber stress for either low or high fiber stretch $\left(p_{\lambda_{1.05}} = 0.13 \text{ and } p_{\lambda_{1.20}} = 0.66\right)$, and there were no significant interactions between gender and ventricle location $\left(p_{\lambda_{1.05}} = 0.31 \text{ and } p_{\lambda_{1.20}} = 0.83\right)$. Right ventricles, however, exhibited larger fiber stress at both low $\left(p_{\lambda_{1.05}} = 0.044\right)$ and high fiber stretch $\left(p_{\lambda_{1.05}} = 0.057\right)$ than left ventricles.

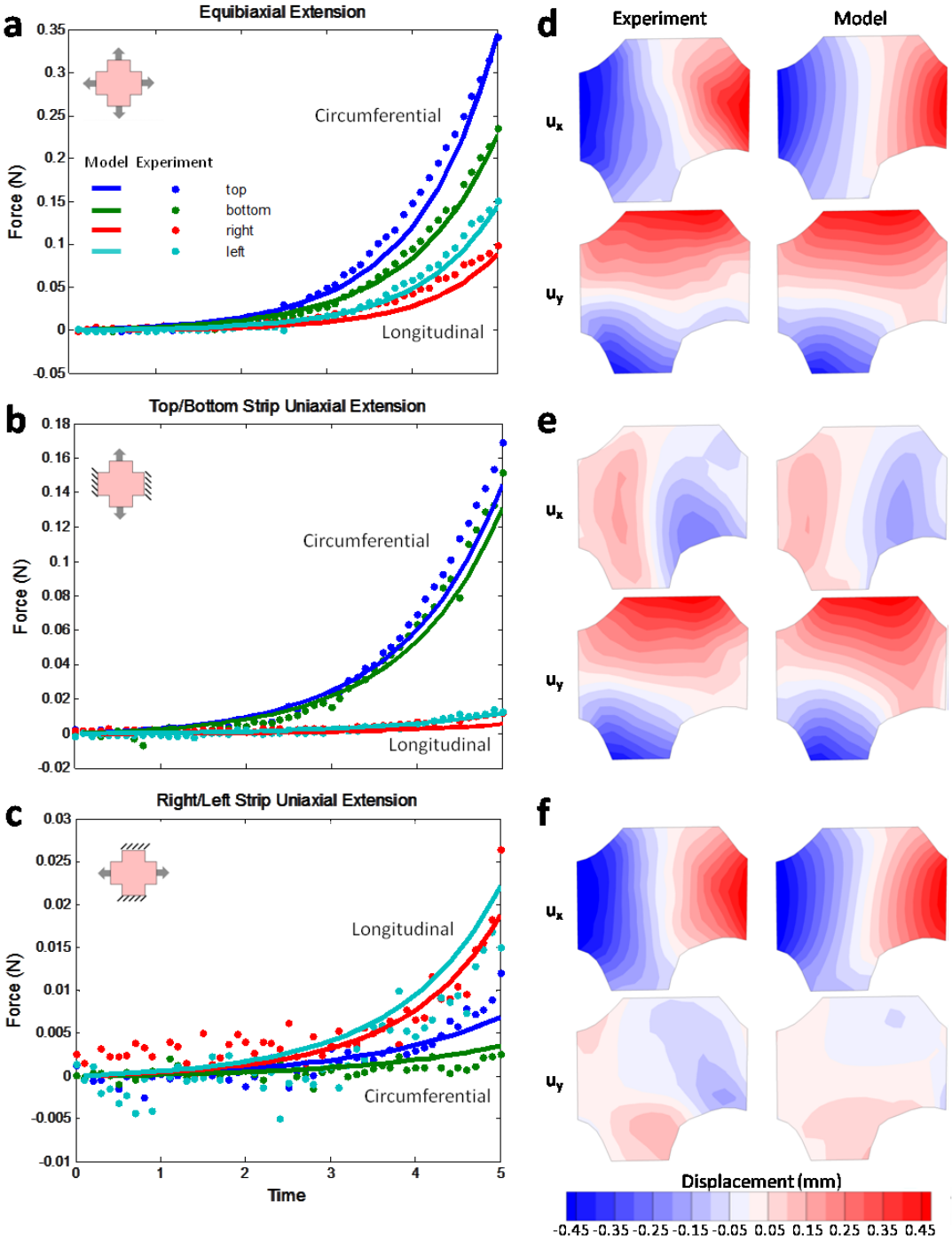

Figure 3.3: Load data and model fit for sample pictured in Figure 3.1b. Equibiaxial (a), circumferential (vertical) strip biaxial (b), and longitudinal (horizontal) strip biaxial loading curves with the model fit. Displacement fields for the experiment and model for the equibiaxial (d), circumferential strip biaxial (e), and longitudinal strip biaxial extensions.

The value of μ, 22.5° from the horizontal, for the representative sample, indicates that the sample had a slight preference for the circumferential direction. In addition, the moderate value of κ, 1.60, suggests some spread in the distribution around μ (88% of the fibers fall within ± 45° of μ and 44% fall within ± 15° of μ when κ = 1.60). The impact of μ is intrinsically linked to the value of κ so an addition variable, the network orientation tensor [130], was used to compare between sample groups. For the NSFM the network orientation tensor is defined as follows

$$\Omega = \begin{bmatrix} \int f(\theta;\kappa,\mu)\cos^2\theta & \int f(\theta;\kappa,\mu)\cos\theta\sin\theta \\ \int f(\theta;\kappa,\mu)\sin\theta\cos\theta & \int f(\theta;\kappa,\mu)\sin^2\theta \end{bmatrix} \qquad \theta \in [0,\pi) \qquad 3.3$$

where Ω is a symmetric tensor for which $\Omega_{11} + \Omega_{22} = 1$ since the fiber population is a described by a bidirectional von Mises distribution. Therefore, only Ω_{11} and Ω_{12} are needed to describe the anisotropic response of each sample. Orientation was set such that Ω_{11} corresponded with the circumferential direction and Ω_{22} corresponded with the longitudinal direction for all samples. The off-diagonal term, Ω_{12}, indicates off-axis alignment. Results from a two-way ANOVA, performed to study the effects of both gender and ventricle location, are shown in Figure 3.4c and d. The effects of gender $\left(p_{\Omega_{11}} = 0.34 \text{ and } p_{\Omega_{12}} = 0.54\right)$ and ventricle location $\left(p_{\Omega_{11}} = 0.29 \text{ and } p_{\Omega_{12}} = 0.09\right)$ on orientation were not significant, and there were no significant interactions $\left(p_{\Omega_{11}} = 0.79 \text{ and } p_{\Omega_{12}} = 0.13, \text{ respectively}\right)$. In our previous study on decellularized right ventricular tissue of female rats [129] the preferred stiffness direction, which is analogous to the preferred fiber direction, was ~ 13.6° from the circumferential, and the anisotropy index was large, indicating a strong preference for the circumferential direction. Therefore, additional t-tests were done to determine if right and left ventricular samples showed significant circumferential alignment. Right ventricular samples showed significant circumferential alignment $\left(p_{\Omega_{11}} = 0.003\right)$, but left ventricular samples did not $\left(p_{\Omega_{11}} = 0.65\right)$.

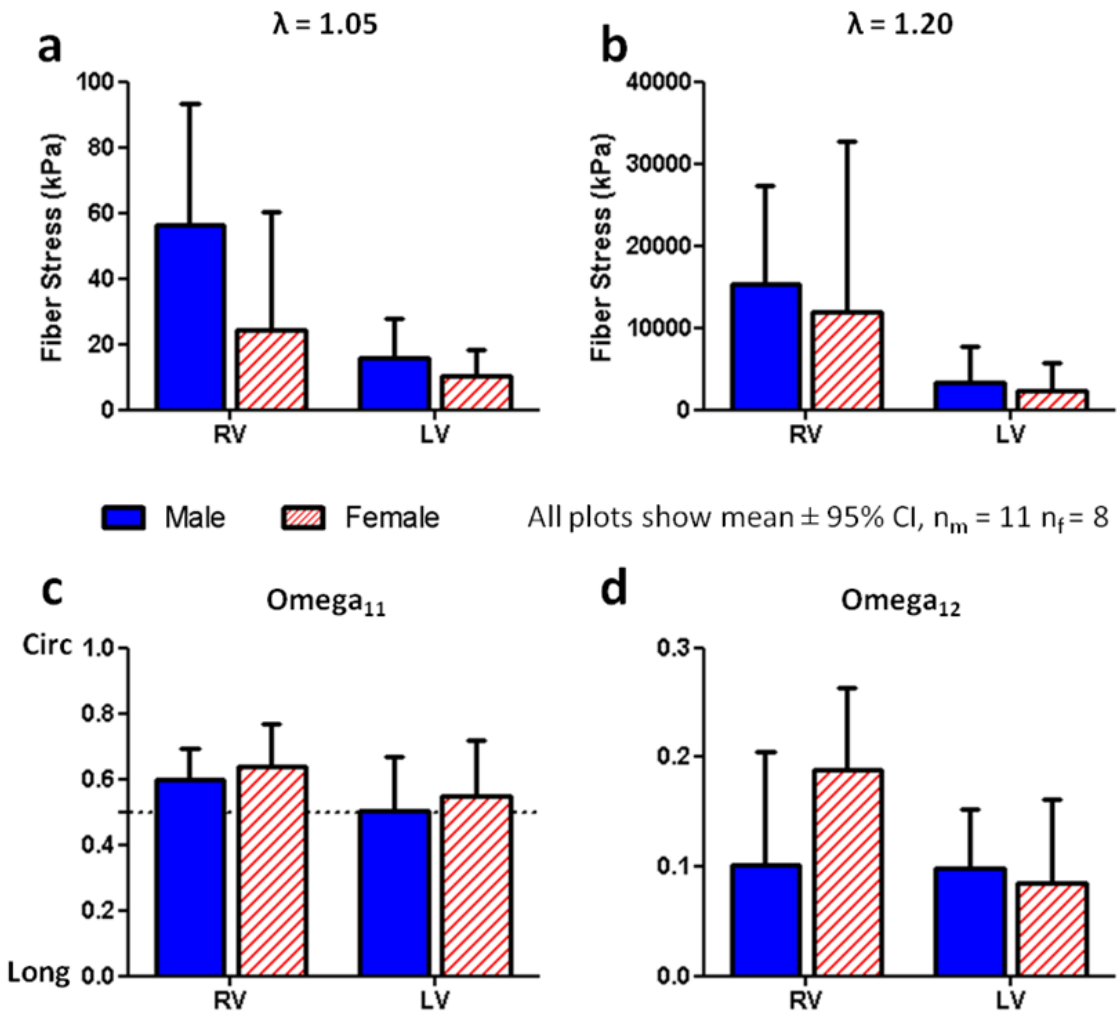

Figure 3.4: (a) Fiber Stress at low (1.05) and high (1.20) fiber stretch. Components of the orientation tensor (Ω_{11} and Ω_{12}) indicating circumferential (c) and off-axis (d) alignment, respectively.

3.5 Discussion

The nonlinear closed-form structural model of planar fibrous tissue mechanics, developed by Raghupathy and Barocas [124], was successful in describing the mechanical behavior of decellularized ventricular wall samples in both equibiaxial and strip biaxial loading. Using four parameters the model matched the loading behavior, both the force curves and the full-field displacement, of the samples for all three extensions.

Surprisingly, right ventricular samples exhibited greater fiber stiffness, as measured by the model stress, at both high and low fiber stretches, than left ventricular samples. Initially, this result was quite puzzling but further analysis on orientation shows on average right ventricular samples were circumferentially aligned whereas on average left ventricular samples were not. The high variation in left ventricle sample orientation underscores the difficulty in dissecting decellularized left ventricular samples to obtain specimens from a consistent location along the ventricle wall. A new or different dissection technique or a higher sample size is suggested for further study of the left ventricle.

We observed no significant difference in the mechanical behavior of decellularized male and female rat ventricular tissue. The heart-to-body weight ratio of female rats was slightly higher than that of male rats prior to decellularization, but this difference was not sustained following decellularization. There were no significant differences between the sexes in fiber stress at either high or low fiber stretch nor were there any significant differences in fiber orientation or anisotropy strength. Thus, though there is evidence to suggest fundamental differences between male and female hearts we found no significant mechanical differences on the ECM level.

Chapter 4: Using Jumps in the Deformation Gradient Field to Segmentation Heterogeneous Tissues

This work was a part of the paper:
Automatic Segmentation of Mechanically Inhomogeneous Tissues
Based on Deformation Gradient Jump
Submitted to IEEE Transactions of Medical Imaging
Witzenburg, C.M., Dhume, R.Y., Lake, S.P. and Barocas, V.H.

4.1 Motivation of Research

A major shortcoming of the GAIM method identified by Raghupathy [115] was its method designed to segment a heterogeneous sample into many homogeneous subregions. In some cases, particularly the samples of [116], manual partitioning based on a prior knowledge of the sample was necessary to match the heterogeneous nature of the tissue analog. The partitioning method within GAIM does not optimize a partition's shape or size and tends to produce partitions with similar proportions. Therefore, in order to capture unique features within the sample, such as the rectangular region in the simulated cruciform made from two orthotropic materials [113] or the central depression in the heterogeneous PDMS sample [116], many superfluous partitions are necessary. The inability of the partitioning method to adjust partition size and shape automatically to fit the sample exacerbates this problem as the scoop size, a specification indicating the number of elements necessary to form a partition, is often minimized to avoid overlooking unique features of the sample. The creation of superfluous partitions reduces the accuracy of the GAIM method and makes it a less compelling technique. In addition, the partitioning method is built into the GAIM method since partitioning choices are dependent on the linear elasticity tensor determined for a subregion. Therefore, if the loading protocol designed for GAIM is not performed partitioning is not possible. In this chapter, we propose instead an automatic partitioning method dependent solely on the sample's deformation field in a small subset of homogeneous loading configurations (equibiaxial and strip biaxial extensions). The approach computationally dissects the

sample domain into many homogeneous subdomains by applying graph theory to the deformation gradient field.

The automatic deformation gradient jump partitioning method successfully determined the *size, shape, and location* of regions with locally similar material properties for: (1) a series of simulated soft tissue samples prescribed with both abrupt and gradual changes in anisotropy strength, prescribed fiber alignment, stiffness, and nonlinearity, (2) tissue analogs (PDMS and collagen gels) which were tested biaxially and speckle tracked (3) and soft tissues which exhibited a natural variation in properties (cadaveric supraspinatus tendon), a pathologic variation in properties (thoracic aorta containing transmural plaque), and active behavior (contracting cardiac sheet). The routine enables the dissection of samples computationally rather than physically, allowing for the study of small tissues specimens with unknown and irregular inhomogeneity.

4.2 Introduction

Tissues are often mechanically inhomogeneous due to variations in properties (e.g., supraspinatus tendon [131,132], pulmonary artery [133], left recurrent laryngeal nerve [134]), variations in active behavior (e.g., myocardial shortening [135]), injury (e.g., whiplash [136]), myocardial [59,60,137] or dermal [13,138,139] scarring, or disease (coronary artery disease [88], idiopathic pulmonary fibrosis [140,141], or cancer [83,142]). Elastography, the imaging of soft tissues to identify regional variations in mechanical properties, has become a major focus for medical imaging [73,143]. In static elastography, the tissue is compressed or elongated slowly, and the distribution of its displacement is captured (e.g., with MR, ultrasound, acoustic or optically) and interpreted.

Displacement tracking is a promising approach for evaluating mechanical variations *in vivo*. New techniques, like MR and ultrasound, have produced full 3D reconstructions of displacement fields within tissues from multiple slices of 2D displacement information,

induced by harmonic excitations (e.g. [144]). MR is widely used to detect tumors in the breast, prostate, liver, etc. [145–147]. Vascular plaques are assessed with intravascular ultrasound by measuring vessel area change in response to applied pressure [148,149]. Speckle tracking echocardiography [150–152], sonomicrometry [153], cardiovascular magnetic resonance tagging [154], and color-coded tissue Doppler echocardiography [155] have all been used to assess regional ventricular function through the measurement of local deformation [156]. Skeletal muscle contraction has been characterized with sonoelastography, which tracks internal tissue displacements following an externally applied perturbation [157].

Full-field strain tracking is also utilized extensively for tissue characterization for experimentation *in vitro* (as reviewed in [158,159]). For some tissue types, the surface of the tissue itself may provide enough unique texture to be tracked without the application of any agent. However, the sample can also be textured through the application of a paint or stain (e.g. [108]) or the dispersion of small particles (e.g. [160]) to achieve a fine, random texture. Additional techniques have also been developed to track surface movement using the microstructure of the tissue such as polarized light (e.g. [161]) and optical coherence tomography [162,163].

In traditional static elastography, a constitutive relation is employed to relate the measured distribution of strain to the predicted stress and determine material parameters. Often, a spatially varying constitutive equation is necessary to capture the structural complexity of biological tissues and account for boundary effects [67,92,107,113,164–167]. Determining how the constitutive equation should vary is still an open question, however, often requiring *a priori* information concerning tissue structure or a computationally intensive iterative approach.

In this work, the concept of network clustering is adapted to the identification of mechanically similar regions within a heterogeneous sample based on a measured displacement field. Two observations inform the process: (1) the normal components of

the stress tensor must be continuous across any interface by Newton's third law, but the deformation gradient need not be so; (2) a displacement field represented by a finite-element grid results in a discontinuous deformation gradient even if the field is smooth in the continuous limit. Thus, the jump in the deformation gradient across an element boundary is a measure of the local change in material properties. Large jumps indicate the element boundary is a good target for segmentation. A third critical observation is that the set of finite elements and interelement deformation gradient jumps can be analyzed using graph theory to identify optimal subpopulations (i.e., partitions). Thus, the objective of this work was to combine graph theory [168,169] with measured deformation gradient jumps to segment a tissue into homogeneous subregions of different mechanical properties.

4.3 Methods: Analysis and Segmentation Scheme

4.3.1 Full-Field Displacement Tracking

Accurate estimation of full-field displacements from motion capture of soft tissue deformation is crucial for tissue segmentation. Accordingly, high-resolution digital video was captured of various tissue equivalent and soft tissue samples during deformation and digital image correlation was utilized to determine full-field displacement per Raghupathy [115,116]. The video was synchronized and downsampled to construct grayscale image sequences corresponding to the loading curves of each extension. The image of the sample before the start of test was used as the reference configuration. Using Abaqus™ (6.11, Simulia, Inc., Providence, RI), the tissue boundary was sketched on top of the reference image and meshed with quadrilateral elements. Successive pairs of images were correlated to track the movement of the mesh throughout the loading sequence. Displacement fields were constructed from movement of the mesh and smoothed to reduce noise.

4.3.2 Deformation Gradient Jump Calculations

The deformation gradient tensor at the midpoint of each element edge was calculated from the bilinear isoparametric representation of the displacement field. For each element edge, the deformation gradient tensor was calculated as follows:

$$F = \begin{bmatrix} \frac{\partial x}{\partial X} & \frac{\partial x}{\partial Y} \\ \frac{\partial y}{\partial X} & \frac{\partial y}{\partial Y} \end{bmatrix} = \begin{bmatrix} \frac{\partial x}{\partial \xi} & \frac{\partial x}{\partial \eta} \\ \frac{\partial y}{\partial \xi} & \frac{\partial y}{\partial \eta} \end{bmatrix} * \begin{bmatrix} \frac{\partial X}{\partial \xi} & \frac{\partial X}{\partial \eta} \\ \frac{\partial Y}{\partial \xi} & \frac{\partial Y}{\partial \eta} \end{bmatrix}^{-1} \quad 4.1$$

where (X, Y) is the initial position, (x, y) is the final position, and (ξ, η) is the computational coordinate. The deformation gradient tensor for each element edge point, j, was

$$F = \left(\sum_{j=1}^{4} \begin{bmatrix} x^j \\ y^j \end{bmatrix} \begin{bmatrix} \frac{\partial \varphi^j}{\partial \xi} & \frac{\partial \varphi^j}{\partial \eta} \end{bmatrix} \right) * \left(\sum_{j=1}^{4} \begin{bmatrix} X^j \\ Y^j \end{bmatrix} \begin{bmatrix} \frac{\partial \varphi^j}{\partial \xi} & \frac{\partial \varphi^j}{\partial \eta} \end{bmatrix} \right)^{-1} \quad 4.2$$

where φ is the bilinear function and j is the index variable looping through the four basis functions for a given element. All shared edges were identified, and the deformation gradient jump was defined as the double contraction of the difference between the deformation tensors across the edge with itself,

$$\Delta_k = \sum_{i=1}^{4} \left(F_i^{\text{element1}} - F_i^{\text{element2}} \right)^2 \quad 4.3$$

where elements 1 and 2 are the two elements sharing the edge k and i is the index variable looping through the four components of the deformation gradient tensor.

4.3.3 Tissue Segmentation

The flow chart in Figure 4.1 summarizes the tissue segmentation scheme. In order to segment the tissue into homogeneous subregions, the finite element geometry for a sample was first converted into an equivalent network. A network node was created for each finite element, and if two elements shared an edge, their corresponding network

nodes were considered connected to form an unweighted graph. After the network had been constructed, it was analyzed to determine the shortest path between each pair of network and a *betweenness* value for each connection nodes using a breadth-first search algorithm (per [169]). The betweenness value for a connection, as defined by Newman [168,169], is the number of geodesic paths (i.e., shortest paths between any given pair of nodes) that run along that connection. If there was more than one geodesic path joining a pair of network nodes, then each path was counted as a fractional path. Next, the network connection betweenness values were multiplied by the deformation gradient jump for the corresponding finite element edge. Thus, the final value of betweenness for each network connection was determined both by the sample geometry and by the deformation gradient jump. Following [168,169], the network connection with the largest value of betweenness was removed. The new, less-connected network was then reanalyzed to determine the new set of shortest paths and the process was repeated. When the network split into disconnected subnetworks, communities were formed, and the network *modularity* was calculated. Modularity [168] is defined to be the difference between the fraction of connections that fall within communities and the expected value of the same quantity if connections are assigned at random.

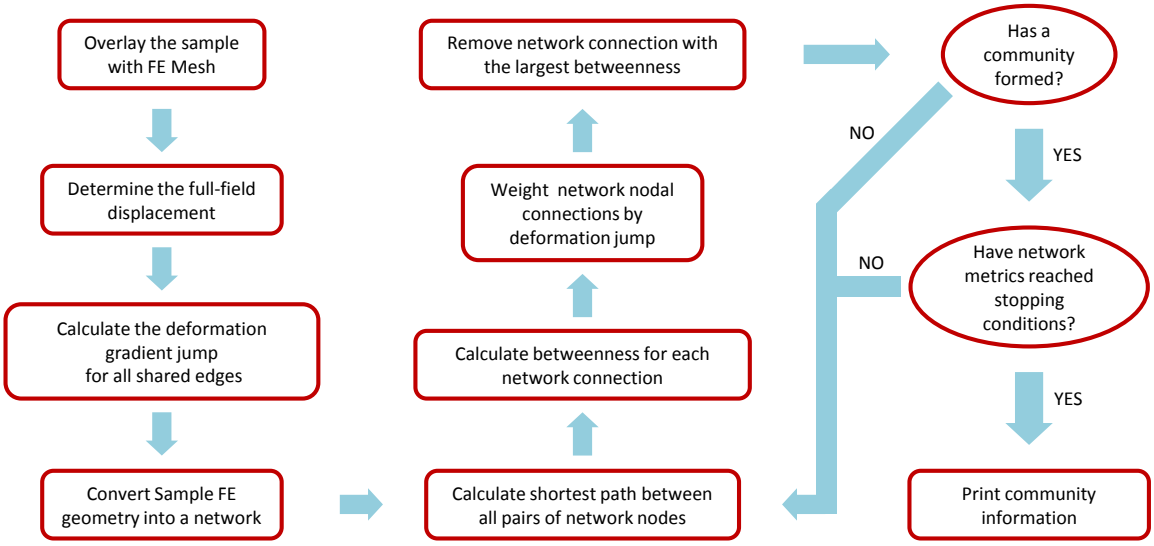

Figure 4.1: Flow chart summarizing tissue segmentation scheme

4.4 Methods Testing and Application of the Segmentation Scheme

4.4.1 Simulated Experiments

To test the tissue segmentation method *in silico*, equibiaxial and strip biaxial extensions were simulated using a closed-form nonlinear fiber-based structural model (NFSM) for soft tissues [124]. Briefly, the fiber contribution is described by a bidirectional a von Mises distribution, and the fiber stretch ratio is related to the second Piola-Kirchoff stress through an exponential stress-strain law [170]. The model uses four parameters; the direction (μ) and degree (κ) of fiber orientation and the small-strain stiffness (A) and nonlinearity (B) of the fibers. Simulation parameters were selected based on previous fits of the NFSM to data from rat myocardium (chapter 3), cadaveric bladder wall [115], and cadaveric annulus fibrosus lamellae [171]. For the first set of simulations, a cruciform sample was generated with a central triangle shaped inclusion; the inclusion varied from the bulk sequentially in prescribed fiber orientation ($\mu_{bulk} = 20°$ and $\mu_{inclusion} = 80°$), strength of alignment ($\kappa_{bulk} = 1.5$ and $\kappa_{inclusion} = 6.0$), stiffness ($A_{bulk} = 5\ kPa$ and $A_{inclusion} = 20\ kPa$), and nonlinearity ($B_{bulk} = 12$ and $B_{inclusion} = 48$). For the second set of simulations, more gradual changes were studied. First, sample orientation was set with anisotropy vectors radially aligned about the sample center. Next, sample anisotropy strength, stiffness, and nonlinearity were maximized in the center of the sample and reduced with radial distance from the center $(\kappa, A, B \sim 1/(1 + \text{radial distance}))$. Figure 4.2 shows the sample geometry and anisotropy as well as full-field deformation gradient for the equibiaxial extension for both simulations for the condition in which the prescribed fiber orientation was allowed to vary, (strip biaxial extension deformation gradient fields are in Appendix C).

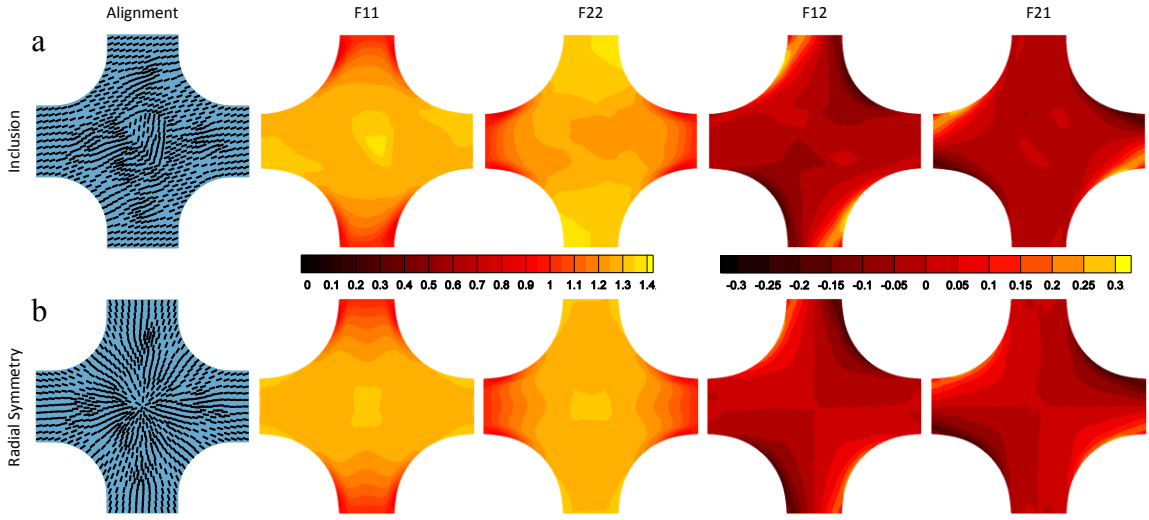

Figure 4.2: Fiber alignment and full-field deformation gradient tensor components for equibiaxial extension of (a) simulated sample with inclusion for which the inclusion varies only in prescribed fiber orientation (80^0 vs. 20^0) and (b) simulated radially symmetric sample for which the prescribed fiber orientation varied.

4.4.2 Experiments on Artificial and Natural Tissues

Strain tracking was performed on experimental data collected from the following samples to provide a wide range of tissue type, heterogeneity, nonlinearity, and anisotropy for the tissue segmentation scheme:

- A heterogeneous polydimethylsiloxane (PDMS) sample [116],
- Two compacted collagen tissue-equivalents with different geometries [116],
- A segment of cadaveric human aorta containing a large plaque,
- A segment of a supraspinatus tendon, and
- A sheet of beating cardiac cells [172].

4.4.2.1 Heterogeneous PDMS

Deformation data from equibiaxial and two strip biaxial extensions performed on a heterogeneous PDMS cruciform, presented previously in the context of inverse methods [115,116], was analyzed. Briefly, a PDMS solution (Sylgard® 184 Silicone Elastomer

Kit; Dow Corning) was created by mixing the curing agent and base (1:10). Since the clear polymer is difficult to image, rice flour was added to opacify the sample. The solution was poured into a custom aluminum mold with a step in the center and was cured at room temperature overnight. The resulting sample was 2.1 mm thick except for the central depression, which was 0.2 mm thick. The thickness difference led to a compliant central region surrounded by a stiffer outer region. Spray paint was used to texture the sample surface for measurement of full-field displacement. The sample was tested at room temperature on an Instron planar biaxial machine (Instron, Norwood, MA). A pre-load was applied (0.01 N) to each of the four arms, and the sample was preconditioned with nine equibiaxial extension cycles (7.5% stretch). Subsequently, a series of mechanical tests, including equibiaxial and strip biaxial extensions, was performed; the equibiaxial and strip biaxial data were used in the current study. During testing, digital video of the textured sample surface was obtained with a spatial resolution of ~ 30 pixels/mm. Full-field displacement tracking was done on each extension. The Green strain, which is a direct function of the deformation gradient, for the equibiaxial extension was reported previously [115] and is markedly higher in the central region of the sample.

4.4.2.2 Collagen Tissue-Equivalents

Deformation data from equibiaxial and two strip biaxial extensions performed on collagen tissue-equivalent cruciforms, presented previously in the context of inverse methods [115,116], were analyzed. The samples were created by seeding neonatal human dermal fibroblasts in a collagen gel-forming solution, detailed in Raghupathy et al. [115,116]. Briefly, the samples were cast in cruciform-shaped Teflon molds such that one sample had vertical arms that were twice as wide as the horizontal, producing moderate vertical alignment in the sample center, and the other sample had arms of equal width, producing a large isotropic zone in the sample center. The samples were incubated for 11 days to allow for cell-induced contraction and remodeling of the collagen network. Prior to biaxial testing, quantitative polarized light imaging (QPLI) was used to quantify the

localized direction and strength of fiber alignment in each collagen tissue equivalent sample. Verhoeff's stain was used to texture the sample surface for measurement of full-field displacement. The sample was immersed in 1% phosphate buffered saline (PBS) and tested at room temperature on a planar biaxial testing machine. Again, a pre-load was applied (0.01 N) to each of the four arms, and the sample was preconditioned with nine equibiaxial extensions (7.5% stretch), followed by a series of extension tests. During testing, digital video of the textured sample surface was obtained with a spatial resolution of ~ 25 pixels/mm. Full-field displacement tracking was done on each extension and Green strain was reported previously [115] for the equibiaxial extension.

4.4.2.3 Arteriosclerotic Plaque

A segment of fresh diseased thoracic human aorta was obtained from the Anatomy Bequest Program at the University of Minnesota. A portion of the ascending thoracic aorta was cut into a cruciform such that a large transmural arteriosclerotic plaque resided in the central region of the sample, and the circumferential and axial orientations of the aorta coincided with the cruciform axes. Verhoeff's stain was used to texture the luminal surface sample for optical strain tracking. The textured sample was attached to a biaxial test machine and immersed in 1% PBS for the duration of the test. After a slight preload, the sample was preconditioned with 7 equibiaxial extensions of 15% grip strain at a rate of 3 mm/min. Following preconditioning, the sample underwent an equibiaxial extension and two strip biaxial extensions of 15% grip strain. During testing, digital video of the luminal surface of the tissue sample was obtained at 24 fps, 1080p HD resolution and spatial resolution of ~ 45 pixels/mm. Full-field displacement tracking was done on each extension, and deformation gradient fields are shown in Appendix C for the equibiaxial extension.

4.4.2.4 Supraspinatus Tendon

A whole supraspinatus tendon (SST) specimen, one of the four tendons comprising the rotator cuff of the shoulder, was obtained from the Anatomy Bequest Program at the University of Minnesota and dissected per Lake et al. [131,132]. A portion of the SST was cut into a cruciform shape such that the transverse and longitudinal orientations coincided with the cruciform axes. The orientation of the sample was noted prior to testing, and Verhoeff stain was applied to texture the bursal surface for optical strain tracking. The sample was attached to a biaxial test machine and immersed in 1% PBS at room temperature for the duration of testing. A pre-load was applied (~ 1 N) to each of the four arms, and the sample was preconditioned with nine equibiaxial extensions (5% stretch). Subsequently, a series of mechanical tests, including equibiaxial and strip biaxial extensions, was performed; the equibiaxial and strip biaxial data were used in the current study. During testing, digital video of the textured sample surface was obtained with a spatial resolution of ~ 15 pixels/mm. Full-field displacement tracking was done on each extension (deformation gradient fields for equibiaxial extension are in Appendix C).

4.4.2.5 Beating Cardiac Sheet

We analyzed the motion of a beating cardiac tissue model using video generously provided by the Healy Group at the University of California, Berkley. Their methods are described elsewhere [172] and are summarized here. Cardiomyocytes were differentiated from healthy human iPS cells per the small molecule WNT-mediated protocol developed by Lian et al. [173]. Single cells were seeded and grown as a monolayer in defined mTeSR1 medium on Matrigel-coated plates at 37℃ and 5% carbon dioxide. The cardiomyocytes formed spontaneously contracting sheets (without pacing) of cells 10 days after the WNT-mediated differentiation protocol. A video of the cells was obtained for multiple beats with a spatial resolution of ~ 0.8 pixels/μm. Full-field displacement tracking was done on grayscale images of the deformation from three successive beats.

4.5 Results

4.5.1 Simulated Experiments

Full-field displacement was determined for both simulations for all conditions. For brevity, results are presented only for the simulation of the sample containing the inclusion with fiber alignment different from the bulk ($\mu_{bulk} = 20°$, $\mu_{inclusion} = 80°$) and the radially symmetric sample with varied alignment (results from other simulations are provided in Appendix C). Figure 4.3a and d show the sum of the normalized deformation gradient jumps from all three extensions for each simulation. The partitions are overlaid on each sample in Figure 4.3b and e with vectors representing the prescribed fiber orientation. All simulations involving the sample containing the inclusion identified the inclusion as a separate material (Appendix C). The partitions determined for the simulated sample with radial symmetry of prescribed fiber orientation show a distinct pinwheel-shaped pattern at the sample center. Similarly, all the simulations involving the radially symmetric sample created a circular pattern of partitions at the sample center (Appendix C). Figure 4.3c and f shows the modularity for the partitioning scheme as a function of the connections removed. The scheme was allowed to continue until 400 connections were removed and the modularity at which communities formed were recorded. While step changes in modularity do correspond with cluster formation, there is no consistent range of modularity values at which the manually determined optimal number of clusters is formed.

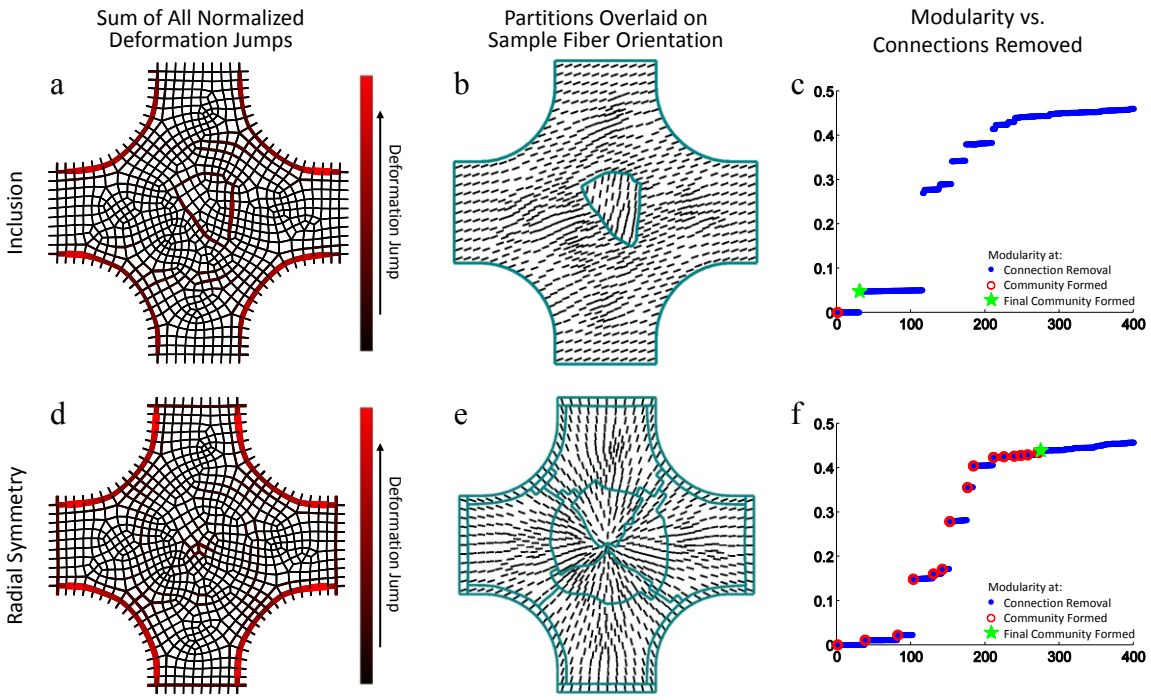

Figure 4.3: Sum of normalized deformation gradient jumps for all three extensions for the simulated sample containing the inclusion with fiber alignment different from the bulk ($\mu_{bulk} = 20^0$ and $\mu_{inclusion} = 80^0$) (a) and for the radially aligned simulated sample with varied fiber alignment (d). Partitions, overlaid on sample geometry with prescribed fiber alignment indicated by vectors, identified inclusion (b) and radial symmetry (e), respectively. Modularity as a function of connections removed for both the simulated sample containing the inclusion (c) and the radially aligned simulated sample (f). Blue dots indicate values when a connection is removed, open red circles indicate when a community is formed, and the green star mark when the final community formed.

4.5.2 Experiments on Artificial and Natural Tissues

4.5.2.1 Heterogeneous PDMS

The sum of the normalized deformation gradient jumps for the three extensions and the partitions resulting from the network community scheme for the PDMS sample are shown in Figure 4.4. It is readily apparent from Figure 4.4a that the 3-D nature of the modification and the deformation leads to a thick ring of high deformation gradient jumps around the compliant central region. The partitioning scheme immediately and compellingly identified the compliant central region of the sample, Figure 4.4b. Figure

4.4c shows the modularity for the partitioning scheme as connections are removed. For this sample, we stopped the partitioning scheme after two communities had been formed.

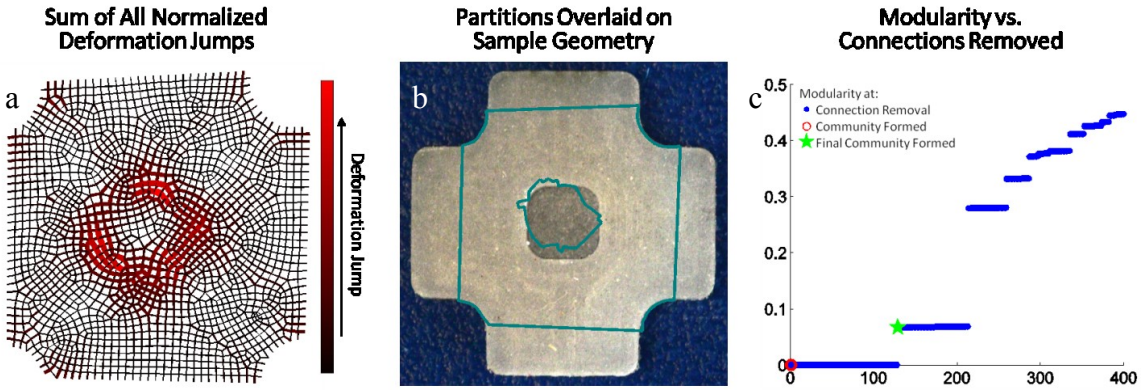

Figure 4.4: (a) Sum of normalized deformation gradient jumps for all three extensions for the heterogeneous PDMS sample. (b) Partitions, overlaid on sample geometry, strongly mirror sample heterogeneity. (c) Modularity as a function of connections removed. Blue dots indicate values when a connection is removed and the green star mark when the final community formed.

4.5.2.2 Collagen Tissue-Equivalents

Figure 4.5a and d show the sum of the normalized deformation gradient jumps from all three extensions for both the collagen tissue-equivalent sample with arms of equal width and the sample with vertical arms twice as wide as horizontal arms. Quantitative polarized light imaging results indicating fiber alignment degree (contour and length of vector) and direction (vector orientation) are shown in Figure 4.5b and e, with the partitioning results overlaid. For the equal arm sample, the large isotropic central area is well-identified as are the strongly-aligned arms. In addition, there is preferential partitioning along the edges of the central region, which exhibited strong off-axis alignment. The partitioning scheme was allowed to generate more communities for the sample with unequal arms as a result of its more complex alignment field. In this case, the scheme had some difficulty identifying the two isotropic zones present away from the center and towards the smaller arms. However, a large partition was placed within the moderately aligned sample center, and preferential partitioning was present along the edges of the sample that exhibited strong off-axis alignment. Figure 4.5c and f show the modularity for the partitioning scheme as connections are removed.

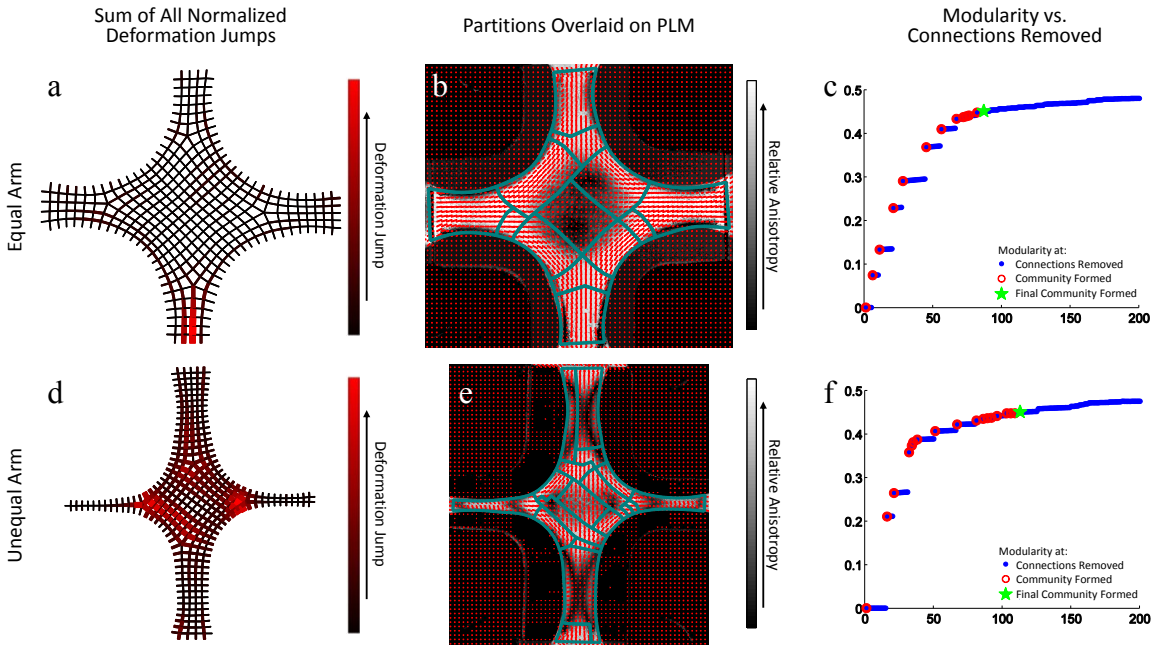

Figure 4.5: Sum of normalized deformation gradient jumps for all three extensions for both the equal (a) and unequal (b) arm collagen cruciform samples. Partitions are overlaid on the QPLI for both the equal (c) and unequal (d) arm collagen cruciform samples. The modularity for both the equal (e) and unequal (f) arm collagen cruciform samples, respectively. Blue dots indicate values when a connection is removed, open red circles indicate when a community is formed, and the green star mark when the final community was allowed to form.

4.5.2.3 Arteriosclerotic Plaque

The sum of the normalized gradient deformation gradient jumps from all three extensions for the sample containing the large arteriosclerotic transmural plaque is shown in Figure 4.6a. The partitioning results are overlaid on an image of the intimal surface sample taken prior to testing in which visible location of the plaque was noted, arrow in Figure 4.6b. The sample was segmented into 10 separate partitions. Of the resulting partitions, one encompasses the plaque with little extraneous tissue. In addition, other partitions seem to identify visually similar regions of the tissue. Figure 4.6c shows the modularity for the partitioning scheme as connections are removed.

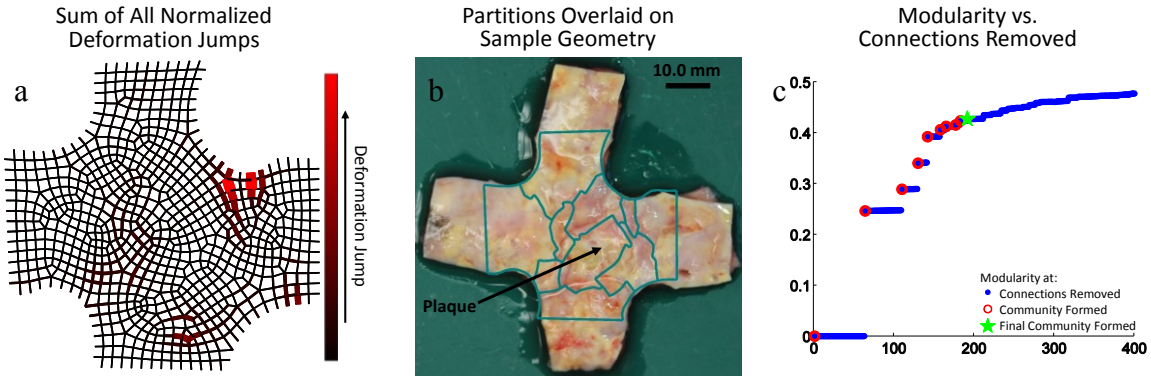

Figure 4.6: (a) Sum of normalized deformation gradient jumps for all three extensions for the aortic sample containing a large arteriosclerotic transmural plaque. (b) Partitions are overlaid on an image of the sample taken prior to testing in which the plaque was identified. (c) The modularity as a function of connections removed. Blue dots indicate values when a connection is removed, open red circles indicate when a community is formed, and the green star mark when the final community was allowed to form.

4.5.2.4 Supraspinatus Tendon

The sum of the normalized deformation gradient jumps from all three extensions are shown for the SST sample in Figure 4.7a. The partitioning results are overlaid on an image of the bursal surface of the sample taken immediately prior to testing, Figure 4.7b. The sample was segmented into 9 separate partitions. Partitions agree with previous results [131,132] suggesting significant mechanical and organizational heterogeneity including horizontal banding along the anterior-posterior axis and increased vertical banding towards the humeral insertion. Figure 4.7c shows the modularity for the partitioning scheme as connections are removed.

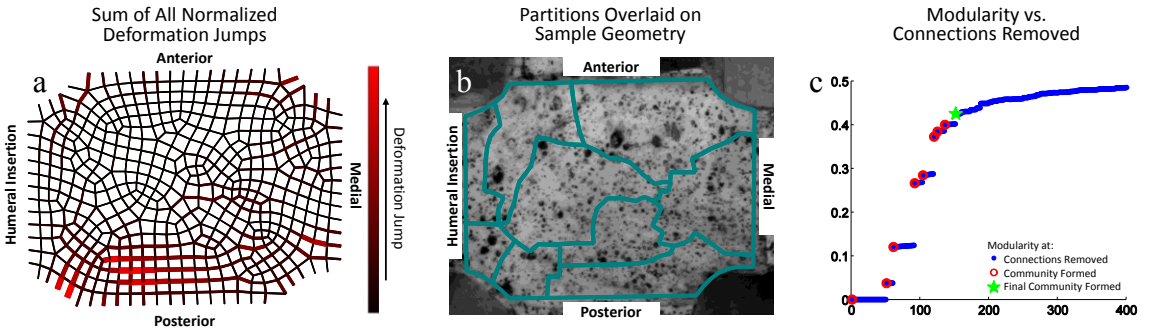

Figure 4.7: (a) Sum of normalized deformation gradient jumps for all three extensions for the SST sample. (b) Partitions are overlaid on an image of the sample taken immediately prior to testing. c) The modularity as a function of connections removed. Blue dots indicate values when a connection is removed, open red circles indicate when a community is formed, and the green star mark when the final community was allowed to form.

4.5.2.5 Beating Cardiac Sheet

The sum of the normalized deformation gradient jumps from three beats of the spontaneously beating cardiac sheet are shown overlaid on an image of the cardiac sheet taken immediately prior to beat one, Figure 4.8a. The partitioning results, Figure 4.8b, are overlaid on the maximum displacement field for beat 1 of the cardiac sheet. The partitions each contain regions of cells that were visually identified by our collaborator Dr. P. Loskill of the Healy Group as beating in unison- both in terms of the magnitude and phase. Figure 4.8c shows the community formation metrics for the partitioning scheme.

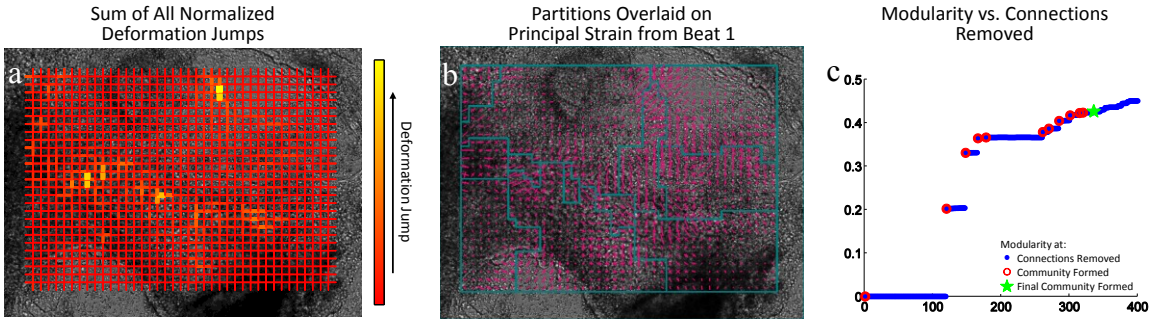

Figure 4.8: (a) Sum of normalized deformation gradient jumps for all three beats of the cardiac sheet. (b) Partitions are overlaid on an image of the sample taken immediately prior to beat 1 with the principal strain indicated by pink vectors. c) The modularity as a function of connections removed. Blue dots indicate values when a connection is removed, open red circles indicate when a community is formed, and the green star mark when the final community was allowed to form.

4.6 Discussion

The tissue segmentation routine determined both the location and size of different materials within a single sample based solely on displacement tracking results for simulated samples, tissue equivalents, and native tissue. It was able to capture regional changes in tissue properties due to pathology, as in the case of the sample containing the large transmural plaque, and natural variation, as in the case of the SST, and was able to describe heterogeneous cell contraction in a cardiac sheet. Although the modularity tended to jump when a new partition was formed, we did not find it to be a useful metric to determine the optimal stopping point of the clustering scheme as has been found

previously [168]. While the stopping metric did not always suspend partitioning at the time point in agreement with manual partitions, community formation typically identified regions of interest early in the partitioning process (e.g. PDMS sample). Direct comparisons between the partitions generated using the method of Raghupathy [116] and those generated using the method presented here are included in Appendix C.

Both the segmentation process and displacement tracking itself are limited by the speckling technique used to texture the sample surface. The coarseness of the FE mesh is dictated by the speckling technique and in turn affects the size and shape of the partitions formed. When the sample surface is discretized into finite elements, they must contain regions with a unique texture in order for DIC to capture surface deformation accurately. The finer a texture is applied to the sample surface, the more refined the mesh can be and therefore the more detailed the displacement tracking and partitioning. Tracking techniques based on inherent image texture [174], measured fiber alignment [161,175,176] , or natural speckle in an ultrasound image [177,178] can all provide the potential for better resolution. It must also be recognized that smoothing the displacement field, which is almost always necessary in DIC-based methods, intrinsically reduces any jumps in the deformation gradient and could reduce the effectiveness of the segmentation scheme.

In applying inverse methods and complicated constitutive equations to heterogeneous tissues, a major stumbling block is the segmentation of the tissue into discrete homogenous zones. Many inverse methods (e.g., [67,92,99,108,109,111,164]), including GAIM, which are applied to soft tissues employ full-field displacement measurements from more than one homogenous loading condition, providing information that can help guide the partitioning process. The jump in the deformation gradient across a finite element boundary is a measure of the local change in material properties. Our method takes advantage of the displacement data by applying graph theory to the deformation gradient to identify mechanically similar regions within a heterogeneous sample, and it has the advantage of segmenting the same finite element mesh that will be used for the

inverse calculation. We also note that the approach could, in principle, be applied to any finite element mesh, such as one might obtain from a thermal map of a tissue [179,180] (using the jump in temperature gradient), and that although only two-dimensional fields were analyzed in the current work, three-dimensional data could be segmented via the same algorithm.

Nondestructive structural characterization (i.e. polarized light, small angle light scattering, optical coherence tomography, etc.) of heterogeneous tissues is not feasible for many tissue types. Thus studies on the mechanical properties of soft tissues that consider regional variability and often involve cutting multiple samples from a single intact tissue specimen present a dilemma: without *a priori* knowledge of regional variability, how should the sample be cut? The proposed method suggests instead mechanically testing the entire specimen and applying the automated computational dissection routine to the full-field deformation *after* testing. Thus, dissection is done computationally rather than physically, allowing for the study of tissues with unknown heterogeneity.

Chapter 5: Stepwise Utilization of Generalized Anisotropic Inverse Mechanics Method for Application to Nonlinear Cardiovascular Soft Tissues

This work is a part of the paper:
A Nonlinear Anisotropic Inverse Method for Computational Dissection of Inhomogeneous Planar Tissues
In Preparation for Computer Methods in Biomechanics and Biomedical Engineering
Witzenburg, C.M. and Barocas, V.H.

5.1 Motivation of Research

Our novel approach, the Generalized Anisotropic Inverse Mechanics (GAIM) method, allows us to dissect specimens computationally rather than physically, so we can nondestructively capture regional differences within a single specimen. Importantly, we can examine transitions between regions; how the tissue varies from one level of stiffness and anisotropy to another and whether these changes are drastic and abrupt or more gradual. In earlier work, GAIM was used to determine regional mechanical properties of a simulated sample [113] and of soft tissue analogs (e.g. collagen gel) [116]. GAIM approximates all specimens as responding linearly, but soft tissues tend to be highly deformable and to exhibit non-linear behavior. GAIM was modified in Chapter 2 to accommodate the large-deformation kinematics exhibited by many soft tissues. The linear approach is sufficient if we simply use the GAIM results to approximate the stiffness and anisotropy of the sample from the eigentensor analysis of the elasticity tensor (i.e. the Kelvin Modulus and anisotropy index) [116,129]. However, the accuracy of the elasticity tensor estimates, particularly for highly nonlinear soft tissues, is suspect. This lack of confidence is especially severe as we begin to compare results from sample to sample and not just from region to region. A more robust technique for analyzing nonlinear samples would be a large improvement. In addition, a more complete description of the material behavior would also be quite advantageous. Thus, it is the

objective of this chapter to extend GAIM not just to provide better metrics describing the stiffness and anisotropy of the nonlinear tissue but to solve for its full stress field.

5.2 Introduction

Soft tissues (e.g. tendons, ligaments, articular cartilage, muscle, blood vessels, heart valve leaflets, etc.) connect, bind, support and protect the body. These load-bearing tissues are fundamental to the body's function as they provide support and protection as well as transmitting force and motion throughout the body. The mechanical behavior of soft tissues is highly dependent on their location and function, which is fundamentally linked to their composition, in particular the concentration and arrangement of the structural extracellular constituents (e.g. collagen, elastin, proteoglycans, etc.). Soft tissues are often naturally inhomogeneous, particularly at insertion or connection points and in cases of disease or injury. In general, soft tissues exhibit directionally dependent behavior which is strongly correlated with the anisotropic arrangement of their fibrous extracellular matrix. Finally, their stress-strain behavior is often highly nonlinear, particularly at the high strain levels in which soft tissues often operate physiologically. The intrinsic complexity of soft tissues presents a tremendous challenge in constitutive modeling.

There have been many studies aimed at determining the heterogeneity of soft tissues. For example, uniaxial and biaxial testing has been completed on small samples cut from different sections of myocardium [41,51,53,137], supraspinatus tendon [131,132,181,182], and aorta [32,183] to determine regional variation. While this approach has yielded valuable information, it is hindered by dissection damage and minimal testable sample size. Indentation can be applied regionally on a single intact specimen to determine the heterogeneous properties of soft tissues, as discussed in Chapter 1, but most elastographic methods assume linearity (infinitesimal deformation) and isotropy, and indentation itself is less relevant to in-vivo function. Inflation is a more

realistic loading modality, but it must be applied globally to a tissue specimen, making it extremely difficult to interrogate a region of the tissue in multiple strain states. Since information acquired about each region only describes it in a single strain state, the material constants determined are often only applicable for the strain state studied. Through the application of many multiaxial protocols, it is possible to impose multiple strain states on each region of a single tissue specimen. In this way, the material is interrogated in multiple physiologically relevant loading modalities.

The complex structure and mechanical behavior of soft tissues make selecting and applying an appropriate constitutive relation difficult. Most often, material parameters are obtained using a forward approach by determining the general characteristics of the tissue, establishing an appropriate theoretical framework, identifying a specific functional form of the relation, and fitting the material parameters to experimental data. There are many prominent strain energy functions which have been developed to consider both the anisotropy and nonlinearity of various soft tissues including Fung-type, neo-Hookean, Mooney-Rivlin, and Ogden relations. Selecting (or in some cases developing) an appropriate constitutive relation is not trivial, as the goal is to describe accurately describe the behavior of the material over a broad range of loading configurations. For example, Humphrey compared various relations in [69] by applying them to the same data set and found that they strongly differed (sometimes reversing) in their descriptions of the tissue in terms of both stiffness and anisotropy reinforcing the idea that even highly successful constitutive relations are limited in their predictive capabilities. This concern leads to the notion of the inverse approach; instead of selecting a strain energy function and fitting the material parameters to experimental data, use experimental data directly to determine the strain energy.

In our previous work [113,116], we presented the Generalized Anisotropic Inverse Mechanics (GAIM) method as a approach to determining the material properties of anisotropic, heterogeneous soft tissues. GAIM uses the given displacement field over the entire sample domain as well as the traction forces on the sample boundary to directly

solve the finite element representation of the Cauchy stress balance for the unknown components of the general linear elasticity tensor. Heterogeneity is managed using a subdomain technique in which the sample area is segmented into many partitions, which are each assumed to have uniform properties. In this way the method is capable of determining the distribution of material parameters: how stiffness and anisotropy change from region to region and whether these changes are drastic and abrupt or more gradual. The linear constitutive equation was modified [129] to accommodate the large-deformation kinematics exhibited by many soft tissues, but the base assumption of linear kinetics remains a serious weakness.

One possible approach to tissue nonlinearity would be to replace the neo-Hookean constitutive law employed with a higher order constitutive equation. For example Tönük and Silver-Thorn [184] fit their experimental results using a James–Green–Simpson nonlinear elastic material model. The use of high-order constitutive equations however, typically requires additional assumptions about the material (isotropy and homogeneity in the case of Tönük and Silver-Thorn) as they create a prohibitive number of independent material coefficients, and our preference is to maintain the maximum amount of flexibility in the constitutive form. In addition, the complexity of the relation increases computation time, sacrificing the tremendous efficiency advantage that comes from the constitutive law being linear with respect to the model parameters. Therefore, while still accounting for the nonlinear kinematics of the deformation as a whole, we approach the problem by considering the mechanical behavior of the tissue in a step-wise fashion.

5.3 Methods

5.3.1 Overall Strategy

The overall strategy begins with data generated from an extensive biaxial loading protocol. The more and varied the loading protocol the wider the span of strain-space investigated for each region of the sample. For a biaxial test, each arm can be extended

independently, leading to a total of 15 permutations, Figure 5.1; while this combination of experiments is by no means exhaustive (e.g. a 2:1 ratio of stretch in the two directions could also be performed), it provides a broad range of deformations to be imposed. Thus, for the current study, all 15 possible protocols in Figure 5.1 were performed.

Shear in the arms and central region of the sample was achieved through the asymmetric stretches. Both the normal and shear forces at the grip were measured by 6-degree-of-freedom load cells (JR3 Inc.). During each extension, a video of the sample surface was taken, allowing measurement of the full-field deformation using digital image correlation (DIC) as described elsewhere [115]. In order to capture the behavior of the tissue at small-strain (Figure 5.1) homogeneous subregions were identified per our previous study (Chapter 4), and the data from all loading protocols were combined per our previous linear approach [129], creating a general, anisotropic, inhomogeneous ***linear*** model of the material behavior at small strain. For larger strains, each element within the sample domain was considered a separate material rather than being grouped into a subdomain. For each element, data from each individual protocol were used to generate a piecewise linear model of the material in the element following the protocol's experimental strain path. Figure 5.1 shows a schematic of the process; for clarity, only the normal force on a single arm is shown and the step size is exaggerated. The determination of step size is an important consideration (detailed in Appendix D) because large steps lose linearity but small steps are more vulnerable to noise effects. The models were used to calculate the second Piola-Kirchhoff (PK2) stress at each strain value for each experimental protocol for every element. The PK2 stress was then integrated along each strain path to generate the strain energy density function for each element. A detailed example illustrating the method on a simulated sample is given in Appendix D.

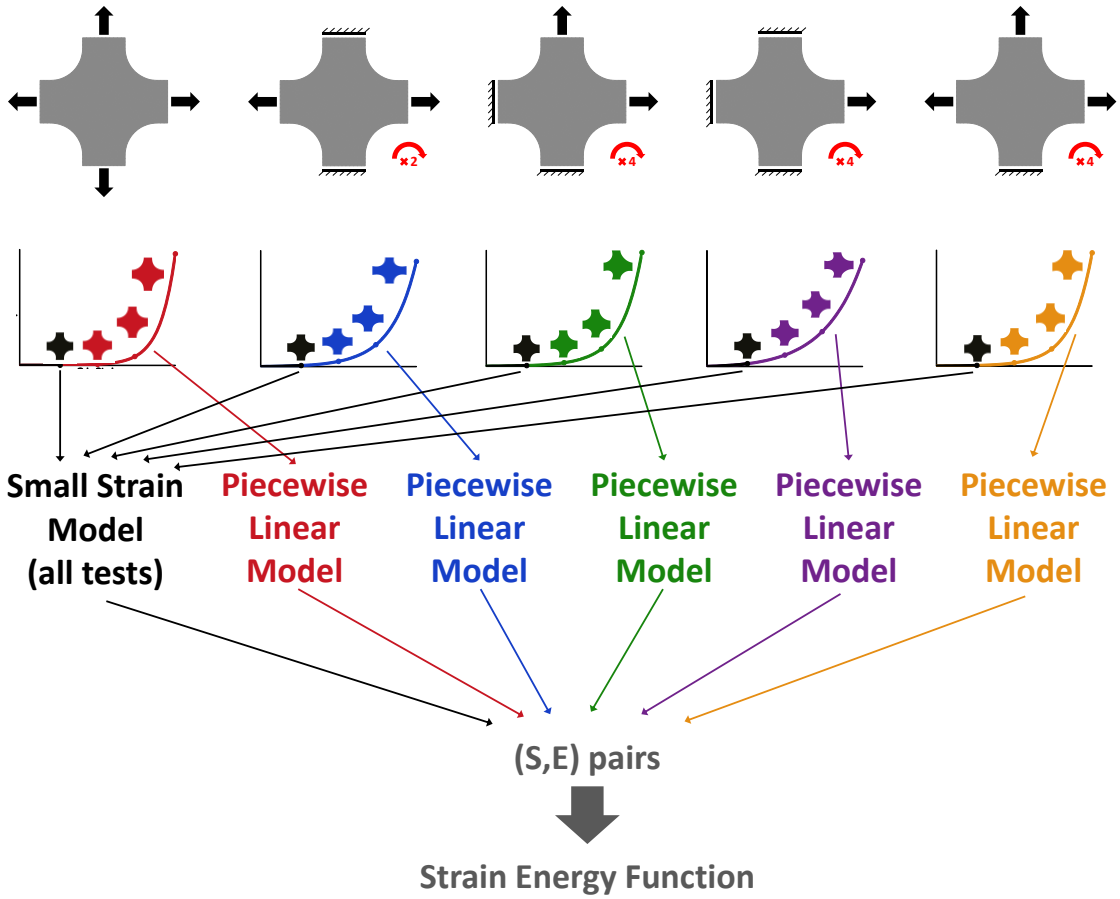

Figure 5.1: Schematic of Method. A set of different biaxial experiments is performed on the sample, providing the displacement fields and grip forces. Combined data from all of the experiments at small-strain (black segments in grip force vs. grip strain plots) are used to specify a small-strain model using our previous linear approach [129]. Data from each individual experiment at larger strain (colored segments in grip force vs. grip strain plots) are used to generate a piecewise linear model for the experiments strain path. The models are used to calculate the PK2 stress at each strain value for each experiment. The PK2 stress is integrated along each strain path to generate the strain energy density function at each strain value. Calculations for the small strain model are by partition, determined using the deformation field per chapter 4, and those in the piecewise linear models are by element, so the strain energy density function is obtained for each element.

5.3.2 Small-Strain Analysis of All Experimental Protocols Simultaneously

Once the step size had been determined, the displacement of each node of the FE mesh and the arm force values at the end of each step were extracted from the raw data. For the first step, GAIM was applied exactly as described previously [129] with one exception. Partitioning the sample into homogenous subdomains, one of the most difficult obstacles in applying GAIM, was done by applying graph theory to the full-field deformation

gradient of the sample under symmetric loading conditions to identify mechanically similar regions, per Chapter 4. Then, following the methods in [129], the force and displacement data for the first step from all 15 extensions were considered simultaneously, and an analogous neo-Hookean generalization of the linear elasticity tensor, K, was determined for each subdomain such that the PK2 stress, S, was defined by

$$S_{ij} = K_{ijkl}E_{kl} \tag{5.1}$$

where E is the Green strain, and K is piecewise constant over each partition. K is determined by solving the Cauchy stress balance

$$\left(F_{mi}K_{ijkl}E_{kl}\right)_{,j} = 0 \tag{5.2}$$

where F is the deformation gradient tensor and differentiation is with respect to the undeformed coordinates. In equation 5.2, F and E were known from the DIC, allowing K to be determined directly. Using the Galerkin finite element method [113], the weak form of equation 5.2 for a sample with an undeformed domain, Ω_0, and boundary Γ_0, is

$$\sum_e \left(\int_{\Gamma_0{}^e} t_i N_A \mathrm{d}\Gamma_0{}^e \right) = \sum_e \left(\int_{\Omega_0{}^e} F_{im}K_{mjqr}E_{qr}N_{A,j}\mathrm{d}\Omega_0{}^e \right) \tag{5.3}$$

where N_A are the Galerkin basis functions at node A of the finite element and the summation is over all elements, e. During biaxial testing, the forces on the grip arms are the combined reaction to the displacement of the sample boundary, essentially quantifying the integral of the force over the sample boundary. Therefore, the traction, t_i, represents the grip force measured at the boundary.

5.3.3 Large-Strain Analysis Following Individual Experimental Paths

It would be attractive simply to continue to apply GAIM to all following steps in the same manner, but as Flynn et al. [111] noted, there is an issue with reference configuration. Consider a point within the material. At the beginning of step 1, the sample is undeformed, and this point is in the same state no matter what extension is about to be imposed. In other words, because the initial state for the first step of *any*

experiment is the tissue's undeformed state, all experiments can be analyzed simultaneously for their first step. At the end of step 1 and thus the beginning of step 2, however, the point has moved, and the location of the point is thus dependent on which loading protocol is being imposed. The reference configuration for the step is no longer the same for all protocols. The rationale for the extensive loading scheme is to ensure that the inverse problem is well posed because it is not possible to determine the material characteristics of a subdomain within the sample without interrogating it in various loading conditions. If GAIM were applied in a stepwise fashion, however, it would no longer be sound to apply the displacement fields and reaction forces from the protocols concurrently. Flynn et al. [111] addressed this issue with an elegant experimental approach - by instituting an extensive incremental loading paradigm that allowed for the establishment of multiple reference configurations. Flynn's technique was highly effective for their homogeneous samples, but it required a 3-fold increase in the number of loading cycles applied to the tissue (increasing their loading scheme from 4 cycles to 12 cycles). Given the larger number of 45 loading cycles required to probe the heterogeneous tissues of interest to us, we have selected to consider all subsequent steps in each protocol separately.

The creation of a separate inverse problem for each experimental protocol causes difficulties in the solution of the matrix equation since it changes the nature of the problem: the initial GAIM step is *overdetermined* due to the large number of loading protocols and the relatively small number of partitions; subsequent steps are *underdetermined* since each element and loading protocol are evaluated separately. An additional constraint must therefore be imposed on the matrix problem during the subsequent steps. Therefore, the K accepted as a solution is that which satisfies the discrete stress balance *and* varies least from the elasticity tensor determined for the previous step. The differential PK2 stress, $\mathbb{S}$, for a step n is equal to

$$\mathbb{S}_{ij}{}^{n} = \mathbb{K}_{ijkl}{}^{n}\mathbb{E}_{ij}{}^{n} \tag{5.4}$$

where $\mathbb{K}$ (differential neo-Hookean elasticity tensor) and $\mathbb{E}$ (differential Green strain) are relative to the sample configuration at the end of step $n-1$. Stress is additive, meaning that

$$S_{ij}{}^{N} = \sum_{n=1}^{N} \mathbb{S}_{ij}{}^{n} \tag{5.5}$$

where $S_{ij}{}^{N}$ is the PK2 stress in reference to the global undeformed sample configuration at the end of step N and the PK2 for the first step is determined from the small-strain analysis. Strain is *not* additive, (i.e. for $N > 1$, $E_{ij}{}^{N} \neq \sum_{n=1}^{N} \mathbb{E}_{ij}{}^{n}$). The finite element discretized form of equation 5.3,

$$\sum_{e}\left(\int_{\Gamma_0{}^{e}} t_i{}^{N} N_{A,j}^{N} \mathrm{d}\Gamma_0{}^{e}\right) = \sum_{e}\left(\int_{\Omega_0{}^{e}} F_{im}{}^{N}\left(\sum_{n=1}^{N} \mathbb{K}_{mjqr}{}^{n}\mathbb{E}_{qr}{}^{n}\right) N_{A,j}^{N} \mathrm{d}\Omega_0{}^{e}\right) \tag{5.6}$$

was revised such that the piecewise discretization was considered. The 1st Piola-Kirchhoff stress can be restated in terms of the known and unknown $\mathbb{K}_{mjqr}$ values. Therefore,

$$\begin{aligned}\sum_{e}\left(\int_{\Gamma_0{}^{e}} t_i{}^{N} N_A \mathrm{d}\Gamma_0{}^{e} - \int_{\Omega_0{}^{e}} F_{im}{}^{N}\left(\sum_{n=1}^{N-1} \mathbb{K}_{mjqr}{}^{n}\mathbb{E}_{qr}{}^{n}\right) N_{A,j} \mathrm{d}\Omega_0{}^{e}\right) \\ = \sum_{e}\left(\int_{\Omega_0{}^{e}} F_{im}{}^{N}\mathbb{K}_{mjqr}^{N}\mathbb{E}_{qr}^{N} N_{A,j} \mathrm{d}\Omega_0{}^{e}\right)\end{aligned} \tag{5.7}$$

is the new finite element discretized form. Under the assumption that $\mathbb{K}_{mjqr}$ is constant over each element, the equation leads to a new global linear matrix equation for all steps beyond the first of the form

$$\mathcal{F}^{N} - \sum_{n=1}^{N-1} M^{n}\mathcal{K}^{n} = M^{N}\mathcal{K}^{N} \tag{5.8}$$

where M is a matrix consisting of the terms that remain when the material parameter terms on the right hand side of equation 5.7 are factored out (defined in Appendix B). Unlike the small-strain execution of GAIM, the system is underdetermined and cannot be

solved in a least-squares sense. Therefore, rather than minimizing a residual force norm the change in the differential neo-Hookean elasticity tensor, $\mathcal{K}^N - \mathcal{K}^{N-1}$, is minimized subject to the constraint that the residual force norm be zero.

5.3.4 Generating and Elemental Constitutive Data Set

The solution of the global matrix equation at each step of each protocol yields a unique neo-Hookean elasticity tensor for each subregion (small-strain) or element (large-strain) within the sample domain. The PK2 stress was obtained from those tensors using equations 5.4 and 5.5. By combining all the PK2 stresses calculated over all segments of all protocols for an element along with the corresponding Green strain, a set of ordered pairs, (E, S), was generated for each element; essentially, each set of pairs (E, S) functions as a mechanical characterization of its element as a unique material.

For a hyperelastic material, the work necessary to deform a body is its intrinsic strain energy density, $W = \int S_{ij} dE_{ij}$. In the case of the piecewise linear model the integration is approximated by a summation (trapezoid rule),

$$W_N^p = \sum_{k=0}^{N} \frac{\left({S_{ij}}^{k+1} + {S_{ij}}^{k}\right)}{2} \left({E_{ij}}^{k+1} - {E_{ij}}^{k}\right) \tag{5.9}$$

where W_N^p is the strain energy at step N for loading protocol p for an element within the sample domain. In this way, a unique data-driven strain energy density function is generated for each element within the sample domain.

5.4 Results

The new stepwise GAIM method, NGAIM, was applied to simulations of biaxial extensions generated based on the closed-form nonlinear fiber-based structural model (NFSM) for soft tissues previously presented in Chapter 4. The two simulations analyzed using NGAIM presented in detail were: (1) the simulation in which the preferred fiber

orientation was set such that the inclusion was rotated relative to the sample bulk, ($\mu_{bulk} = 20°$ and $\mu_{inclusion} = 80°$) and (2) the simulation in which the preferred fiber orientation was radially aligned. The displacement for each node of the sample mesh was determined by the NSFM as were the grip arm forces.

The full stress-fields for the equibiaxial and right-arm-only extensions for the simulation with the inclusion are shown for the final time step in Figure 5.1 and Figure 5.2, respectively, alongside the stress-fields determined by GAIM, per [129] (i.e. Chapter 2), as well as those determined by NGAIM. Though GAIM, as applied per [129], was capable of quantifying the stiffness and anisotropy of heterogeneous samples ([116] and Chapter 2) the stepwise nonlinear GAIM, NGAIM, shows dramatic improvement in the estimation of full-field stress. This observation is particularly true for the right-arm-only extension, for which the scale bar must be adjusted to visualize the results from GAIM.

The full stress-fields for the equibiaxial and right-arm-only extensions for the simulation with radial alignment are shown for the final time step in Figures 5.3 and 5.4, respectively, alongside the stress-fields determined by GAIM, per Chapter 2 [129], as well as those determined by NGAIM. Again, there is striking improvement in the estimation of stress, particularly for the right-arm-only extension, for which the scale bar must be adjusted to visualize the results.

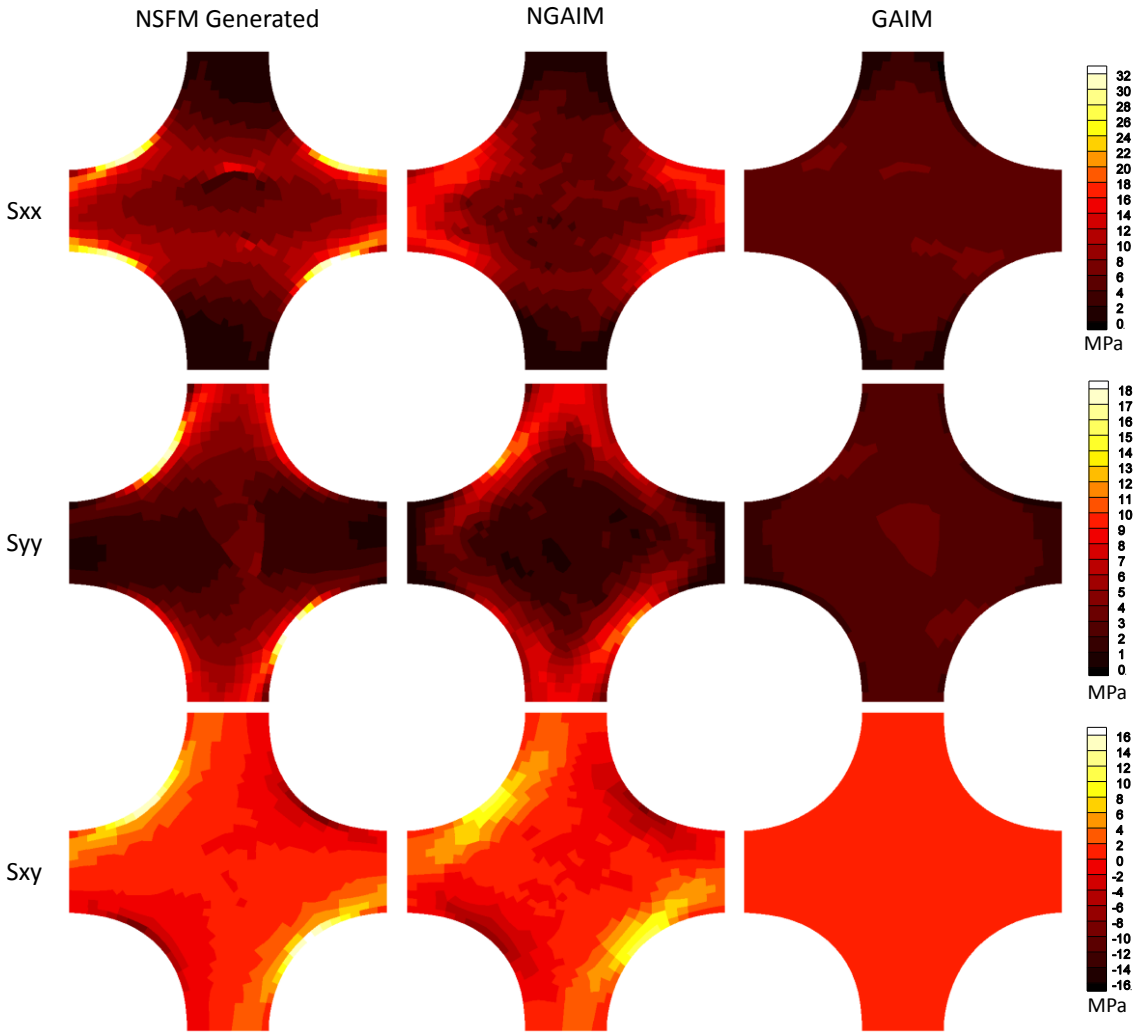

Figure 5.1: Stress field for the simulated sample containing an inclusion at the end of the final time step for the equibiaxial extension.

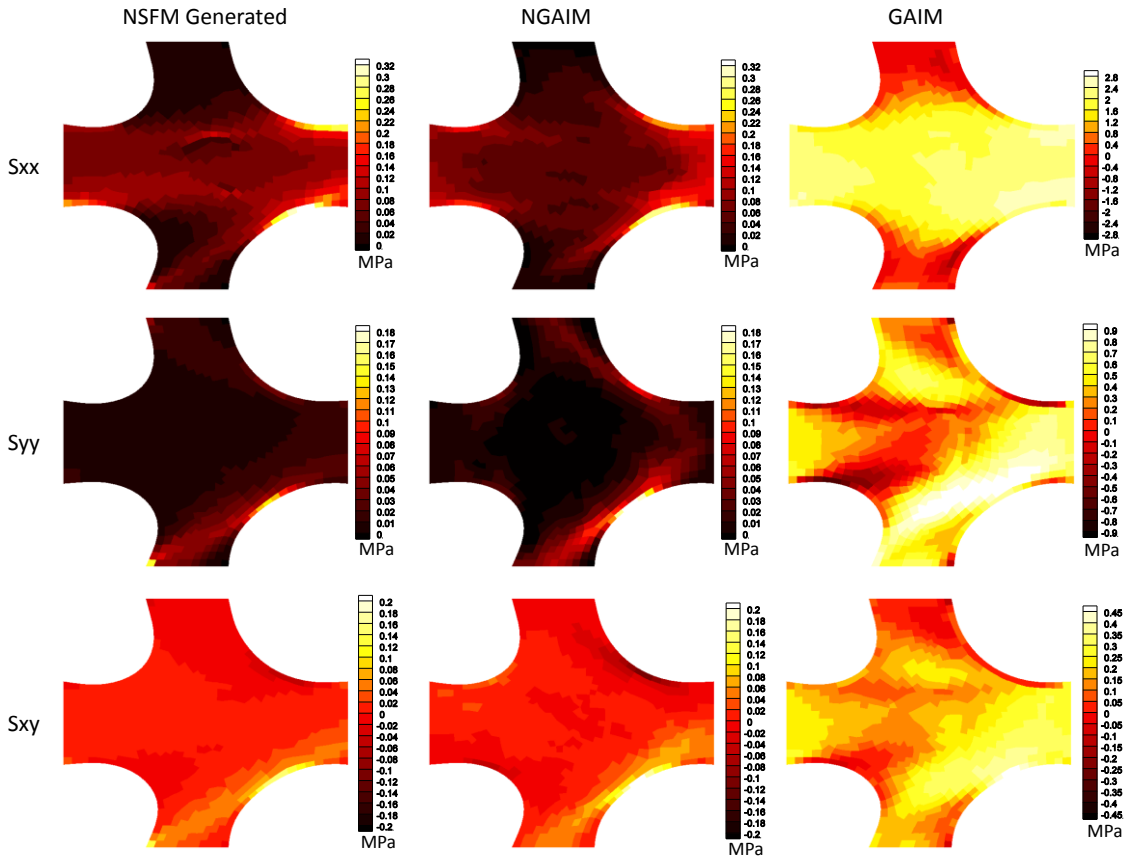

Figure 5.2: Stress field for the simulated sample containing an inclusion at the end of the final time step for the right-arm-only extension.

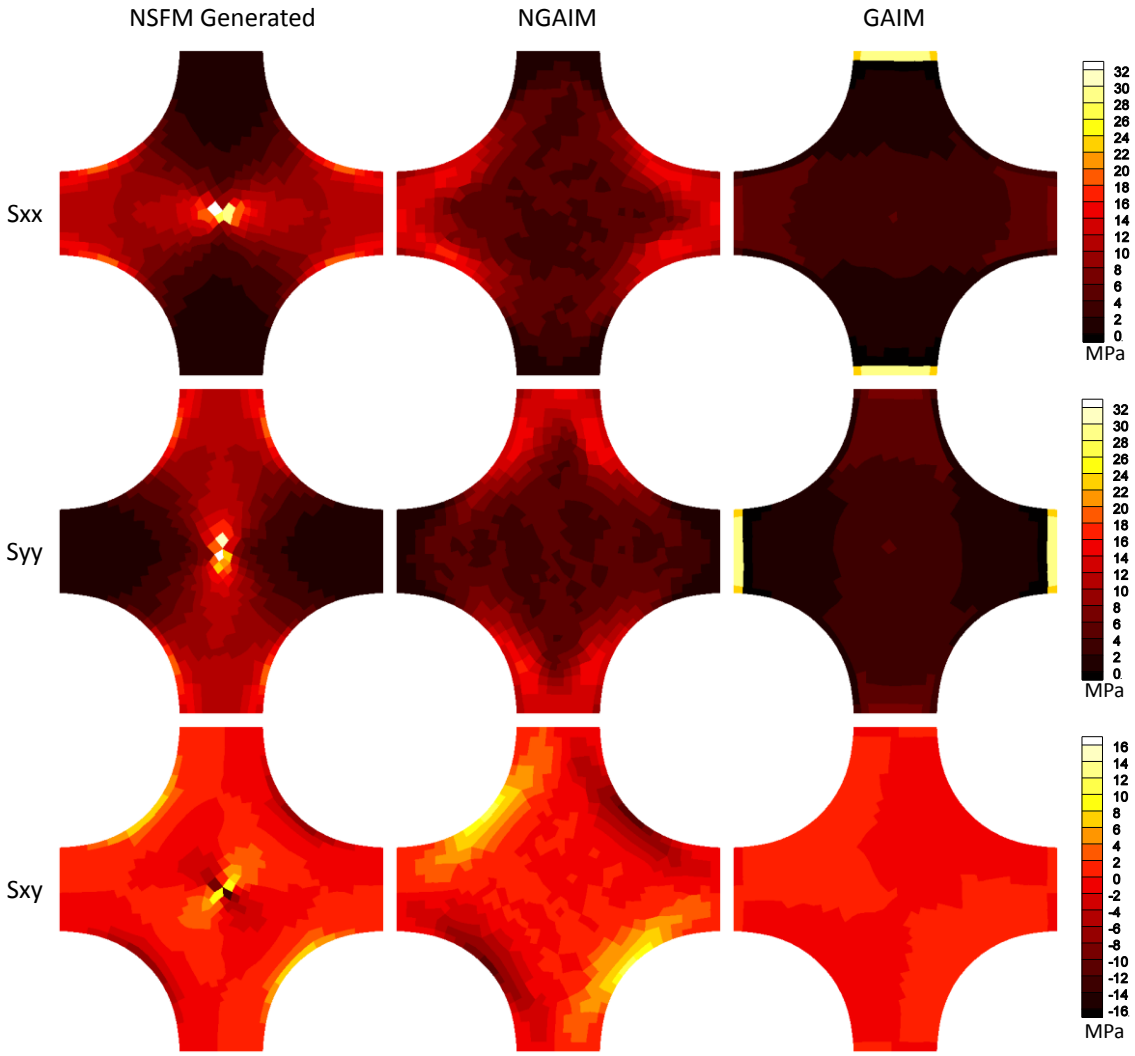

Figure 5.3: Stress field for the simulated sample with radial alignment at the end of the final time step for the equibiaxial extension.

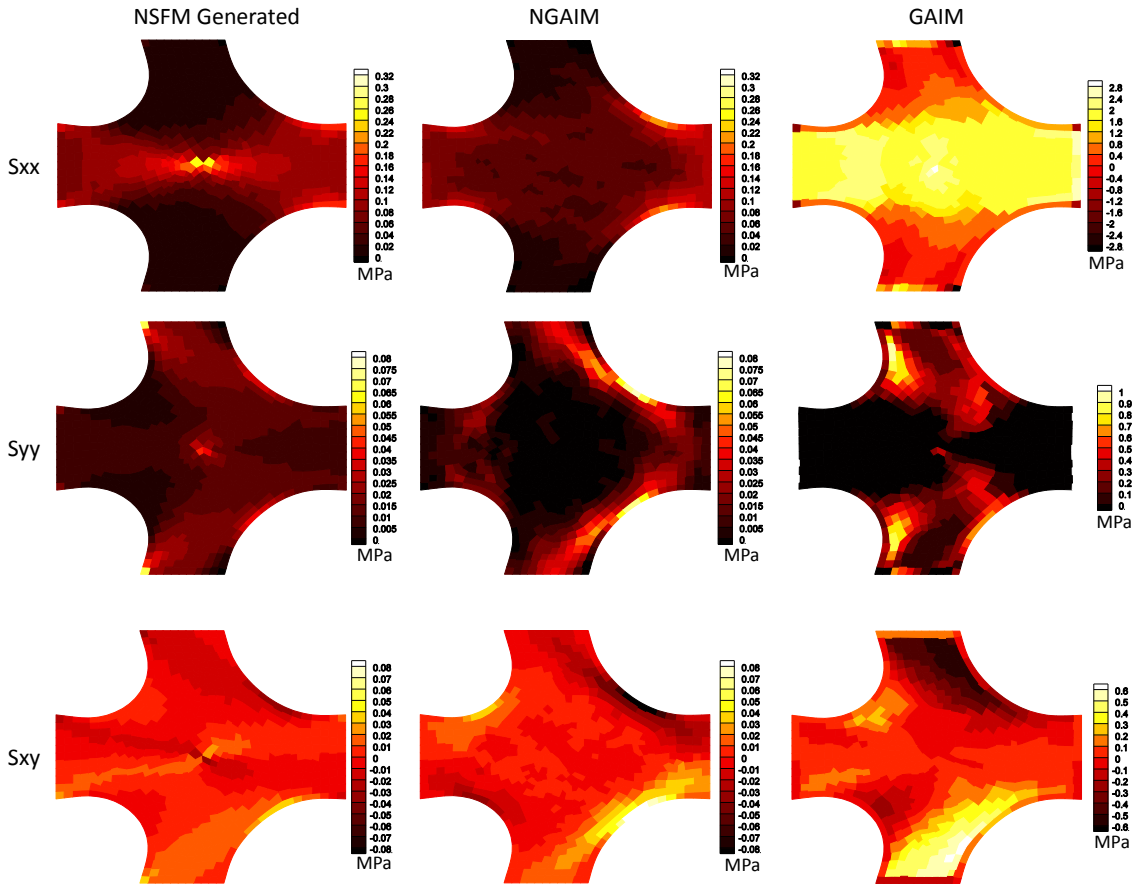

Figure 5.4: Stress field for the simulated sample with radial alignment at the end of the final time step for the right-arm-only extension.

However, the improvement is even clearer when all time steps are considered. First, consider the simulation with the inclusion. For clarity, two elements within the central region of cruciform shaped sample will be analyzed, one located in the middle of the inclusion and the other location outside of the inclusion, Figure 5.5a. Figure 5.6 shows the strain energy vs. Green strain component curves for the two elements for the equibiaxial and right-arm-only extensions. The plots are projections of the full $W - E_{xx} - E_{yy} - E_{xy}$ space, leading to the sometimes counterintuitive curves. It is clear from these plots that in addition to capturing the strain energy better within the sample at the end of the loading protocol, NGAIM better captures the strain energy within the sample throughout the loading protocol. In Figures 5.7 and 5.8, a direct comparison between the strain energy generated from the NFSM and that determined by NGAIM is shown for the

two elements. There is excellent agreement between the NGAIM prediction and NFSM generated strain energies.

The NGAIM approach also performed well on the simulated data for a sample with radial fiber alignment. Two elements were again selected for further analysis, one near the middle of the sample and one towards the curved edge, as shown in Figure 5.5b. Again, Figure 5.9 shows the strain energy vs. Green strain component curves for the two elements for the equibiaxial and right-arm-only extensions. NGAIM better captures the strain energy within the sample throughout the loading protocol. In Figures 5.10 and 5.11, a direct comparison of the strain energy from the NFSM and NGAIM is shown for the two elements of interest and there is good agreement between the NGAIM prediction and NFSM generated strain energies.

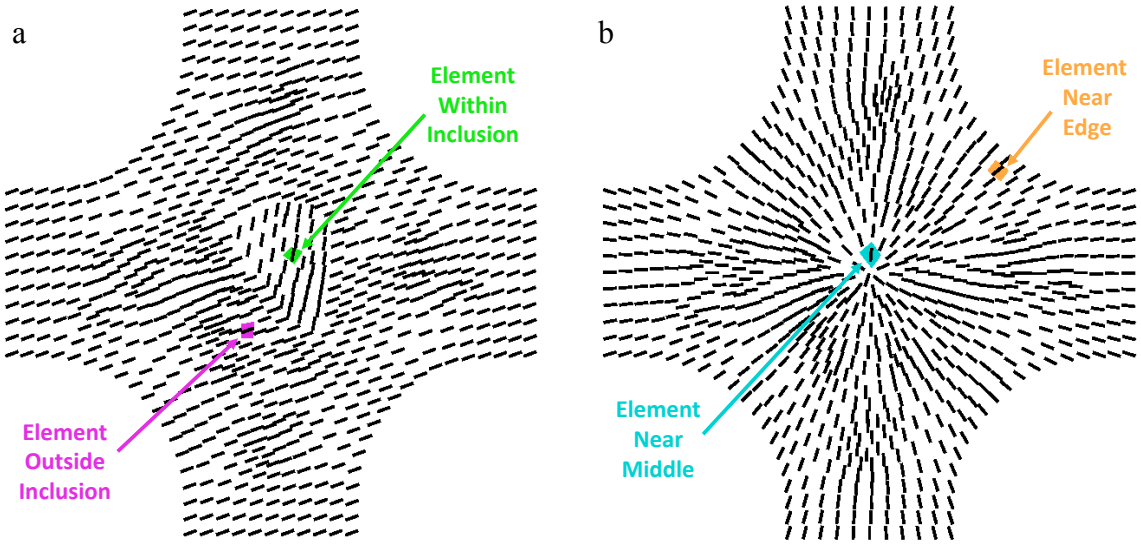

Figure 5.5: The elements selected for further analysis. For the simulation involving the inclusion (a) they are within the center of the sample in the middle of the inclusion and just outside of the inclusion. For the simulation with radial alignment (b) they are near the center of the sample and near its edge .

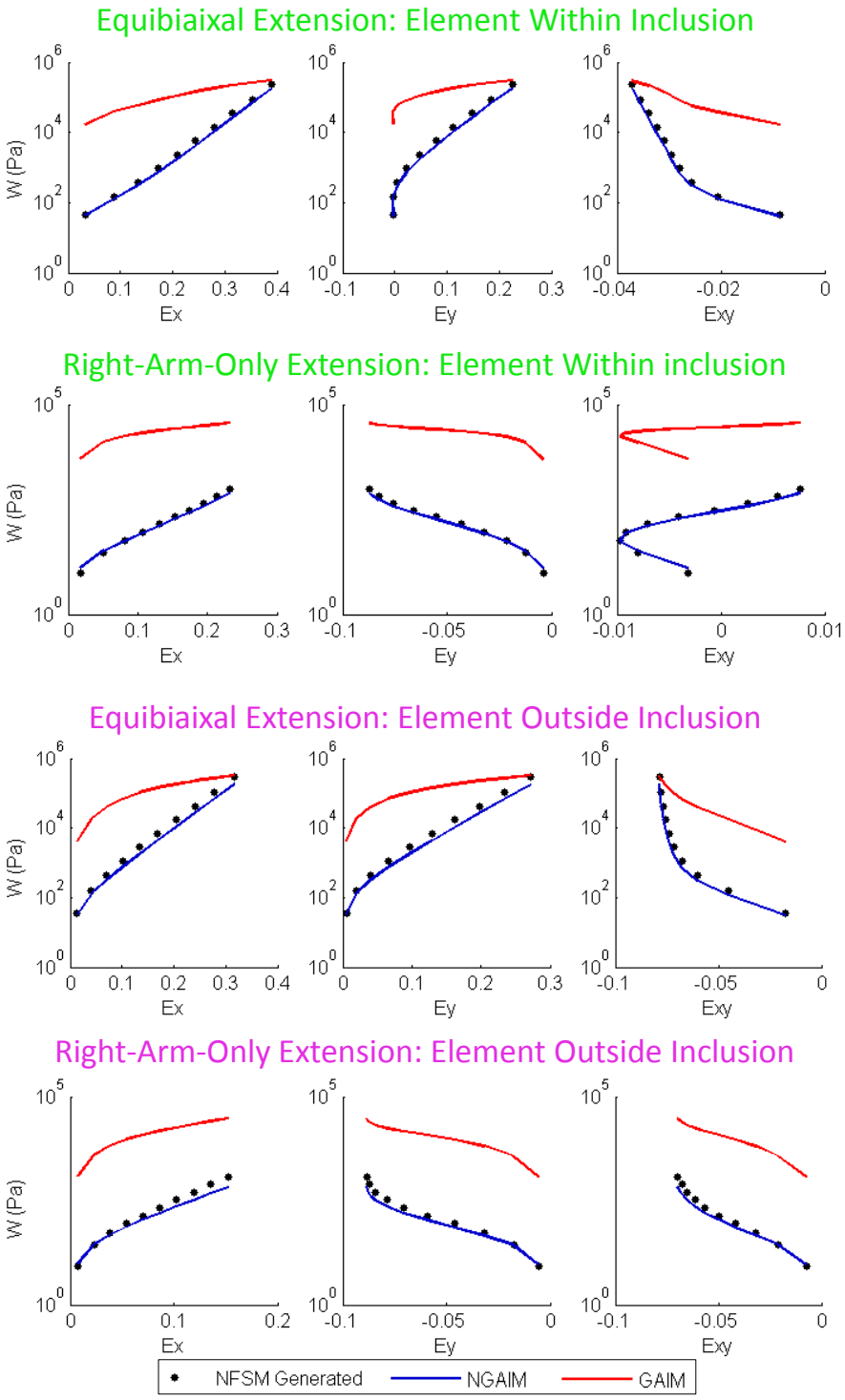

Figure 5.6: Strain energy vs. Green strain component for the equibiaxial and right-arm-only extensions for the element in the middle of the inclusion and the element just outside of the inclusion. The black dots indicate the strain energy generated from NSFM model, the red line indicates the strain energy determined by the original linear GAIM method, and the blue line indicates the strain energy determined by the stepwise nonlinear GAIM method, NGAIM.

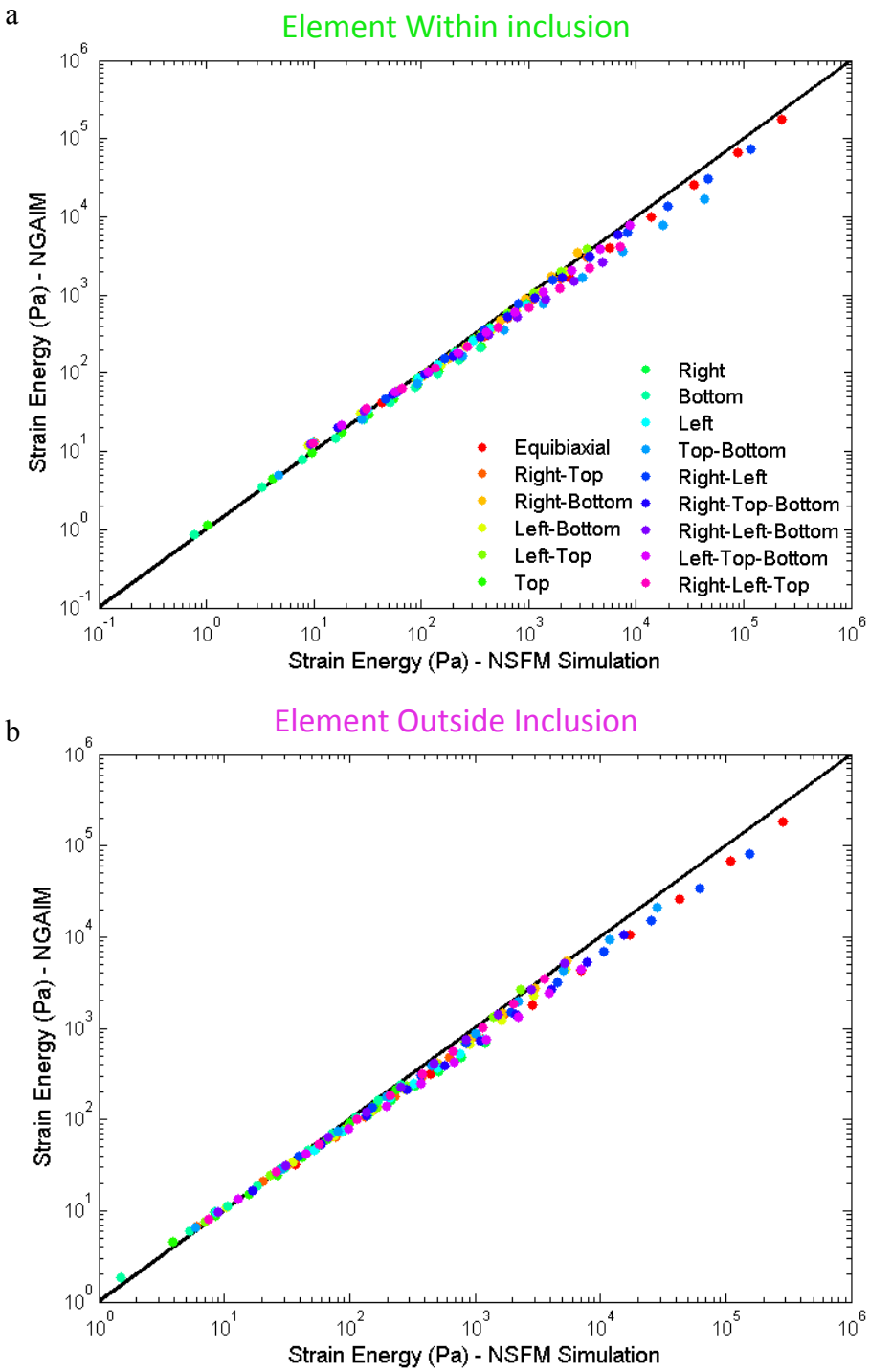

Figure 5.7: Strain energy determined using the stepwise GAIM method vs. the strain energy generated by the NSFM simulation for all biaxial extensions (colored dots) for the element within the inclusion (a) and the element just outside of the inclusion (b). The diagonal black line indicates a perfect prediction.

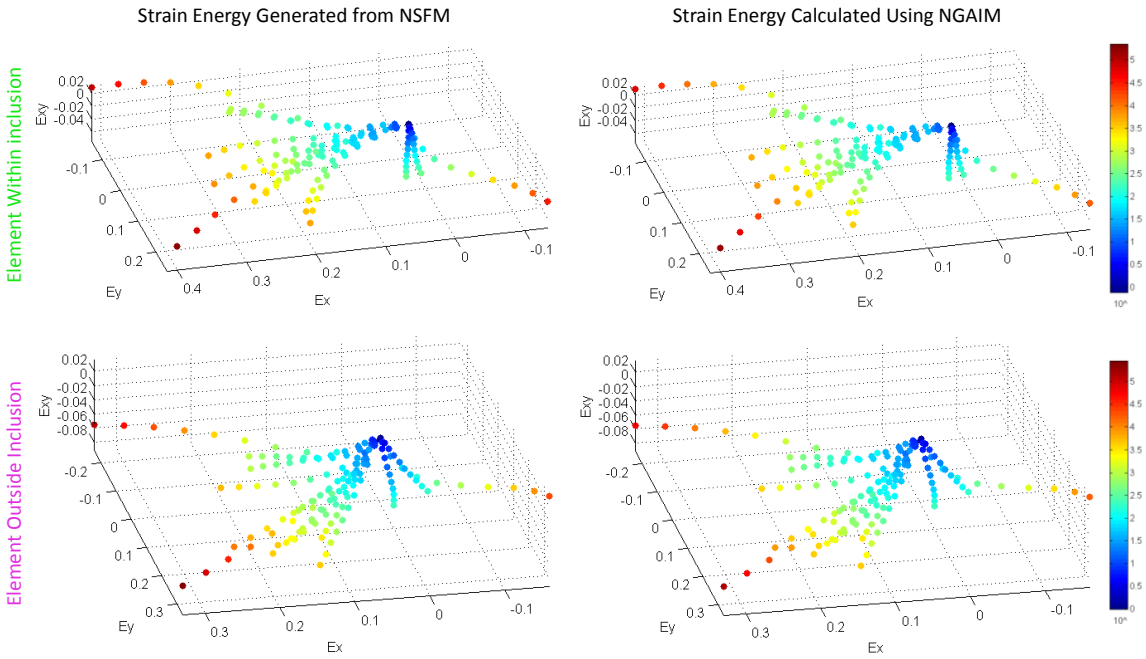

Figure 5.8: Strain energy generated by the NSFM model and strain energy calculated using the stepwise GAIM method for all extensions plotted in strain space for both the element within the inclusion and the element just outside the inclusion.

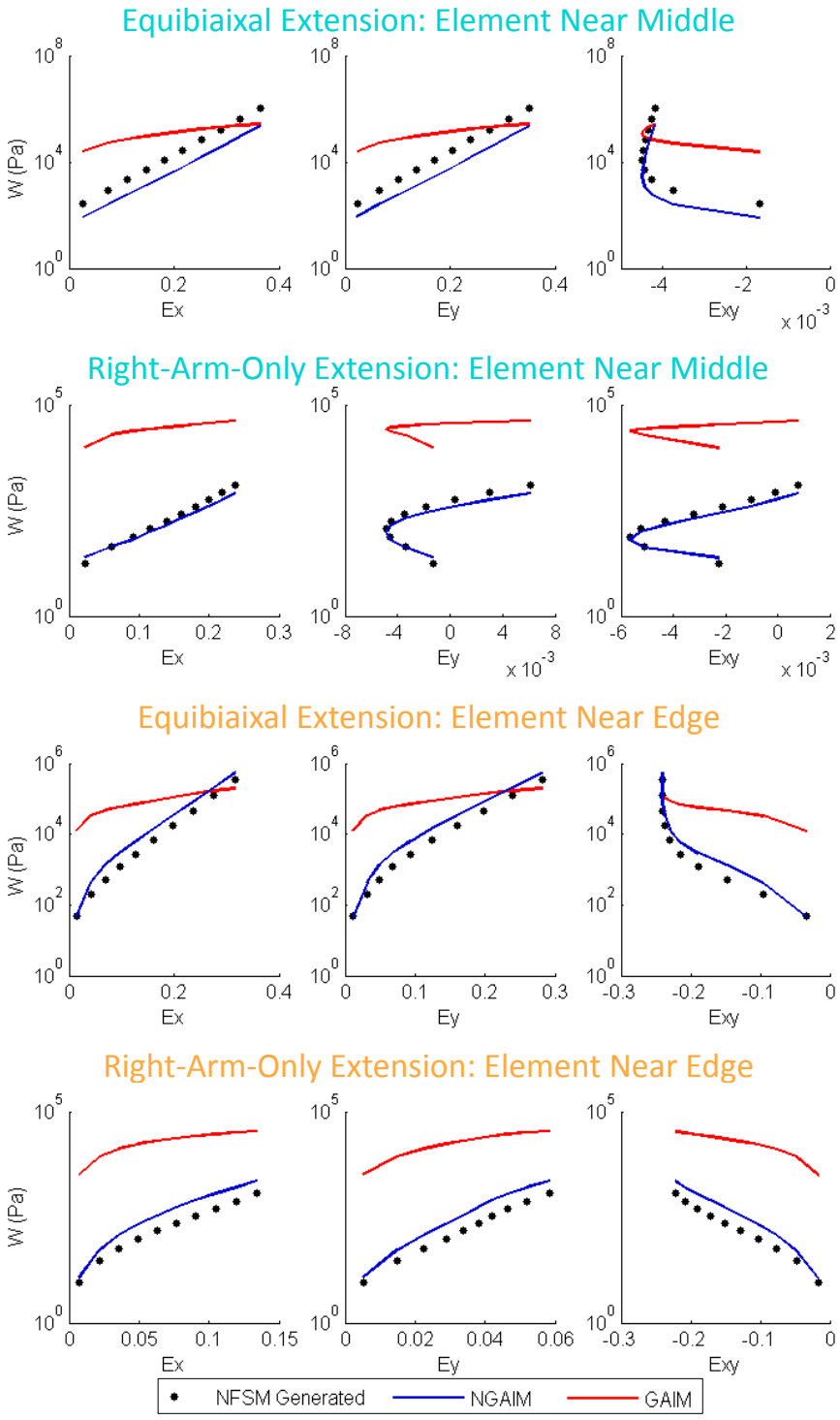

Figure 5.9: Strain energy vs. Green strain component for the equibiaxial and right-arm-only extensions for the element near the middle and the element near the edge of the radially aligned sample. The black dots indicate the strain energy generated from NSFM model, the red line indicates the strain energy determined by the original linear GAIM method, and the blue line indicates the strain energy determined by the stepwise nonlinear GAIM method, NGAIM.

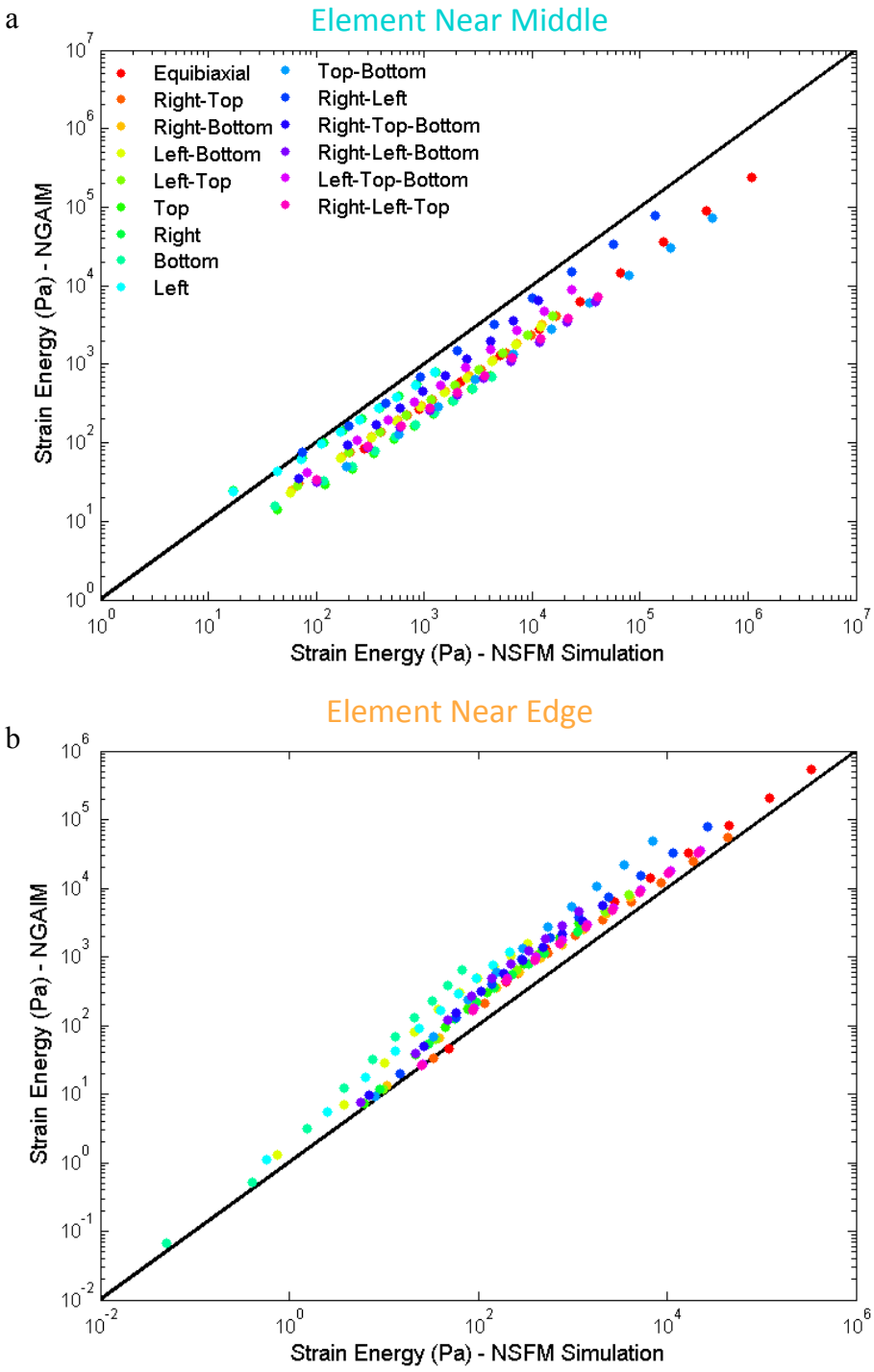

Figure 5.10: Strain energy determined using the stepwise GAIM method vs. the strain energy generated by the NSFM for all biaxial extensions (colored dots) for the element near the center (a) and an element near the edge (b) of the radially aligned simulation. The diagonal black line indicates a perfect prediction.

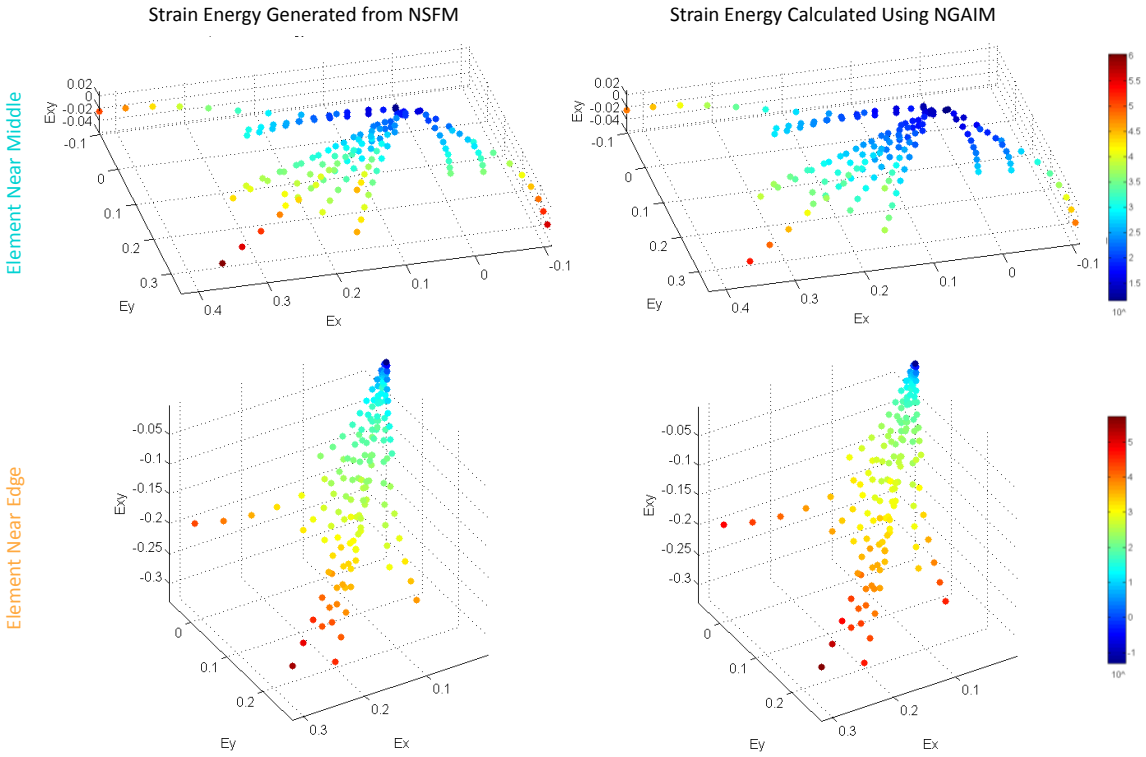

Figure 5.11: Strain energy generated by the NSFM model and strain energy calculated using the stepwise GAIM method for all extensions plotted in strain space for both the element near the center and the element near the edge of the radially aligned sample.

Next, the NFSM parameters, A, B, κ and μ, were fit to the stress-strain curves determined for each element by NGAIM using a nonlinear simplex search, fminsearch, in Matlab. The maximum Kelvin modulus, E_K, anisotropy index, r, and preferred stiffness direction, θ, determined in the small-strain analysis were used to generate the initial guesses for the NFSM parameters following the method of [115]. Appendix A details how the elasticity tensor components are used to calculated E_K, r, and θ. The initial guess for the degree of anisotropy, κ, was determined from r,

$$\kappa = \frac{r}{1 - r^2} \tag{5.10}$$

and the initial guess for the preferred fiber direction, μ, was set to the preferred stiffness direction, θ. The product AB can be determined directly from E_K,

$$AB = \frac{2\kappa * E_K * I_0(\kappa)}{\kappa I_1(\kappa)\sqrt{4 + \frac{1}{\kappa^2}} + 2\kappa I_0(\kappa) - I_1(\kappa)} \tag{5.11}$$

where I_0 and I_1 are modified Bessel functions of first kind and zeroth and first orders, respectively. Since the product AB cannot be separated for small-strain data, the initial guess for B was determined from an exponential fit of equation 3.2 to the equibiaxial grip force vs. grip stretch data. The exponential fit of the equibiaxial data yielded a $B = 12.9$ for the simulation with the inclusion and a $B = 12.7$ for the simulation with radial symmetry in which fiber direction was prescribed. The initial guess for A was determined using 5.11. The fitted parameters are compared to those utilized to generate the simulations using NFSM in Figures 5.12 and 5.13 for the simulation with the inclusion and the simulation with radial alignment, respectively. For both simulations, the stepwise application of GAIM was able to recapture the prescribed NFSM parameters well. In particular, for the simulation with the inclusion, there is very good agreement been the fiber orientation prescribed and the fiber orientation recovered both within the inclusion and at the inclusion border. For the simulation with radial alignment fiber direction is well-recovered. An additional fit was performed for both simulations with varied alignment in which the initial value of B set to 1 in order to gauge the influence of initial guess on the final fit, results are given in Appendix D.

An additional unrelated strain energy function was fit to the NGAIM results in order to demonstrate the flexibility of NGAIM. The strain energy density function utilized, the four-fiber family model, is a popular model [185–192] used to describe the mechanical behavior of arteries. The strain energy function W is

$$W = \frac{c}{2}(I_1 - 2) + \sum_{k=1}^{4} \frac{c_{1(k)}}{4 * c_{2(k)}}\left\{\exp\left[c_{2(k)} * \left(I_{4(k)} - 1\right)^2\right] - 1\right\} \tag{5.12}$$

where c, $c_{1(k)}$, $c_{2(k)}$, are material parameters and the invariants I_1 and $I_{4(k)}$ are

$$I_1 = \mathrm{tr}\mathbf{C}, I_{4(k)} = \mathbf{M}_{\alpha_k}\left(\mathbf{C}\mathbf{M}_{\alpha_k}\right) \text{ for } k = 1, 2, 3, 4 \tag{5.13}$$

where $\mathbf{C}$ is the right Cauchy-Green deformation tensor. The fiber orientations are defined in the reference configuration by unit vector $\mathbf{M}_{\alpha_k}$, which depend on angle α_k defined between the direction of the k^{th} family of collagen fibers and the horizontal direction for the cruciform shaped sample. Following [185], although the constitutive model (Eqn. 5.12) includes four collagen-fiber families characterized by fiber angles α_k, a fiber angle was assumed to be oriented along the vertical axis ($\alpha_1 = 90^0$), a fiber angle was assumed to be oriented along the horizontal axis ($\alpha_2 = 0^0$), and the remaining fiber angles were assumed to be symmetrically oriented diagonal fibers (i.e. $\alpha_2 = \alpha$ and $\alpha_3 = -\alpha$). Additionally, fibers were assumed to have similar behaviors (i.e. $c_{1(k)} = c_1$ and $c_{2(k)} = c_2$). Consequently, from Eq. 5.12 and the assumptions, 4 parameters were fit ($c, c_1, c_2,$ and α). Initial guesses for both simulations for each parameter were based on best-fit values from [185], and a nonlinear simplex search, fminsearch, in Matlab was used to fit the four-fiber family model strain energy to the NGAIM strain energy. The fits for both the NSFM model and the four-fiber family model are shown in Figures 5.14 and 5.15, which includes the direct comparison of the strain energy generated by the NSFM simulation and the strain energy determined by NGAIM from Figures 5.7 and 5.10, respectively. Though modifications to the four-fiber family model utilized could improved the strain energy determined; it matches fairly well with both the true simulation and NGAIM strain energy values. The best-fit four-fiber family model parameters for the elements of interest for both the simulation with the inclusion as well the radially aligned simulation are given in Appendix D.

The new stepwise GAIM method, NGAIM, was applied to the remaining simulations (previously presented in Chapter 4) of biaxial extensions generated based on the closed-form nonlinear fiber-based structural model (NFSM) for soft tissues. Simulations included the cruciform sample with a central triangle shaped inclusion for which the inclusion varied from the bulk sequentially in strength of alignment ($\kappa_{bulk} = 1.5$ and $\kappa_{inclusion} = 6.0$), stiffness ($A_{bulk} = 5\ kPa$ and $A_{inclusion} = 20\ kPa$), and nonlinearity ($B_{bulk} = 12$ and $B_{inclusion} = 48$) as well as the radially varying cruciform sample

with sample anisotropy strength, stiffness, and nonlinearity maximized in the center of the sample and reduced with radial distance from the center ($\kappa, A, B \sim 1/(1 +$ radial distance)), sequentially. The NSFM parameters determined by fitting the stress-stain behavior predicted by the stepwise GAIM method compared with the NSFM parameters used to generate the simulated sample are shown for each simulation in Appendix D.

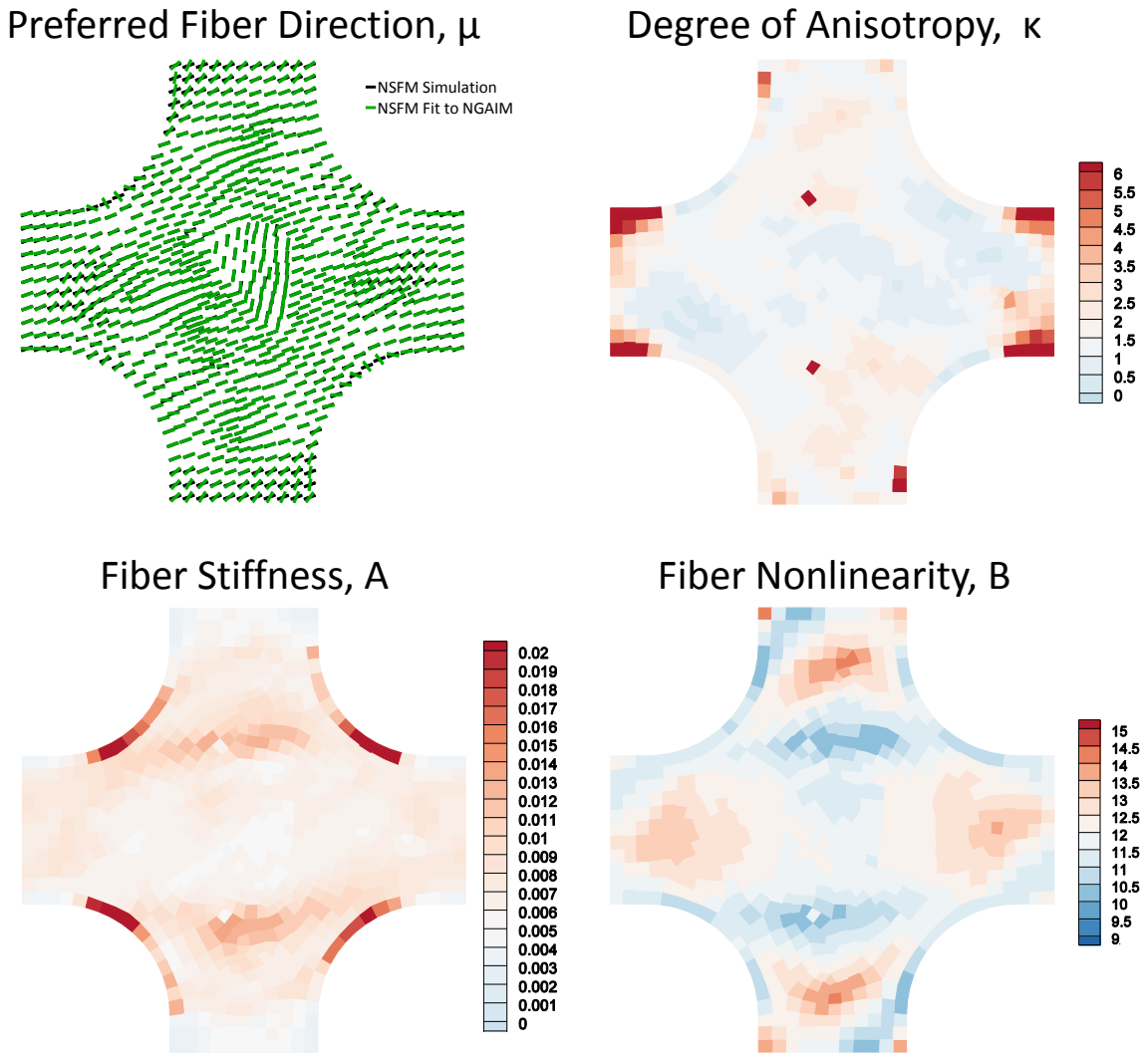

Figure 5.12: NSFM parameters determined by fitting the stress-stain behavior predicted by the stepwise GAIM method compared with the NSFM parameters used to generate the simulated sample with the inclusion with prescribed fiber strength. The preferred fiber direction prescribed for NSFM is in black and the one recovered by the stepwise application of GAIM is in green. All other parameters are shown on scales which place the original values at the center.

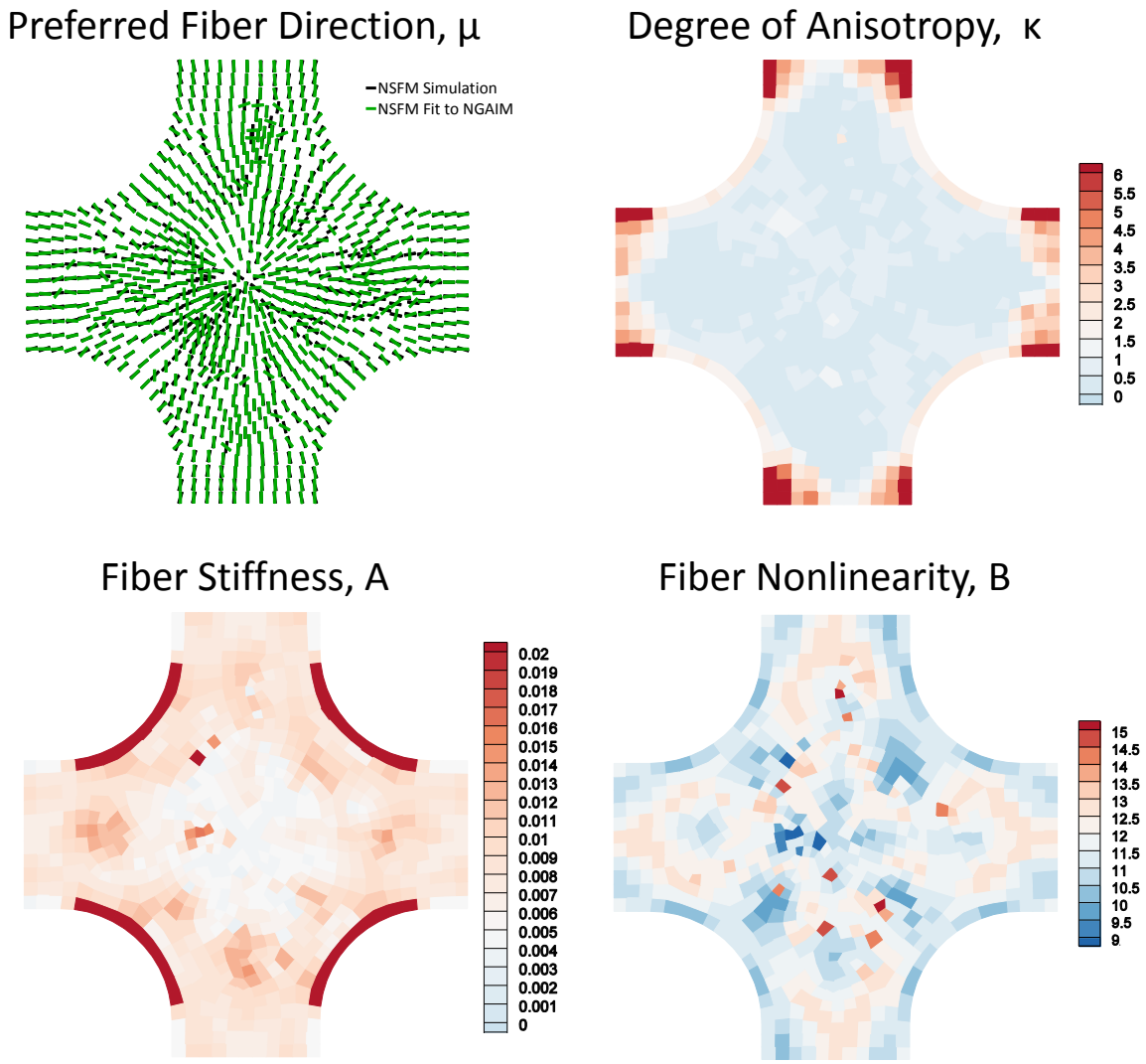

Figure 5.13: NSFM parameters determined by fitting the stress-stain behavior predicted by the stepwise GAIM method compared with the NSFM parameters used to generate the simulated sample with radial alignment. The preferred fiber direction prescribed for NSFM is in black and the one recovered by the stepwise application of GAIM is in green. All other parameters are shown on scales which place the original values at the center.

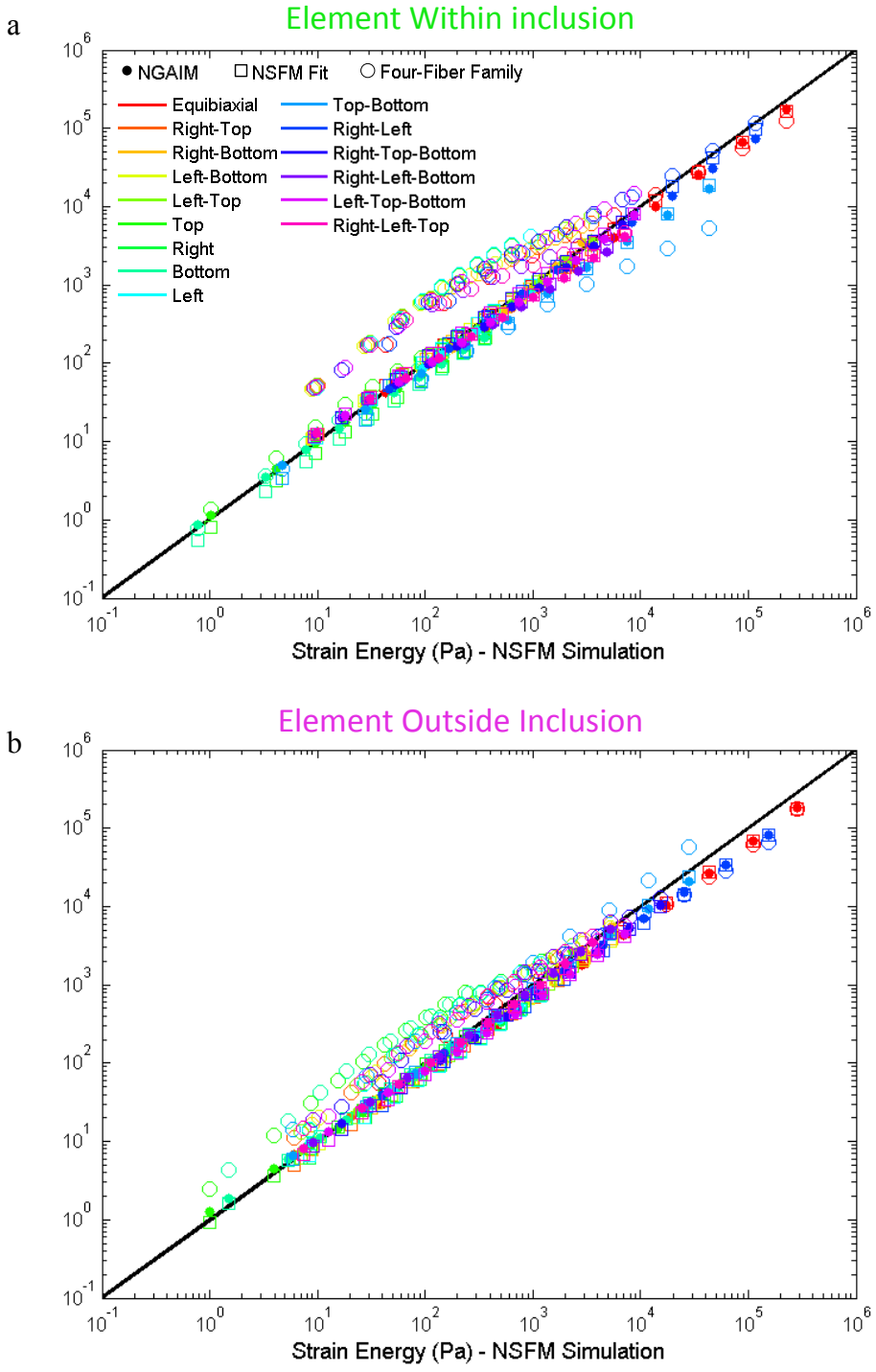

Figure 5.14: Strain energy determined using NGAIM (colored dots), the strain energy determined by the NSFM fit to the NGAIM results (colored squares), and the strain energy determined using the four-fiber family model (colored circles) vs. the strain energy generated by the NSFM simulation for all biaxial extensions for the element within the inclusion (a) and the element just outside of the inclusion (b). The diagonal black line indicates a perfect prediction.

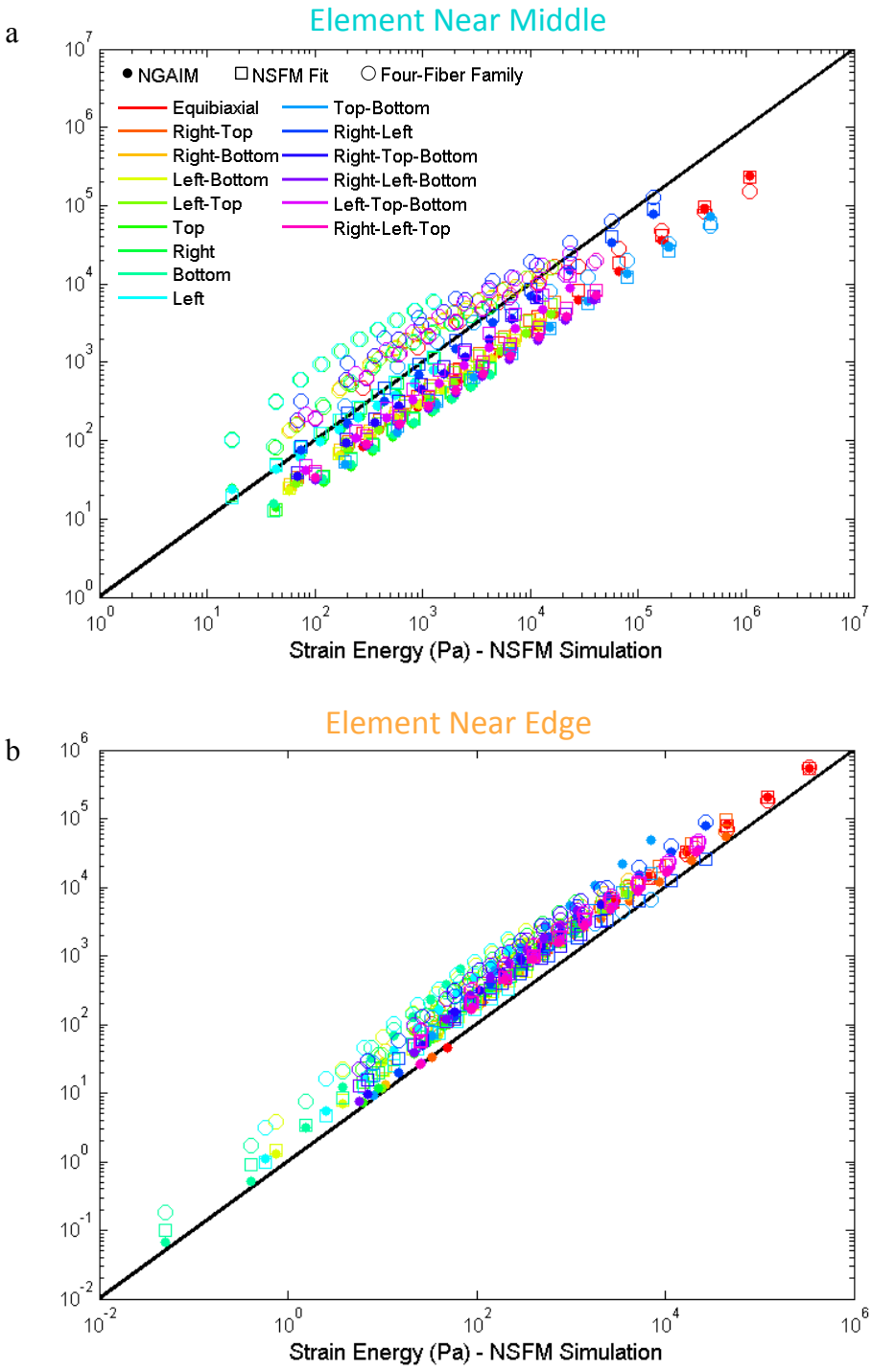

Figure 5.15: Strain energy determined using NGAIM (colored dots), the strain energy determined by the NSFM fit to the NGAIM results (colored squares), and the strain energy determined using the four-fiber family model (colored circles) vs. the strain energy generated by the NSFM simulation for the element near the center (a) and an element near the edge (b) of the radially aligned simulation. The diagonal black line indicates a perfect prediction.

5.5 Discussion

The GAIM method allows for the computational dissection of samples, enabling the capture of regional differences within a single sample nondestructively. Not only does it capture gross differences between regions, but also how stiffness and anisotropy change from region to region and whether these changes are drastic and abrupt or more gradual. A limitation of GAIM was its inability to capture the nonlinear behavior of soft tissues, particular cardiovascular soft tissues which operate at large-strain. The key to extending GAIM was to discretize each nonlinear curve into many short linear segments which allows for the consideration of the nonlinear force-displacement curves without sacrificing the tremendous efficiency advantage of the linear model. The NGAIM method generates a set a piecewise elasticity tensors describing the material behavior of a particular element within the sample for part of one test protocol. Multiplying a tensor by the strain measured experimentally in that region during that portion of the testing protocol yields a stress. By combining all the stresses calculated over all segments of all protocols for a particular region a set of stress-strain curves were determined from which a unique data-driven strain energy density function was generated.

The *in silico* results for NGAIM show good agreement between the strain energy and full-field stress recovered by NGAIM and that generated by the NSFM. In particular, as shown in Figure 5.6 and Figure 5.9 the behavior of the sample throughout testing, and not just at its endpoint, is captured. The NSFM parameters utilized to generate the simulation are well-recovered for the simulation involving the inclusion, particularly within the inclusion and at its border. For the radially aligned sample, an interesting pattern developed in the recovery of the NSFM parameters. The degree of anisotropy recovered within the center of the sample is lower than that prescribed, and in some elements close to zero, indicating the center of the sample is relatively isotropic. Therefore, the fiber angle recovered within the center becomes less relevant as the sample is no longer anisotropic. The inability to distinguish degree of anisotropy and fiber direction in the recovery of the model parameters reaffirms observations discussed in Chapter 3

suggesting that if this model is to be coupled with NGAIM, in the future a network orientation tensor may be a more appropriate metric for evaluating anisotropy. It also affirms the visual description of this sample, which as a whole has no predominant direction of alignment.

Functional limitations to NGAIM remain. In particular, the biaxial testing system is ill-suited to the generation of shear strain causing limitations in the strain-space spanned for each element, observed in part in both Figure 5.8 and Figure 5.11 as the E_{xy} axis is relatively shorter than the E_{xx} and E_{yy} axes. The decision to employ 6-degree-of-freedom load cells (JR3 Inc.), which allow for the measurement of both the normal and shear forces at the grip, was motivated by this limitation. A tester that utilizes multiple load cells (like that of Hoffman, Grigg, and colleagues [111,193]) would also allow for more detailed force measurements at the sample boundary and the direct imposition of shear. As indicated by Sacks [194], however when asymmetric loading is introduced in this manner during planar biaxial testing, there is the potential for out-of-plane deformation. Sacks suggests rotating the test specimen such that the fiber and cross-fiber directions do not coincide with the test machine axes and the use of rotating carriages to induce shear and avoid wrinkling. A multiaxial tester like that of Nielsen and colleagues [107,108], is a more involved, sophisticated approach to the introduction of shear. It allows for a broader strain space to be imposed on each region of the sample while controlling against out-of-plane deformation. In addition, though it is more experimentally demanding, the tester allows for more detailed measurement of force at the sample boundary.

Large onus is placed on the accuracy of the values for the analogous elasticity tensors calculated in step one using this method. The need for accuracy in step one has motivated many of the decisions to change how GAIM is implemented. Most importantly, it was strong motivation to change the partitioning scheme. Previously, GAIM utilized a partitioning scheme that ascribed elements to subdomains based on the residual force norm [115]. The ability of a group of elements to describe the material behavior across their partition was assessed by computing the 95% confidence intervals for the

components of the analogous elasticity tensor. However, at step one the reaction forces measured for the material are often quite low suggesting that the 95% confidence interval may no longer be adequate or appropriate. The deformation gradient jump method, described in Chapter 4, is capable of partitioning simulated data, tissue analogs, and real tissues into homogenous subdomains based on the deformation alone without considering the reaction forces. Thus, partitioning decisions are now independent of analogous elasticity tensor estimation. Another decision that was influenced by the need to ensure accuracy in the first step was the continued use of the extensive loading protocol. The GAIM method requires a large number of extensions be applied to tissue samples. The series of biaxial experiments poses practical challenges to biaxial testing as the potential for damage or irrecoverable deformation increases with the number of protocols performed. However, as the step-wise application of GAIM relies so heavily on step 1 of the various protocols it becomes even more crucial that the matrix problem for step 1 is grossly over-determined. Sensitivity to noise, particularly at the low force levels measured, must be minimized. Therefore, we have selected to continue using the extensive loading scheme. Finally, the method to determine an appropriate step size was strongly influenced by the need for accuracy in step 1. When determining step size the need to capture as much of the mechanical behavior of the tissue as possible within a single step must be balanced with the need to fit the behavior linearly.

The NGAIM method builds on the work of Raghupathy et al. [113] adding the capacity to analyze nonlinear samples to the original method for heterogeneous, anisotropic samples. The inverse method of Cox et al. [84], captures anisotropy by combining force and deformation gradient data and incorporates nonlinearity through the use of a constitutive framework developed by Holzapfel et al. [86]. However, it relies on indentation as a loading mode, and heterogeneity is determined through controlled, repeated application of a compressive force, a loading modality not representative of physiologic conditions. The inverse method proposed by Seshaiyer and Humphrey [92] also incorporates nonlinearity, anisotropy and heterogeneity. They utilize the principle of virtual work and a computationally demanding Marquardt-Levenberg regression to determine the best-fit

values of the material parameters. The NGAIM method does not require a fully integrated FEM simulation and in the large-strain analysis can be parallelized to maximize efficiency. Thus, it can be run on a standard computer (vs. a supercomputer) in a matter of minutes to hours. As in our approach, Seshaiyer and Humphrey divide the sample domain into homogeneous subdomains allowing for more robust estimations of local material parameters without assuming total homogeneity. Kroon and Holzapfel [67] propose an alternative inverse method, which enabled the investigation of the distribution of anisotropic material properties. However, both groups are limited as their methods apply to inflation are do not consider shear. Hoffman, Grigg, and colleagues [111] propose an elegant inverse method for the determination anisotropic, nonlinear properties of planar soft tissues subjected to a variety of biaxial loading conditions encompassing both tension and shear. They capture the nonlinear behavior of the tissue with through an incremental force-displacement approach which allows for the calculation of a tangent stiffness. However, their approach is limited by the need to test multiple specimens from different physical locations to investigate heterogeneity.

The main advantage of the NGAIM method is its flexibility. NGAIM generates a data-driven strain energy field for each element within the sample domain. Once this strain energy field is determined, *any* strain energy function can be used to describe the element's material behavior. In this chapter the NSFM, the close-form structural model of planar fibrous tissue mechanics developed by Raghupathy and Barocas [124], as well as a version of the four-fiber family model [185] were fit to the strain energy fields. The ability of NGAIM to generate a full strain energy field also allows for the comparison of various strain energy relations. It can be determined whether one function is more appropriate than another for a particular material or loading configuration. Next steps involve applying the method to both tissue analogs (e.g. anisotropic cell-compacted collagen cruciforms) and tissue specimens (e.g. infarcted myocardium and/or ascending aorta) to validate the method *in vitro* as well as *in silico.*

Chapter 6: Modeling and Experiments of Multidirectional Failure of the Porcine Ascending Aorta[a]

This work was a part of two papers:

Prefailure and Failure Mechanics of the Porcine Ascending Thoracic Aorta: Experiments and a Multiscale Model
Journal of Biomechanical Engineering, 2014, 136 (2)
Shah, S.B., Witzenburg, C.M., Hadi, M.F., Wagner, H.P, Goodrich, J.M., Alford, P.W. and Barocas, V.H.

and

Failure of the Porcine Ascending Aorta: Multidirectional Experiments and a Unifying Model
In Preparation for Circulation Research
Witzenburg, C.M., Dhume, R.Y., Shah, S.B., Wagner, H.P., Quindlen, J., Alford, P.W. and Barocas, V.H.

6.1 Motivation of Research

It is the goal of this thesis to provide a description of the mechanical behavior of cardiovascular soft tissues. Though the stepwise utilization of GAIM allows for the characterization of heterogeneous, anisotropic, nonlinear tissues, it relies on data obtained from planar biaxial tests, treating the tissue as two-dimensional. Up to this point, all material characteristics have been considered as homogeneous transmurally (averaged by the sample thickness). Most cardiovascular soft tissues, however, have a layered structure with varying transmural properties. For example, the aorta consists of three distinct layers: the intima, media, and adventitia, each with different mechanical properties [26,27,195,196]. Biomechanically, the development, dissection, and rupture of an ascending thoracic aortic aneurysm (ATAA) is a local phenomenon and is highly dependent on this layered structure. An aneurysm is a weakening of the vessel wall which causes it to dilate or bulge as blood is pumped through it. Dissection occurs when the aorta dilates, forming an aneurysm, and a tear in the intimal wall allows blood to flow

[a]The multiscale modeling work was completed in succession by Sachin B. Shah and Rohit Y. Dhume

into the media, which subsequently splits apart. Consequently, this chapter will detour from GAIM in order to investigate the three-dimensional loading of ascending aorta.

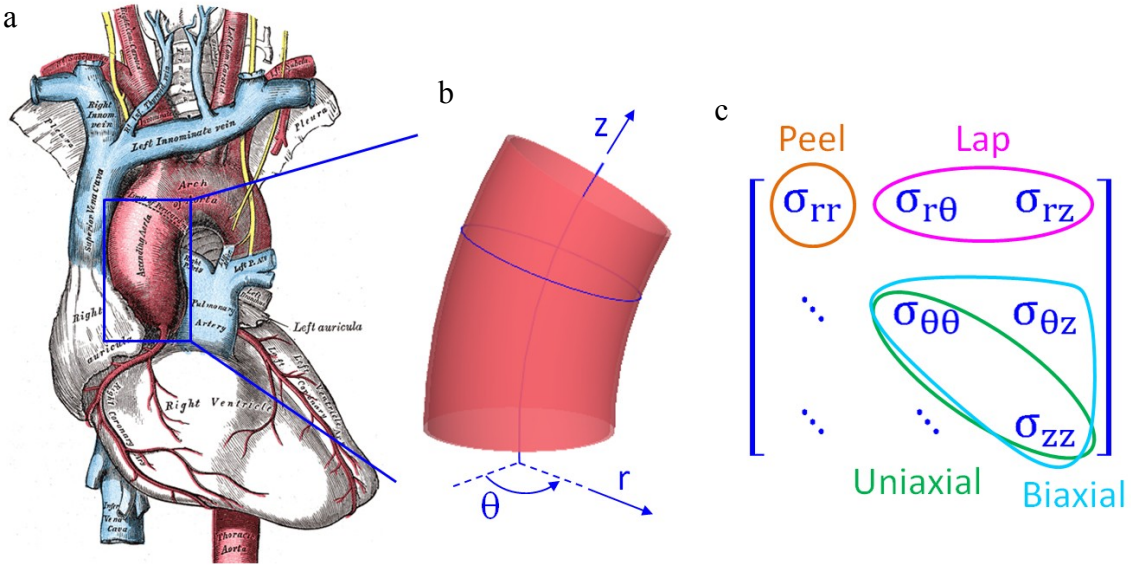

Figure 6.1: The Ascending Thoracic Aorta. (a) Illustration of the heart with the ascending aorta selected [21]. (b) Geometry of the ascending aorta. (c) The three-dimensional stress tensor for the aorta with the respective tests indicating the loading investigated

Tissue from the ascending aorta has been tested in a variety of configurations (reviewed by [197]) with uniaxial and biaxial tensile tests being the most prevalent. In-plane uniaxial and equibiaxial tension tests [198,199] provide information on tensile failure along the medial lamella ($\sigma_{\theta\theta}, \sigma_{zz}$) and biaxial tension tests can provide information on in-plane shear ($\sigma_{\theta z}$). However, while the dominant stresses in these tests may be responsible for rupture, they do not drive dissection. Stress near an advancing dissection includes a combination of radial tension (σ_{rr}) and transmural shear ($\sigma_{r\theta}, \sigma_{rz}$), so a testing strategy that probes all possible stresses is imperative. Peel tests on pieces of artery [199,200] or aneurysm [183] provide insight into the failure behavior of the tissue in radial tension (σ_{rr}), loading perpendicular to the medial lamella. To examine transmural shear ($\sigma_{rz}, \sigma_{r\theta}$), we propose utilizing a shear lap test to characterize failure under a shear force along the medial lamella. In this study, we provide a more complete picture of aneurysm failure mechanics using in-plane uniaxial and biaxial, shear lap, and peel tests to cover all three-dimensional loading modalities and leverage these into computational

models of multidirectional failure. To our knowledge, we are the first to generate data on the shear strength of aortic tissue in this manner.

6.2 Introduction

Ascending thoracic aortic aneurysms (ATAA) are dilatations of the arterial wall that result primarily from a weakening in the middle smooth muscle layer, or media, of the artery [22,24,201]. Aneurysm dissection and rupture pose serious risk of mortality and are the primary concerns for patients with an ATAA [22,24,201,202]. Cystic medial degeneration (which can be caused by disease, injury, or hereditary condition [24,201]) weakens the aortic wall, allowing for the formation of aneurysms and subsequent dissection. Aneurysm growth and dissection is further driven by increased hemodynamic loading within the media [203]. Ascending aortic dissection, the most prominent failure mode, occurs when the hemodynamic stresses within the media exceed the capacity of its collagen and elastin constituents, causing it to peel apart [183]. Ultimately, the tear can propagate axially along the length of the aorta, either proximally or distally, and in the absence of clinical intervention, may lead to further complications such as ischemia, aortic regurgitation, cardiac tamponade, aortic rupture, and death [22].

Ascending aortic aneurysms have an incidence rate of 10.4 per 100,000 person-years [204], with significant risk of dissection or rupture [204]. Clinically, ATAA management balances the risk of aneurysm rupture with the risk of surgery-related complications and death [24,201]. Risk of rupture is correlated with aneurysm diameter [24,204]; aneurysms greater than 6 cm in diameter exhibit a significantly higher risk of rupture [24]. Thus, for patients without valvular disorders, current guidelines indicate surgical intervention for ATAA diameters greater than 5.5cm and monitoring for those less than 5.5 cm [24].

In spite of clinical guidelines and what is known about the pathogenesis of aneurysms, dissection and rupture occur in a significant number of patients whose aneurysms are less than 5.5 cm in diameter [25], suggesting that a better understanding of the dissection

process is needed. Experimental studies have investigated the mechanical failure of aortic media [183,199,205], but only a few theoretical models have attempted to emulate this response [206–208]. The most notable work to date, by Gasser and Holzapfel [207], employs constitutive finite element (FE) modeling with two independent continuous and cohesive zones to model the fiber network and ground matrix, respectively. While the Gasser–Holzapfel model is capable of describing the mechanical behavior of the aorta, it fails to capture complex fiber-fiber and fiber-matrix interactions or address failure at the microscopic scale. A model employing microscale mechanics and structure to determine the macroscale response would have potential to incorporate greater anatomical detail and could be applied to a broader range of conditions. This work represents an initial attempt to apply such multiscale concepts to the mechanics of the ascending thoracic aorta (ATA).

The objectives of this study were (1) to characterize the prefailure and failure response of healthy porcine ascending aorta tissue under multiple loading configurations spanning the entire three-dimensional stress space: uniaxial, biaxial, peel, and shear lap loading and (2) to describe that response with a multiscale, FE damage model.

6.3 Methods: Experiment

Ascending aortic tissue was obtained from healthy adolescent male swine (~ 6 months; 88 ± 10kg, mean ± SD) following an unrelated *in vivo* study on right atrial radiofrequency ablation. Immediately upon harvesting, specimens were stored in 1% phosphate-buffered saline solution (PBS) at 4℃ overnight. All experiments were performed within 48h of harvest.

A ring of tissue was dissected from the ascending aorta, distal to the aortic valve and proximal to the brachiocephalic trunk (Figure 6.2a), and then cut open along its superior edge to obtain a flat, rectangular tissue sample (Figure 6.2b). The rectangular tissue

specimen was then divided into small sections, either axially or circumferentially aligned, for mechanical testing:

- ~ 20mm x 20mm square samples for biaxial tests
- ~ 20mm x 5mm rectangular samples for uniaxial tests
- ~ 10mm x 5mm rectangular samples for peel tests
- ~ 10mm x 5mm rectangular samples for lap tests

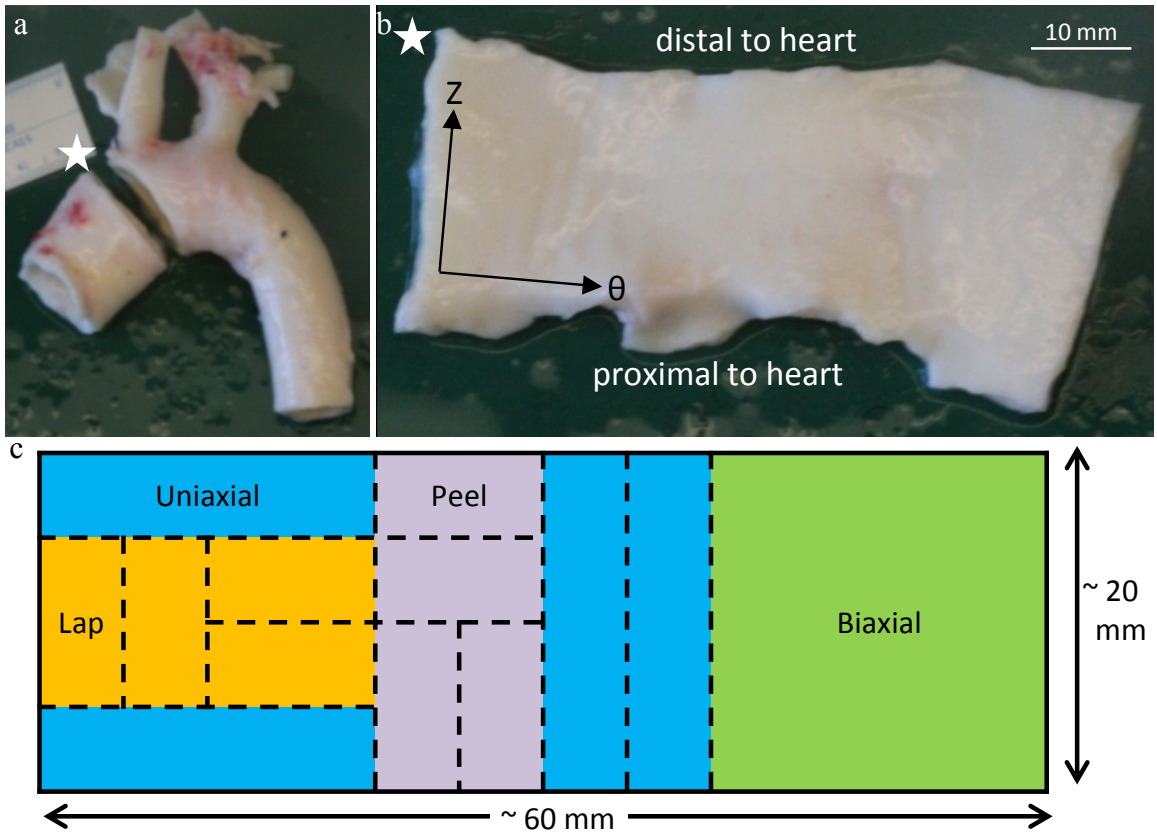

Figure 6.2: (a) Porcine aortic arch with ascending aortic ring removed. The white star represents a marker used to keep track of tissue sample orientation. (b) The ring was cut open along its superior edge and laid flat with the intimal surface up and the axial, Z, and circumferential, θ, directions along the vertical and horizontal, respectively. Axial and circumferential directions shown with black arrows. (c) Schematic showing a typical sectioning and testing plan for an ascending aortic specimen.

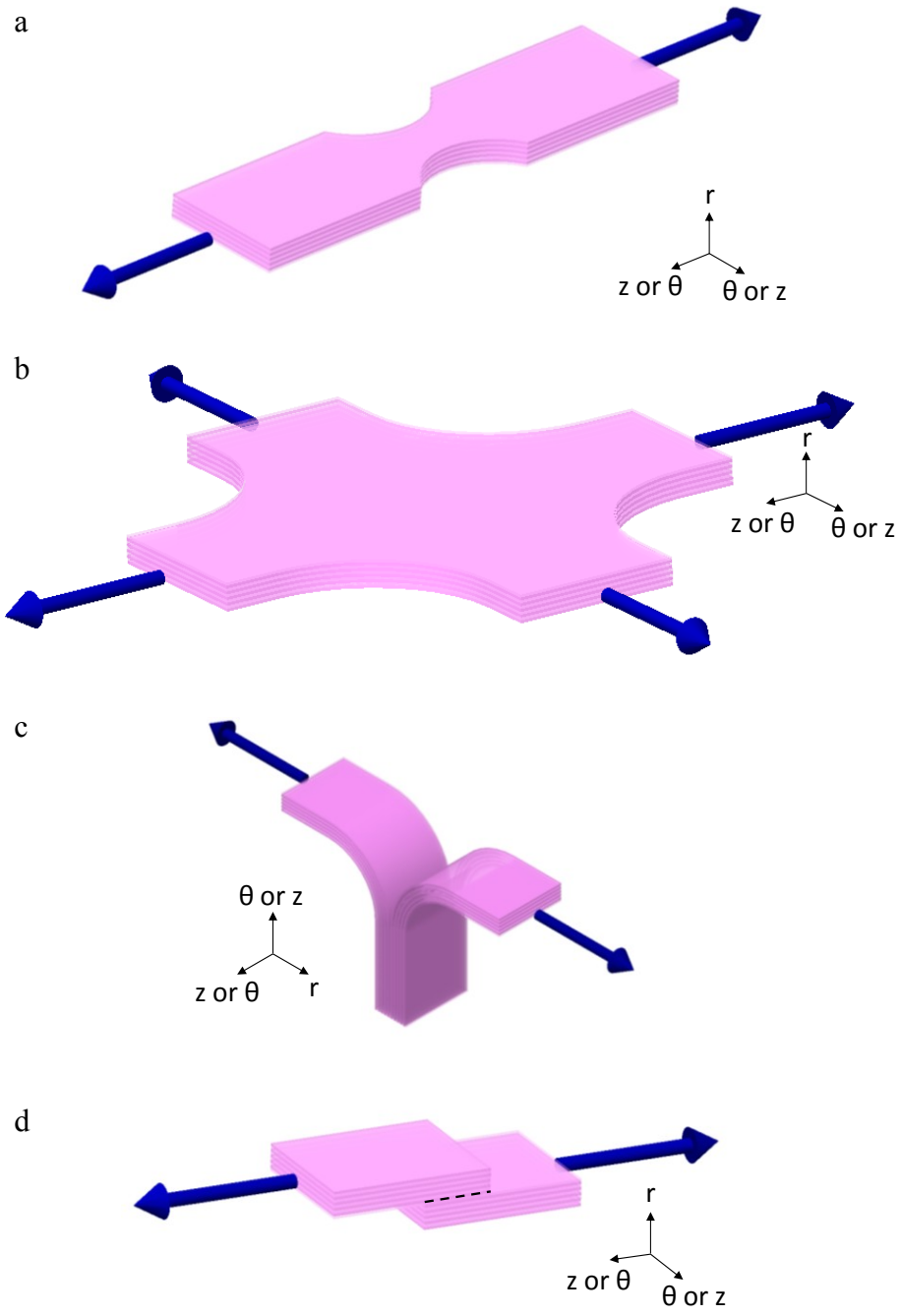

Figure 6.3: Schematics of all mechanical tests. (a) Uniaxial test: samples were cut and mounted such that the direction of pull corresponded with either the axial or circumferential orientation of the vessel. (b) Equibiaxial test: samples were cut and mounted such that the directions of pull corresponded with the axial and circumferential orientations of the vessel. (c) Peel test: samples were cut and mounted such that the vertical direction corresponded with either the axial or circumferential orientation of the vessel. b) Lap test: samples were cut and mounted such that the direction of pull corresponded with either the axial or circumferential orientation of the vessel; dotted black line indicates overlap length.

Several samples were obtained from each aorta; a typical sectioning and testing plan is shown in Figure 6.2. The tissue was characterized in tension along the medial lamella using planar biaxial tests ($\sigma_{\theta\theta}, \sigma_{zz}, \sigma_{\theta z}$) and uniaxial tests ($\sigma_{\theta\theta}, \sigma_{zz}$), in tension perpendicular to the medial lamella using peel tests (σ_{rr}), and in shear along the medial lamella using shear lap tests ($\sigma_{rz}, \sigma_{r\theta}$), schematics of all tests are shown in Figure 6.3. Samples were stored in 1% PBS at 4˚C when not undergoing mechanical testing and immersed in 1% PBS at room temperature during mechanical testing.

6.3.1 Uniaxial Extension to Failure

Rectangular tissue strips with the long axis in either the circumferential or axial orientation were cut. A 5mm circular biopsy punch was used to create a dog-bone shape (Figure 6.3a). Images of each sample were taken to determine its initial unloaded dimensions. Verhoeff's stain was used to texture the luminal surface of the media for optical displacement mapping. Mechanical testing was conducted on a computer-controlled, uniaxial testing machine (MTS, Eden Prairie, MN). Samples were placed in a custom rig and extended at a rate of 3mm/ min until failure. Force was measured using a 5N load cell. The deformation of the tissue's luminal surface was recorded (~ 157 pixels/mm) at a rate of one image per 5s. The force measured was divided by the undeformed cross-sectional area at the failure point in the neck in order to calculate the first Piola–Kirchhoff stress. Image analysis and strain tracking was performed per previous studies (e.g., Ref. [129]) to determine the local Green strain. Samples that did not fail in the neck region of the dog-bone (~ 28% of samples) were not included in the analysis. Peak tensile stress was evaluated at the point of failure.

6.3.2 Equibiaxial Extension

Biaxial samples were created by cutting a cruciform shape (Figure 6.3b) from an approximately square section of tissue such that the circumferential and axial directions

remained parallel to the arms. Verhoeff's stain was used to texture the luminal surface of the media for optical displacement mapping. The biaxial testing method was similar to that of previous studies (e.g., Ref. [129]) with a slight preload (~ 0.1 N) applied to each cruciform arm. Samples were loaded onto a biaxial tester (Instron, Norwood, MA) with four 5N load cells using a custom rig. Each sample was preconditioned with nine equibiaxial extensions to 40% grip strain. Following preconditioning, an experimental equibiaxial extension was performed at a strain rate of 3 mm/min to 40% grip strain, a subfailure load in contrast to the failure loading for uniaxial samples. During this extension, images of the tissue's speckled luminal surface and the forces at each grip were recorded. Again, local Green strain was determined using image analysis and strain tracking per our previous studies [129]. Forces in the axial and circumferential arms were divided by the respective undeformed cross-sectional areas in order to calculate the first Piola–Kirchhoff stress.

6.3.3 Peel to Failure

The peel test, (Figure 6.3c), measures the adhesive force between two layers as they are pulled apart. For each rectangular sample designated for peel testing, a ~ 4.0mm incision was made parallel to the plane of the aortic wall to initiate delamination (aortic dissection in vivo). The incision was made such that the delamination plane was approximately centered within the medial layer, thus separating the sample into two flaps of approximately equal thickness. Images of the sample were taken to determine its initial unloaded dimensions. There was a moderate variation in the exact location of the incision with respect to the center of the media due to sample size and cutting technique. If the delamination plane was outside the middle third of the sample thickness, the sample was discarded. Lines were drawn on the side of the sample with Verhoeff's stain in order to track the progress of failure.

The two flaps of the delaminated section of the tissue sample were then mounted in a custom gripping system with sandpaper on either side to prevent slipping and secured to a

uniaxial tester. Samples were cut and mounted on uniaxial testing machine (MTS, Eden Prairie, MN), such that the vertical direction, as shown in Figure 6.3c, was either axial or circumferential with respect to the vessel. The two flaps were peeled apart causing the tissue sample to delaminate, at a constant displacement rate of 3 mm/min, and force was measured with a 5N load cell. Preliminary tests showed no significant dependence on grip speed in the range of 1 to 10 mm/min, so a single velocity was used for all subsequent experiments. Images of the side of the sample were recorded every five seconds throughout testing to capture the progression of failure.

6.3.4 Shear Lap Failure

The shear lap test, (Figure 6.3d), produces large shear stresses in the overlap region. Rectangular samples designated for shear lap testing were specially shaped to test their shear strength. A ~ 3.5 mm incision was made on each end of the sample approximately centered within the medial layer and separating each end of the sample into two flaps of approximately equal thickness. The flap containing the intimal surface was removed from one end, and the flap containing the adventitial surface was removed from the other, resulting in the shear lap sample shape with an overlap length (black dotted line in Figure 6.3d) of ~ 3.0 mm. Images of the sample were taken to determine its initial unloaded dimensions. Again, there was a moderate variation in incision location with respect to the center of the media due to sample size and cutting technique, therefore if either incision surface was measured to be outside the middle third of the sample thickness the sample was discarded. Verhoeff's stain was used to texture the side of the sample for optical strain tracking.

The specially cut sample was then mounted in a custom gripping system with sandpaper on either side to prevent slipping and secured to a uniaxial tester (MTS, Eden Prairie, MN). The height of the grips was adjusted such that the overlap surface was along the horizontal, and an image of the sample was taken to determine its initial unloaded dimensions. Each sample was extended to failure at a constant displacement rate of 3

mm/min, and force was measured with a 5N load cell. During testing, digital video of the side the sample was obtained at 24 fps, 1080p HD resolution, and spatial resolution of ~ 103 pixels/mm. Image analysis and strain tracking were performed per our previous studies [116,129].

6.4 Methods: Model

The multiscale model (Figure 6.4, Refs. [209–211]) was made up of elements at three scales: the FE domain at the millimeter (mm) scale, representative volume elements (RVE) at the micrometer (μm) scale, and the fibers with radii at the nanometer (nm) scale. Each FE element contained eight Gauss points, and each Gauss point was associated with an RVE. Each RVE was comprised of a discrete fiber network in parallel with a nearly incompressible neo-Hookean component to represent the nonfibrous material (matrix) [210]. The matrix and fiber network were functionally independent, with the sole exception that fiber network failure dictated simultaneous matrix failure. Stresses developed by the network and the matrix were additive (Table 6.1). Matrix material was considered homogenous throughout the model; however, each element was assigned a unique set of fiber networks, and new networks were generated for each model simulation replicate.

The macroscale and microscale stress and strain were coupled as described previously [212], and the corresponding governing equations are outlined in Table 6.1. In brief, displacements applied to the macroscale model were passed down to individual RVEs. Pre-oriented Delaunay networks within the RVE stretched and rearranged in response to the displacements, generating net forces on the boundary network nodes. From these net forces, a volume-averaged stress was determined for each Gauss point within the element. The macroscopic displacement field was updated until the overall Cauchy stress balance was satisfied. Rigid boundary conditions were placed at the edges of the grip while the rest of the surface was free to move. Model simulations were run at the

Minnesota Supercomputing Institute on 32-core parallel processors, with clock times averaging 4–6 h per simulation.

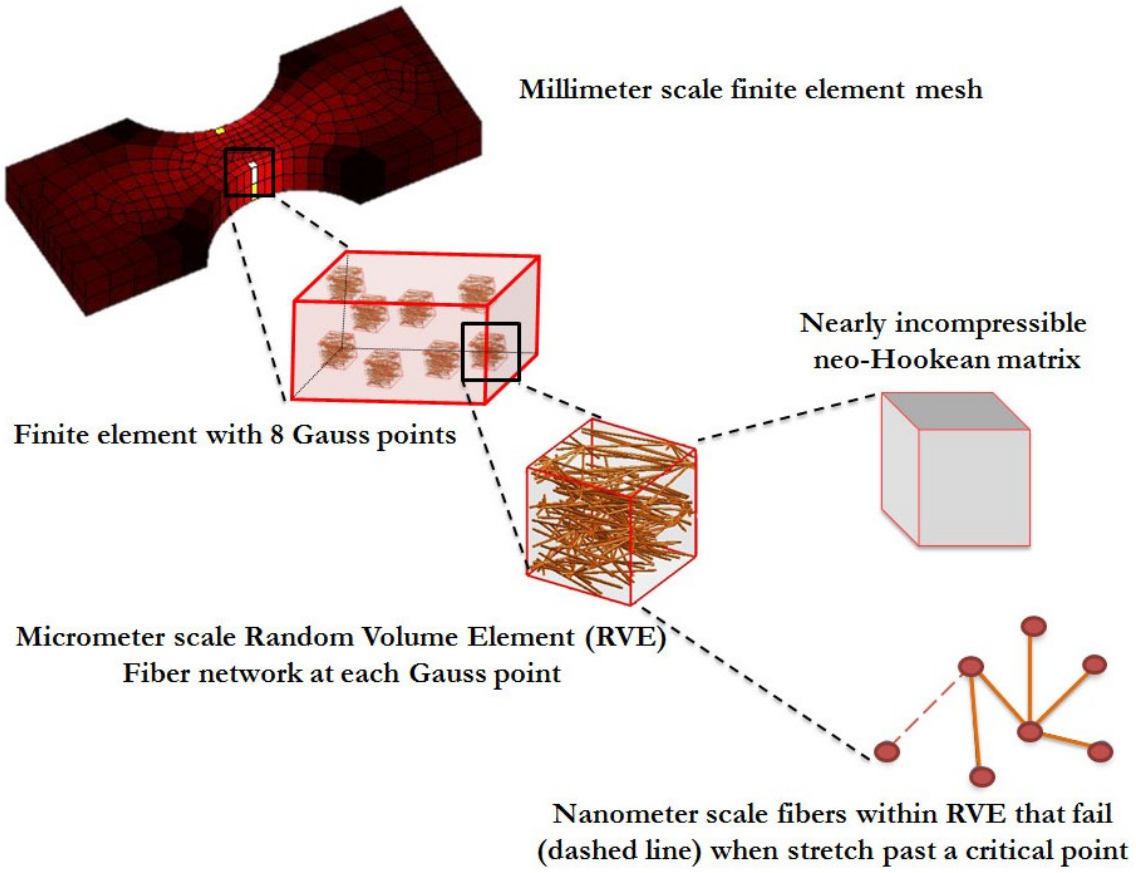

Figure 6.4: Synopsis of multiscale model. Sample geometries (uniaxial, biaxial, peel, or shear lap) were developed into millimeter sized finite element meshes. Each element consisted of eight Gauss points that dictated its stress-strain response. Each Gauss point consisted of representative volume elements (RVE) composed of a nanoscale fiber network in parallel with a nearly incompressible neo-Hookean matrix. Deformation of the macroscale structure caused the fiber network to stretch and reorient to reach force equilibrium. Fibers that stretched beyond a critical value were considered failed and their modulus of elasticity was reset to a near-zero value.

Table 6.1: Governing equations applied within the model, as well as the scale at which each equation and its parameters are applied

Equation	Description	Scale	Parameters
$\sigma_{ij,j} = \frac{1}{V}\oint_{\partial V}(\sigma_{ij}^{L} - \sigma_{ij})u_{k,j}n_k dS$	Macroscale Volume-Averaged Stress Balance [212]	Tissue	σ: macroscale averaged Cauchy stress
			V: RVE volume
			σ^{L}: microscale stress
			u: RVA boundary displacement
			n: normal vector to RVE boundary
$\sigma_{ij} = \frac{1}{V}\int \sigma_{ij}^{L}\, dV = \frac{1}{V}\sum_{bc}\int x_i\, f_j$	Volume-Averaged Stress of RVE [212]	Network	bc: boundary for all RVE cross links
			x: boundary coordinate
			f: force acting on boundary
$F_f = \frac{E_f A_f}{\beta}\left(e^{\beta\varepsilon_G} - 1\right)$ and $E_f \approx 0$ when $\lambda_f > \lambda_{\text{crit}}$	Fiber Constitutive Equation [49,211,213,214]	Fiber	F_f: fiber force
			E_f: Young's modulus of fiber at infinitesimal strain
			A_f: fiber cross-sectional area
			ε_G: fiber Green Strain
			β: fitting parameter for fiber nonlinearity
			λ_f: fiber stretch
			λ_{crit}: fiber stretch at failure
$\sigma_{ij}^{m} = \frac{G}{J}(B_{ij} - \delta_{ij}) + \frac{2Gv}{J(1-2v)}\delta_{ij}\ln(J)$	Matrix Governing Equation [210]	Matrix	σ^{M}: matrix Cauchy stress
			G: shear modulus
			J: deformation tensor determinant
			B: left Cauchy-Green deformation tensor
			v: Poisson's ratio

6.4.1 Model Specification and Parameter Estimation

Table 6.2 summarizes the key parameters of the model. The orientation of the fiber network, which plays a critical role in the mechanical response, was described by the orientation tensor Ω. The components of Ω correspond to the degree of alignment in the coordinate directions, with the trace of Ω equal to 1 by construction (further details in Ref. [210]). Previous studies have shown that collagen fibers within the arterial media have strong preferential orientation in the circumferential direction ($\Omega_{\theta\theta}$) while some percentage of fibers are mainly oriented in the axial direction (Ω_{zz}) and even smaller

percentage in the radial direction (Ω_{rr}) [32,196,215–217]. Based on those studies, the average orientation for collagen fiber networks in the media $[\Omega_{\theta\theta}\ \Omega_{zz}]$ was extrapolated to be $[0.62\ 0.37]$ [215]. The initial network orientation tensor components $[\Omega_{\theta\theta}\ \Omega_{zz}\ \Omega_{rr}]$ were, therefore, specified to be $[0.6, 0.3, 0.1] \pm [0.039, 0.040, 0.006] -$ an orientation state close to that measured in Ref. [215], but with a small amount of alignment in the r direction to maintain the integrity of the network. A single network was used to represent the combined contribution of the collagen and elastin components, with a volume fraction of 5% [210]. Fiber radius was set to 100 nm to replicate fiber geometry reported for elastic lamellae in arterial walls [218,219]. The matrix was modeled as nearly incompressible with a Poisson's ratio, υ, of 0.49.

Four model parameters — fiber small-strain Young's modulus E_f, critical fiber failure stretch λ_{crit}, matrix shear modulus G, and a fiber nonlinear mechanics parameter, β — were regressed to the experimental data. The model was fit to the maximum experimental stress, rupture and 40% strain, for uniaxial and equibiaxial experiments, respectively, while not including post rupture or unloading conditions. The model was not fit to the peel or shear lap data since convergence for these two geometries could not be achieved. A value of 31.4 kPa was used as an initial guess and an upper bound for the matrix shear modulus based on the work of Holzapfel [26]. Fitted parameters were chosen to minimize the total sum of squared error between the model and experimental force curves for both the uniaxial and biaxial configurations. Both simulations were repeated ten times. Each replicate used unique randomly selected networks that were generated using the same network criteria, Table 6.1.

Table 6.2: Values for parameters used within the model, as well as justification for parameter values. The last four parameters in the table (shown in bold) were regressed to the combined uniaxial/biaxial data set.

Symbol	Description	Value	Justification
Ω	Network Orientation	$\Omega_{\theta\theta} = 0.6,\ \Omega_{zz} = 0.3,\ \Omega_{rr} = 0.1$	Extrapolated from structural histology [215]
A_f	Cross-sectional area	31,416 nm^2	Elastin fiber radius 100nm [218,219]
Φ	Fiber volume fraction	0.05	Based on Ref. [211]
N	Poisson's ratio	0.49	Nearly incompressible [210]
w_u	Uniaxial undeformed dimensions	Width = 5.00 mm	Measured in Experiment
l_u		Length = 13.0 mm	
t_u		Thickness = 1.5 mm	
w_b	Biaxial undeformed dimensions	Width = 6.00 mm	Measured in Experiment
l_b		Grip-to-Grip Length = 15.0 mm	
t_b		Thickness = 1.5 mm	
$\boldsymbol{E_f}$	**Fiber modulus of elasticity**	**2.51 MPa**	**Fit to data**
$\boldsymbol{\lambda_{crit}}$	**Lambda critical fiber failure**	**2.17**	**Fit to data**
$\boldsymbol{G}$	**Matrix shear modulus**	**1.7 kPa**	**Fit to data**
$\boldsymbol{\beta}$	**Nonlinearity fitting parameter**	**2.35**	**Fit to data**

6.5 Results

6.5.1 Statistical Analysis

Unless otherwise specified, all p-values were calculated for this chapter using unpaired two-tailed t-tests with Bonferroni correction and assuming equal variances (GraphPad Prism v. 5.03). A p-value less than 0.05 was deemed significant. All values are reported as mean ±95% confidence intervals unless noted.

6.5.2 Uniaxial Extension to Failure

Uniaxial samples from both the circumferential (n = 11) and axial (n = 11) orientations were loaded to failure. Tensile stress, the grip force normalized by the undeformed cross-sectional area of the neck of the dogbone, was plotted as a function of grip stretch for a

representative circumferentially aligned uniaxial sample, Figure 6.5a. The stress-strain response was nonlinear, characteristic of many tissues [220]. As expected, anisotropic behavior was observed in the tensile stress of the tissue. Peak stress was significantly ($p < 0.001$) higher in the circumferential versus axial orientation (Figure 6.5b; 2510 ± 979 kPa versus 750 ± 228 kPa). Model simulation results showed similar anisotropy ($p < 0.001$) (Figure 6.5b; 2362 ± 10.3 kPa versus 958 ± 3.6 kPa) when using the parameters (Table 6.1) that were regressed to the combined uniaxial and biaxial data sets.

The media on the inner curvature of the arch is typically thicker than the outer [221], likely because the vessel remodels to balance the higher circumferential wall stresses caused by the curvature [222]. To verify that this remodeling does not affect the failure mechanics of the tissue, we compared the peak stress and strain of samples taken from the inner and outer curvature. Regional analysis found no significant difference in peak stress between uniaxial samples taken from the interior versus exterior of the aortic arch for either the circumferential or axial orientations (p-values ranged from 0.10 to 0.28). No significant difference in peak stretch was observed between interior and exterior axial uniaxial samples; however, a significant difference ($p = 0.04$) was observed for circumferential uniaxial samples. Samples near the exterior of the arch exhibited 9.6% larger stretch at peak stress than those from the interior.

No significant difference was noted in experimental stretch at peak stress between the circumferential and axial directions (Figure 6.5c; 1.99 ± 0.07 versus 1.92 ± 0.16, $p = 0.36$). The averaged experimental stress-stretch curves for both the circumferential and axial orientations are shown in Figure 6.6 along with the best-fit model curves. The specified and regressed model parameters of Table 6.1 allowed the model to match the experimental prefailure and failure results to within the 95% confidence intervals for both orientations.

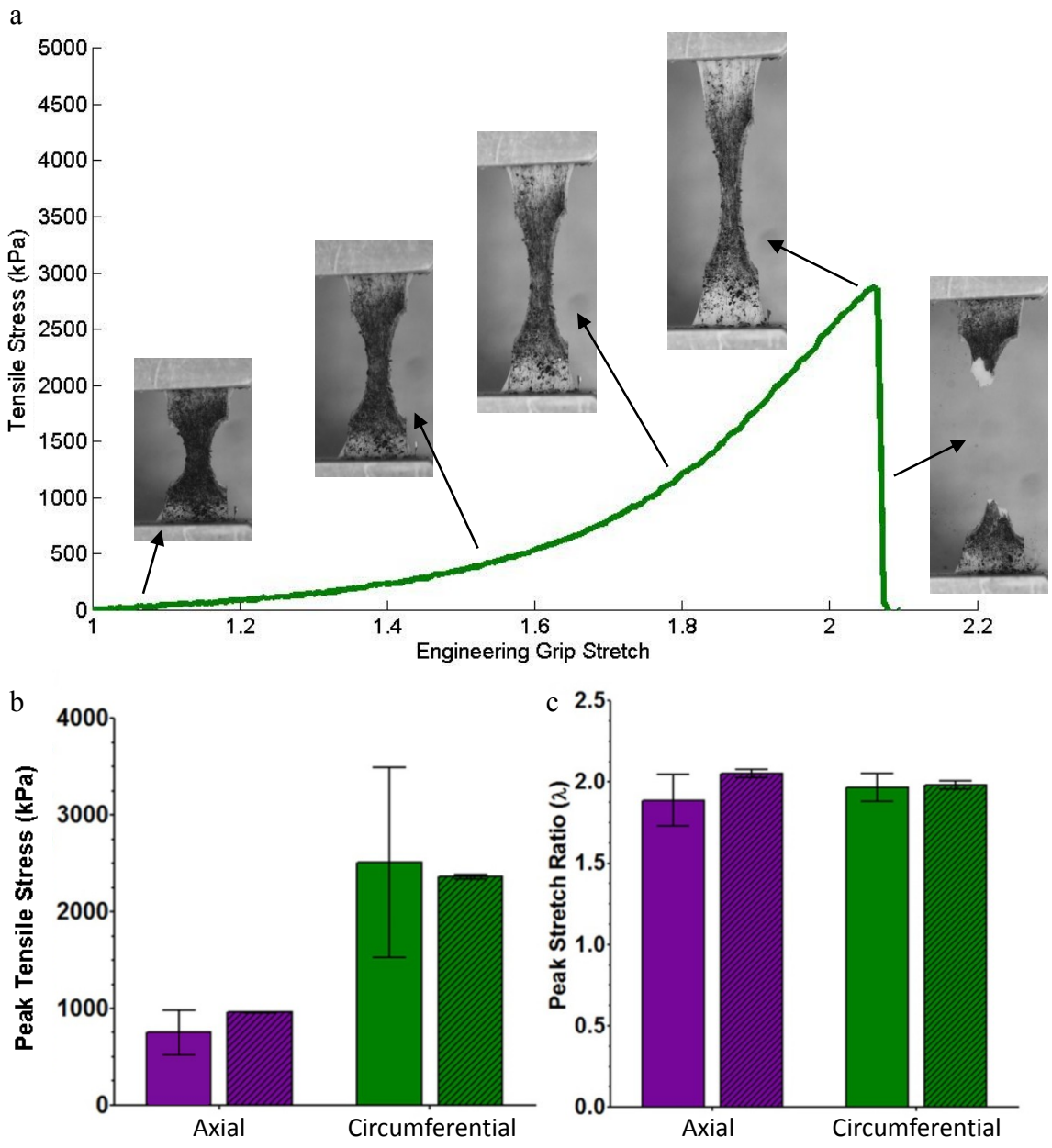

Figure 6.5: (a) Typical measured tensile stress vs. grip stretch response in a circumferentially oriented uniaxial sample. (b) Peak tensile stress of ascending aortic samples for both uniaxial experiment (solid, n = 11) and model (diagonal lines, n = 11). (c) Stretch of ascending aortic samples at peak stress for both uniaxial experiment (solid, n = 11) and model (diagonal lines, n = 11).

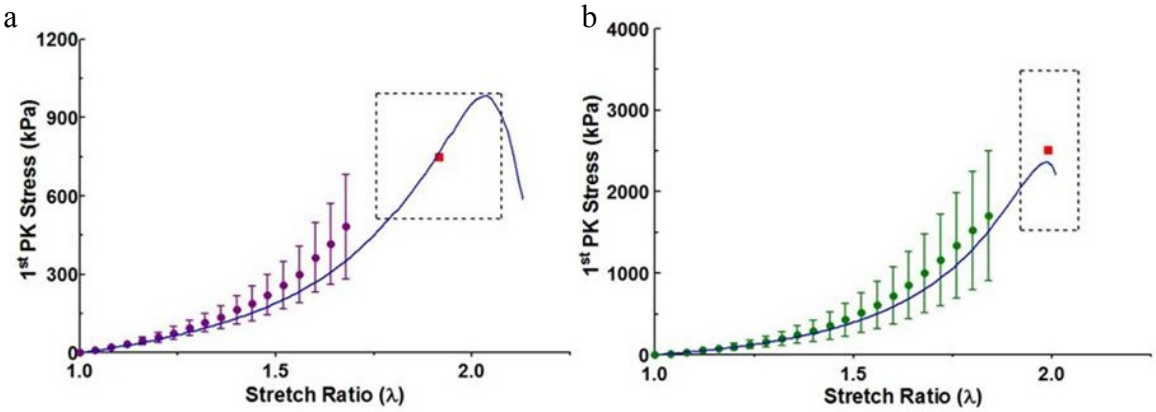

Figure 6.6: (a) First Piola–Kirchhoff stress as a function of stretch ratio for the experiment (dots with 95% confidence interval) and model (solid blue line). Colored dots represent the mean experimental stress, and error bars depict the 95% confidence interval. The red square indicates the mean peak tensile stress and stretch, and the surrounding dotted black box indicates the 95% confidence interval for the peak experimental stress and corresponding stretch for (a) axial and (b) circumferential orientations.

The neck region of the simulated uniaxial samples (both circumferential and axial) experienced the largest strains and stresses (not shown), as expected, and also the largest degree of fiber reorientation (Figure 6.7a and b). Fibers within the neck region were analyzed for their mean fiber orientation tensor Ω. As the simulated uniaxial sample was stretched, its fiber alignment changed from an initial orientation tensor $[\Omega_{\theta\theta}\ \Omega_{zz}\ \Omega_{rr}]$ ~ [0.6 0.3 0.1] and steadily increased along the direction of stretch.

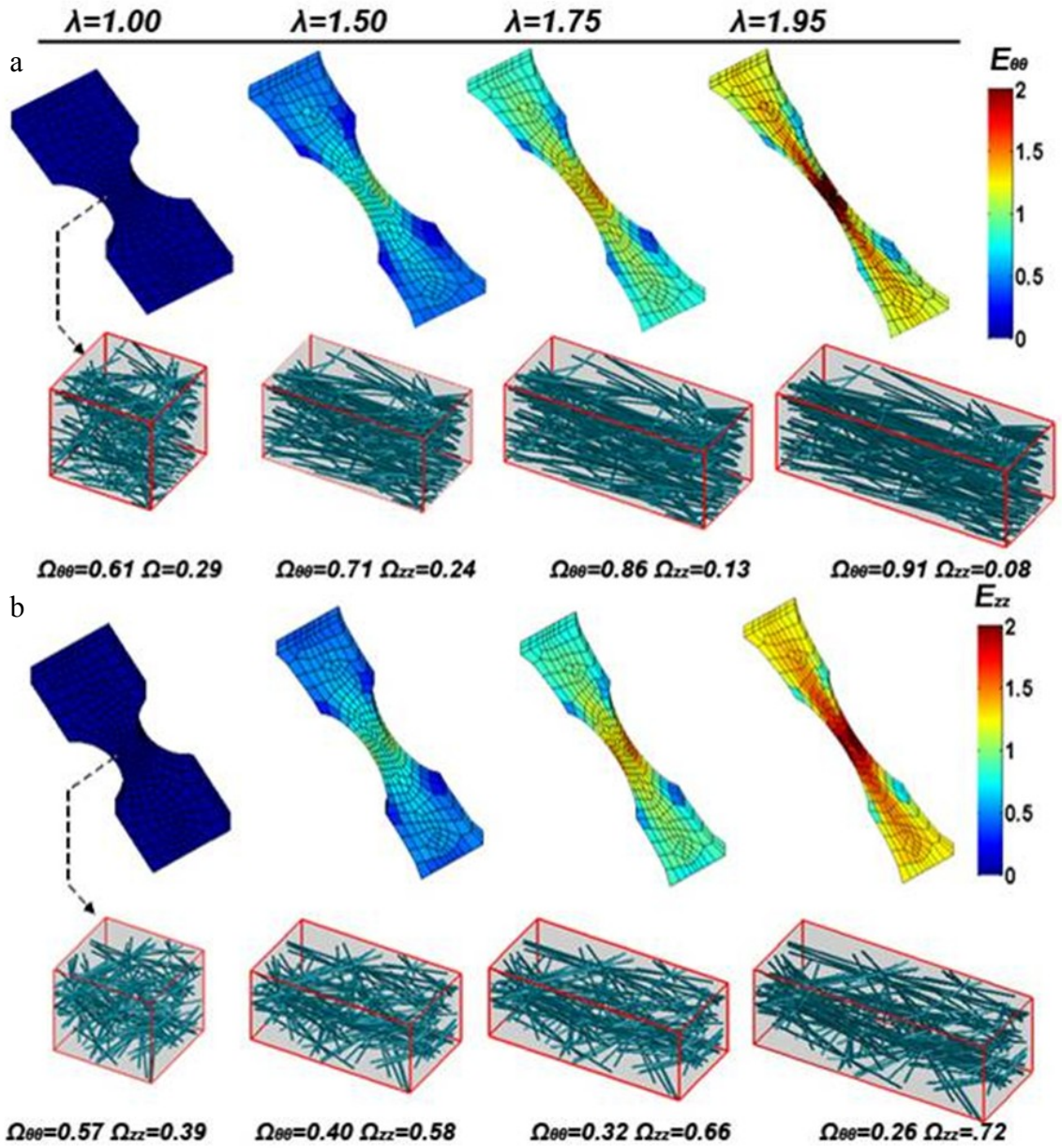

Figure 6.7: (a) Model circumferential Green strain $E_{\theta\theta}$ along the axis of pull plotted over the deformed model mesh at given sample stretches ($\boldsymbol{\lambda}$). A representative neck region RVE network is shown and its corresponding fiber orientation tensor. (b) Model axial Green strain E_{zz} along the axis of pull plotted over the deformed model mesh at a given sample stretch ($\boldsymbol{\lambda}$). A representative neck region RVE network is shown and its corresponding fiber orientation tensor.

6.5.3 Equibiaxial Extension

The first Piola-Kirchoff stress was plotted as a function of grip stretch for a representative biaxial sample, Figure 6.8a. All biaxial samples (n = 9), as with uniaxial samples, exhibited a nonlinear stress-strain response, and as all samples exhibited similar behavior, it is reasonable to consider the mean response (Figure 6.8b dotted lines). The tissue showed similar anisotropy under equibiaxial loading as under uniaxial loading. At peak extension, the stress ratio (circumferential to axial) was 1.44. The 95% confidence intervals for the two orientations overlapped each other (Figure 6.8b shaded area).

The biaxial model (Figure 6.8c solid line) was in good agreement with the experiments. Stresses in the circumferential direction were slightly overpredicted but remained well within the 95% confidence interval (Figure 6.8c). Similar to the uniaxial simulations, regions with higher strains had greater changes in fiber rotation and fiber stretch (Figure 6.9). However, regions with the largest strain, the arms, are not the region of interest (Figure 6.9a and b). Figure 6.9c depicts an element from the central region of the biaxial sample, showing the change in its fiber orientation. As expected for equibiaxial extension, in-plane fiber orientation of the elements in this region showed little change.

6.5.4 Fitted Model Parameters

The model parameters (fiber small-strain Young's modulus E_f = 2.51 MPa, critical fiber failure stretch λ_{crit} = 2.17, matrix shear modulus G = 1.7 kPa, and the nonlinear fitting parameter β = 2.35) were regressed to the experimental data from both the uniaxial and biaxial experiments.

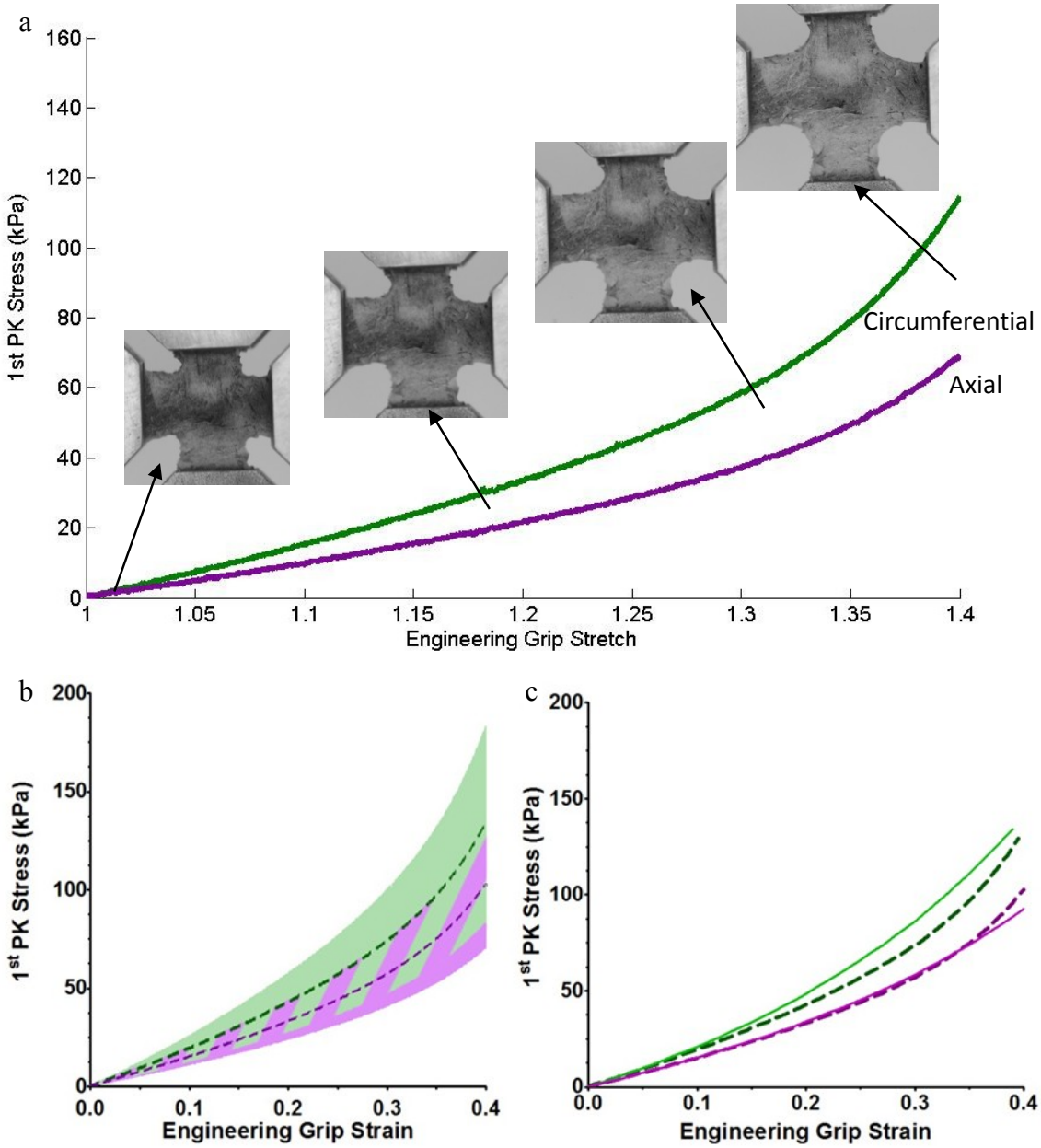

Figure 6.8: (a) First Piola-Kirchoff stress as a function of engineering grip stretch for a representative biaxial sample. (b) Mean first Piola–Kirchhoff stress as a function of grip strain for the biaxial experiments (dashed purple line for axial and dashed green line for circumferential, n = 9) with 95% confidence interval (purple and green shaded areas, respectively). The striped shaded area represents overlap of the 95% confidence interval of the two orientations ($p < 0.05$). (c) Mean biaxial model first Piola–Kirchhoff stress as a function of grip strain (solid purple line for axial and solid green line for circumferential, n = 10) compared to mean experimental results (dashed purple and green lines, respectively, n = 9).

6.5.5 Peel to Failure

Peel samples from both the circumferential ($n = 13$) and axial ($n = 23$) orientations were loaded to failure. Peel tension, grip force normalized by the specimen width, was used to measure delamination stress. When plotted as a function of grip displacement, following an initial peak, peel tension plateaus until total sample failure. Figure 6.10a shows force-per-width as function of displacement for a peel sample oriented in the circumferential direction with the plateau region marked with red triangles. Initial and end points of the plateau region were calculated by splining the data into 20 sections and determining where the slope was approximately equal to 0. The value of peel tension in the plateau region was averaged in order to determine the peel stress of each sample. The standard deviation of peel tension within the plateau region was evaluated to assess the degree of fluctuation during the peeling process. The average tension of the plateau region for this sample was 63.8 mN/mm with a standard deviation of 4.02 mN/mm.

A summary of the average peel tension and standard deviation of peel tension for all samples is shown in Figure 6.10b and c. The mean average peel tension was significantly higher ($p < 0.01$) for samples aligned axially vs. circumferentially, (97.0 ± 12.7 vs. 68.8 ± 14.2 mN/mm, respectively) with an anisotropy ratio of 1.4. The mean standard deviation of peel tension showed similar anisotropy ($p < 0.001$) for samples aligned axially vs. circumferentially, (12.66 ± 2.22 vs. 5.78 ± 1.04 mN/mm, respectively). The anisotropic response was present even when the mean standard deviation was normalized by mean average peel tension ($p < 0.05$, 0.145 ± 0.037 vs. 0.088 ± 0.017, respectively).

Regional analysis was performed to determine whether sample location had an effect on mean average or mean standard deviation of peel tension. First, samples, taken from both the axial and circumferential directions, were grouped according to their distance from the inner and outer curvature of the aortic arch. No significant difference (all p-values > 0.10) was observed. Then, axially oriented samples were grouped by where peel failure was initiated (proximal or distal to the heart). No significant difference was seen in mean

average peel tension or mean standard deviation of peel tension between the two groups (all p-values > 0.60).

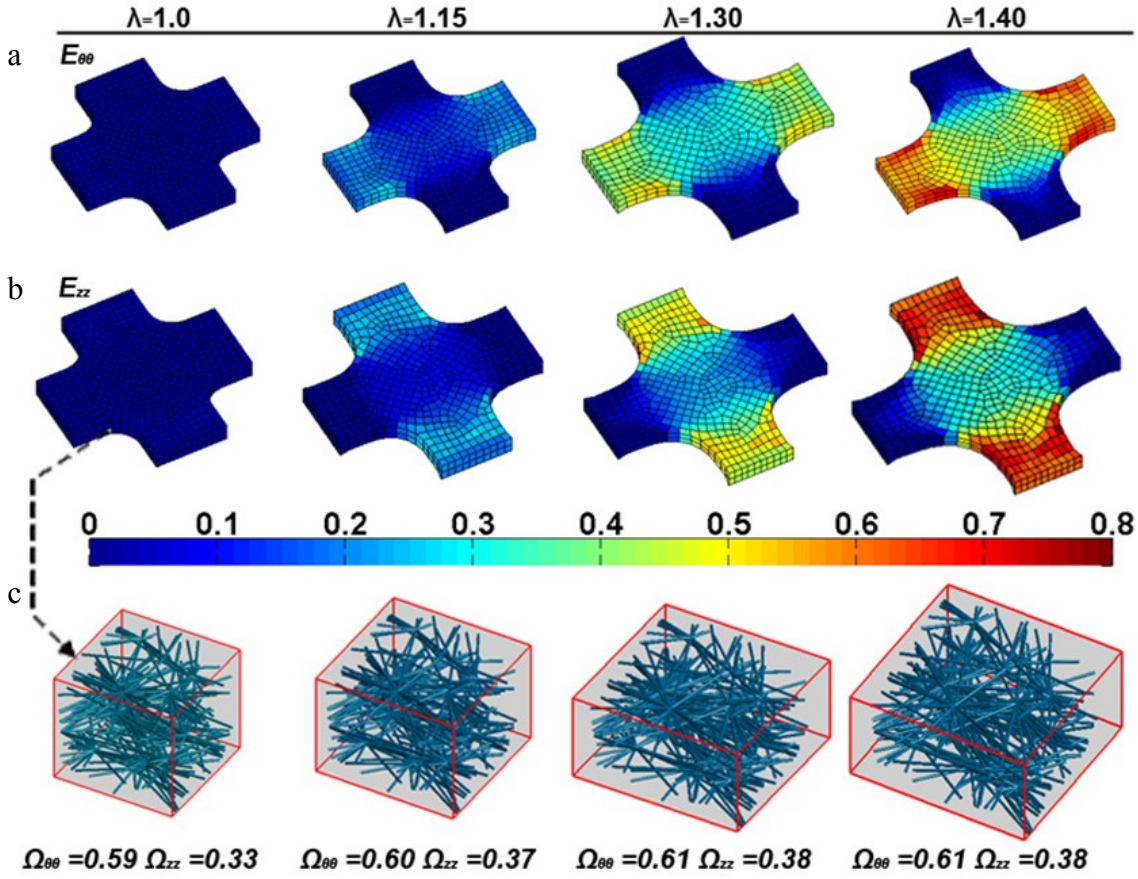

Figure 6.9: (a) Model equibiaxial Green strain $E_{\theta\theta}$ plotted over the deformed model mesh at various sample stretches ($\boldsymbol{\lambda}$). (b) Model equibiaxial Green strain E_{zz} plotted over the deformed model mesh at various sample stretches ($\boldsymbol{\lambda}$). (c) A sample center region RVE network is shown and its corresponding fiber orientation tensors for the stretches depicted in (a) and (b).

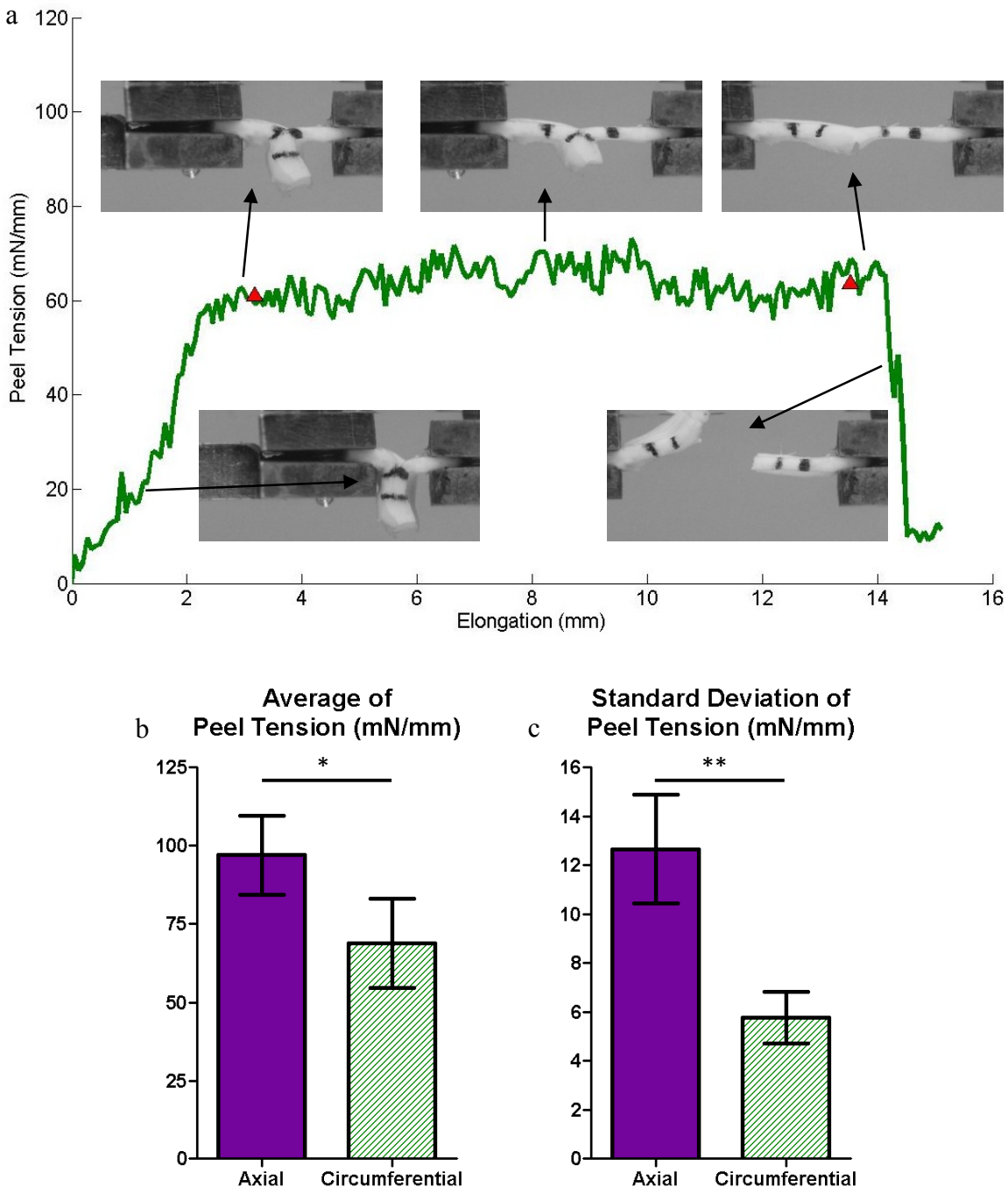

Figure 6.10: (a) Peel tension as a function of elongation for a circumferentially oriented peel sample with marks (red triangles) indicating the plateau region. Experimental mean average of peel tension (b) and standard deviation of peel tension (c) for samples oriented both axially (n = 23) and circumferentially (n =13). Error bars depict the 95% confidence interval and * indicates $p < 0.01$ and ** indicates $p < 0.001$.

6.5.6 Shear Lap Failure

Shear lap samples from both circumferential (n = 28) and axial (n = 26) orientations were loaded to failure. Force curves for shear lap samples (Figure 6.11a) exhibited catastrophic failure similar to uniaxial tests, in sharp contrast to the steady loads of a peel test. The maximum force per overlap area, the peak shear stress, was used to characterize sample failure. In Figure 6.11b and c, the red square indicates the mean peak shear stress and failure stretch, and the surrounding dotted black box indicates the 95% confidence interval, respectively, for circumferentially and axially oriented samples. Circumferentially oriented samples exhibited significantly higher ($p = 0.013$) peak shear stresses than axially aligned samples (185.4 ± 28.4 kPa vs. 143.7 ± 16.0 kPa, respectively). In both the axial and circumferential directions, shear lap failure stress is less than 20% of the failure stress necessary for uniaxial failure. The grip strain at failure, defined as the change in grip-to-grip distance divided by the original grip-to-grip distance, was used to quantify further the compliance of the tissue. Greater grip strain was necessary to fail samples aligned in the axial direction compared with those in the circumferential direction (1.63 ± 0.16 vs. 1.43 ± 0.17, respectively). Greater distensibility in the axial direction was a consistent trend throughout the samples, though the difference was significant ($p = 0.07$) only at the 90% confidence level.

While in a loaded stress state an axially aligned lap sample was fixed by immersion in 10% buffered neutral formalin solution overnight, embedded in paraffin, and prepared for histological investigation per standard techniques. Sections were stained with hematoxylin and eosin (HE) stain, Masson's trichrome stain, or Verhoeff's Von Gieson (VVG) consecutively. Figure 6.12 shows a deformed porcine thoracic aortic specimen with HE stain and a schematic detailing the global location of the image. The portion of the specimen in tension (bottom) shows marked radial compaction in comparison to the unloaded specimens. At the overlap surface, it appears that the shear stress is causing the elastic lamina to fold over on itself, causing detachment from the loaded neighboring lamina. Thus, failure along the lamella is translated to failure across lamella.

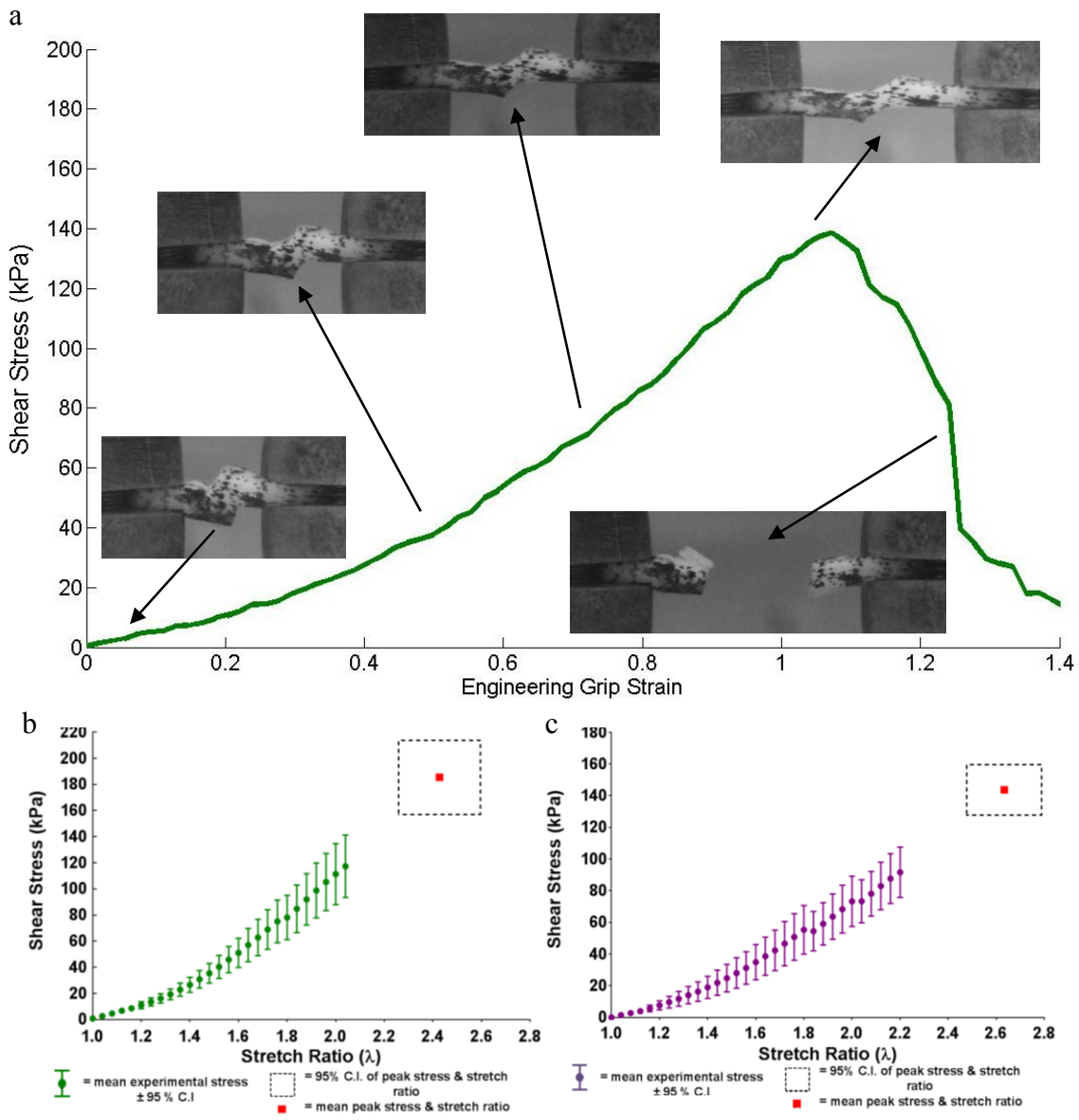

Figure 6.11: (a) Shear stress as a function of engineering grip strain for a circumferentially oriented lap sample. Mean shear stress as a function of stretch ratio for the circumferentially (b) and axially (c) aligned shear lap samples (dots with 95% confidence interval). Colored dots represent the mean experimental stress and error bars depict the 95% confidence interval. The red square indicates the mean peak shear stress and stretch, and the surrounding dotted black box indicates the 95% confidence interval for the peak experimental stress and corresponding stretch.

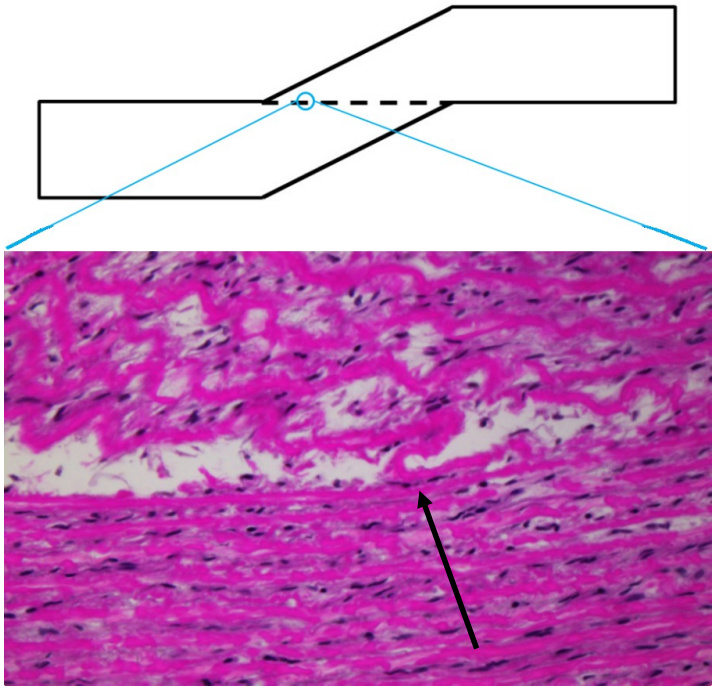

Figure 6.12: HE stain of lap sample fixed immediately prior to failure showing folding of medial lamina (black arrow) in the overlap region.

Unlike the peel test, which has been used previously to investigate aortic tissue [183,199], to the authors' knowledge the shear lap test has never been used to investigate aorta or other cardiovascular soft tissues (Though Gregory et al. used a similar test to investigate the shear properties of the annulus fibrosus [223]). Therefore, strain tracking was performed, per our previous studies [116,129], in order to verify that the shear lap test, as applied to the ascending thoracic aorta, produced large shear strains in the overlap region. As expected, the displacements were primarily in the pull direction, and shear strain was largest in the overlap region (Figure 6.13a and b). In order to investigate the strain behavior of the tissue more fully, a line was drawn at the edge of the overlap surface, Figure 6.13c, and strains tangential and normal to the overlap edge were calculated (some samples were not analyzed due to poor speckling, n = 15 and n = 19 for axial and circumferential samples, respectively). The maximum strain in each direction was determined (Figure 6.13d). For both the axially and circumferentially aligned samples, the shear strain, E_{nt}, was large in the overlap region, as desired. For the axially oriented samples, the shear strain was higher than both the normal ($p < 0.1$) and

tangential strains ($p < 0.01$). For the circumferentially oriented samples it was significantly higher than the tangential strain ($p < 0.05$), and comparable to the normal strain ($p = 0.26$).

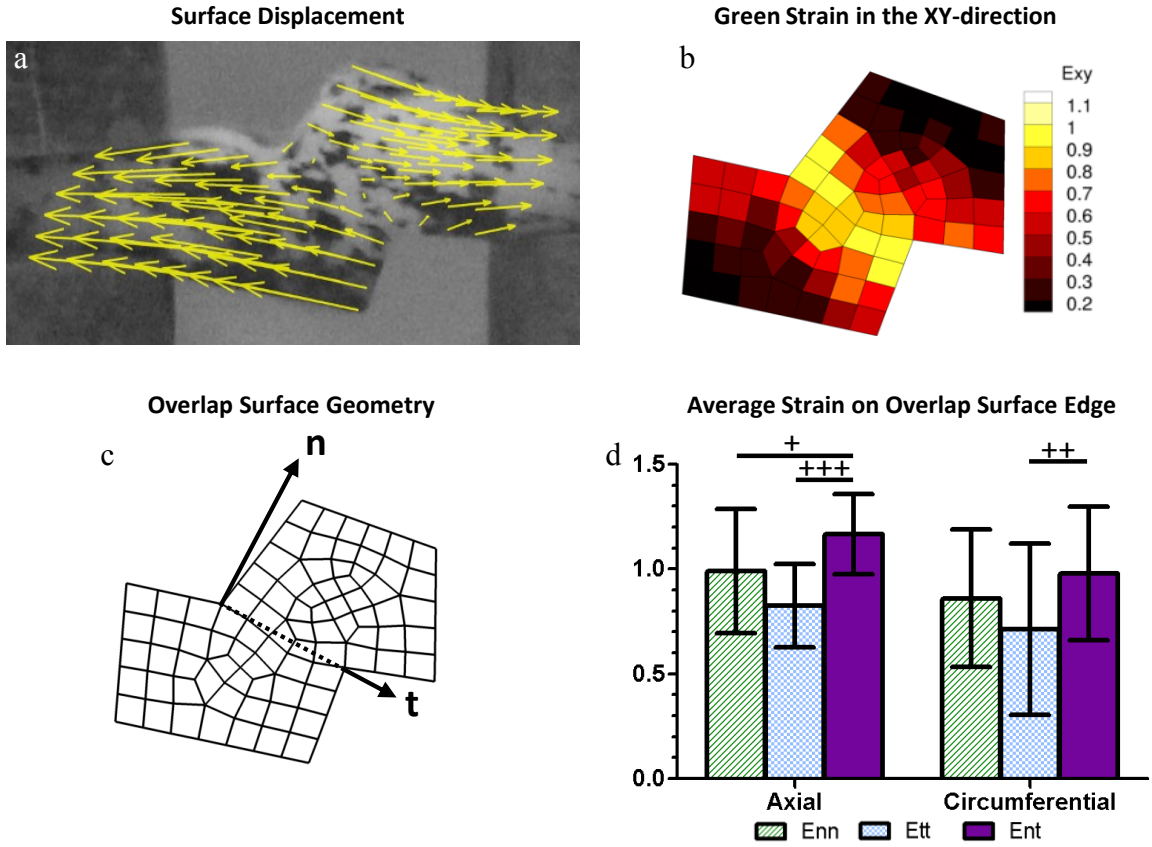

Figure 6.13: (a) Displacement of the representative sample pictured in Figure 6.11a, adjusted to zero displacement at the center. (b) Strain of the representative sample in the xy-direction. (c) Dotted line showing overlap surface edge and vectors with normal and tangential directions. (d) Average strain on the overlap surface edge for both axially (n = 15) and circumferentially (n = 19) oriented samples. Error bars indicate 95% confidence intervals. One, two, and three plus signs indicate $p < 0.10$, $p < 0.05$, and $p < 0.01$, respectively.

6.6 Discussion

This study investigated tensile properties of the porcine ascending thoracic aorta using a range of mechanical tests that interrogated the tissue in all directions. Shear lap tests reveal that failure occurs at much lower stresses (~ 5 to 10X), than during uniaxial

extension [198,224], which is consistent with the laminate nature of the media. The typical anisotropic behavior observed in uniaxial and biaxial tests, i.e. higher strength in the circumferential vs. axial direction, was also seen in shear lap tests but was reversed for peel failure, consistent with others' observations [183,199,200]. We hypothesize that this difference is due to the anisotropy of the tissue combined with the sample shape and orientation.

Our experimental data are consistent with previous studies. Garcıa-Herrera et al. [225] performed uniaxial tests using young (25 ± 3 years), healthy, human ascending aortic tissue and observed similar anisotropic behavior, stretch at peak stress, and peak tensile stress. Their reported tensile stress of 2180 ± 240 kPa for circumferential and 1140 ± 100 kPa for axial samples are similar to our uniaxial results (2510 ± 979 kPa and 750 ± 228 kPa for circumferential and axial samples, respectively). Vorp et al. [198], however, observed no significant difference in peak tensile stress between human specimens oriented axially and circumferentially, possibly due to greater subject age (51 ± 6 years). Stretch at failure showed no significant difference between the circumferential and axial cases and was similar to values reported by Garcıa-Herrera et al. (2.35 ± 10 versus 2.00 ± 0.1 in circumferential and axial, respectively) and to our values (1.92 ± 0.16 and 1.99 ± 0.07 for axial and circumferential, respectively). An equibiaxial study by Nicosia et al. [226] on healthy, porcine aortic root wall showed similar directional dependence with stresses at 30% strain of approximately 50 kPa and 90 kPa in the axial and circumferential directions, respectively, comparable to our results of 58.4 kPa and 76.2 kPa. Unlike the results of Nicosia et al., which remained linear up to 40% strain, our results were pronouncedly nonlinear. Sommer et al. [199], performed peel tests on nonpathologic human abdominal aortas (36 to 75 years) and observed similar anisotropic behavior. Their reported values for average peel tension (22.9 ± 2.9 mN/mm and 34.8 ± 15.5 mN/mm for circumferential and axial samples, respectively, mean ± SD), while significantly lower than our values have a similar anisotropy ratio, (1.5 to our 1.4). Their average standard deviations for the directions showed strong anisotropy, which we also observed. In addition, Sommer et al. presented histological images of the dissection

surface fixed under load which show the surface to be much rougher for samples oriented axially than those oriented circumferentially and suggest that the orientation of the fibrous components may explain the higher resisting peel tension and variance in peel tension observed for axial samples. Pasta et al. [183], performed peel tests on both nonaneurysmal ascending aorta and nondissected aTAAs from human subjects (41 to 79 years). Again, the typical plateau behavior of a peel test was observed as well as strong anisotropy favoring the axial direction. Average peel tension for the nonaneurysmal aorta was close to the range determined in this study, (126.0 ± 6.6 mN/mm and 149.0 ± 7.6 mN/mm for circumferential and axial samples, respectively, mean ± SD) and exhibited a similar anisotropic ratio, (1.2 to our 1.4). No analysis was done on the fluctuation of peel strength throughout the plateau. To the author's knowledge shear lap testing has not been performed on tissue from elastic arteries before and though there has been some work to characterize vessels in torsion [105], shear failure was not studied.

Having confirmed that our experimental data are consistent with previous studies, we will focus on the model for the remainder of the discussion. The multiscale model was able to reproduce the ex vivo testing results in both the uniaxial and biaxial testing configurations. The advantage of a multiscale model is to link observed macroscale properties to changes in microscale structure (Table 6.1 and Figure 6.4). The model was able to capture the anisotropic response in both the uniaxial and biaxial simulations, in agreement with our experimental results. It is important to note that our study, similar to other studies [197], is limited in that physiological strain rates are higher than those used; thus, the model should be seen as approaching the quasi-static limit. The model demonstrated smaller confidence intervals (for both peak tensile stress and peak stretch) relative to experimental results, suggesting the method to model fiber failure could be modified to increase variance. Additionally, variance could be increased by using a stochastic element for fiber failure or by introducing more variability in the model networks. A stochastic failure model would be consistent with the wide range of failure lengths seen for fibers such as collagen, where λ_{crit} can range from 1.2 to 1.7 [227].

In-plane fiber rotation (in the area of interest) was more prevalent in uniaxial than biaxial simulations (Figure 6.7 and Figure 6.9). Fibers in the uniaxial circumferential simulations were predominately aligned in the direction of pull and, therefore, could only stretch and not rotate at the onset of macroscale strain. Fibers in uniaxial axial simulations were predominately aligned perpendicular to the direction of pull; therefore, when macroscale strain was applied, fibers first rotated and then extended. The rotation of fibers resulted in lower forces in uniaxial axial simulations for the same amount of macroscale strain in uniaxial circumferential results. The model permits for free rotation of fibers, which overestimates a fiber's capacity to rotate, as in vivo obstacles such as neighboring fibers and matrix are not taken into account in fiber rotation.

An important simplification of the tissue microstructure in the model was that a single, idealized network of uniform-diameter fibers was employed in parallel with a neo-Hookean component to account for all structural contributions including collagen, elastin, extracellular matrix, cells, and interstitial fluid. Even with this simplification, the complex mechanical response of both uniaxial and biaxial extension was still captured. We expected the neo-Hookean component to dominate at low strain, representing elastin, while the fiber network would dominate at high strains, representing collagen. Therefore, initial model fiber parameters were chosen to simulate collagen, but those values led to vastly overpredicted forces (data not shown). When fiber model parameters were fit to the experimental data, the resulting values (Table 6.2) described the behavior of elastin more closely than collagen, suggesting that elastin plays a dominant role dictating behavior in the tissue in in-plane tension. A previous study also indicated that intrinsic elastic properties dictate distensibility of the aorta [228]. In addition, a collagen-based fiber network would not be able to achieve a stretch of 2.0 since collagen fibers have a λ_{crit} closer to 1.4 [211], while elastin can reach stretches up to 3 [229]. Histological evidence supports a large elastin contribution as studies have shown more elastin than collagen exists in the ascending aorta (by dry weight 35% elastin, 22% collagen [32]). Hence, our fitted λ_{crit} value of 2.17 represents the combined effect of the two proteins.

Our fitted value (2.51MPa) of small strain Young's modulus is within the range of values reported for elastin (estimated 0.3 -10 MPa) in vessel walls [26,230,231].

6.7 Modeling Modification

We have investigated the biomechanical tensile properties of the aortic media in the circumferential and axial orientations, which are relevant to rupture of the vessel, but dissection of ATAA depends strongly on the strength of the tissue in the shear and radial tension [232]. The model failed to capture the biomechanics of the tissue in both the peel and shear lap geometries. Currently, the model does not consider the concentric, circumferential layers of elastin, collagen, and smooth muscle, which form the medial lamellae [233]. We therefore propose the modification of the single, idealized network presented herein arguing that by revising the simplified microstructural organization of this model we will be able to capture the tissue's biomechanics in modalities more relevant to dissection. The tissue-specific network is designed to capture the different fibrous materials within the aortic wall.

The aorta is organized into thick concentric medial fibrocellular layers which can be represented by discrete structural and functional units [195]. The lamellar unit, detailed by Clark and Glagov [27], consists of an elastic lamina sandwiched between two sheets of smooth muscle cells. Therefore, the network is designed to simulate the architecture of this discrete lamellar unit. Histological analysis was done in order to visualize the lamellar unit. Portions of unloaded porcine ascending aorta were cut such that the transmural structure was aligned in the circumferential (i.e. horizontal) direction and fixed in 10% buffered neutral formalin solution overnight, embedded in paraffin, and prepared for histological investigation per standard techniques. Sections were stained consecutively with HE stain (Figure 6.14a) to visualize smooth muscle cell nuclei, Masson's trichrome stain (Figure 6.14b) to visualize collagen, and VVG stain (Figure 6.14c) to visualize elastin.

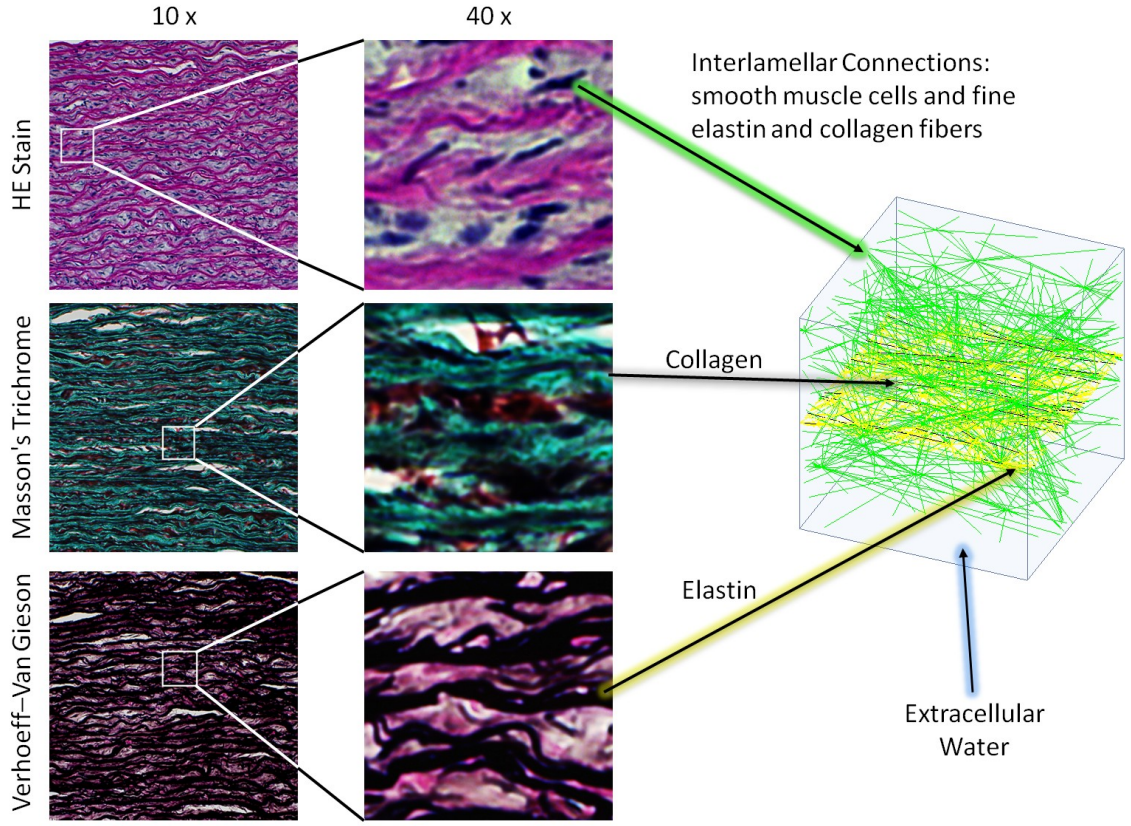

Figure 6.14: Lamellar Structure of Thoracic Aorta at 10x and 40x magnification. HE stain allows visualization of smooth muscle cell nuclei (dark purple) as well as elastic lamina (pink layers). Masson's trichrome stain allows visualization of collagen (blue) within the lamina and smooth muscle (red). VVG stain of allows visualization of elastin in both the lamina (black) as well as in the interlamellar space (purple). The model network mimics the lamellar unit structure of the thoracic aorta; combining collagen and elastin into a 2D sheet to represent the elastic lamina, connecting lamina with fibrous interlamellar connections, and filling the remaining volume with a nearly incompressible matrix.

The final network structure is shown in Figure 6.14d. The elastic lamina is represented by a 2D sheet of elastin and collagen fibers. Previous studies have shown that collagen fibers within the arterial media have a strong preferential orientation in the circumferential direction [27,32,195,215,234], so collagen fibers within the elastin-collagen sheet are generated such that they exhibit strong circumferential orientation. Fiber stiffness, nonlinearity, and failure stretch are quantified using the results of Lai et al. [209]. Histological and compositional evidence [27,32,195,215,234] supports a large elastin contribution, with more elastin than collagen within the ascending aortic wall. Therefore, based on the histological observations of Sokolis [32], the overall ratio of elastin to

collagen within the 2D sheet is set to ~ 1.6. Elastin fibers are generated such that orientation is approximately isotropic within the plane and fiber stiffness, nonlinearity, and failure stretch are set to the values fit in Table 6.2. The radial properties of the aorta are less well established [235], but extremely important as it is the interlamellar connections that dictate delamination and thus aortic dissection. The structural components that radially connect lamina are an unclear combination of smooth muscle cells, fine collagen fibers, and fine elastin fibers [199,235]. Figure 6.15a shows a specimen for which the layers were peeled apart highlighting the importance of both the smooth muscle cells (solid arrow) and fine collagen fibers (dashed arrow) within the interlamellar connections. A fine elastin fiber, discussed in Maclean et al. [235], connecting two parallel lamina is shown in Figure 6.15b. The interlamellar connections within the model network were designed to encompass the combined effect of all structural components contributing to radial strength. They favor the circumferential direction as smooth muscle cells exhibit strong preferential circumferential alignment. Initial fiber parameters (fiber stiffness, nonlinearity, and failure stretch) for the interlamellar connections are specified based on a fit of Maclean's experimental stress-strain behavior of the upper thoracic aorta subjected to radial failure [235]. The volume fraction for the tissue-specific network was set to 5% [234].

In addition to the smooth muscle cells and connective tissues present within the lamellar unit there is also fluid, primarily extracellular water [195], causing the deformation to be nearly isochoric. Therefore, similarly to the simplified network, a nonfibrillar, neo-Hookean the extracellular matrix) is added to the network with a Poisson's ratio, $\upsilon = 0.49$, (nearly incompressible) [210]. Again, the fiber network and nonfibrous material operate as functionally independent until failure, at which point network failure dictated simultaneous matrix failure. Stresses developed by the new tissue-specific network and matrix are additive as in other constrained mixture type models [236].

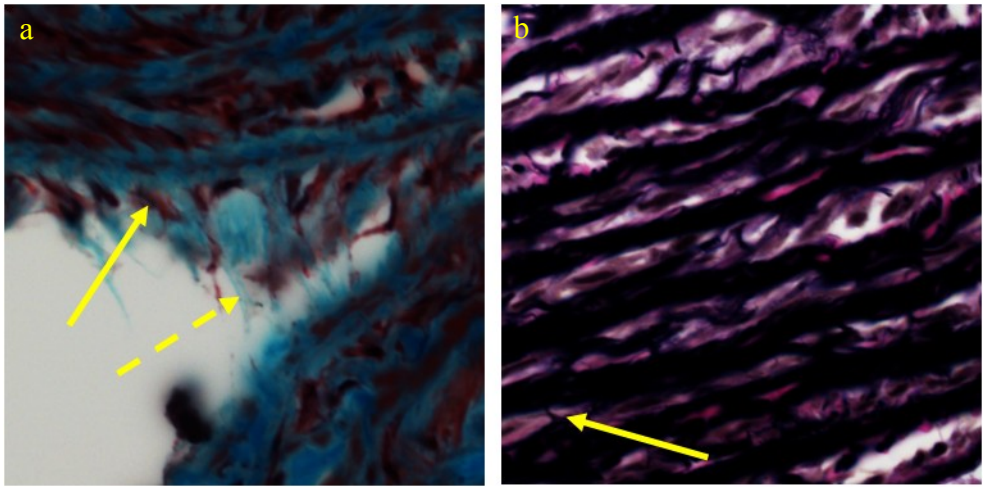

Figure 6.15: (a) Masson's trichrome stain of aortic layers at point of failure in peel test with smooth muscle cells (solid arrow) and fine collagen fibers (dashed arrow) indentified within the interlamellar connections. (b) VVG stain of aortic layers with a fine elastin fiber, connecting two parallel lamina indicated (solid arrow).

Creating a model which can replicate experimental results from all mechanical tests performed (equibiaxial, uniaxial, peel and shear lap), to fully represent failure as seen in ATAA, is important to determining whether the model can have predictive in addition to analytical value. As we move forward to more patient-based geometries and simulations involving more realistic combined loading situations validation of the model in multi-dimensional loading will be crucial. To properly investigate the radial and shear loading conditions the simplified microstructural organization of the model presented in this chapter will need to be revised/expanded and the proposed change in microstructure is promising. The lamellae's structure is an essential component in modeling dissection of ATAA as radial and shear loading involve failure of the interlamellar connections rather than the lamina itself. In spite of the simplifications, the good agreement between the multiscale model and the experiment, for both prefailure and failure behavior in uniaxial and biaxial tests, indicates a high potential for use in the more complex geometry, architecture, and loading configuration that arise in ATAA.

Chapter 7: Conclusion

The soft tissues of the cardiovascular system have unique load-bearing capabilities. The ventricle walls themselves expand and contract over 2.5 billion times during the average human life span [195]. The elastic nature of the ascending aorta is crucial to the maintenance of continuous blood flow as blood ejected during systole is partly stored by expansion of the aortic wall and then moved forward during diastole by elastic recoil. This work couples theoretical and experimental methods for the mechanical characterization of complex cardiovascular soft tissues evaluating their multiaxial mechanical behavior. The methods herein address the intrinsic complexity of cardiovascular soft tissues (heterogeneity, anisotropy, and nonlinearity) adding significantly to the current understanding of these tissues. The paragraphs that follow provide a brief overview of the most relevant and interesting results of this work.

7.1 Modifying GAIM for Nonlinear Kinematics and Applying it to Rat Right Ventricle (Chapter 2)

In order to characterize fully a cardiovascular soft tissue, its behavior must be considered in a variety of loading modalities. In chapter 1, the various loading modalities (indentation, inflation, and extension) typically imposed in the study of soft tissues were discussed as well as a number of relevant constitutive models and inverse approaches. The Generalized Anisotropic Inverse Mechanics (GAIM) method was introduced in chapter 1, and its ability to provide general tissue characteristics in terms of stiffness, anisotropy strength, and preferred orientation was highlighted. However, the linear assumption implicit in GAIM limited its utility, particularly in the case of cardiovascular soft tissues, which exhibit markedly nonlinear behavior when operating at physiologic strain levels. Consequently, the first modification to GAIM was to the stress relation (Eqn. 2.1) to account for nonlinear kinematics by considering the Green strain rather than linear strain and the 2nd Piola-Kirchoff stress rather than the Cauchy stress. The resulting elasticity tensor was analogous to the linear elasticity (with the same major and minor

symmetries), but quantified the material as neo-Hookean. The large-deformation extension of the GAIM method was capable of quantifying regional variation in both the stiffness and anisotropy of the decellularized ventricle.

In addition to the extension of GAIM, the mechanical consequences of the removal of the cellular content of the ventricle by perfusion decellularization were determined. GAIM indicated higher stiffnesses for the perfusion-decellularized ventricular tissue in comparison to the control, which was consistent with the change in sample thickness suggesting that the cellular contribution to stiffness was small. Mechanical anisotropy did not vary between the decellularized and control samples nor did they show significant differences in the spatial variation of their mechanical properties. Therefore, we concluded that perfusion decellularization does not show regional preference and that perfusion decellularized tissue can be used as a model for studying mechanical changes to the heart's extracellular matrix.

7.2 Applying the Closed-Form Nonlinear Structural Model to Rat Ventricle (Chapter 3)

As discussed in chapter 1, a common technique for the characterization of soft tissues involves identifying an appropriate strain energy relation and fitting its associated material parameters to experimental data. Determining an appropriate strain energy relation which captures the complex behavior of soft tissues is difficult. One common technique is to represent the tissue as a fiber-reinforced composite, combining a continuous matrix and a population of fibers, and assuming the constituents deform affinely with both macroscopic deformation and stress being additive. In chapter 3, one such model, a close-form structural model of planar fibrous tissue mechanics (NFSM) developed by Raghupathy and Barocas [124], was utilized to describe the biaxial behavior of rat ventricle. The model was selected due to its ability to describe a wide range of material responses with a relatively small number of parameters and its closed-form nature which causes it to be very efficient computationally. It showed great success in describing the mechanical behavior of rat heart ventricle in a variety of biaxial loading

configurations, as demonstrated by comparison between experimental and model force-displacement graphs and full-field deformations. The efficient nature of the NSFM combined with its ability to describe the nonlinear, anisotropic multiaxial behavior of cardiovascular soft tissues made it an attractive model for the computational simulations considered in chapters 4 and 5.

7.3 An Alternative Approach to Computational Dissection (Chapter 4)

The partitioning scheme utilized to separate the sample domain into homogenous subdomains was a shortcoming of the GAIM method [113]. It tended to create many partitions that were all similar in size and shape and often created many superfluous partitions. The deformation gradient field jump segmentation method of chapter 4 is a major advancement in the computational dissection of heterogeneous tissues. It uses the jump in the deformation gradient across a finite element boundary as a measure of the local change in material properties and employs graph theory to determine the boundaries of mechanically similar regions. The method identified the location, size, and shape of different homogeneous regions for simulated tissue samples (prescribed with both abrupt and gradual changes in anisotropy strength, prescribed fiber alignment, stiffness, and nonlinearity), for tissue analogs (PDMS and collagen gels), and actual soft tissue samples (cadaveric supraspinatus tendon and thoracic aorta containing transmural plaque). Many studies considering the heterogeneous properties of soft tissues (including our own in chapter 6), are hindered by the cutting process itself: the tissue must be cut into many small sections for testing and each section is assumed homogeneous. The proposed computational dissection method offers an attractive alternative allowing non-destructive segmentation to adjust to the unique physical boundaries of a sample post-testing.

7.4 Capturing Large-Strain Nonlinear Behavior by Applying GAIM Discretely (Chapter 5)

The NGAIM method is the culmination of a long journey. In order to apply NGAIM, a sufficient set of biaxial experimental protocols must be performed on a tissue specimen

and the full-field strain and grip normal and shear forces must be measured. Raghupathy [115] created a robust image correlation technique for the accurate estimation of full-field displacements from motion capture of soft tissues. Since errors in the displacement field are amplified due to the gradient operator utilized in GAIM and the inverse method is direct, making it more sensitive to errors than iterative methods, this was a crucial step in the development of GAIM. The acquisition of six degree of freedom load cells [171] has enabled the measurement of both the normal and shear forces at the grip arm. As the load cells measure both force in the direction of pull and force perpendicular to the direction of pull, the linear system in the arms is well-conditioned despite their low levels of transverse displacement. In addition, asymmetric sample shape and asymmetric sample configuration (i.e. aligning material axes such that they do not correspond with machine axes) as demonstrated by Sacks [194], are means of generating higher shear strains. Unique multiaxial testing devices [108,111] are capable of imposing planar loading conditions which better span strain space and more deeply investigate shear. Finally, the creation of a new deformation gradient jump based partitioning scheme (chapter 4) enabled better sample segmentation.

The work of Raghupathy [113,115] cannot be overstated as it is the foundation on which NGAIM relies. The approach directly solves the finite element representation of the stress balance to determine the material properties of anisotropic, inhomogeneous samples. The modification of chapter 2 allowed for the consideration of nonlinear kinematics, but it is the approach of chapter 5 which enables NGAIM to consider fully the tissue's nonlinear behavior. The key to extending GAIM was to consider the nonlinear force-displacement curves without sacrificing the tremendous efficiency advantage of the linear model. My strategy involved discretizing each nonlinear curve into many short linear segments, from which a set of piecewise neo-Hookean elasticity tensors were calculated. For the first step, the GAIM method, as applied in chapter 2, is utilized to determine the neo-Hookean elasticity tensor. For the remaining steps, a piecewise linear model is utilized and the neo-Hookean elasticity tensor is constrained such that it both

satisfies the stress balance and varies minimally from the preceding step's elasticity tensor.

The power of NGAIM is two-fold: (1) it allows for the computational dissection of complex, heterogeneous soft tissues enabling the discernment of regional variation within a single tissue and providing information about how the tissue transitions and (2) it generates data-driven strain-energy functions for each region within the tissue. NGAIM, as an analytical method can be applied to examine regional mechanical differences in planar, nonlinear, anisotropic, highly extensible tissue samples from all over the body. Diverse conditions such as dermal wound healing, fibrotic lung disease, myocardial infarction, and tendon/ligament injury, all involve spatial variations in tissue mechanics and could be studied utilizing the NGAIM approach.

7.5 Multidirectional Failure of Ascending Aorta (Chapter 6)

In chapter 6, we consider a different cardiovascular soft tissue, ascending aorta. A traditional approach to heterogeneity was used in which porcine ascending aorta was cut into many samples, each sample was mechanically interrogated, and analysis assumes homogeneity. The main advance in the study was the use of two novel test methods, the peel test and the shear lap test, to measure material failure in radial tension and transmural shear, respectively. The peel test results confirmed observations made by others [183,199] suggesting that the typical anisotropy expected of arteries (higher circumferential vs. axial stiffness) is reversed in the transmural direction. As Sommer [199] suggested, this may be a protective mechanism since dissection in the axial direction is often associated with failure across elastic laminae whereas dissection in the circumferential direction typically propagates between adjacent laminae. Though the shear lap test has been used on annulus fibrosus [223], it has not been applied to cardiovascular soft tissues. The loading curve for the shear lap failure of ascending aorta showed catastrophic failure similar to that of a uniaxial test rather than the sliding behavior seen by Gregory et al. [223]. The failure behavior observed for the shear lap test

retained the typical anisotropy expected of arteries, but required a much lower stress than that of uniaxial failure consistent with the laminate nature of the artery.

The work of chapter 6 highlights an important assumption implicit within NGAIM (and GAIM) which may hinder its use. Though often planar, cardiovascular tissues generally have a layered structure with varying transmural properties. In addition, characteristics that we wish to study - the failure of the ascending aorta in aneurysm and the growth and remodeling of the tissue following injury (e.g. myocardial infarction) - have transmural as well as planar heterogeneity. If these tissues are to be studied effectively, the implicit assumption in our analysis, that the displacement experienced by biaxial samples is uniform through the tissue's thickness and that the mechanical properties determined can be interpreted as a transmural average, must be addressed. These presumptions are likely only true if the tissue is separated into layers and each layer is biaxially tested separately. Thus, combining the traditional experimental approach to heterogeneity with the new computational NGAIM approach.

However, as shown by the shear lap and peel test results, the interlamellar connections attaching the layers are important to tissue function, critical in the case of an ascending aortic aneurysm. The multiscale model presented in chapter 6 with the proposed three-component network has the potential to capture the three-dimensional response of the aorta by linking microscale failure to the macroscale response. However, as indicated by Hadi et al. [211], even the multiscale model proposed is limited in that the network structure (both the organization and proportions of its constituents) is allowed only limited random variation. In order to consider heterogeneous tissues, experimentally derived material parameters are needed to guide network design. Leveraging the capacity of GAIM to determine regional variation with the predictive three-dimensional capabilities of the multiscale model holds great promise for the characterization of complex cardiovascular tissues.

In conclusion, the work presented in this thesis marks the development and use of novel theoretical and experimental approaches for the analysis of complex cardiovascular soft tissues. An analysis method was developed, NGAIM, that can be applied to examine regional mechanical differences in planar, nonlinear, anisotropic, heterogeneous, tissue samples from all over the body. Finally, the partnering was proposed which exploits the characterization capacity of NGAIM with the predictive capacity of the multiscale model to create full three-dimensional simulations of cardiovascular soft tissue behavior.

Bibliography

[1] "By Blausen Medical Communications, Inc. (Donated via OTRS, see ticket for details) [CC-BY-3.0 (http://creativecommons.org/licenses/by/3.0)], via Wikimedia Commons."

[2] Humphrey J. D., 2002, Cardiovascular Solid Mechanics: Cells, Tissues, and Organs, Springer Science & Business Media, New York, NY.

[3] "By DanielChangMD revised original work of DestinyQx; Redrawn as SVG by xavax (Wikimedia Commons, File:Wiggers Diagram.png.) [CC-BY-SA-2.5 (http://creativecommons.org/licenses/by-sa/2.5)], via Wikimedia Commons."

[4] Smith S. C., Benjamin E. J., Bonow R. O., Braun L. T., Creager M. a, Franklin B. a, Gibbons R. J., Grundy S. M., Hiratzka L. F., Jones D. W., Lloyd-Jones D. M., Minissian M., Mosca L., Peterson E. D., Sacco R. L., Spertus J., Stein J. H., and Taubert K. a, 2011, "AHA/ACCF Secondary Prevention and Risk Reduction Therapy for Patients with Coronary and other Atherosclerotic Vascular Disease: 2011 update: a guideline from the American Heart Association and American College of Cardiology Foundation.," Circulation, **124**(22), pp. 2458–73.

[5] Go A. S., Mozaffarian D., Roger V. L., Benjamin E. J., Berry J. D., Blaha M. J., Dai S., Ford E. S., Fox C. S., Franco S., Fullerton H. J., Gillespie C., Hailpern S. M., Heit J. a, Howard V. J., Huffman M. D., Judd S. E., Kissela B. M., Kittner S. J., Lackland D. T., Lichtman J. H., Lisabeth L. D., Mackey R. H., Magid D. J., Marcus G. M., Marelli A., Matchar D. B., McGuire D. K., Mohler E. R., Moy C. S., Mussolino M. E., Neumar R. W., Nichol G., Pandey D. K., Paynter N. P., Reeves M. J., Sorlie P. D., Stein J., Towfighi A., Turan T. N., Virani S. S., Wong N. D., Woo D., and Turner M. B., 2014, "Executive summary: heart disease and stroke statistics--2014 update: a report from the American Heart Association.," Circulation, **129**(3), pp. 399–410.

[6] Armstrong P. W., Collen D., and Antman E., 2003, "Fibrinolysis for acute myocardial infarction: the future is here and now.," Circulation, **107**(20), pp. 2533–7.

[7] Faxon D., and Lenfant C., 2001, "Timing is everything: motivating patients to call 9-1-1 at onset of acute myocardial infarction.," Circulation, **104**(11), pp. 1210–1.

[8] Garcia E. A., Likourezos A., Ramsay C., Hoffman S., Niles C., Pearl-Davis M., Podolsky S., and Davidson S. J., 2010, "Evaluation of emergency medicine community educational program.," West. J. Emerg. Med., **11**(5), pp. 416–8.

[9] Morrison L. J., Verbeek P. R., McDonald a C., Sawadsky B. V, and Cook D. J., 2014, "Mortality and prehospital thrombolysis for acute myocardial infarction: A meta-analysis.," JAMA, **283**(20), pp. 2686–92.

[10] Moser D. K., Kimble L. P., Alberts M. J., Alonzo A., Croft J. B., Dracup K., Evenson K. R., Go A. S., Hand M. M., Kothari R. U., Mensah G. a, Morris D. L., Pancioli A. M., Riegel B., and Zerwic J. J., 2006, "Reducing delay in seeking treatment by patients with acute coronary syndrome and stroke: a scientific statement from the American Heart Association Council on cardiovascular nursing and stroke council.," Circulation, **114**(2), pp. 168–82.

[11] Spertus J. a, Radford M. J., Every N. R., Ellerbeck E. F., Peterson E. D., and Krumholz H. M., 2003, "Challenges and opportunities in quantifying the quality of care for acute myocardial infarction: summary from the Acute Myocardial Infarction Working Group of the American Heart Association/American College of Cardiology First Scientific Forum on Quality ," Circulation, **107**(12), pp. 1681–91.

[12] Topol E. J., 2003, "Current status and future prospects for acute myocardial infarction therapy.," Circulation, **108**(16 Suppl 1), pp. III6–13.

[13] Holmes J. W., Borg T. K., and Covell J. W., 2005, "Structure and mechanics of healing myocardial infarcts.," Annu. Rev. Biomed. Eng., **7**, pp. 223–53.

[14] Levy W. C., Mozaffarian D., Linker D. T., Sutradhar S. C., Anker S. D., Cropp A. B., Anand I., Maggioni A., Burton P., Sullivan M. D., Pitt B., Poole-Wilson P. a, Mann D. L., and Packer M., 2006, "The Seattle Heart Failure Model: prediction of survival in heart failure.," Circulation, **113**(11), pp. 1424–33.

[15] Abdel-Latif A., Bolli R., Tleyjeh I. M., Montori V. M., Perin E. C., Hornung C. A., Zuba-Surma E. K., Al-Mallah M., and Dawn B., 2007, "Adult bone marrow-derived cells for cardiac repair: a systematic review and meta-analysis.," Arch. Intern. Med., **167**(10), pp. 989–97.

[16] Ter Horst K. W., 2010, "Stem cell therapy for myocardial infarction: are we missing time?," Cardiology, **117**(1), pp. 1–10.

[17] Herdrich B. J., and Gorman R. C., 2010, "Progenitor Cells for the Treatment of Acute Myocardial Infarction.," Adv. Skin Wound Care, **1**, pp. 519–525.

[18] Dvir T., Leor J., and Cohen S., 2011, Myocardial Tissue Engineering, Springer Berlin Heidelberg, Berlin, Heidelberg.

[19] Fujimoto K. L., Tobita K., Merryman W. D., Guan J., Momoi N., Stolz D. B., Sacks M. S., Keller B. B., and Wagner W. R., 2007, "An elastic, biodegradable cardiac patch induces contractile smooth muscle and improves cardiac remodeling and function in subacute myocardial infarction.," J. Am. Coll. Cardiol., **49**(23), pp. 2292–300.

[20] Dotter C. T., Roberts D. J., and Steinberg I., 1950, "Aortic Length: Angiocardiographic Measurements," Circulation, **2**(6), pp. 915–920.

[21] Gray H., 1918, "The Aorta," Anatomy of the Human Body, W.H. Lewis, ed., Lea & Febiger, Philadelphia.

[22] Isselbacher E. M., 2005, "Thoracic and abdominal aortic aneurysms.," Circulation, **111**(6), pp. 816–28.

[23] Mao S. S., Ahmadi N., Shah B., Beckmann D., Chen A., Ngo L., Flores F. R., Gao Y. L., and Budoff M. J., 2008, "Normal thoracic aorta diameter on cardiac computed tomography in healthy asymptomatic adults: impact of age and gender.," Acad. Radiol., **15**(7), pp. 827–34.

[24] Davies R. R., Goldstein L. J., Coady M. A., Tittle S. L., Rizzo J. A., Kopf G. S., and Elefteriades J. A., 2002, "Yearly rupture or dissection rates for thoracic aortic aneurysms: simple prediction based on size," Ann. Thorac. Surg., **73**(1), pp. 17–28.

[25] Pape L. a, Tsai T. T., Isselbacher E. M., Oh J. K., O'gara P. T., Evangelista A., Fattori R., Meinhardt G., Trimarchi S., Bossone E., Suzuki T., Cooper J. V, Froehlich J. B., Nienaber C. a, and Eagle K. a, 2007, "Aortic diameter >or = 5.5 cm is not a good predictor of type A aortic dissection: observations from the International Registry of Acute Aortic Dissection (IRAD).," Circulation, **116**(10), pp. 1120–7.

[26] Holzapfel G., 2001, "Biomechanics of soft tissue," The handbook of materials behavior models, J. Lemaitre, ed., Boston, MA, pp. 1049–1063.

[27] Clark J. M., and Glagov S., 2000, "Transmural organization of the arterial media. The lamellar unit revisited.," Arteriosclerosis, **5**(1), pp. 19–34.

[28] Wolinsky H., and Glagov S., 1964, "Structural Basis for the Static Mechanical Properties of the Aortic Media," Circ. Res., **14**(5), pp. 400–413.

[29] Fung Y. C., 1997, Biomechanics: Circulation, Springer Science & Business Media, New York.

[30] Farand P., Garon A., and Plante G. E., 2007, "Structure of large arteries: orientation of elastin in rabbit aortic internal elastic lamina and in the elastic lamellae of aortic media.," Microvasc. Res., **73**(2), pp. 95–9.

[31] Streeter D. D., Spotnitz H. M., Patel D. P., Ross J., and Sonnenblick E. H., 1969, "Fiber Orientation in the Canine Left Ventricle during Diastole and Systole," Circ. Res., **24**(3), pp. 339–347.

[32] Sokolis D. P., Boudoulas H., and Karayannacos P. E., 2008, "Segmental differences of aortic function and composition: clinical implications.," Hellenic J. Cardiol., **49**(3), pp. 145–54.

[33] Rowe A. J., Finlay H. M., and Canham P. B., 2003, "Collagen biomechanics in cerebral arteries and bifurcations assessed by polarizing microscopy.," J. Vasc. Res., **40**(4), pp. 406–15.

[34] Sacks M. S., and Chuong C. J., 1998, "Orthotropic mechanical properties of chemically treated bovine pericardium.," Ann. Biomed. Eng., **26**(5), pp. 892–902.

[35] Chen J., Song S.-K., Liu W., McLean M., Allen J. S., Tan J., Wickline S. a, and Yu X., 2003, "Remodeling of cardiac fiber structure after infarction in rats quantified with diffusion tensor MRI.," Am. J. Physiol. Heart Circ. Physiol., **285**(3), pp. H946–54.

[36] Zhang S., Crow J. A., Yang X., Chen J., Borazjani A., Mullins K. B., Chen W., Cooper R. C., McLaughlin R. M., and Liao J., 2010, "The correlation of 3D DT-MRI fiber disruption with structural and mechanical degeneration in porcine myocardium.," Ann. Biomed. Eng., **38**(10), pp. 3084–95.

[37] McCormick R. J., Musch T. I., Bergman B. C., and Thomas D. P., 1994, "Regional differences in LV collagen accumulation and mature cross-linking after myocardial infarction in rats.," Am. J. Physiol., **266**(1 Pt 2), pp. H354–9.

[38] Humphrey J. D., Strumpf R. K., and Yin F. C., 1990, "Determination of a constitutive relation for passive myocardium: II. Parameter estimation.," J. Biomech. Eng., **112**(3), pp. 340–6.

[39] Doyle J. M., and Dobrin P. B., 1971, "Finite deformation analysis of the relaxed and contracted dog carotid artery," Microvasc. Res., **3**(4), pp. 400–415.

[40] Patel D. J., and Fry D. L., 1969, “The Elastic Symmetry of Arterial Segments in Dogs,” Circ. Res., **24**(1), pp. 1–8.

[41] Sacks M. S., and Chuong C. J., 1993, “Biaxial mechanical properties of passive right ventricular free wall myocardium.,” J. Biomech. Eng., **115**(2), pp. 202–5.

[42] Humphrey J. D., Strumpf R. K., and Yin F. C., 1990, “Determination of a constitutive relation for passive myocardium: I. A new functional form.,” J. Biomech. Eng., **112**(3), pp. 333–9.

[43] Humphrey J. D., Strumpf R. K., and Yin F. C., 1990, “Biaxial mechanical behavior of excised ventricular epicardium.,” Am. J. Physiol., **259**(1 Pt 2), pp. H101–8.

[44] Kang T., Humphrey J. D., and Yin F. C., 1996, “Comparison of biaxial mechanical properties of excised endocardium and epicardium.,” Am. J. Physiol., **270**(6 Pt 2), pp. H2169–76.

[45] Delfino A., 1996, “Analysis of stress field in a model of the human carotid bifurcation,” Ecole Polytechnique Federale de Lausanne.

[46] Harkness M. L. R., Harkness R. D., and McDonald D. a., 1957, “The Collagen and Elastin Content of the Arterial Wall in the Dog,” Proc. R. Soc. B Biol. Sci., **146**(925), pp. 541–551.

[47] Fischer G. M., and Llaurado J. G., 1966, “Collagen and Elastin Content in Canine Arteries Selected from Functionally Different Vascular Beds,” Circ. Res., **19**(2), pp. 394–399.

[48] Tower T. T., and Tranquillo R. T., 2001, “Alignment maps of tissues: II. Fast harmonic analysis for imaging.,” Biophys. J., **81**(5), pp. 2964–71.

[49] Billiar K. L., and Sacks M. S., 2000, “Biaxial mechanical properties of the natural and glutaraldehyde treated aortic valve cusp--Part I: Experimental results.,” J. Biomech. Eng., **122**(1), pp. 23–30.

[50] Bronzino E. J. D., 2000, “McCulloch, A. D. ‘ Cardiac Biomechanics.’”

[51] Demer L. L., and Yin F. C., 1983, “Passive biaxial mechanical properties of isolated canine myocardium.,” J. Physiol., **339**, pp. 615–30.

[52] Omens J. H., McCulloch a D., and Criscione J. C., 2003, “Complex distributions of residual stress and strain in the mouse left ventricle: experimental and theoretical models.,” Biomech. Model. Mechanobiol., **1**(4), pp. 267–77.

[53] Ghaemi H., Behdinan K., and Spence a D., 2009, “In vitro technique in estimation of passive mechanical properties of bovine heart part I. Experimental techniques and data.,” Med. Eng. Phys., **31**(1), pp. 76–82.

[54] Gao F., Watanabe M., and Matsuzawa T., 2006, “Stress analysis in a layered aortic arch model under pulsatile blood flow.,” Biomed. Eng. Online, **5**, p. 25.

[55] Thubrikar M. J., Agali P., and Robicsek F., 1999, “Wall stress as a possible mechanism for the development of transverse intimal tears in aortic dissections.,” J. Med. Eng. Technol., **23**(4), pp. 127–34.

[56] Poullis M. P., Warwick R., Oo A., and Poole R. J., 2008, “Ascending aortic curvature as an independent risk factor for type A dissection, and ascending aortic aneurysm formation: a mathematical model.,” Eur. J. Cardiothorac. Surg., **33**(6), pp. 995–1001.

[57] Freeman R. V, and Otto C. M., 2005, “Spectrum of calcific aortic valve disease: pathogenesis, disease progression, and treatment strategies.,” Circulation, **111**(24), pp. 3316–26.

[58] Sacks M. S., and Schoen F. J., 2002, “Collagen fiber disruption occurs independent of calcification in clinically explanted bioprosthetic heart valves.,” J. Biomed. Mater. Res., **62**(3), pp. 359–71.

[59] Fomovsky G. M., and Holmes J. W., 2010, “Evolution of scar structure, mechanics, and ventricular function after myocardial infarction in the rat.,” Am. J. Physiol. Heart Circ. Physiol., **298**(1), pp. H221–8.

[60] Fomovsky G., Rouillard A., and Holmes J., 2012, “Regional mechanics determine collagen fiber structure in healing myocardial infarcts,” J. Mol. Cell. Cardiol., **52**(5), pp. 1083–1090.

[61] Holzapfel G. a, and Ogden R. W., 2009, “Constitutive modelling of passive myocardium: a structurally based framework for material characterization.,” Philos. Trans. A. Math. Phys. Eng. Sci., **367**(1902), pp. 3445–75.

[62] Shadwick R. E., 1999, “Mechanical design in arteries.,” J. Exp. Biol., **202**(Pt 23), pp. 3305–13.

[63] Edvardsen T., 2002, “Quantitative Assessment of Intrinsic Regional Myocardial Deformation by Doppler Strain Rate Echocardiography in Humans: Validation Against Three-Dimensional Tagged Magnetic Resonance Imaging,” Circulation, **106**(1), pp. 50–56.

[64] Fung Y. C., 1993, Biomechanics: Mechanical Properties of Living Tissues, Springer Science & Business Media, New York, NY.

[65] Kubo S., "Inverse Problems Related to the Mechanics and Fracture of Solids and Structures," JSME Int. J.

[66] Avril S., Bonnet M., Bretelle A.-S., Grédiac M., Hild F., Ienny P., Latourte F., Lemosse D., Pagano S., Pagnacco E., and Pierron F., 2008, "Overview of Identification Methods of Mechanical Parameters Based on Full-field Measurements," Exp. Mech., **48**(4), pp. 381–402.

[67] Kroon M., and Holzapfel G. a, 2008, "Estimation of the distributions of anisotropic, elastic properties and wall stresses of saccular cerebral aneurysms by inverse analysis," Proc. R. Soc. A Math. Phys. Eng. Sci., **464**(2092), pp. 807–825.

[68] Martins P. a. L. S., Natal Jorge R. M., and Ferreira a. J. M., 2006, "A Comparative Study of Several Material Models for Prediction of Hyperelastic Properties: Application to Silicone-Rubber and Soft Tissues," Strain, **42**(3), pp. 135–147.

[69] Humphrey J. D., 1999, "An evaluation of pseudoelastic descriptors used in arterial mechanics.," J. Biomech. Eng., **121**(2), pp. 259–62.

[70] Chuong C. J., and Fung Y. C., 1986, "On Residual Stresses in Arteries," J. Biomech. Eng., **108**(2), p. 189.

[71] Von Maltzahn W. W., Warriyar R. G., and Keitzer W. F., 1984, "Experimental measurements of elastic properties of media and adventitia of bovine carotid arteries.," J. Biomech., **17**(11), pp. 839–47.

[72] Takamizawa K., and Hayashi K., 1987, "Strain energy density function and uniform strain hypothesis for arterial mechanics.," J. Biomech., **20**(1), pp. 7–17.

[73] Greenleaf J. F., Fatemi M., and Insana M., 2003, "Selected methods for imaging elastic properties of biological tissues.," Annu. Rev. Biomed. Eng., **5**, pp. 57–78.

[74] Gao L., Parker K. J., Lerner R. M., and Levinson S. F., 1996, "Imaging of the elastic properties of tissue—A review," Ultrasound Med. Biol., **22**(8), pp. 959–977.

[75] Bonnet M., and Constantinescu A., 2005, "Inverse problems in elasticity," Inverse Probl., **21**(2), pp. R1–R50.

[76] Zamir E. a., and Taber L. a., 2004, “On the Effects of Residual Stress in Microindentation Tests of Soft Tissue Structures,” J. Biomech. Eng., **126**(2), p. 276.

[77] Zamir E. a., Srinivasan V., Perucchio R., and Taber L. a., 2003, “Mechanical Asymmetry in the Embryonic Chick Heart During Looping,” Ann. Biomed. Eng., **31**(11), pp. 1327–1336.

[78] Alford P. W., and Taber L. a., 2003, “Regional epicardial strain in the embryonic chick heart during the early looping stages,” J. Biomech., **36**(8), pp. 1135–1141.

[79] Costa K. D., and Yin F. C., 1999, “Analysis of indentation: implications for measuring mechanical properties with atomic force microscopy.,” J. Biomech. Eng., **121**(5), pp. 462–71.

[80] Gokhale N. H., Barbone P. E., and Oberai A. a, 2008, “Solution of the nonlinear elasticity imaging inverse problem: the compressible case,” Inverse Probl., **24**(4), p. 045010.

[81] Goenezen S., Barbone P., and Oberai A. a, 2011, “Solution of the nonlinear elasticity imaging inverse problem: The incompressible case.,” Comput. Methods Appl. Mech. Eng., **200**(13-16), pp. 1406–1420.

[82] Tyagi M., Goenezen S., Barbone P. E., and Oberai A. a, 2014, “Algorithms for quantitative quasi-static elasticity imaging using force data.,” Int. j. numer. method. biomed. eng., pp. 1–16.

[83] Goenezen S., Dord J.-F., Sink Z., Barbone P. E., Jiang J., Hall T. J., and Oberai A. a, 2012, “Linear and nonlinear elastic modulus imaging: an application to breast cancer diagnosis.,” IEEE Trans. Med. Imaging, **31**(8), pp. 1628–37.

[84] Cox M. a J., Driessen N. J. B., Boerboom R. a, Bouten C. V. C., and Baaijens F. P. T., 2008, “Mechanical characterization of anisotropic planar biological soft tissues using finite indentation: experimental feasibility.,” J. Biomech., **41**(2), pp. 422–9.

[85] Cox M. a J., Kortsmit J., Driessen N., Bouten C. V. C., and Baaijens F. P. T., 2010, “Tissue-engineered heart valves develop native-like collagen fiber architecture.,” Tissue Eng. Part A, **16**(5), pp. 1527–37.

[86] Holzapfel G. A., Gasser T. C., and Ogden R. A. Y. W., 2001, “A New Constitutive Framework for Arterial Wall Mechanics and a Comparative Study of Material Models,” pp. 1–48.

[87] Chai C.-K., Akyildiz A. C., Speelman L., Gijsen F. J. H., Oomens C. W. J., van Sambeek M. R. H. M., van der Lugt A., and Baaijens F. P. T., 2013, "Local axial compressive mechanical properties of human carotid atherosclerotic plaques-characterisation by indentation test and inverse finite element analysis.," J. Biomech., **46**(10), pp. 1759–66.

[88] Chai C.-K., Speelman L., Oomens C. W. J., and Baaijens F. P. T., 2014, "Compressive mechanical properties of atherosclerotic plaques--indentation test to characterise the local anisotropic behaviour.," J. Biomech., **47**(4), pp. 784–92.

[89] Karduna a R., Halperin H. R., and Yin F. C., 1997, "Experimental and numerical analyses of indentation in finite-sized isotropic and anisotropic rubber-like materials.," Ann. Biomed. Eng., **25**(6), pp. 1009–16.

[90] Bischoff J. E., 2004, "Static Indentation of Anisotropic Biomaterials Using Axially Asymmetric Indenters—a Computational Study," J. Biomech. Eng., **126**(4), p. 498.

[91] Humphrey J. D., Halperin H. R., and Yin F. C. P., 1991, "Small Indentation Superimposed on a Finite Equibiaxial Stretch: Implications for Cardiac Mechanics," J. Appl. Mech., **58**(4), p. 1108.

[92] Seshaiyer P., and Humphrey J. D., 2003, "A Sub-Domain Inverse Finite Element Characterization of Hyperelastic Membranes Including Soft Tissues," J. Biomech. Eng., **125**(3), p. 363.

[93] Pedrigi R. M., David G., Dziezyc J., and Humphrey J. D., 2007, "Regional mechanical properties and stress analysis of the human anterior lens capsule.," Vision Res., **47**(13), pp. 1781–9.

[94] Genovese K., Lee Y.-U., Lee a Y., and Humphrey J. D., 2013, "An improved panoramic digital image correlation method for vascular strain analysis and material characterization.," J. Mech. Behav. Biomed. Mater., **27**, pp. 132–42.

[95] Kroon M., and Holzapfel G. a, 2008, "A new constitutive model for multi-layered collagenous tissues.," J. Biomech., **41**(12), pp. 2766–71.

[96] Kroon M., 2010, "A numerical framework for material characterisation of inhomogeneous hyperelastic membranes by inverse analysis," J. Comput. Appl. Math., **234**(2), pp. 563–578.

[97] Lu J., and Zhao X., 2009, "Pointwise Identification of Elastic Properties in Nonlinear Hyperelastic Membranes—Part I: Theoretical and Computational Developments," J. Appl. Mech., **76**(6), p. 061013.

[98] Zhao X., Chen X., and Lu J., 2009, "Pointwise Identification of Elastic Properties in Nonlinear Hyperelastic Membranes—Part II: Experimental Validation," J. Appl. Mech., **76**(6), p. 061014.

[99] Zhao X., Raghavan M. L., and Lu J., 2011, "Identifying heterogeneous anisotropic properties in cerebral aneurysms: a pointwise approach.," Biomech. Model. Mechanobiol., **10**(2), pp. 177–89.

[100] Chen K., Fata B., and Einstein D. R., 2008, "Characterization of the highly nonlinear and anisotropic vascular tissues from experimental inflation data: a validation study toward the use of clinical data for in-vivo modeling and analysis.," Ann. Biomed. Eng., **36**(10), pp. 1668–80.

[101] Einstein D. R., Freed A. D., Stander N., Fata B., and Vesely I., 2005, "Inverse parameter fitting of biological tissues: a response surface approach.," Ann. Biomed. Eng., **33**(12), pp. 1819–30.

[102] Kyriacou S. K., Shah A. D., and Humphrey J. D., 1997, "Inverse Finite Element Characterization of Nonlinear Hyperelastic Membranes," J. Appl. Mech., **64**(2), p. 257.

[103] Kyriacou S. K., Humphrey J. D., and Schwab C., 1996, "Finite element analysis of nonlinear orthotropic hyperelastic membranes," Comput. Mech., **18**(4), pp. 269–278.

[104] Kyriacou S. K., and Humphrey J. D., 1996, "Influence of size, shape and properties on the mechanics of axisymmetric saccular aneurysms," J. Biomech., **29**(8), pp. 1015–1022.

[105] Humphrey J. D., Kang T., Sakarda P., and Anjanappa M., 1993, "Computer-aided vascular experimentation: a new electromechanical test system.," Ann. Biomed. Eng., **21**(1), pp. 33–43.

[106] Humphrey J. D., and Na S., 2002, "Elastodynamics and Arterial Wall Stress," Ann. Biomed. Eng., **30**(4), pp. 509–523.

[107] Nielsen P. M. F., Malcolm D. T. K., Hunter P. J., and Charette P. G., 2002, "Instrumentation and procedures for estimating the constitutive parameters of inhomogeneous elastic membranes.," Biomech. Model. Mechanobiol., **1**(3), pp. 211–8.

[108] Malcolm D. T. K., Nielsen P. M. F., Hunter P. J., and Charette P. G., 2002, "Strain measurement in biaxially loaded inhomogeneous, anisotropic elastic membranes.," Biomech. Model. Mechanobiol., **1**(3), pp. 197–210.

[109] Flynn C., Taberner A. J., Nielsen P. M. F., and Fels S., 2013, "Simulating the three-dimensional deformation of in vivo facial skin.," J. Mech. Behav. Biomed. Mater., **28**, pp. 484–94.

[110] Flynn C., Taberner A., and Nielsen P., 2011, "Modeling the mechanical response of in vivo human skin under a rich set of deformations.," Ann. Biomed. Eng., **39**(7), pp. 1935–46.

[111] Flynn D. M., Peura G. D., Grigg P., and Hoffman a H., 1998, "A finite element based method to determine the properties of planar soft tissue.," J. Biomech. Eng., **120**(2), pp. 202–10.

[112] Cox M. a J., Driessen N. J. B., Bouten C. V. C., and Baaijens F. P. T., 2006, "Mechanical characterization of anisotropic planar biological soft tissues using large indentation: a computational feasibility study.," J. Biomech. Eng., **128**(3), pp. 428–36.

[113] Raghupathy R., and Barocas V. H., 2010, "Generalized anisotropic inverse mechanics for soft tissues.," J. Biomech. Eng., **132**(8), p. 081006.

[114] Sacks M. S., 2001, "Biaxial Mechanical Evaluation of Planar Biological Materials," pp. 199–246.

[115] Raghupathy R., 2011, "Form from Function: Generalized Anisotropic Inverse Mechanics for Soft Tissues," University of Minnesota.

[116] Raghupathy R., Witzenburg C., Lake S. P., Sander E. A., and Barocas V. H., 2011, "Identification of regional mechanical anisotropy in soft tissue analogs.," J. Biomech. Eng., **133**(9), p. 091011.

[117] Ott H. C., Matthiesen T. S., Goh S.-K., Black L. D., Kren S. M., Netoff T. I., and Taylor D. a, 2008, "Perfusion-decellularized matrix: using nature's platform to engineer a bioartificial heart.," Nat. Med., **14**(2), pp. 213–21.

[118] Wainwright J. M., Czajka C. a, Patel U. B., Freytes D. O., Tobita K., Gilbert T. W., and Badylak S. F., 2010, "Preparation of cardiac extracellular matrix from an intact porcine heart.," Tissue Eng. Part C. Methods, **16**(3), pp. 525–32.

[119] Weymann A., Loganathan S., Takahashi H., Schies C., Claus B., Hirschberg K., Soós P., Korkmaz S., Schmack B., Karck M., and Szabó G., 2011, "Development and Evaluation of a Perfusion Decellularization Porcine Heart Model," Circ. J., **75**(4), pp. 852–860.

[120] Emery J. L., Omens J. H., and McCulloch A. D., 1997, "Biaxial mechanics of the passively overstretched left ventricle.," Am. J. Physiol., **272**(5 Pt 2), pp. H2299–305.

[121] Fomovsky G. M., Thomopoulos S., and Holmes J. W., 2010, "Contribution of extracellular matrix to the mechanical properties of the heart.," J. Mol. Cell. Cardiol., **48**(3), pp. 490–6.

[122] Cowin S. C., and Mehrabadi M. M., 1995, "Anisotropic Symmetries of Linear Elasticity," Appl. Mech. Rev., **48**(5), pp. 247–285.

[123] Thomson W., 1856, "Elements of a Mathematical Theory of Elasticity," Philos. Trans. R. Soc. London, **146**, pp. 481–498.

[124] Raghupathy R., and Barocas V. H. V., 2009, "A closed-form structural model of planar fibrous tissue mechanics," J. Biomech., **42**(10), pp. 1424–1428.

[125] Wang B., Borazjani A., Tahai M., Curry A. L. D. J., Simionescu D. T., Guan J., To F., Elder S. H., and Liao J., 2010, "Fabrication of cardiac patch with decellularized porcine myocardial scaffold and bone marrow mononuclear cells.," J. Biomed. Mater. Res. A, **94**(4), pp. 1100–10.

[126] Costa K. D., Holmes J. W., and Mcculloch A. D., 2001, "Modelling cardiac mechanical properties in three dimensions," Philos. Trans. R. Soc. A Math. Phys. Eng. Sci., **359**(1783), pp. 1233–1250.

[127] Salton C. J., Chuang M. L., O'Donnell C. J., Kupka M. J., Larson M. G., Kissinger K. V, Edelman R. R., Levy D., and Manning W. J., 2002, "Gender differences and normal left ventricular anatomy in an adult population free of hypertension. A cardiovascular magnetic resonance study of the Framingham Heart Study Offspring cohort.," J. Am. Coll. Cardiol., **39**(6), pp. 1055–60.

[128] Capasso J. M., Remily R. M., Smith R. H., and Sonnenblick E. H., 1983, "Sex differences in myocardial contractility in the rat.," Basic Res. Cardiol., **78**(2), pp. 156–71.

[129] Witzenburg C., Raghupathy R., Kren S. M., Taylor D. a, and Barocas V. H., 2012, "Mechanical changes in the rat right ventricle with decellularization.," J. Biomech., **45**(5), pp. 842–9.

[130] Sander E. a, and Barocas V. H., 2009, "Comparison of 2D fiber network orientation measurement methods.," J. Biomed. Mater. Res. A, **88**(2), pp. 322–31.

[131] Lake S. P., Miller K. S., Elliott D. M., and Soslowsky L. J., 2010, "Tensile properties and fiber alignment of human supraspinatus tendon in the transverse direction demonstrate inhomogeneity, nonlinearity, and regional isotropy.," J. Biomech., **43**(4), pp. 727–32.

[132] Lake S. P., Miller K. S., Elliott D. M., and Soslowsky L. J., 2009, "Effect of fiber distribution and realignment on the nonlinear and inhomogeneous mechanical properties of human supraspinatus tendon under longitudinal tensile loading.," J. Orthop. Res., **27**(12), pp. 1596–602.

[133] Fata B., Carruthers C. a, Gibson G., Watkins S. C., Gottlieb D., Mayer J. E., and Sacks M. S., 2013, "Regional structural and biomechanical alterations of the ovine main pulmonary artery during postnatal growth.," J. Biomech. Eng., **135**(2), p. 021022.

[134] Williams M. J., Utzinger U., Barkmeier-Kraemer J. M., and Vande Geest J. P., 2014, "Differences in the microstructure and biomechanical properties of the recurrent laryngeal nerve as a function of age and location.," J. Biomech. Eng., **136**(8), pp. 1–9.

[135] Clark N. R., Reichek N., Bergey P., Hoffman E. a., Brownson D., Palmon L., and Axel L., 1991, "Circumferential myocardial shortening in the normal human left ventricle. Assessment by magnetic resonance imaging using spatial modulation of magnetization," Circulation, **84**(1), pp. 67–74.

[136] Quinn K. P., and Winkelstein B. a, 2011, "Detection of altered collagen fiber alignment in the cervical facet capsule after whiplash-like joint retraction.," Ann. Biomed. Eng., **39**(8), pp. 2163–73.

[137] Novak V. P., Yin F. C. P., and Humphrey J. D., 1994, "Regional mechanical properties of passive myocardium," J. Biomech., **27**(4), pp. 403–412.

[138] Jor J. W. Y., Parker M. D., Taberner A. J., Nash M. P., and Nielsen P. M. F., 2013, "Computational and experimental characterization of skin mechanics: identifying current challenges and future directions.," Wiley Interdiscip. Rev. Syst. Biol. Med., **5**(5), pp. 539–56.

[139] Chao C. Y. L., Ng G. Y. F., Cheung K.-K., Zheng Y.-P., Wang L.-K., and Cheing G. L. Y., 2013, "In vivo and ex vivo approaches to studying the biomechanical properties of healing wounds in rat skin.," J. Biomech. Eng., **135**(10), pp. 101009–8.

[140] Booth A. J., Hadley R., Cornett A. M., Dreffs A. a, Matthes S. a, Tsui J. L., Weiss K., Horowitz J. C., Fiore V. F., Barker T. H., Moore B. B., Martinez F. J.,

Niklason L. E., and White E. S., 2012, “Acellular normal and fibrotic human lung matrices as a culture system for in vitro investigation.,” Am. J. Respir. Crit. Care Med., **186**(9), pp. 866–76.

[141] Liu F., Mih J. D., Shea B. S., Kho A. T., Sharif A. S., Tager A. M., and Tschumperlin D. J., 2010, “Feedback amplification of fibrosis through matrix stiffening and COX-2 suppression.,” J. Cell Biol., **190**(4), pp. 693–706.

[142] Lyshchik A., Higashi T., Asato R., Tanaka S., Ito J., Hiraoka M., Insana M. F., Brill A. B., Saga T., and Togashi K., 2007, “Cervical lymph node metastases: diagnosis at sonoelastography--initial experience.,” Radiology, **243**(1), pp. 258–67.

[143] Ophir J., Cespedes I., Garra B., Ponnekanti H., Huang Y., and Maklad N., 1996, “Elastography: Ultrasonic imaging of tissue strain and elastic modulus in vivo,” Eur. J. Ultrasound, **3**(1), pp. 49–70.

[144] Gilchrist C. L., Xia J. Q., Setton L. A., and Hsu E. W., 2004, “High-Resolution Determination of Soft Tissue Deformations Using MRI and First-Order Texture Correlation,” IEEE Trans. Med. Imaging, **23**(5), pp. 546–553.

[145] Perumpail R. B., Levitsky J., Wang Y., Lee V. S., Jin N., Yang G., Jr B. D. B., Miller F. H., and Omary R. A., 2013, “Elastography Stiffness Readings in Liver Transplants,” **19**(9), pp. 1121–1126.

[146] Manduca a, Oliphant T. E., Dresner M. a, Mahowald J. L., Kruse S. a, Amromin E., Felmlee J. P., Greenleaf J. F., and Ehman R. L., 2001, “Magnetic resonance elastography: non-invasive mapping of tissue elasticity.,” Med. Image Anal., **5**(4), pp. 237–54.

[147] Sinkus R., Tanter M., Bercoff J., Siegmann K., Pernot M., Athanasiou a., and Fink M., 2008, “Potential of MRI and Ultrasound Radiation Force in Elastography: Applications to Diagnosis and Therapy,” Proc. IEEE, **96**(3), pp. 490–499.

[148] Hoeks A. P., Brands P. J., Willigers J. M., and Reneman R. S., 1999, “Non-invasive measurement of mechanical properties of arteries in health and disease.,” Proc. Inst. Mech. Eng. H., **213**(3), pp. 195–202.

[149] Hoit B. D., 2011, “Strain and strain rate echocardiography and coronary artery disease.,” Circ. Cardiovasc. Imaging, **4**(2), pp. 179–90.

[150] Goffinet C., and Vanoverschelde J., 2007, “Speckle Tracking Echocardiography,” Eur. Cardiol. Rev., **3**(1), pp. 1–3.

[151] Helle-Valle T., Crosby J., Edvardsen T., Lyseggen E., Amundsen B. H., Smith H.-J., Rosen B. D., Lima J. a C., Torp H., Ihlen H., and Smiseth O. a, 2005, "New noninvasive method for assessment of left ventricular rotation: speckle tracking echocardiography.," Circulation, **112**(20), pp. 3149–56.

[152] Tseng L., and Li P., 2011, "3D cardiac strain imaging using plane wave excitation and feature tracking," 2011 IEEE International Ultrasonics Symposium, IEEE, pp. 740–743.

[153] Parker K. M., Clark A. P., Goodman N. C., Glover D. K., and Holmes J. W., 2014, "Comparison of Quantitative Wall-Motion Analysis and Strain for Detection of Coronary Stenosis with Three-Dimensional Dobutamine Stress Echocardiography.," Echocardiography, pp. 1–12.

[154] Götte M. J. W., Germans T., Rüssel I. K., Zwanenburg J. J. M., Marcus J. T., van Rossum A. C., and van Veldhuisen D. J., 2006, "Myocardial strain and torsion quantified by cardiovascular magnetic resonance tissue tagging: studies in normal and impaired left ventricular function.," J. Am. Coll. Cardiol., **48**(10), pp. 2002–11.

[155] Gorcsan J., Gulati V. K., Mandarino W. a, and Katz W. E., 1996, "Color-coded measures of myocardial velocity throughout the cardiac cycle by tissue Doppler imaging to quantify regional left ventricular function.," Am. Heart J., **131**(6), pp. 1203–13.

[156] Spotnitz H. M., 2000, "Macro design, structure, and mechanics of the left ventricle.," J. Thorac. Cardiovasc. Surg., **119**(5), pp. 1053–77.

[157] Levinson S. F., and Shinagawat M., 1995, "0021-9290(94)00173-l," **28**(10), pp. 1145–1154.

[158] Pan B., Qian K., Xie H., and Asundi A., 2009, "Two-dimensional digital image correlation for in-plane displacement and strain measurement: a review," Meas. Sci. Technol., **20**(6), p. 062001.

[159] Sutton M. A., Orteu J. J., and Schreier H. W., 2009, Image correlation for shape, motion and deformation measurements: basic concepts, theory and applications, Springer New York, New York.

[160] Kelly D. J., Azeloglu E. U., Kochupura P. V, Sharma G. S., and Gaudette G. R., 2007, "Accuracy and reproducibility of a subpixel extended phase correlation method to determine micron level displacements in the heart.," Med. Eng. Phys., **29**(1), pp. 154–62.

[161] Quinn K. P., and Winkelstein B. a, 2010, “Full field strain measurements of collagenous tissue by tracking fiber alignment through vector correlation.,” J. Biomech., **43**(13), pp. 2637–40.

[162] Rogowska J., 2004, “Optical coherence tomographic elastography technique for measuring deformation and strain of atherosclerotic tissues,” Heart, **90**(5), pp. 556–562.

[163] Kennedy B. F., Kennedy K. M., and Sampson D. D., 2014, “A Review of Optical Coherence Elastography: Fundamentals, Techniques and Prospects,” IEEE J. Sel. Top. Quantum Electron., **20**(2), pp. 272–288.

[164] Liu Y., Sun L. Z., and Wang G., 2005, “Tomography-based 3-D anisotropic elastography using boundary measurements.,” IEEE Trans. Med. Imaging, **24**(10), pp. 1323–33.

[165] Plewes D. B., Bishop J., Samani A., and Sciarretta J., 2000, “Visualization and quantification of breast cancer biomechanical properties with magnetic resonance elastography.,” Phys. Med. Biol., **45**(6), pp. 1591–610.

[166] Kallel F., and Bertrand M., 1996, “Tissue elasticity reconstruction using linear perturbation method.,” IEEE Trans. Med. Imaging, **15**(3), pp. 299–313.

[167] Girard M. J. A., Downs J. C., Bottlang M., Burgoyne C. F., and Suh J. F., 2009, “Peripapillary and posterior scleral mechanics--part II: experimental and inverse finite element characterization.,” J. Biomech. Eng., **131**(5), p. 051012.

[168] Newman M. E. J., 2004, “Analysis of weighted networks.,” Phys. Rev. E. Stat. Nonlin. Soft Matter Phys., **70**(5 Pt 2), p. 056131.

[169] Newman M. E. J., 2001, “Scientific collaboration networks. II. Shortest paths, weighted networks, and centrality,” Phys. Rev. E, **64**(1), p. 016132.

[170] Billiar K. L., and Sacks M. S., 2000, “Biaxial mechanical properties of the native and glutaraldehyde-treated aortic valve cusp: Part II--A structural constitutive model.,” J. Biomech. Eng., **122**(4), pp. 327–35.

[171] Nagel T. M., 2014, “Mechanics of the Annulus Fibrosus Lamellae Under Physiologic Loading Conditions,” University of Minnesota.

[172] Ma Z., Koo S., Finnegan M. a, Loskill P., Huebsch N., Marks N. C., Conklin B. R., Grigoropoulos C. P., and Healy K. E., 2014, “Three-dimensional filamentous human diseased cardiac tissue model.,” Biomaterials, **35**(5), pp. 1367–77.

[173] Lian X., Hsiao C., Wilson G., Zhu K., Hazeltine L. B., Azarin S. M., Raval K. K., Zhang J., Kamp T. J., and Palecek S. P., 2012, "Robust cardiomyocyte differentiation from human pluripotent stem cells via temporal modulation of canonical Wnt signaling.," Proc. Natl. Acad. Sci. U. S. A., **109**(27), pp. E1848–57.

[174] O'Connell G. D., Johannessen W., Vresilovic E. J., and Elliott D. M., 2007, "Human internal disc strains in axial compression measured noninvasively using magnetic resonance imaging.," Spine (Phila. Pa. 1976)., **32**(25), pp. 2860–8.

[175] Chandran P. L., and Barocas V. H., 2004, "Microstructural Mechanics of Collagen Gels in Confined Compression: Poroelasticity, Viscoelasticity, and Collapse," J. Biomech. Eng., **126**(2), p. 152.

[176] Al-Qaisi M. K., and Akkin T., 2008, "Polarization-sensitive optical coherence tomography based on polarization-maintaining fibers and frequency multiplexing.," Opt. Express, **16**(17), pp. 13032–41.

[177] Casper A. J., Liu D., Ballard J. R., and Ebbini E. S., 2013, "Real-time implementation of a dual-mode ultrasound array system: in vivo results.," IEEE Trans. Biomed. Eng., **60**(10), pp. 2751–9.

[178] Jiang J., and Hall T. J., 2009, "A generalized speckle tracking algorithm for ultrasonic strain imaging using dynamic programming.," Ultrasound Med. Biol., **35**(11), pp. 1863–79.

[179] He X., and Bischof J. C., 2003, "Quantification of temperature and injury response in thermal therapy and cryosurgery.," Crit. Rev. Biomed. Eng., **31**(5-6), pp. 355–422.

[180] Zhang J., Sandison G. a., Murthy J. Y., and Xu L. X., 2005, "Numerical Simulation for Heat Transfer in Prostate Cancer Cryosurgery," J. Biomech. Eng., **127**(2), p. 279.

[181] Szczesny S. E., Peloquin J. M., Cortes D. H., Kadlowec J. a, Soslowsky L. J., and Elliott D. M., 2012, "Biaxial tensile testing and constitutive modeling of human supraspinatus tendon.," J. Biomech. Eng., **134**(2), p. 021004.

[182] Huang C.-Y., Wang V. M., Pawluk R. J., Bucchieri J. S., Levine W. N., Bigliani L. U., Mow V. C., and Flatow E. L., 2005, "Inhomogeneous mechanical behavior of the human supraspinatus tendon under uniaxial loading.," J. Orthop. Res., **23**(4), pp. 924–30.

[183] Pasta S., Phillippi J. a, Gleason T. G., and Vorp D. a, 2012, "Effect of aneurysm on the mechanical dissection properties of the human ascending thoracic aorta.," J. Thorac. Cardiovasc. Surg., **143**(2), pp. 460–7.

[184] Tönük E., and Silver-Thorn M. B., 2003, "Nonlinear elastic material property estimation of lower extremity residual limb tissues.," IEEE Trans. Neural Syst. Rehabil. Eng., **11**(1), pp. 43–53.

[185] Masson I., Boutouyrie P., Laurent S., Humphrey J. D., and Zidi M., 2008, "Characterization of arterial wall mechanical behavior and stresses from human clinical data.," J. Biomech., **41**(12), pp. 2618–27.

[186] Baek S., Gleason R. L., Rajagopal K. R., and Humphrey J. D., 2007, "Theory of small on large: Potential utility in computations of fluid–solid interactions in arteries," Comput. Methods Appl. Mech. Eng., **196**(31-32), pp. 3070–3078.

[187] Gleason R. L., Dye W. W., Wilson E., and Humphrey J. D., 2008, "Quantification of the mechanical behavior of carotid arteries from wild-type, dystrophin-deficient, and sarcoglycan-delta knockout mice.," J. Biomech., **41**(15), pp. 3213–8.

[188] Wan W., Yanagisawa H., and Gleason R. L., 2010, "Biomechanical and microstructural properties of common carotid arteries from fibulin-5 null mice.," Ann. Biomed. Eng., **38**(12), pp. 3605–17.

[189] Sokolis D. P., Sassani S., Kritharis E. P., and Tsangaris S., 2011, "Differential histomechanical response of carotid artery in relation to species and region: mathematical description accounting for elastin and collagen anisotropy.," Med. Biol. Eng. Comput., **49**(8), pp. 867–79.

[190] Di Achille P., Celi S., Di Puccio F., and Forte P., 2011, "Anisotropic AAA: computational comparison between four and two fiber family material models.," J. Biomech., **44**(13), pp. 2418–26.

[191] Eberth J. F., Taucer a I., Wilson E., and Humphrey J. D., 2009, "Mechanics of carotid arteries in a mouse model of Marfan Syndrome.," Ann. Biomed. Eng., **37**(6), pp. 1093–104.

[192] Wicker B. K., Hutchens H. P., Wu Q., Yeh a T., and Humphrey J. D., 2008, "Normal basilar artery structure and biaxial mechanical behaviour.," Comput. Methods Biomech. Biomed. Engin., **11**(5), pp. 539–51.

[193] Khalsa P. S., Hoffman a H., and Grigg P., 1996, "Mechanical states encoded by stretch-sensitive neurons in feline joint capsule.," J. Neurophysiol., **76**(1), pp. 175–87.

[194] Sacks M. S., 2014, “Engineering A Method for Planar Biaxial Mechanical Testing That Includes In-Plane Shear e,” **121**(October 1999), pp. 551–555.

[195] Humphrey J. D., 2002, Cardiovascular Solid Mechanics: Cells, Tissues, and Organs.

[196] Hiltner A., Cassidy J. J., and Baer E., 1985, “Mechanical Properties of Biological Polymers,” Annu. Rev. Mater. Sci., **15**(1), pp. 455–482.

[197] Avanzini A., Battini D., Bagozzi L., and Bisleri G., 2014, “Biomechanical evaluation of ascending aortic aneurysms.,” Biomed Res. Int., p. 820385.

[198] Vorp D. a, Schiro B. J., Ehrlich M. P., Juvonen T. S., Ergin M. A., and Griffith B. P., 2003, “Effect of aneurysm on the tensile strength and biomechanical behavior of the ascending thoracic aorta.,” Ann. Thorac. Surg., **75**(4), pp. 1210–4.

[199] Sommer G., Gasser T. C., Regitnig P., Auer M., and Holzapfel G. a, 2008, “Dissection properties of the human aortic media: an experimental study.,” J. Biomech. Eng., **130**(2), p. 021007.

[200] Tong J., Sommer G., Regitnig P., and Holzapfel G. a, 2011, “Dissection properties and mechanical strength of tissue components in human carotid bifurcations.,” Ann. Biomed. Eng., **39**(6), pp. 1703–19.

[201] Elefteriades J. a, 2002, “Natural history of thoracic aortic aneurysms: indications for surgery, and surgical versus nonsurgical risks.,” Ann. Thorac. Surg., **74**(5), pp. S1877–80; discussion S1892–8.

[202] Bonnichsen C. R., Sundt T. M., Anavekar N. S., Foley T. A., Morris M. F., Martinez M. W., Williamson E. E., Glockner J. F., and Araoz P. A., 2011, “Aneurysms of the ascending aorta and arch: the role of imaging in diagnosis and surgical management.,” Expert Rev. Cardiovasc. Ther., **9**(1), pp. 45–61.

[203] Guo D., Hasham S., Kuang S.-Q., Vaughan C. J., Boerwinkle E., Chen H., Abuelo D., Dietz H. C., Basson C. T., Shete S. S., and Milewicz D. M., 2001, “Familial Thoracic Aortic Aneurysms and Dissections : Genetic Heterogeneity With a Major Locus Mapping to 5q13-14,” Circulation, **103**(20), pp. 2461–2468.

[204] Clouse W. D., Hallett J. W., Schaff H. V., Spittell P. C., Rowland C. M., Ilstrup D. M., and Melton L. J., 2004, “Acute aortic dissection: population-based incidence compared with degenerative aortic aneurysm rupture.,” Mayo Clin. Proc., **79**(2), pp. 176–80.

[205] Tam a S., Sapp M. C., and Roach M. R., 1998, "The effect of tear depth on the propagation of aortic dissections in isolated porcine thoracic aorta.," J. Biomech., **31**(7), pp. 673–6.

[206] Guan J., Chu B., Zhang Y., Zeng K., and Qiao A., 2010, "Three-Dimensional Computational Simulation of Bypassed Aortic Dissection," 2010 International Conference on Biomedical Engineering and Computer Science, IEEE, pp. 1–4.

[207] Gasser T. C., and Holzapfel G. A., 2006, "Modeling the propagation of arterial dissection," Eur. J. Mech. - A/Solids, **25**(4), pp. 617–633.

[208] Li B., 2013, "Mathematical Modelling of Aortic Dissection," University of Glasgow.

[209] Lai V. K., Lake S. P., Frey C. R., Tranquillo R. T., and Barocas V. H., 2012, "Mechanical behavior of collagen-fibrin co-gels reflects transition from series to parallel interactions with increasing collagen content.," J. Biomech. Eng., **134**(1), p. 011004.

[210] Stylianopoulos T., and Barocas V. H., 2007, "Multiscale, structure-based modeling for the elastic mechanical behavior of arterial walls.," J. Biomech. Eng., **129**(4), pp. 611–8.

[211] Hadi M., 2012, "Multiscale model predicts tissue-level failure from collagen fiber-level damage," J. Biomech. Eng., **134**(9), pp. 1–24.

[212] Chandran P. L., and Barocas V. H., 2007, "Deterministic material-based averaging theory model of collagen gel micromechanics.," J. Biomech. Eng., **129**(2), pp. 137–47.

[213] Hurschler C., Loitz-Ramage B., and Vanderby R., 1997, "A structurally based stress-stretch relationship for tendon and ligament.," J. Biomech. Eng., **119**(4), pp. 392–9.

[214] Driessen N. J. B., Bouten C. V. C., and Baaijens F. P. T., 2005, "A Structural Constitutive Model For Collagenous Cardiovascular Tissues Incorporating the Angular Fiber Distribution," J. Biomech. Eng., **127**(3), p. 494.

[215] Timmins L. H., Wu Q., Yeh A. T., Moore J. E., and Greenwald S. E., 2010, "Structural inhomogeneity and fiber orientation in the inner arterial media.," Am. J. Physiol. Heart Circ. Physiol., **298**(5), pp. H1537–45.

[216] Hoffman A. S., Grande L. A., and Park J. B., 1977, "Sequential enzymolysis of human aorta and resultant stress-strain behavior.," Biomater. Med. Devices. Artif. Organs, **5**(2), pp. 121–45.

[217] Haskett D., Johnson G., Zhou A., Utzinger U., and Vande Geest J., 2010, "Microstructural and biomechanical alterations of the human aorta as a function of age and location.," Biomech. Model. Mechanobiol., **9**(6), pp. 725–36.

[218] Haslach H. W., 2010, Maximum Dissipation Non-Equilibrium Thermodynamics and its Geometric Structure, Springer New York, New York, NY.

[219] Winlove, C. P., and Parker K. H., 1987, "The Influence of the Elastin Lamellae on Mass Transport in the Arterial Wall," Adv. Microcirc., **13**, pp. 74–81.

[220] Roach M. R., and Burton A. C., 1957, "The reason for the shape of the distensibility curves of arteries.," Can. J. Biochem. Physiol., **35**(8), pp. 681–90.

[221] Han H. C., and Fung Y. C., 1991, "Species dependence of the zero-stress state of aorta: pig versus rat.," J. Biomech. Eng., **113**(4), pp. 446–51.

[222] Alford P. W., and Taber L. A., 2008, "Computational study of growth and remodelling in the aortic arch.," Comput. Methods Biomech. Biomed. Engin., **11**(5), pp. 525–38.

[223] Gregory D. E., Veldhuis J. H., Horst C., Wayne Brodland G., and Callaghan J. P., 2011, "Novel lap test determines the mechanics of delamination between annular lamellae of the intervertebral disc.," J. Biomech., **44**(1), pp. 97–102.

[224] Iliopoulos D. C., Deveja R. P., Kritharis E. P., Perrea D., Sionis G. D., Toutouzas K., Stefanadis C., and Sokolis D. P., 2009, "Regional and directional variations in the mechanical properties of ascending thoracic aortic aneurysms.," Med. Eng. Phys., **31**(1), pp. 1–9.

[225] García-Herrera C. M., Atienza J. M., Rojo F. J., Claes E., Guinea G. V, Celentano D. J., García-Montero C., and Burgos R. L., 2012, "Mechanical behaviour and rupture of normal and pathological human ascending aortic wall.," Med. Biol. Eng. Comput., **50**(6), pp. 559–66.

[226] Nicosia M. A., Kasalko J. S., Cochran R. P., Einstein D. R., and Kunzelman K. S., 2002, "Biaxial mechanical properties of porcine ascending aortic wall tissue.," J. Heart Valve Dis., **11**(5), pp. 680–6; discussion 686–7.

[227] Pins G. D., Huang E. K., Christiansen D. L., and Silver F. H., 1997, "Effects of static axial strain on the tensile properties and failure mechanisms of self-assembled collagen fibers," J. Appl. Polym. Sci., **63**(11), pp. 1429–1440.

[228] Okamoto R. J., Xu H., Kouchoukos N. T., Moon M. R., and Sundt T. M., 2003, "The influence of mechanical properties on wall stress and distensibility of the dilated ascending aorta," J. Thorac. Cardiovasc. Surg., **126**(3), pp. 842–850.

[229] Mukherjee D. P., Kagan H. M., Jordan R. E., and Franzblau C., 1976, "Effect of hydrophobic elastin ligands on the stress-strain properties of elastin fibers.," Connect. Tissue Res., **4**(3), pp. 177–9.

[230] Koenders M. M. J. F., Yang L., Wismans R. G., van der Werf K. O., Reinhardt D. P., Daamen W., Bennink M. L., Dijkstra P. J., van Kuppevelt T. H., and Feijen J., 2009, "Microscale mechanical properties of single elastic fibers: the role of fibrillin-microfibrils.," Biomaterials, **30**(13), pp. 2425–32.

[231] Wenger M. P. E., Bozec L., Horton M. a, and Mesquida P., 2007, "Mechanical properties of collagen fibrils.," Biophys. J., **93**(4), pp. 1255–63.

[232] Van Baardwijk C., and Roach M. R., 1987, "Factors in the propagation of aortic dissections in canine thoracic aortas.," J. Biomech., **20**(1), pp. 67–73.

[233] Rhodin J. A. G., 1979, "Architecture of the Vessel Wall," Handbook of Physiology, R.M. Berne, ed.

[234] Snowhill P. B., Foran D. J., and Silver F. H., 2004, "A Mechanical Model of Porcine Vascular Tissues-Part I: Determination of Macromolecular Component Arrangement and Volume Fractions," Cardiovasc. Eng., **4**(4), pp. 281–294.

[235] MacLean N. F., Dudek N. L., and Roach M. R., 1999, "The role of radial elastic properties in the development of aortic dissections.," J. Vasc. Surg., **29**(4), pp. 703–10.

[236] Gleason R. L., Taber L. a., and Humphrey J. D., 2004, "A 2-D model of flow-induced alterations in the geometry, structure, and properties of carotid arteries.," J. Biomech. Eng., **126**(3), pp. 371–81.

[237] Mehrabadi M. M., and Cowin S. C., 1990, "Eigentensors of Linear Anisotropic Elastic Materials," Q. J. Mech. Appl. Math., **43**(1), pp. 15–41.

[238] Hughes T. J. R., 1987, The Finite Element Method: Linear Static and Dynamic Finite Element Analysis, Prentice-Hall, Englewood Cliffs, NJ.

[239] Witzenburg C., Vanderheiden S., Nagel T. M., Kren S. M., Taylor D. A., and Barocas V. H., 2012, "Sex Differences in the Mechanical Behavior of the Decellularized Rat Left Ventricle," ASME 2012 Summer Bioengineering Conference, Parts A and B, ASME, p. 1277.

Appendix A: Kelvin Moduli - Determining Stiffness and Anisotropy

For a general linear, elastic material the stress-strain relation is

$$\sigma_{ij} = C_{ijkl}\varepsilon_{kl} \tag{A.1}$$

where C is the symmetric fourth-order elasticity tensor, σ is the Cauchy stress, and ε is the linear strain. When the fourth-rank elasticity tensor, C, is compacted into a two-dimensional matrix using major and minor symmetries and then converted into a second-order tensor, $\hat{C}$, the relation becomes

$$\hat{\sigma}_i = \hat{C}_{ij}\hat{\varepsilon}_j \tag{A.2}$$

The eigenvalue problem of $\hat{C}$ is what Lord Kelvin [123] referred to as principal elasticities, and these represent symmetry states where $\hat{C}$ takes a strain $\hat{\epsilon}$ and produces a stress $\hat{\sigma}$ that is parallel to it [122,237].

$$\left(\hat{C}_{ij} - \Lambda\delta_{ij}\right)\hat{\varepsilon}_j = 0 \tag{A.3}$$

where the eigenvalues, Λ, are the so-called Kelvin moduli. For an isotropic material there is one eigentensor of dilatational mode, and two eigentensors of isochoric (distortional) mode. The largest Kelvin modulus is associated with the dilatational mode and can be converted into a Young's modulus, as done previously by Raghupathy [113]. For most soft tissues, materials with a single symmetric fiber distribution, the largest Kelvin modulus also corresponds to a dilatation mode [36]. Therefore, for this analysis, we use the largest Kelvin modulus, E_k, as a measurement of the stiffness of the tissue because it is related to a stretch in the direction of average fiber orientation.

The corresponding eigenvectors, (u, v, w), can be normalized and then projected back into tensor form as a strain eigentensor

$$\hat{\varepsilon} = \begin{bmatrix} u \\ v \\ w \end{bmatrix} \quad \longrightarrow \quad \varepsilon = \begin{bmatrix} u & \frac{w}{\sqrt{2}} \\ \frac{w}{\sqrt{2}} & v \end{bmatrix} \tag{A.4}$$

The strain eigentensor $\hat{\varepsilon}$ is a strain state and is used to determine the orientation of the material. If this strain state is applied to the material the stress produced is parallel to the strain. The principal directions (θ_1, θ_2) and principal values (λ_1, λ_2) of the strain eigentensor give a measure of the preferred fiber orientation, denoted θ, as well as the strength of alignment. Strength of alignment is indicated by an anisotropy index, denoted r, which is determined by the principal values of $\hat{\varepsilon}$, where $\lambda_1 > \lambda_2$.

$$r = \frac{|\lambda_1| - |\lambda_2|}{|\lambda_1| + |\lambda_2|} \tag{A.5}$$

The anisotropy index, r, gives a measure of the degree of alignment similar to the normalized retardation determined from quantitative polarized light imaging. The values of r vary from 0 for an isotropic sample to 1 for a perfectly aligned sample. For example, if the sample were orthotropic with $C_{1111} = 1\ MPa$, $C_{2222} = 2\ MPa$, and $C_{1212} = C_{1122} = 0.5\ MPa$ the resulting value of r would be 0.41.

Appendix B: Extension of the Inverse Matrix Formulation to Account for Nonlinear Kinematics

Consider a body (occupying domain Ω with boundary Γ) undergoing elastic deformation in the undeformed configuration. For a neo-Hookean material the 2nd Piola Kirchhoff stress is determined by equation 2.1, $S_{ij} = K_{ijkl}E_{kl}$, and the stress balance is given by equation 2.2, $\left(F_{mi}K_{ijkl}E_{kl}\right)_{,j} = 0$, where S is the 2nd Piola-Kirchhoff stress, E is the Green strain, F is the deformation gradient tensor, K is the neo-Hookean elasticity tensor (an elasticity tensor analogous to C in linear elasticity) and differentiation is with respect to the undeformed coordinates. Using the Galerkin finite element method [238], the weak form of equation 2.2 is

$$\int_{\Omega_0} \left(F_{mi}K_{ijkl}E_{kl}\right)_{,j} w_i \mathrm{d}\Omega_0 = 0 \qquad \text{B.1}$$

where w is the test function. The forces measured on the grip arms during biaxial testing are the combined reaction to the displacement of the sample boundary, essentially quantifying the integral of the force over the sample boundary. Therefore, it can be assumed that deformation is applied using a traction boundary condition such that

$$F_{mi}S_{ij}n_j = t_i \quad \text{on} \quad \Gamma_0 \qquad \text{B.2}$$

where n is the normal vector on the boundary and t is the prescribed traction vector at the boundary. Applying the traction boundary condition and integrating by parts yields

$$\int_{\Gamma_0} F_{mi}K_{ijkl}E_{kl}w_i n_j \mathrm{d}\Gamma_0 = \int_{\Omega_0} F_{mi}K_{ijkl}E_{kl}w_{i,j} \mathrm{d}\Omega_0 \qquad \text{B.3}$$

Substituting in the traction vector, t_i,

$$\int_{\Gamma_0} t_i w_i \mathrm{d}\Gamma_0 = \int_{\Omega_0} F_{mi}K_{ijkl}E_{kl}w_{i,j} \mathrm{d}\Omega_0 \qquad \text{B.4}$$

Using the Galerkin basis functions, N_A, for the test functions, the finite element discretized form is

$$\sum_e \left(\int_{\Gamma_0{}^e} t_i N_A \mathrm{d}\Gamma_0{}^e \right) = \sum_e \left(\int_{\Omega_0{}^e} F_{im} K_{mjqr} E_{qr} N_{A,j} \mathrm{d}\Omega_0{}^e \right) \quad \text{B.5}$$

where index A corresponds to the node in the finite element, and the summation denotes the assembly over all finite elements. Following [113,115], the goal of the GAIM method is to determine the component of the neo-Hookean elasticity tensor, K_{mjqr}, and their variation over the domain Ω_0. Assuming K_{mjqr} is constant over each element the equation is restated as a global linear matrix equation

$$\mathcal{F} = M\mathcal{K} \quad \text{B.6}$$

where, $\mathcal{K}$ is the column vector of K_{mjqr} components for all partitions, $\mathcal{F}$ is the assembled column vector of nodal forces (both tractions and reactions), and M is a matrix consisting of the terms that remain when the material parameter terms on the right hand side of equation B.5 are factored out. For two dimensions, the elemental $\mathcal{K}$ vector, denoted $\mathcal{K}^e$ is analogous to the elemental elasticity vector,

$$\mathcal{K}^e = [K_{1111}\ K_{2222}\ K_{1212}\ K_{2212}\ K_{1112}\ K_{1122}]^T \quad \text{B.7}$$

The elemental M matrix, denoted M^e, is given by

$$M^e = \left[M_1^e\ M_2^e\ \cdots\ M_{n_{en}}^e \right]^T \quad \text{B.8}$$

where n_{en} is the number of nodes in each element. Each M_A^e matrix is the integral of m_A^e over the element and represents the contribution to node A with m_A^e given by

$$m_A^e = \begin{bmatrix} F_1 N_{A,1} E_1 & F_3 N_{A,1} E_1 \\ F_2 N_{A,2} E_2 & F_4 N_{A,2} E_2 \\ \left(F_1 N_{A,2} E_3 + F_2 N_{A,1} E_3\right) & \left(F_3 N_{A,2} E_3 + F_4 N_{A,1} E_3\right) \\ \left(F_2 N_{A,2} E_3 + F_1 N_{A,2} E_2 + F_2 N_{A,1} E_2\right) & \left(F_4 N_{A,2} E_3 + F_3 N_{A,2} E_2 + F_4 N_{A,1} E_2\right) \\ \left(F_1 N_{A,1} E_3 + F_1 N_{A,2} E_1 + F_2 N_{A,1} E_1\right) & \left(F_3 N_{A,1} E_3 + F_3 N_{A,2} E_1 + F_4 N_{A,1} E_1\right) \\ \left(F_1 N_{A,1} E_2 + F_2 N_{A,2} E_1\right) & \left(F_3 N_{A,1} E_2 + F_4 N_{A,2} E_1\right) \end{bmatrix} \quad \text{B.9}$$

In obtaining equation B.9 we have used the fact that K_{mjqr} has the same major and minor symmetries as the linear elasticity tensor, collapsed the strain terms into a vector ($E_1 = E_{11},\ E_2 = E_{22},\ E_3 = 2E_{12}$), and collapsed the deformation gradient tensor terms into a vector ($F_1 = F_1,\ F_2 = F_{12},\ F_3 = F_{21},\ F_4 = F_{22}$). Equation B.6 is the nodal force balance and contributes one equation for each spatial dimension for every node.

Appendix C: Deformation Gradient Fields, Simulation Results, and Comparison with Existing Method for Automatic Segmentation Method

C.1 Deformation Gradient Fields

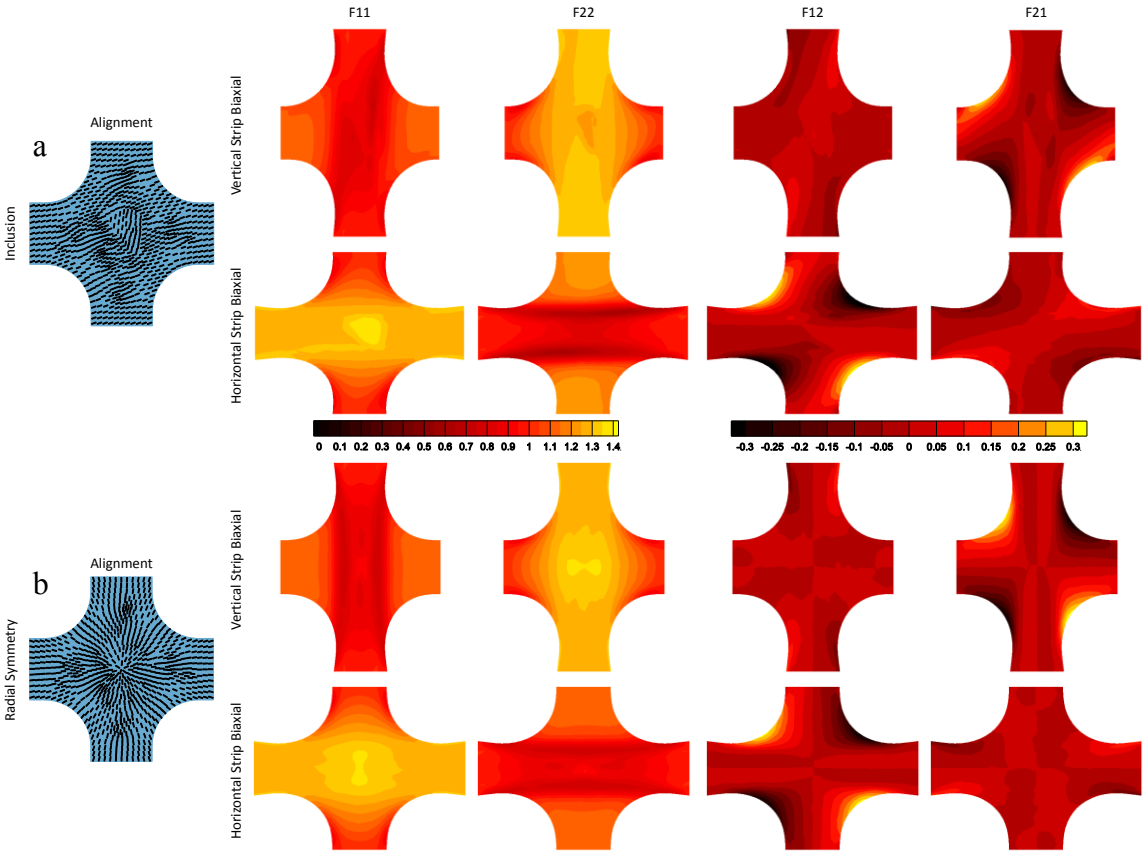

Figure C.1: Fiber alignment and full-field deformation gradient tensor components for strip biaxial extensions of (a) simulated sample with inclusion for which the inclusion varies only in prescribed fiber orientation (80^0 vs. 20^0) and (b) simulated radially symmetric sample for which the prescribed fiber orientation varied.

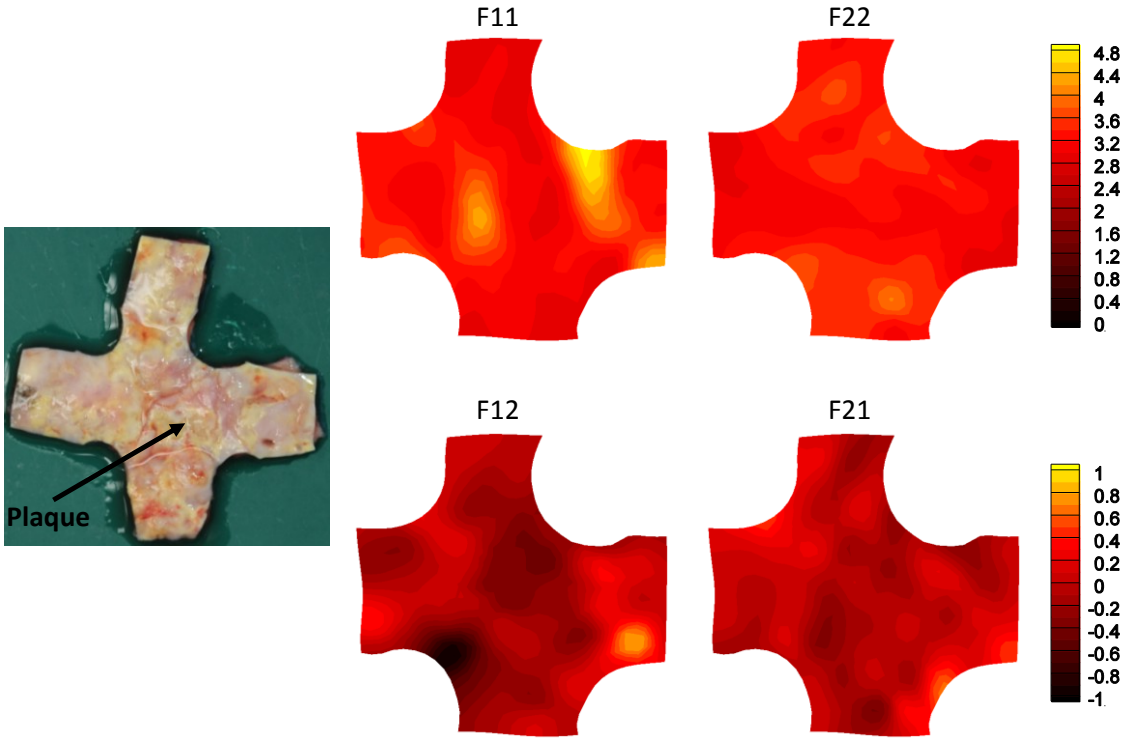

Figure C.2: Full-field deformation gradient tensor components for equibiaxial extension of aortic sample containing a large arteriosclerotic transmural plaque.

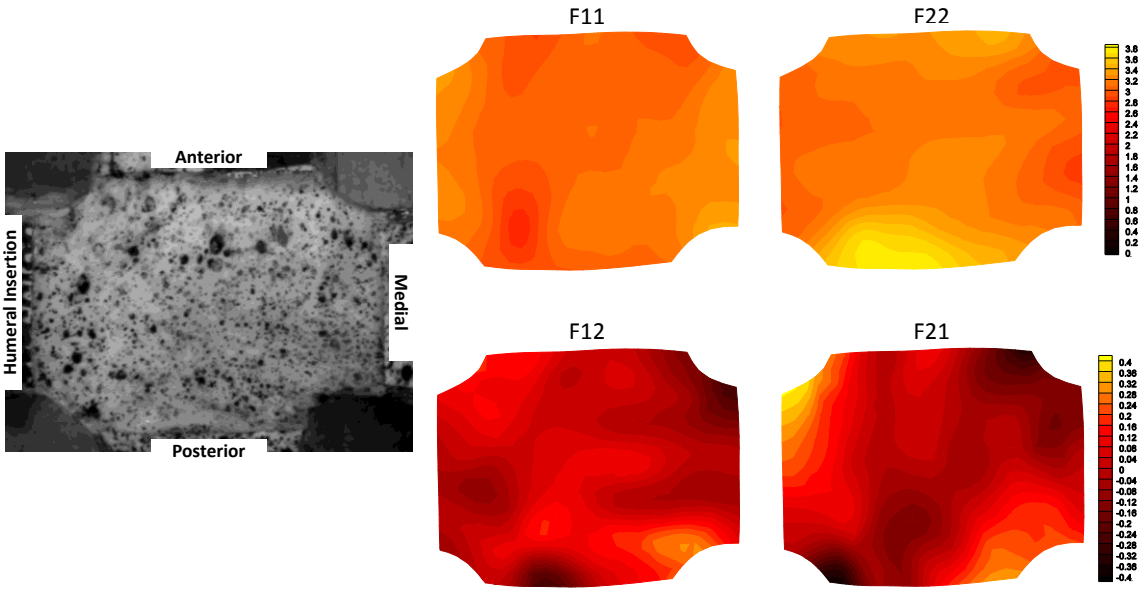

Figure C.3: Full-field deformation gradient tensor components for equibiaxial extension of supraspinatus tendon sample.

C.2 Results for Additional Simulations

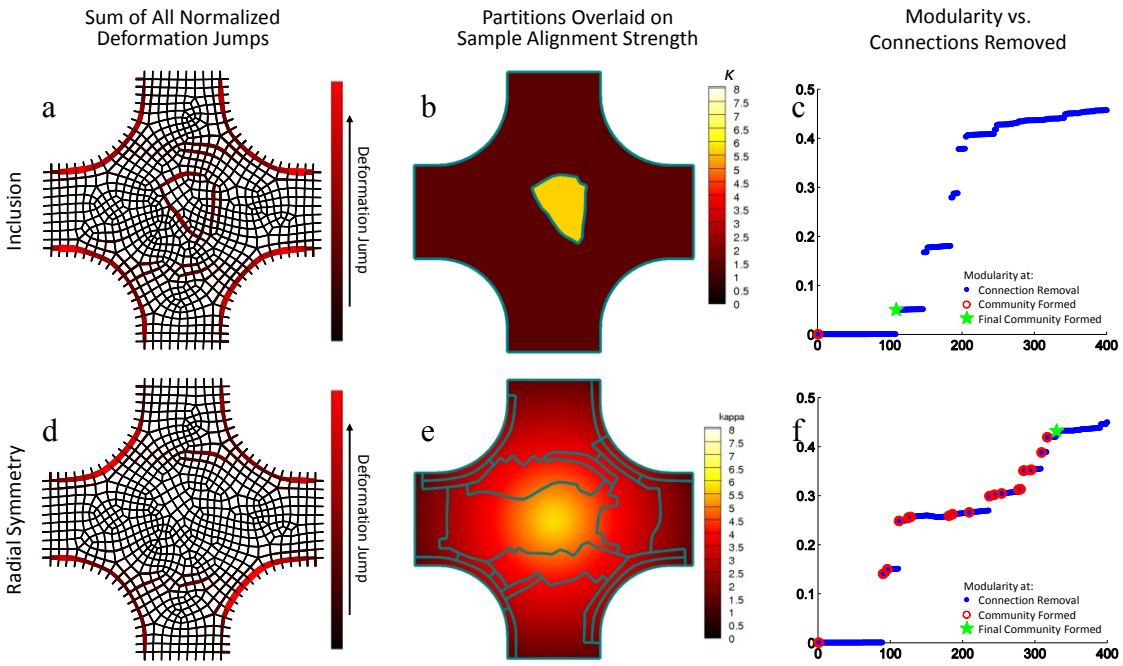

Figure C.4: Sum of normalized deformation gradient jumps for all three extensions for the simulated sample containing the inclusion with strength of alignment different from the bulk ($\kappa_{bulk} = 1.5$ and $\kappa_{inclusion} = 6.0$) (a) and for the radially aligned simulated sample with varied strength of alignment (d). Partitions, overlaid on sample geometry with contour map indicating strength of alignment, identified inclusion (b) and radial symmetry (e), respectively. Modularity as a function of connections removed for both the simulated sample containing the inclusion (c) and the radially aligned simulated sample (f). Blue dots indicate values when a connection is removed, open red circles indicate when a community is formed, and the green stars mark when the final community formed.

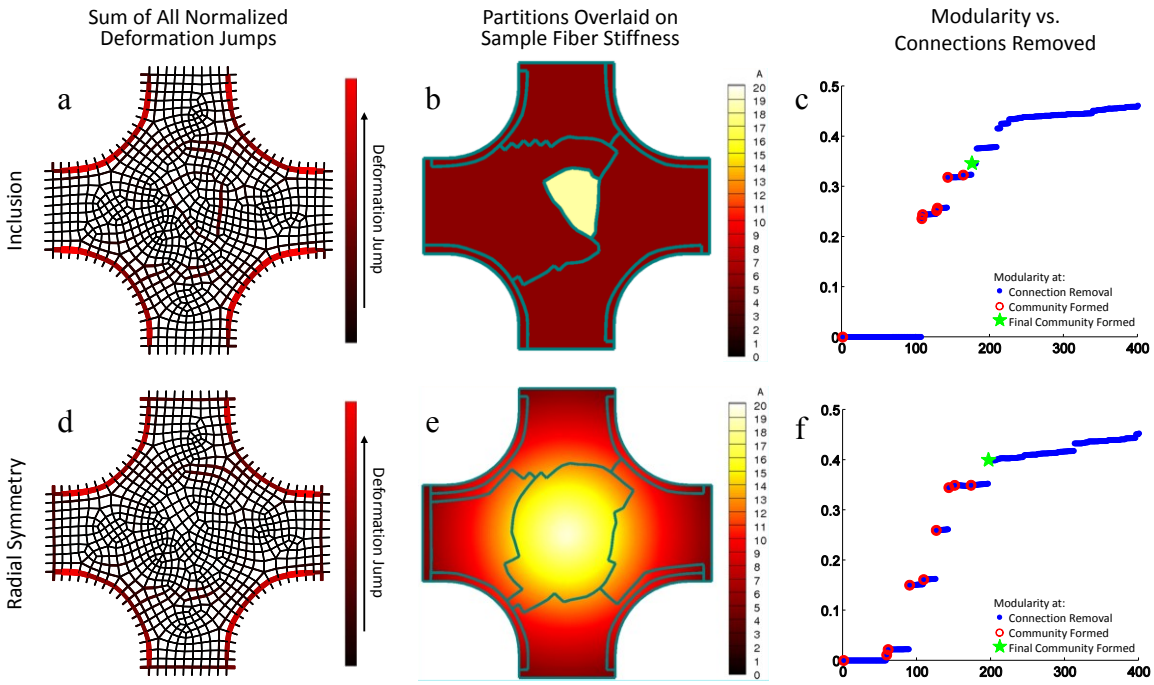

Figure C.5: Sum of normalized deformation gradient jumps for all three extensions for the simulated sample containing the inclusion with stiffness different from the bulk ($A_{bulk} = 5\ kPa$ and $A_{inclusion} = 20\ kPa$)(a) and for the radially aligned simulated sample with varied stiffness (d). Partitions, overlaid on sample geometry with contour map indicating stiffness, identified inclusion (b) and radial symmetry (e), respectively. Modularity as a function of connections removed for both the simulated sample containing the inclusion (c) and the radially aligned simulated sample (f). Blue dots indicate values when a connection is removed, open red circles indicate when a community is formed, and the green stars mark when the final community formed.

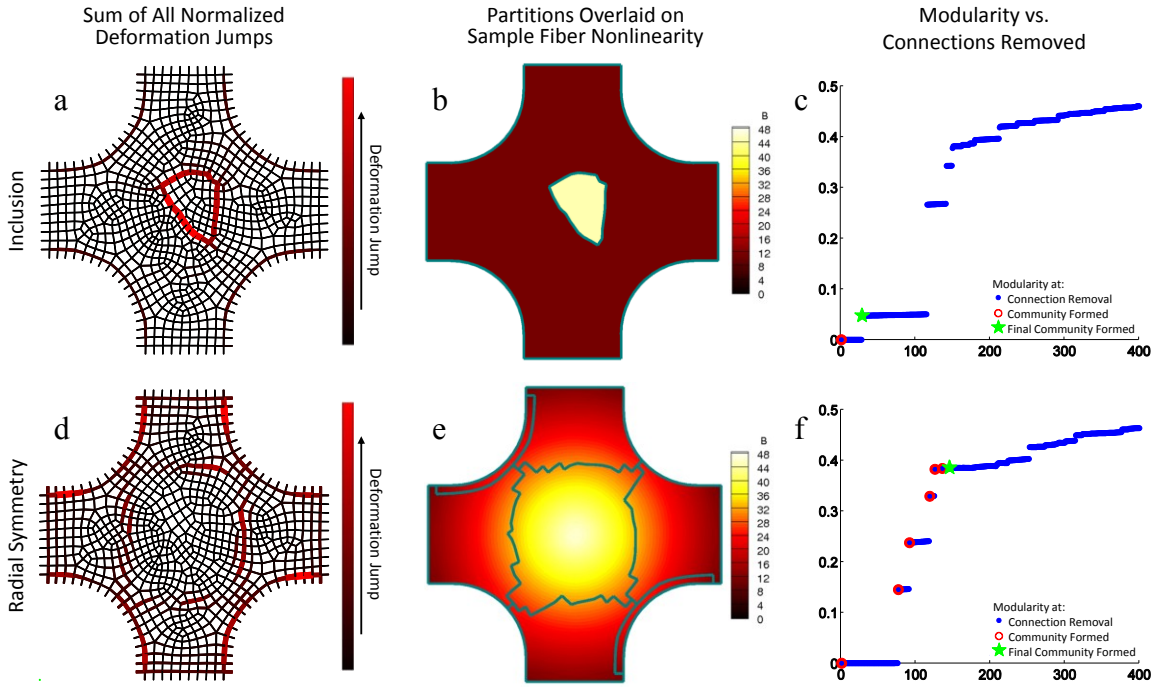

Figure C.6: Sum of normalized deformation gradient jumps for all three extensions for the simulated sample containing the inclusion with stiffness different from the bulk ($B_{bulk} = 12$ and $B_{inclusion} = 48$) (a) and for the radially aligned simulated sample with varied nonlinearity (d). Partitions, overlaid on sample geometry with contour map indicating nonlinearity, identified inclusion (b) and radial symmetry (e), respectively. Modularity as a function of connections removed for both the simulated sample containing the inclusion (c) and the radially aligned simulated sample (f). Blue dots indicate values when a connection is removed, open red circles indicate when a community is formed, and the green stars mark when the final community formed.

C.3 Comparison of the Automatic Segmentation Scheme Presented in Chapter 4 and the Partitioning Method from GAIM

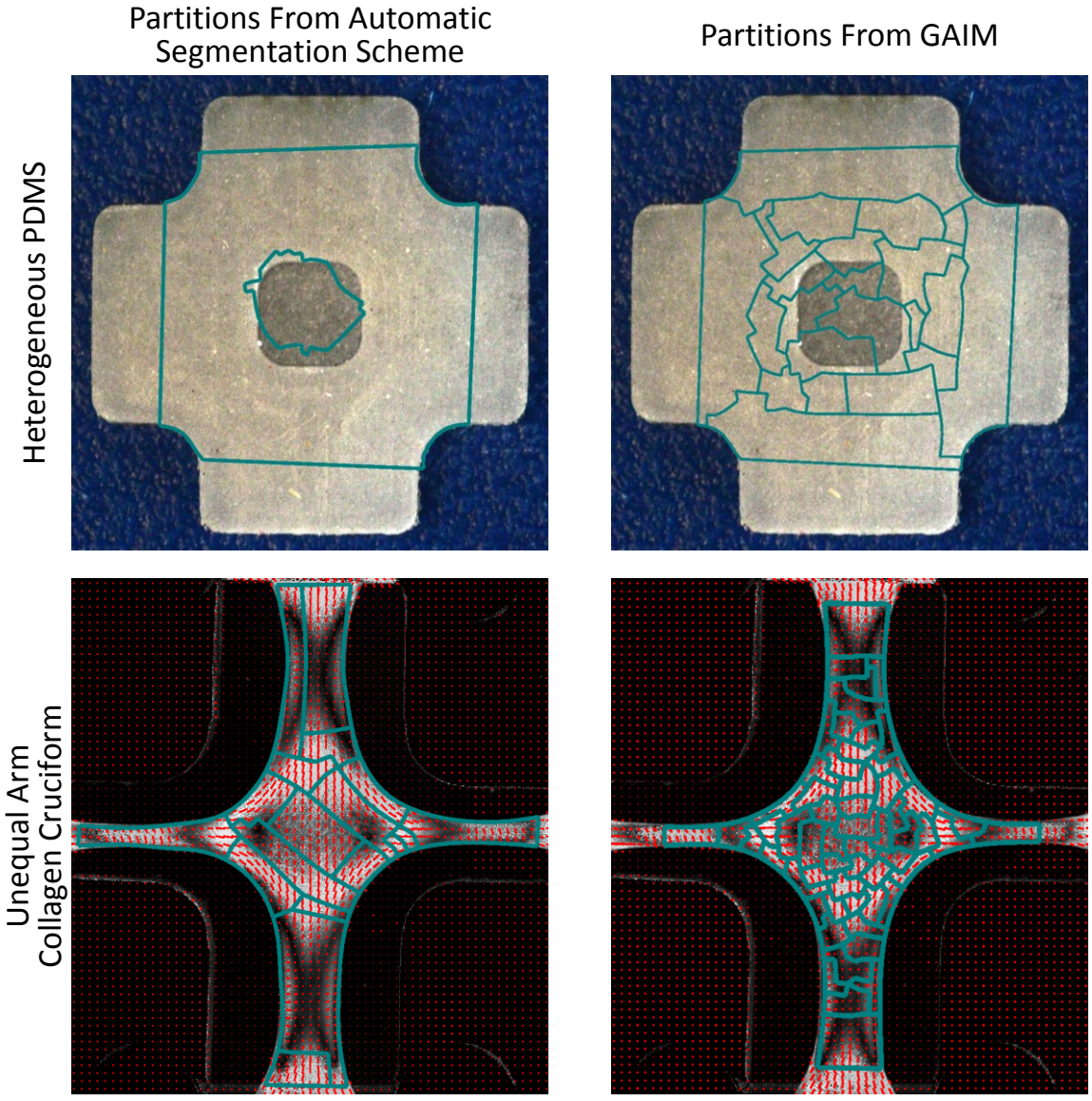

Figure C.7: Partitioning results for the heterogeneous PDMS sample and the collagen tissue-equivalent sample incubated for 11 days from both the original GAIM partitioning method [116] and the new automatic segmentation scheme, Chapter 4.

Appendix D: Method Example and Step Size Determination for Stepwise Utilization of Generalized Anisotropic Inverse Mechanics Method

D.1 Method Example

In order to illustrate the discretization of GAIM into multiple steps, data from the simulation involving an inclusion, which was partitioned in Chapter 4, will be used. Experimentally, a cruciform sample is speckled (to facilitate image correlation) and deformed under various biaxial conditions, as described previously [116,129]. Digital image correlation is used to generate full-field strain for the sample for every extension [115]. Per the GAIM protocol, prior to each extension, the tissue is returned to the initial unloaded configuration. Full-field deformation and grip forces for each loading condition were simulated using the closed-form structural model of planar fibrous tissue mechanics (NSFM) of Raghupathy and Barocas [124] used previously for the characterization of a variety of soft tissues [115,171,239]. Anisotropy strength ($\kappa = 1.5$), stiffness ($A = 5\ kPa$), and nonlinearity ($B = 12$) were set to best fit values for rat myocardium determined previously [239]. Following the work of Raghupathy and Barocas [113], the preferred fiber orientation was set such that the inclusion was rotated relative to the sample bulk, ($\mu_{bulk} = 20°$ and $\mu_{inclusion} = 80°$). The displacement for each node of the sample mesh was determined by the NSFM. Figure D.1 shows the sample geometry and anisotropy as well as full-field deformation for the equibiaxial and right-arm-only extensions at maximum grip strain (30%) for the simulation. There is a large horizontal displacement of the center of the sample in the asymmetric loading protocol. The grip strain vs. time and grip force vs. time curves for the equibiaxial extension and the right-arm-only extension are shown in Figure D.2. Forces on the left and bottom arms are shown as negative for clarity; as this is a static analysis the overall force balance must be maintained. The shear forces at the arms are included in the analysis since they can be obtained using 6-degree-of-freedom load cells (JR3 Inc., Woodland California). When applying GAIM, a linear approximation is made concerning the material behavior, in

essence generating a higher-dimension analog of a secant modulus rather than a full description of the nonlinear behavior of the tissue. Clearly, this is not a reasonable assumption for cardiovascular soft tissues and should not be extended beyond the small-strain behavior.

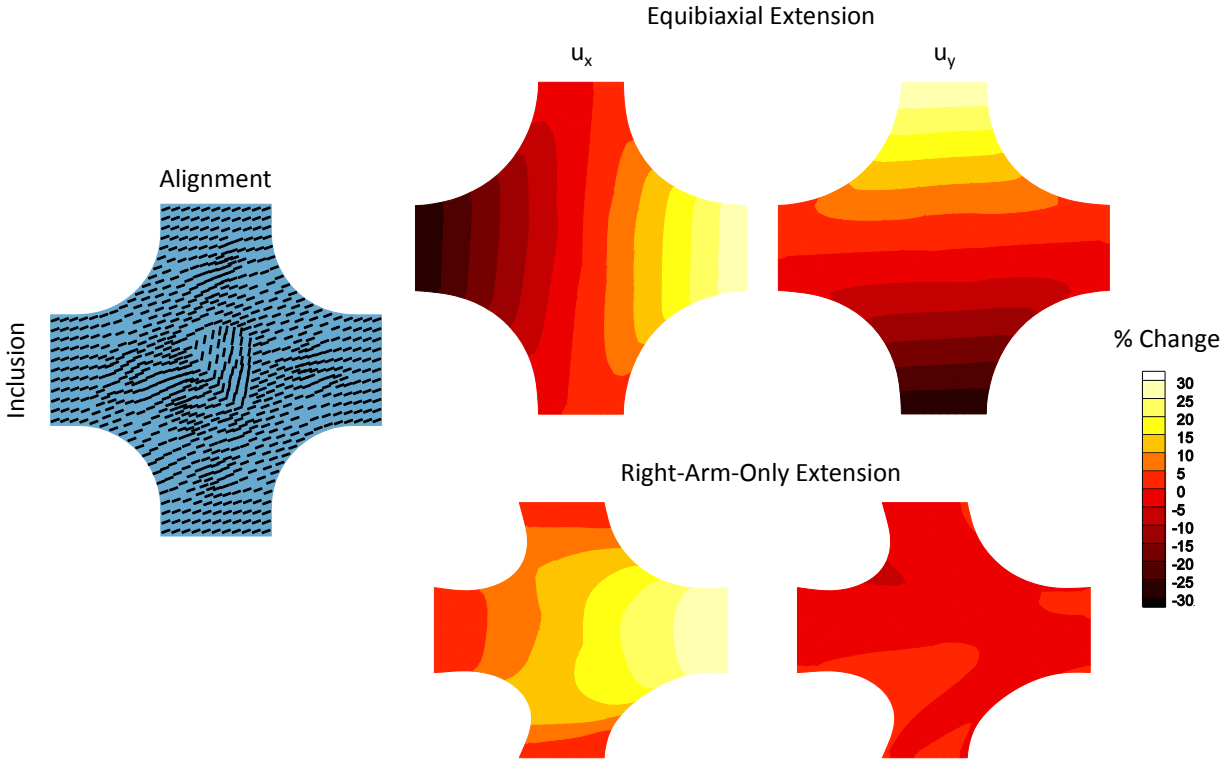

Figure D.1: The full-field deformation for the equibiaxial and right-arm-only extensions at maximum grip strain for the simulated sample containing an inclusion in which the fiber orientation is rotated.

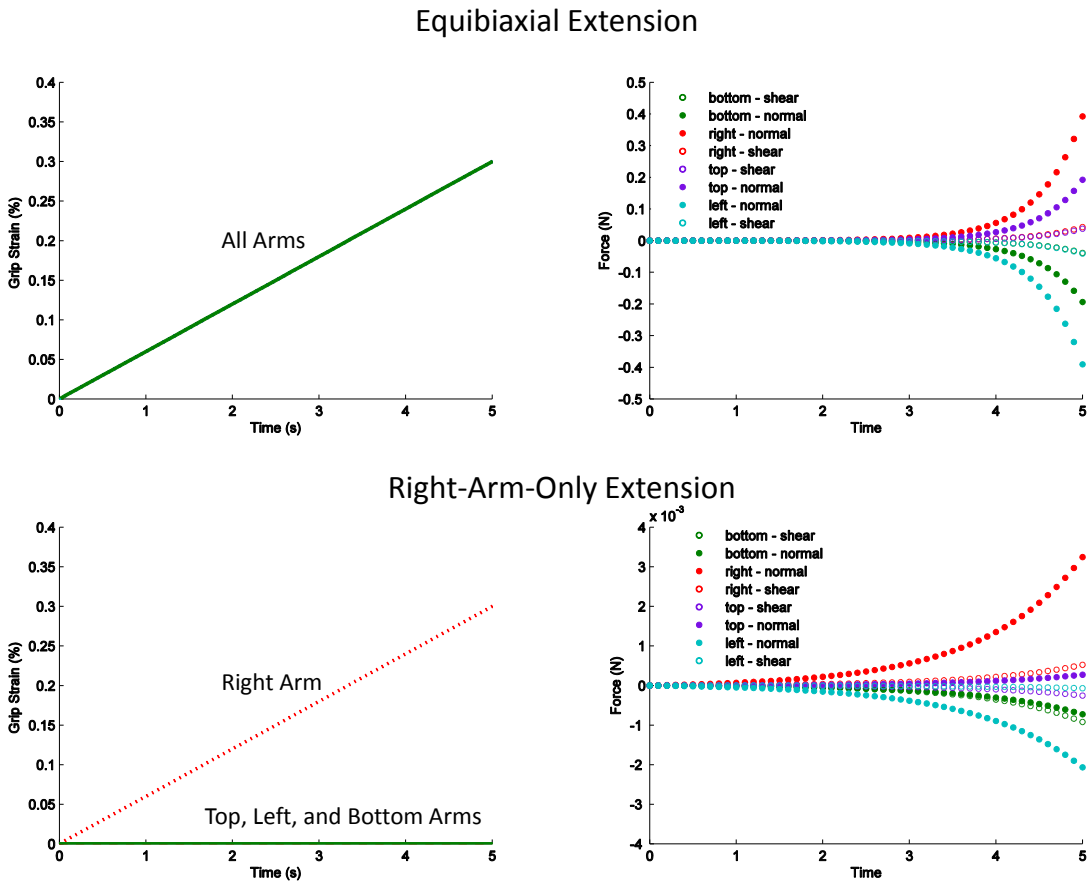

Figure D.2: The grip strain vs. time and grip force vs. time for the equibiaxial and right-arm-only extensions for the simulated sample. The sample exhibits marked nonlinearity in both extensions.

D.2 Step Size Determination

To fit GAIM to the data in a stepwise manner, first an appropriate step size must be determined. In order to determine step size, lines were fit to the force vs. time curves for each biaxial extension, as shown in Figure D.3 for the representative simulation discussed in the previous section. The coefficient of determination, r-squared, was used to evaluate the linear fit. If the slope of the data was sufficiently non-zero (in this case, $|slope| > 5.6e-7$), then the r-squared value was calculated. The minimum r-squared value calculated for all steps and all protocols and if it was less than 0.9 (the level at which a stepwise linear approximation was deemed appropriate), the step size was reduced. For the representative simulated sample, a step size of 0.5 seconds was selected and the

minimum r-squared value calculated for all steps and all protocols was 0.9044. The displacement fields for the sample at the end of each step for the equibiaxial and right-arm-only extensions are shown in Figure D.4 a and b, respectively.

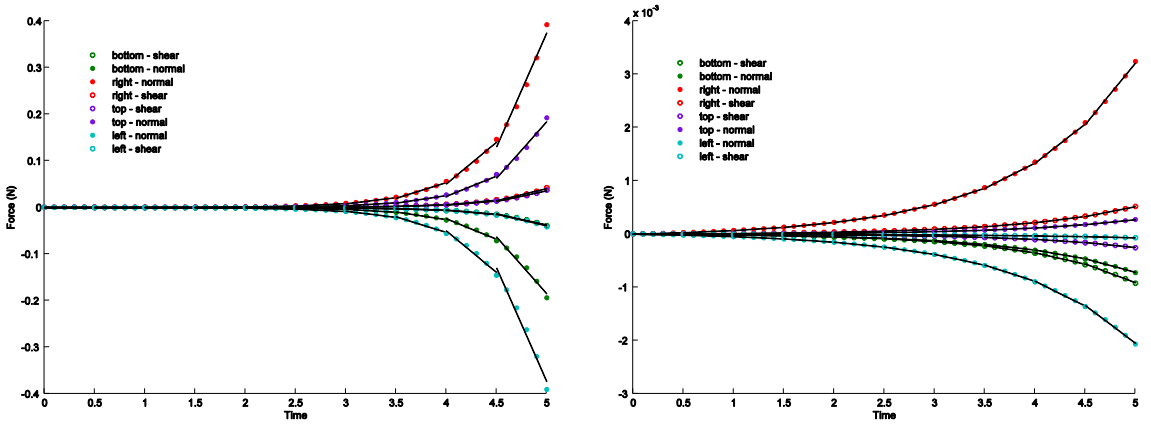

Figure D.3: Final step size fits for the equibiaxial and right-arm-only extensions for the simulated sample containing an inclusion in which the fiber orientation is rotated, shown in Figure D.1. Ten steps were utilized to describe the force behavior.

The step size is an important specification when implementing nonlinear GAIM. The NSFM simulation has nearly infinite time resolution, so any step size can be accommodated. Experimentally, there are practical limits that limit how much step size can be reduced. The resolution and data acquisition rate of available load cells must be considered. In addition, if full-field displacement is determined optically, both frame rate and spatial resolution must be considered. The maximum displacement of a node in any step of the representative simulation is 0.09 mm, which assuming a spatial resolution similar to that achieved previously [116,129], is equivalent to approximately 8 pixels, a value that is reasonable given the image analysis and strain tracking methods utilized experimentally [115,116]. The measurement of loads at low levels require load cells with excellent resolution and accuracy. In addition, precise levels of preload and preconditioning must be applied carefully. For experimental data obtained using the biaxial tester (Instron[b]), load cells (JR3 Inc. [171]) and digital camera (Cannon, 24 fps, 1080p HD resolution) available at the University of Minnesota, a step size of 0.5 seconds is reasonable.

[b] Available at the University of Minnesota http://bme.umn.edu/research/tissuemech.html

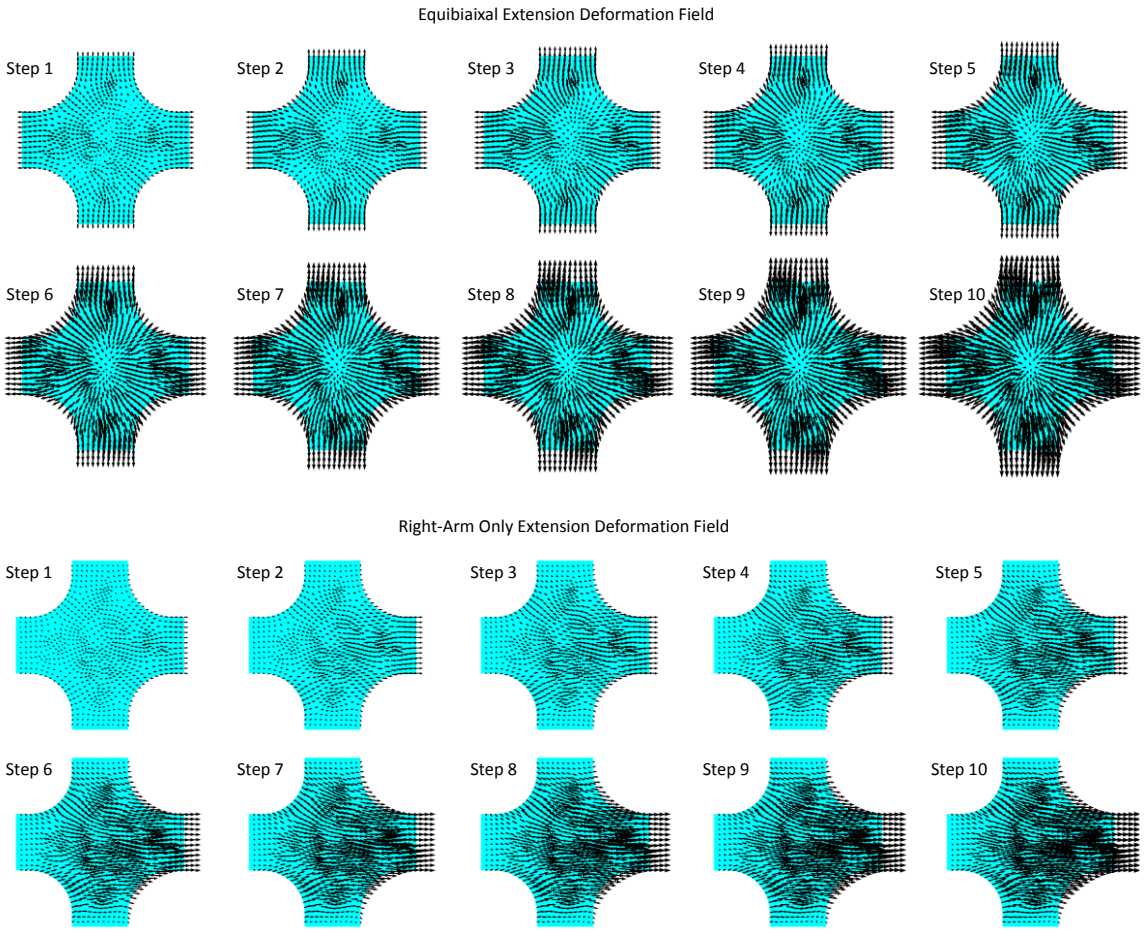

Figure D.4: Displacement field for equibiaxial and right-arm-only extensions for the representative simulation at the end of each step.

D.3 NSFM Fitting of NGAIM Results

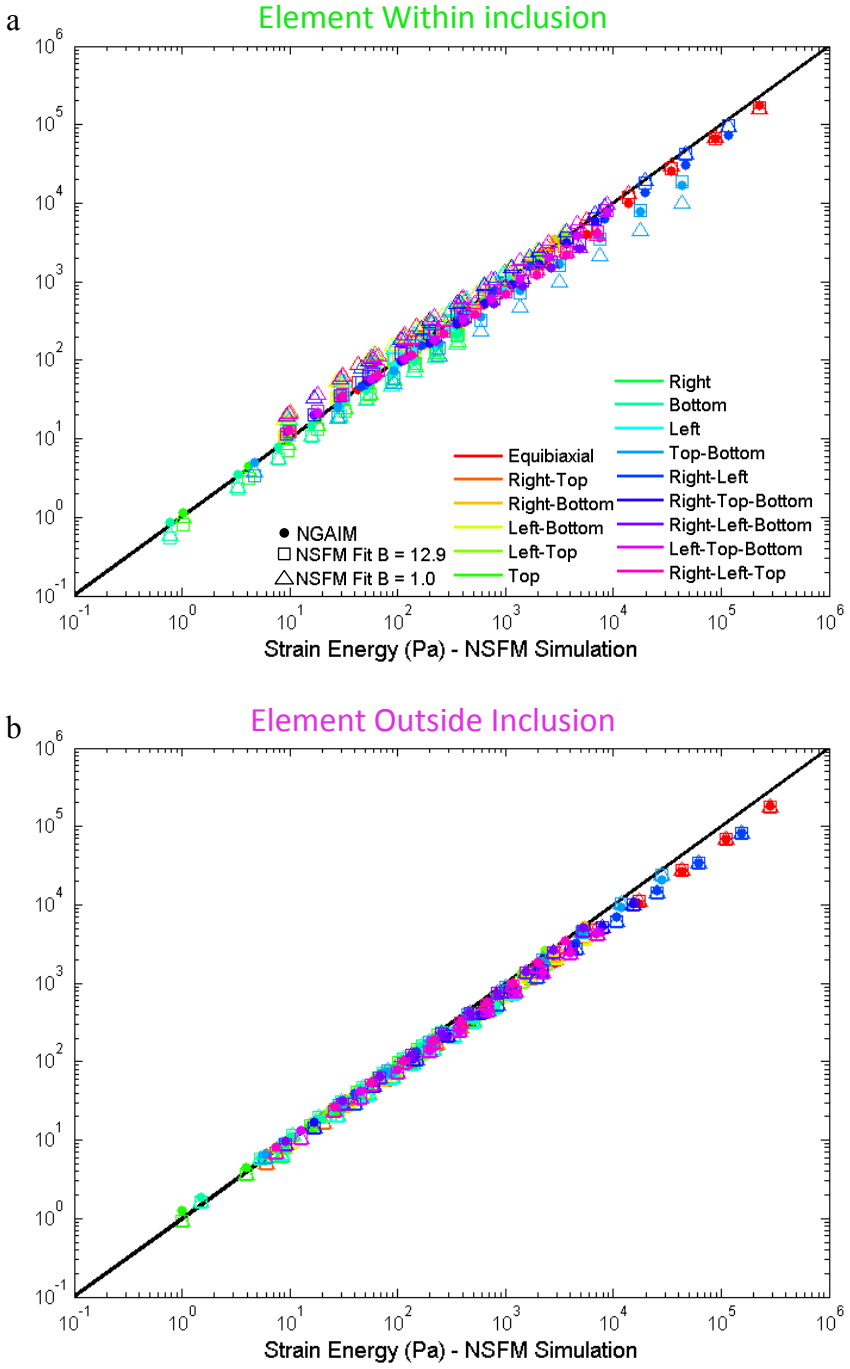

Figure D.5: Strain energy determined using NGAIM (colored dots), strain energy determined by the NSFM fit with an initial value of B = 12.9 (colored squares), and strain energy determined by the NSFM fit with an initial value of B =1.0 (colored triangles) vs. the strain energy generated by the NSFM simulation with prescribed alignment for all biaxial extensions for the element within the inclusion (a) and the element just outside of the inclusion (b). The diagonal black line indicates a perfect prediction.

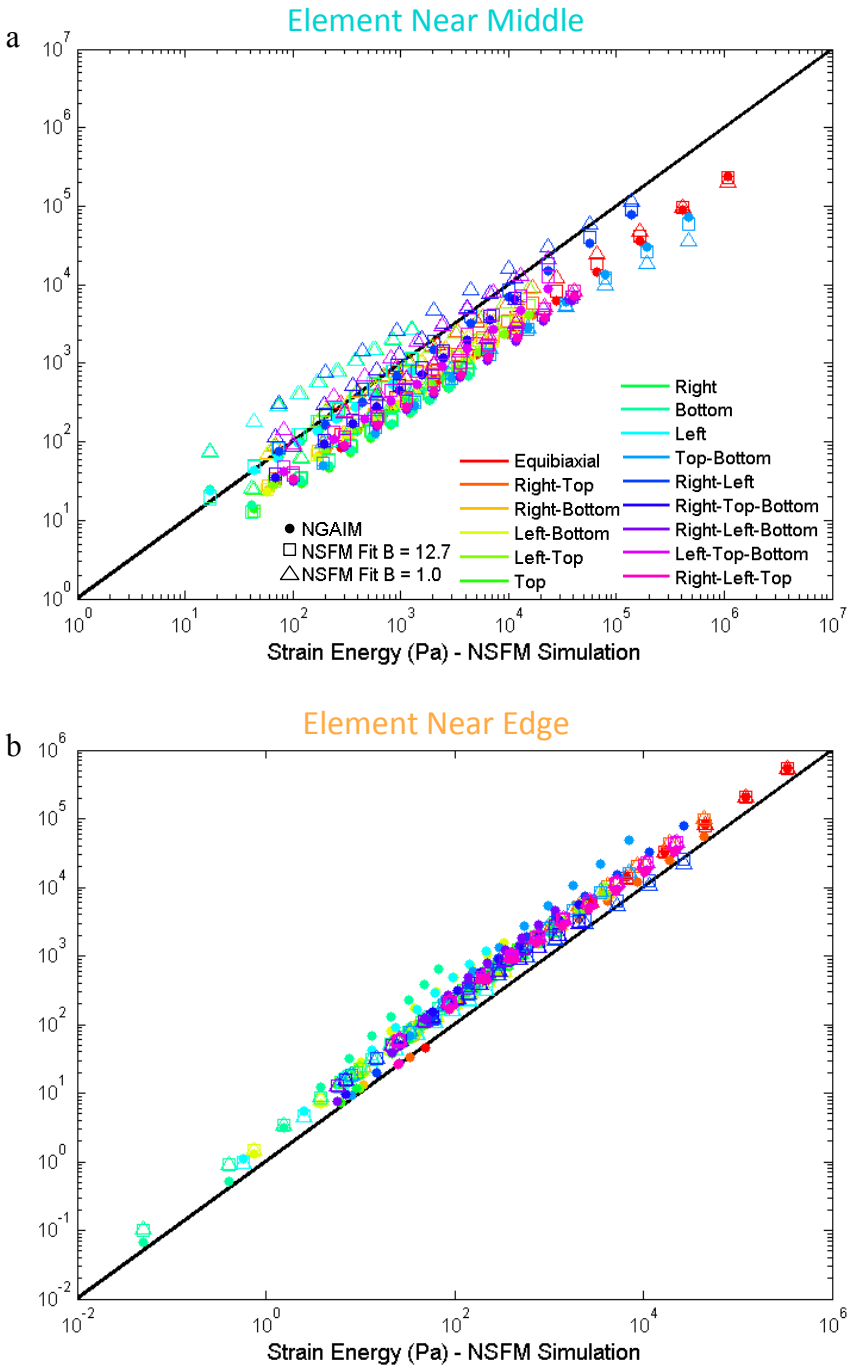

Figure D.6: Strain energy determined using NGAIM (colored dots), strain energy determined by the NSFM fit with an initial value of B = 12.7 (colored squares), and strain energy determined by the NSFM fit with an initial value of B =1.0 (colored triangles) vs. the strain energy generated by the NSFM simulation with prescribed alignment for all biaxial extensions for the element near the center (a) and an element near the edge (b) of the radially aligned simulation. The diagonal black line indicates a perfect prediction.

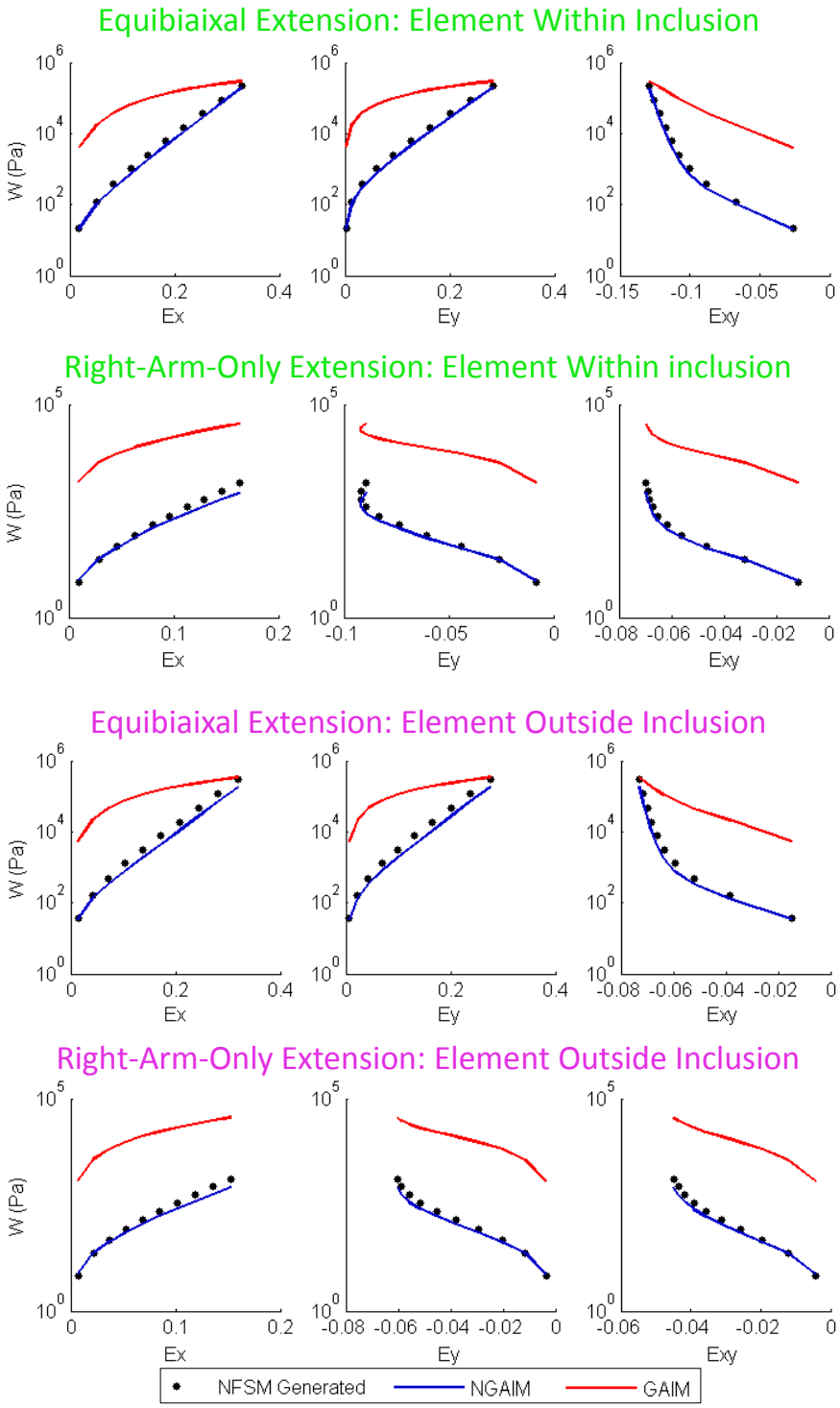

Figure D.7: Strain energy vs. Green strain component for the equibiaxial and right-arm-only extensions for the element in the middle of the inclusion and the element just outside of the inclusion for the NSFM simulation with prescribed strength of alignment. The black dots indicate the strain energy generated from NSFM model, the red line indicates the strain energy determined by the original linear GAIM method, and the blue line indicates the strain energy determined by the stepwise nonlinear GAIM method, NGAIM.

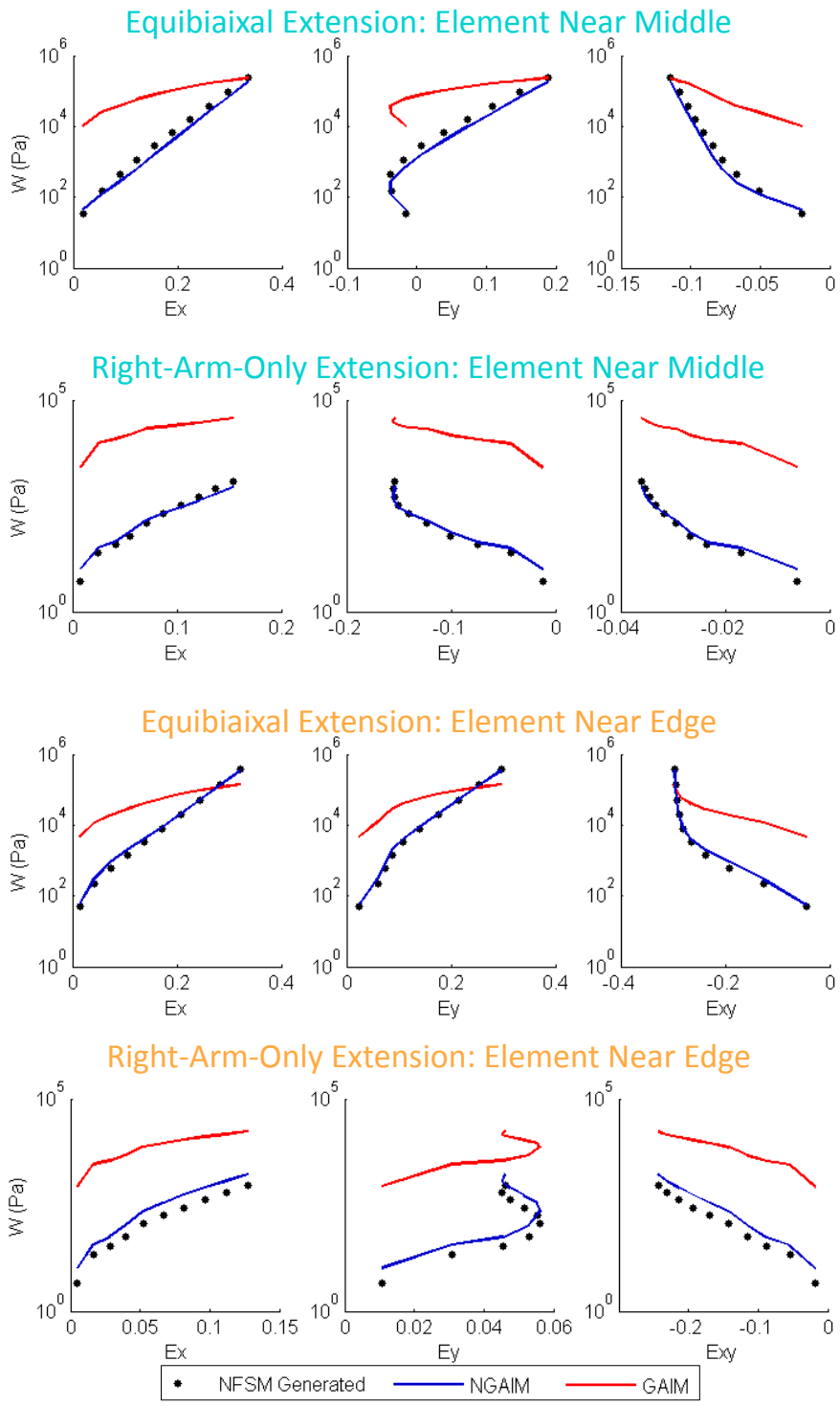

Figure D.8: Strain energy vs. Green strain component for the equibiaxial and right-arm-only extensions for the element near the middle and the element near the edge of the NSFM simulation with radially prescribed strength of alignment. The black dots indicate the strain energy generated from NSFM model, the red line indicates the strain energy determined by the original linear GAIM method, and the blue line indicates the strain energy determined by the stepwise nonlinear GAIM method, NGAIM.

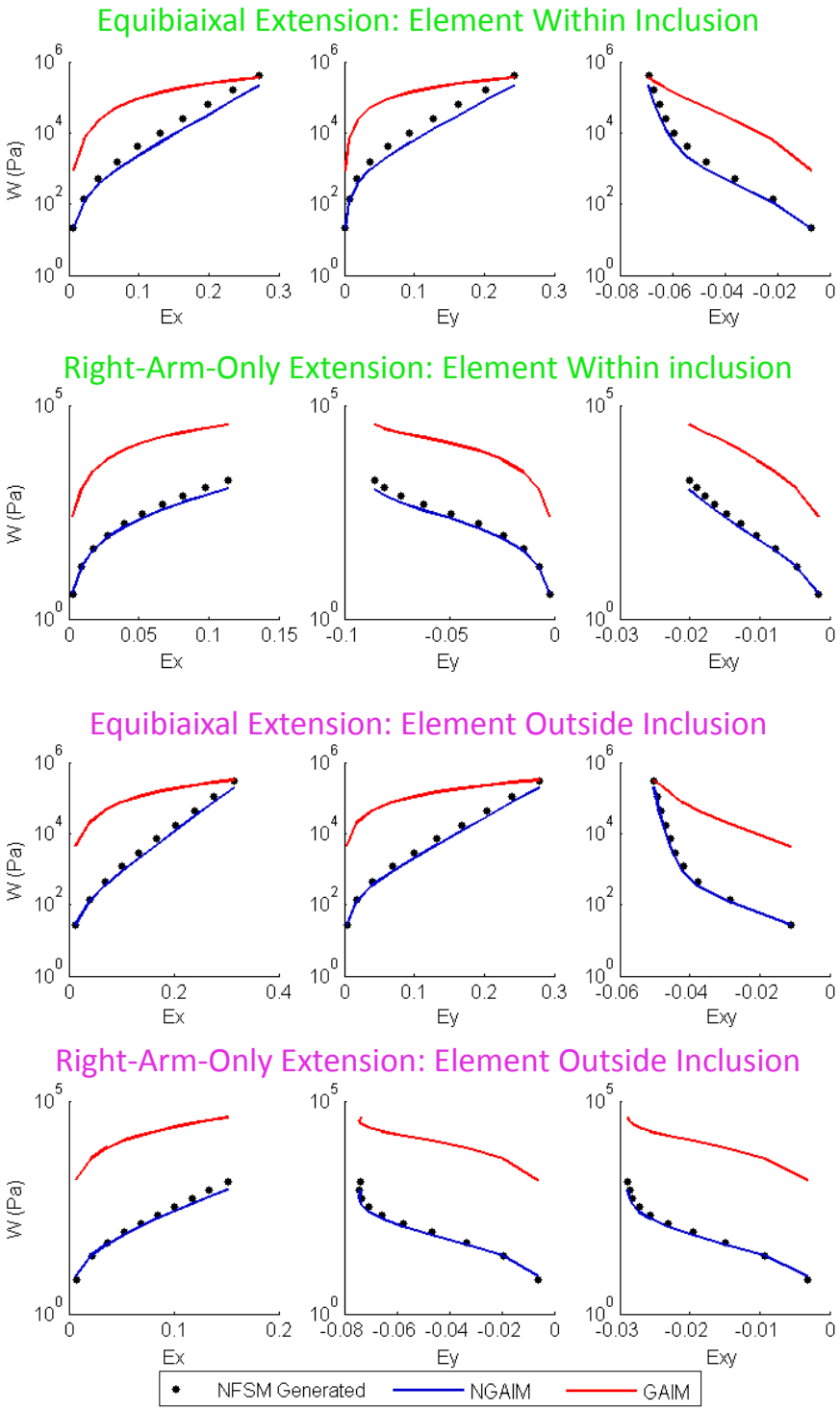

Figure D.9: Strain energy vs. Green strain component for the equibiaxial and right-arm-only extensions for the element in the middle of the inclusion and the element just outside of the inclusion for the NSFM simulation with prescribed fiber stiffness. The black dots indicate the strain energy generated from NSFM model, the red line indicates the strain energy determined by the original linear GAIM method, and the blue line indicates the strain energy determined by the stepwise nonlinear GAIM method, NGAIM.

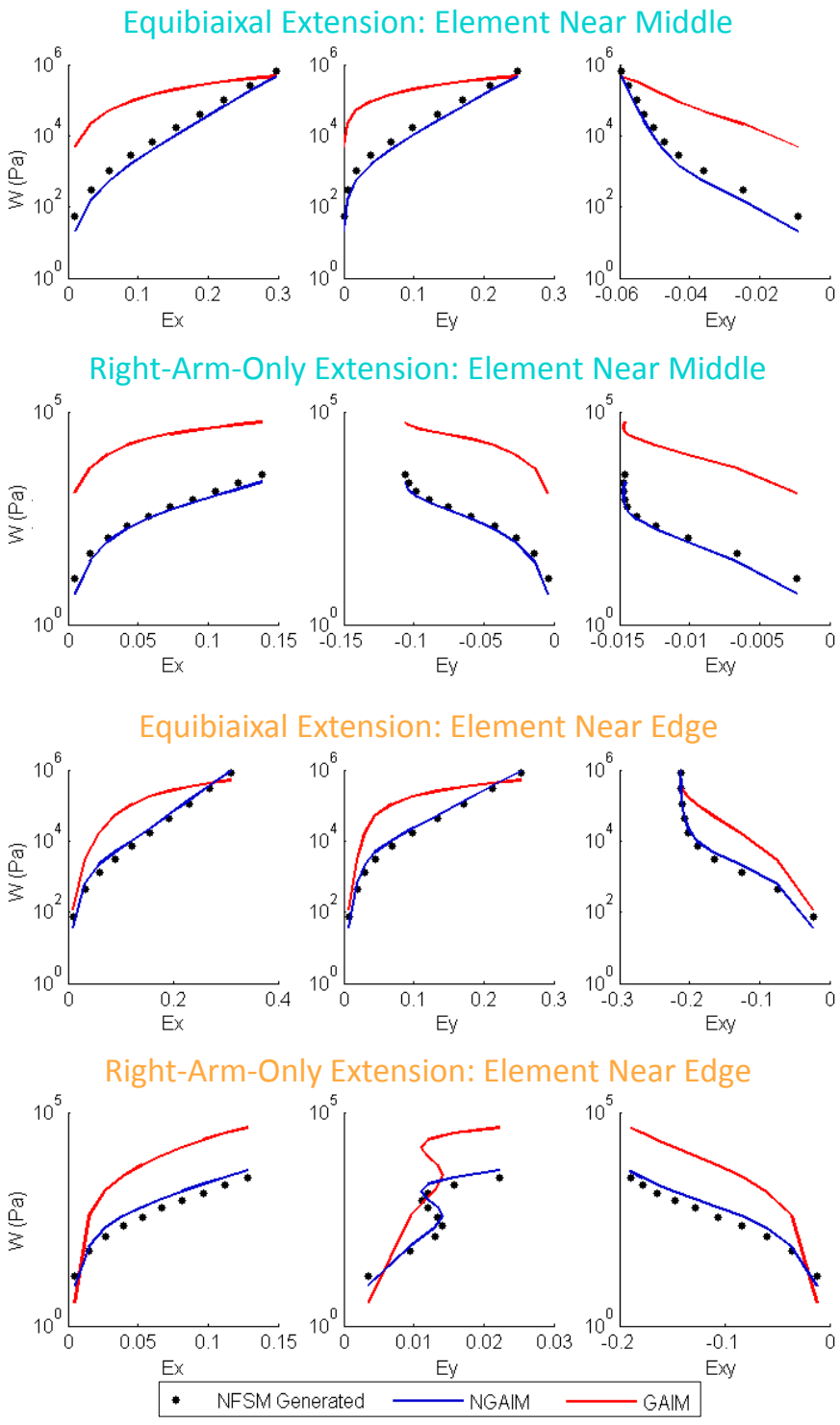

Figure D.10: Strain energy vs. Green strain component for the equibiaxial and right-arm-only extensions for the element near the middle and the element near the edge of the NSFM simulation with radially prescribed fiber stiffness. The black dots indicate the strain energy generated from NSFM model, the red line indicates the strain energy determined by the original linear GAIM method, and the blue line indicates the strain energy determined by the stepwise nonlinear GAIM method, NGAIM.

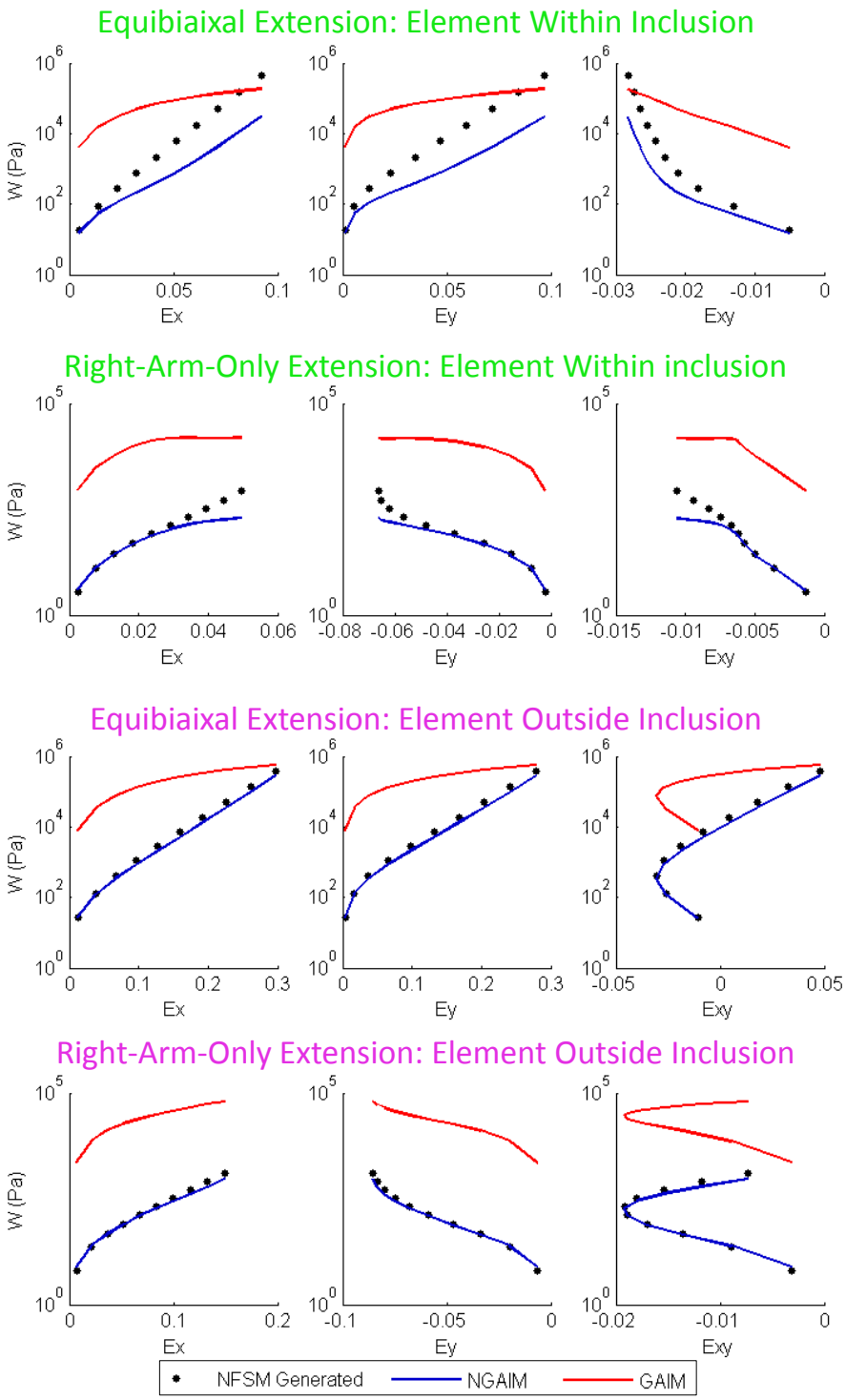

Figure D.11: Strain energy vs. Green strain component for the equibiaxial and right-arm-only extensions for the element in the middle of the inclusion and the element just outside of the inclusion for the NSFM simulation with prescribed fiber nonlinearity. The black dots indicate the strain energy generated from NSFM model, the red line indicates the strain energy determined by the original linear GAIM method, and the blue line indicates the strain energy determined by the stepwise nonlinear GAIM method, NGAIM.

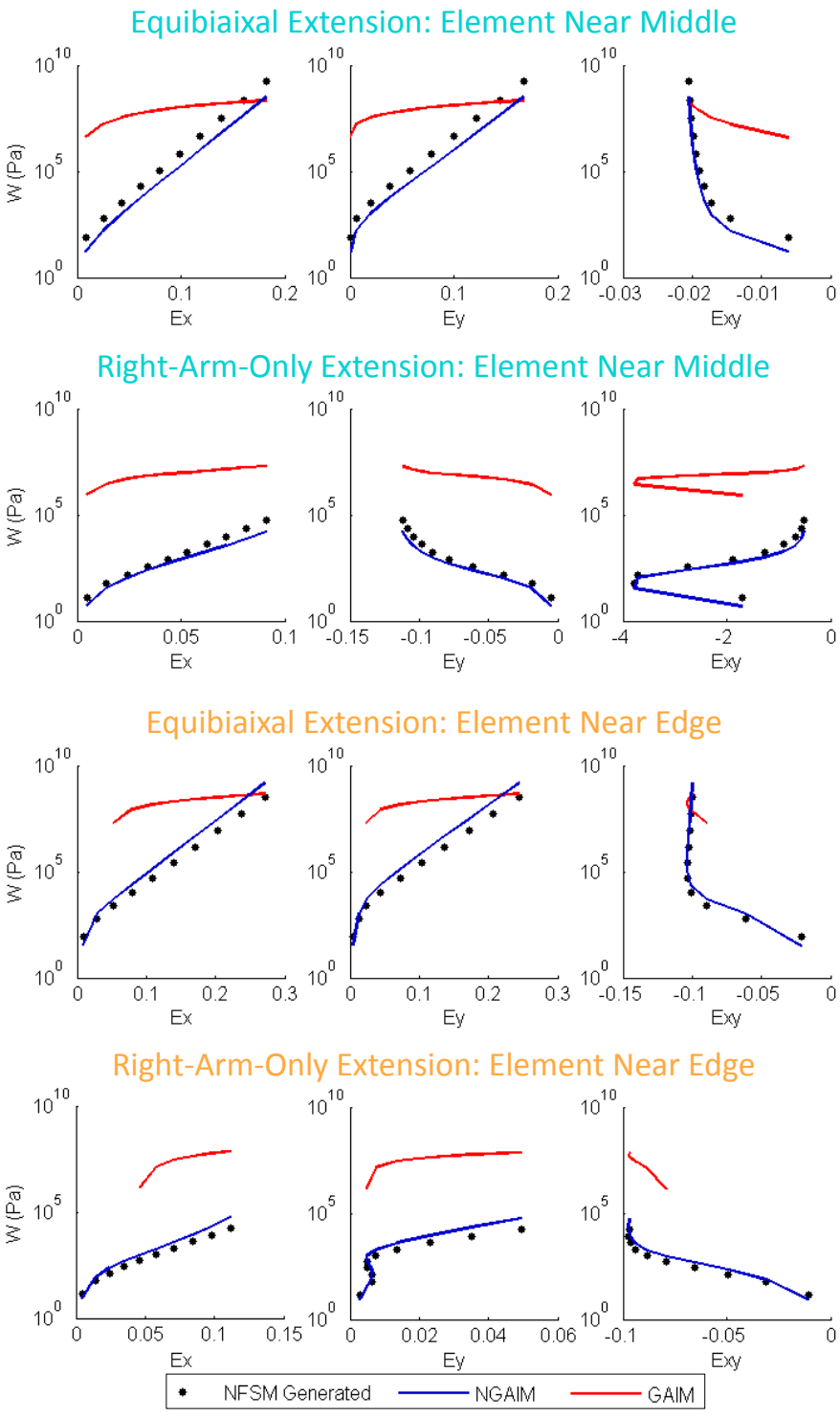

Figure D.12: Strain energy vs. Green strain component for the equibiaxial and right-arm-only extensions for the element near the middle and the element near the edge of the NSFM simulation with radially prescribed fiber nonlinearity. The black dots indicate the strain energy generated from NSFM model, the red line indicates the strain energy determined by the original linear GAIM method, and the blue line indicates the strain energy determined by the stepwise nonlinear GAIM method, NGAIM.

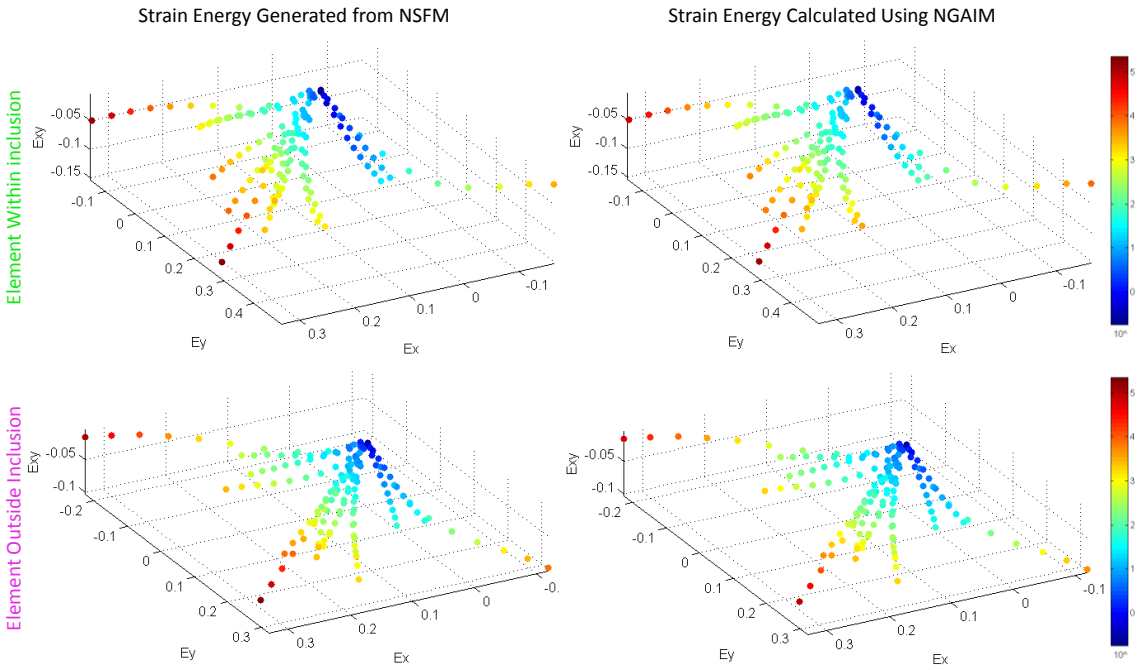

Figure D.13: Strain energy generated by the NSFM simulation with prescribed alignment and strain energy calculated using the NGAIM method for all extensions plotted in strain space for both the element within the inclusion and the element just outside the inclusion.

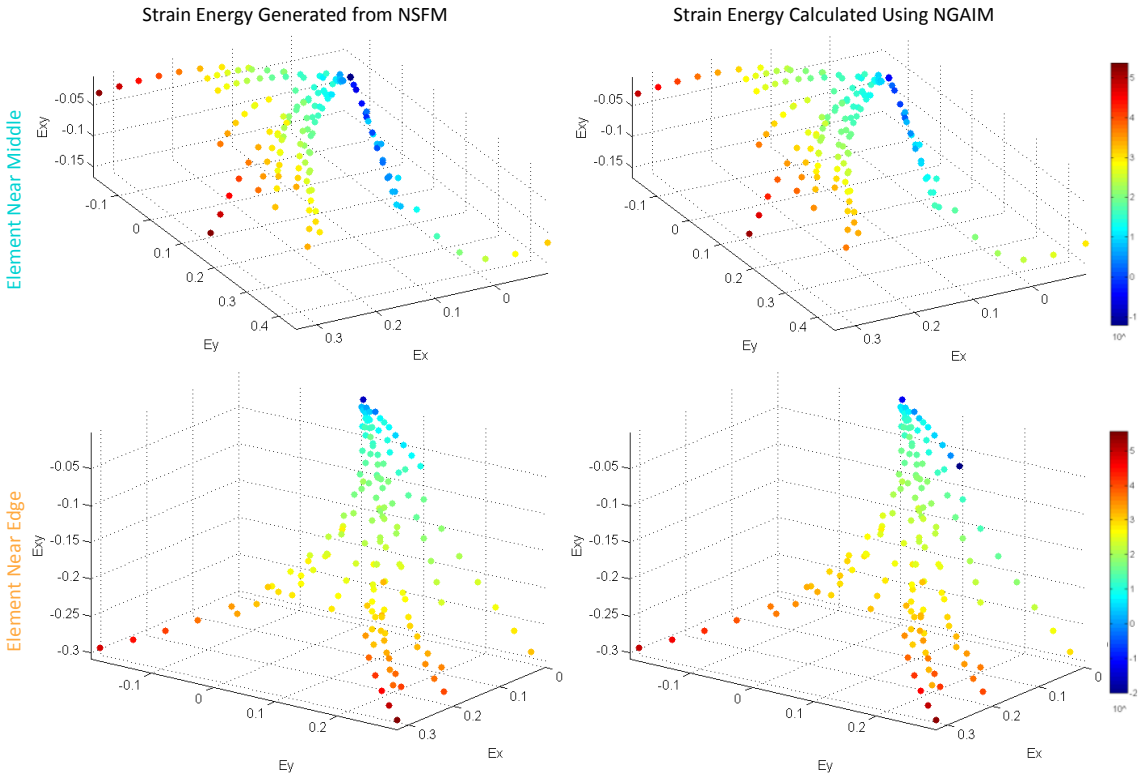

Figure D.14: Strain energy generated by the NSFM simulation with prescribed alignment and strain energy calculated using the NGAIM method for all extensions plotted in strain space for both the element near the center and the element near the edge of the radially symmetric sample.

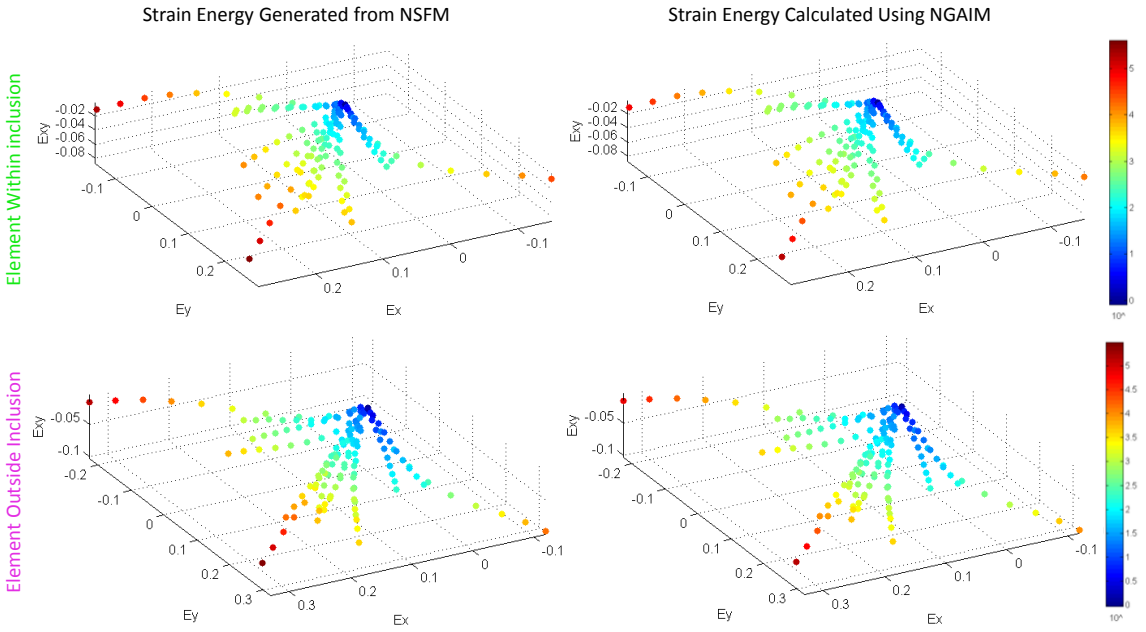

Figure D.15: Strain energy generated by the NSFM simulation with prescribed fiber stiffness and strain energy calculated using the NGAIM method for all extensions plotted in strain space for both the element within the inclusion and the element just outside the inclusion.

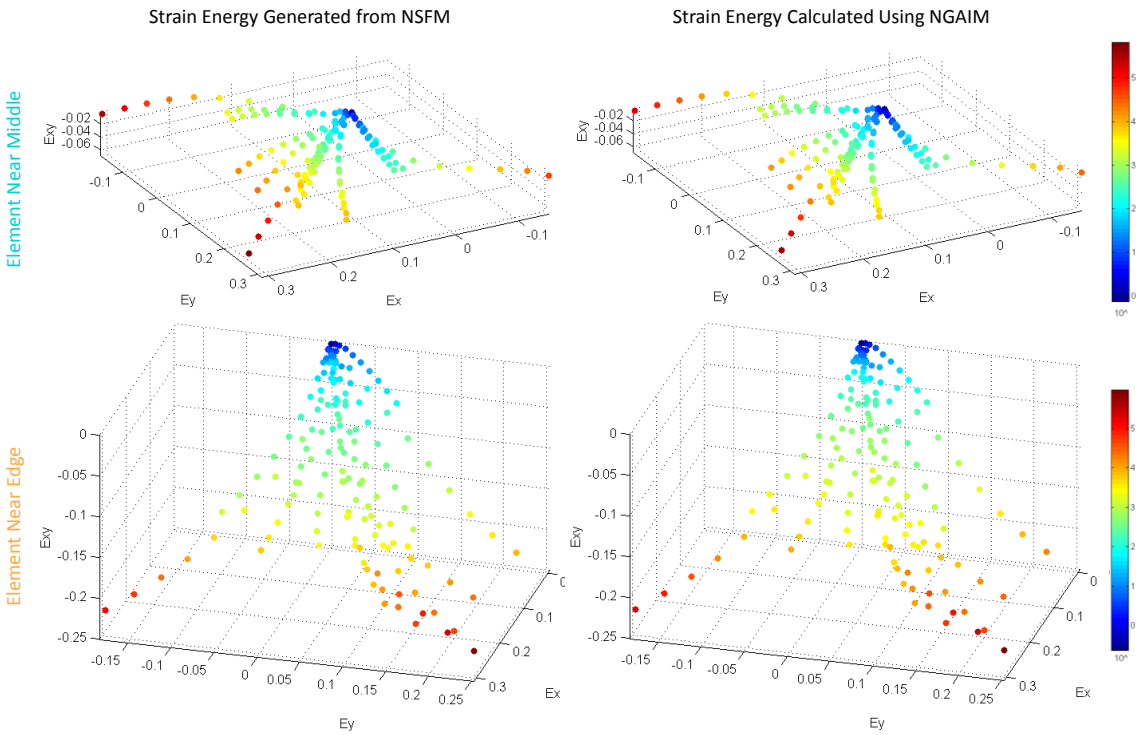

Figure D.16: Strain energy generated by the NSFM simulation with prescribed fiber stiffness and strain energy calculated using the NGAIM method for all extensions plotted in strain space for both the element near the center and the element near the edge of the radially symmetric sample.

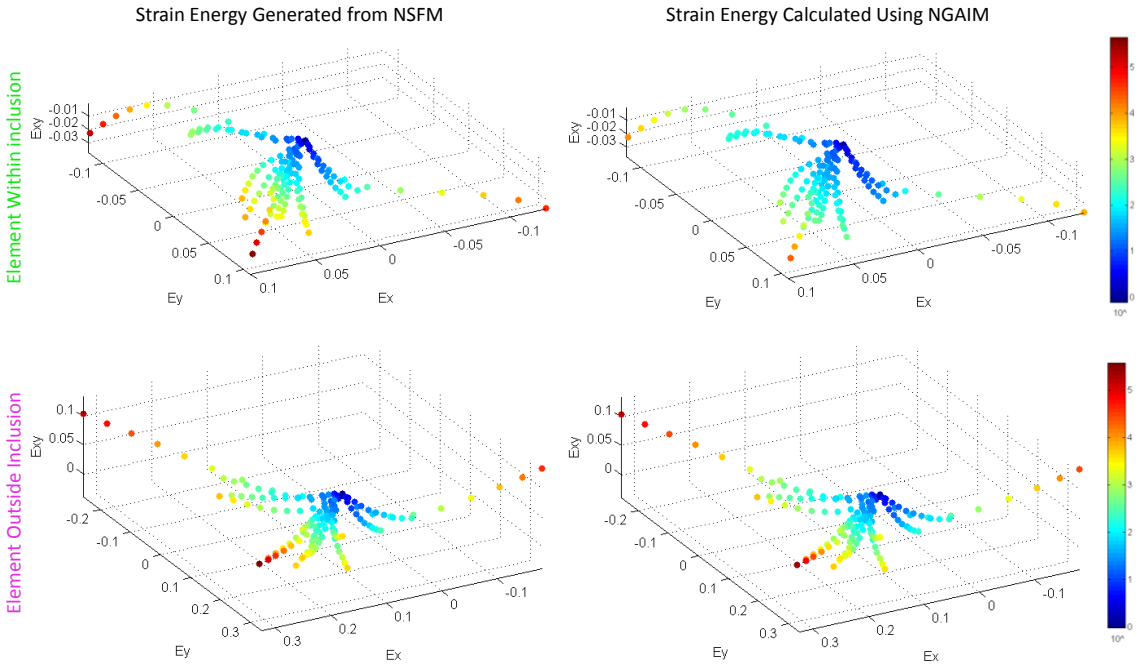

Figure D.17: Strain energy generated by the NSFM simulation with prescribed fiber nonlinearity and strain energy calculated using the NGAIM method for all extensions plotted in strain space for both the element within the inclusion and the element just outside the inclusion.

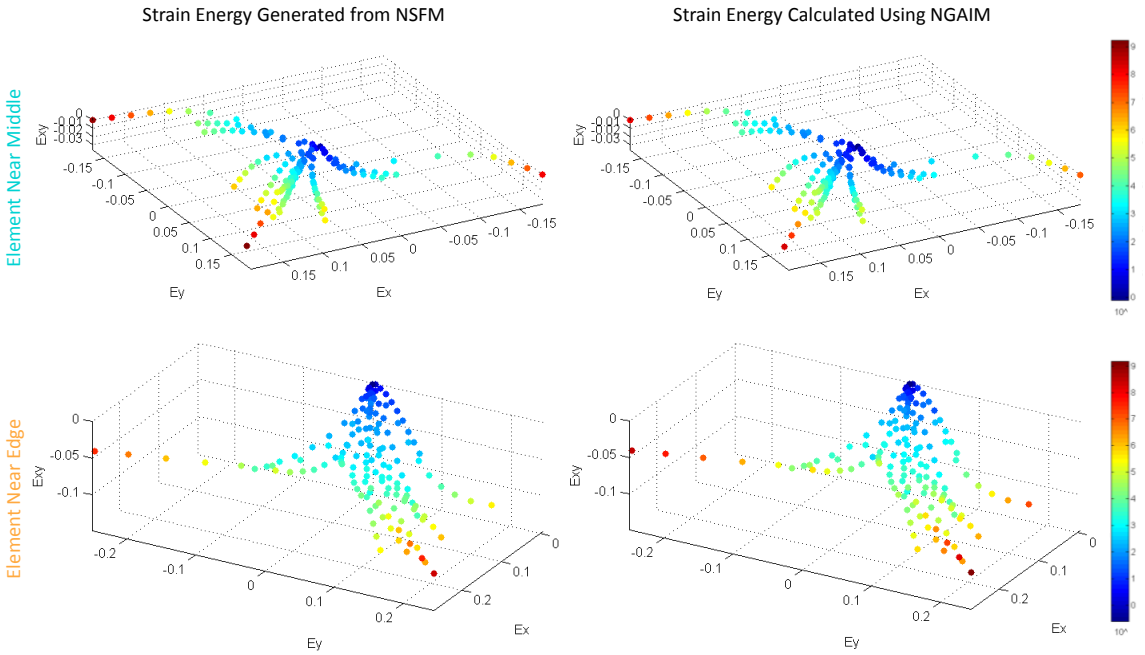

Figure D.18: Strain energy generated by the NSFM simulation with prescribed fiber nonlinearity and strain energy calculated using the NGAIM method for all extensions plotted in strain space for both the element near the center and the element near the edge of the radially symmetric sample.

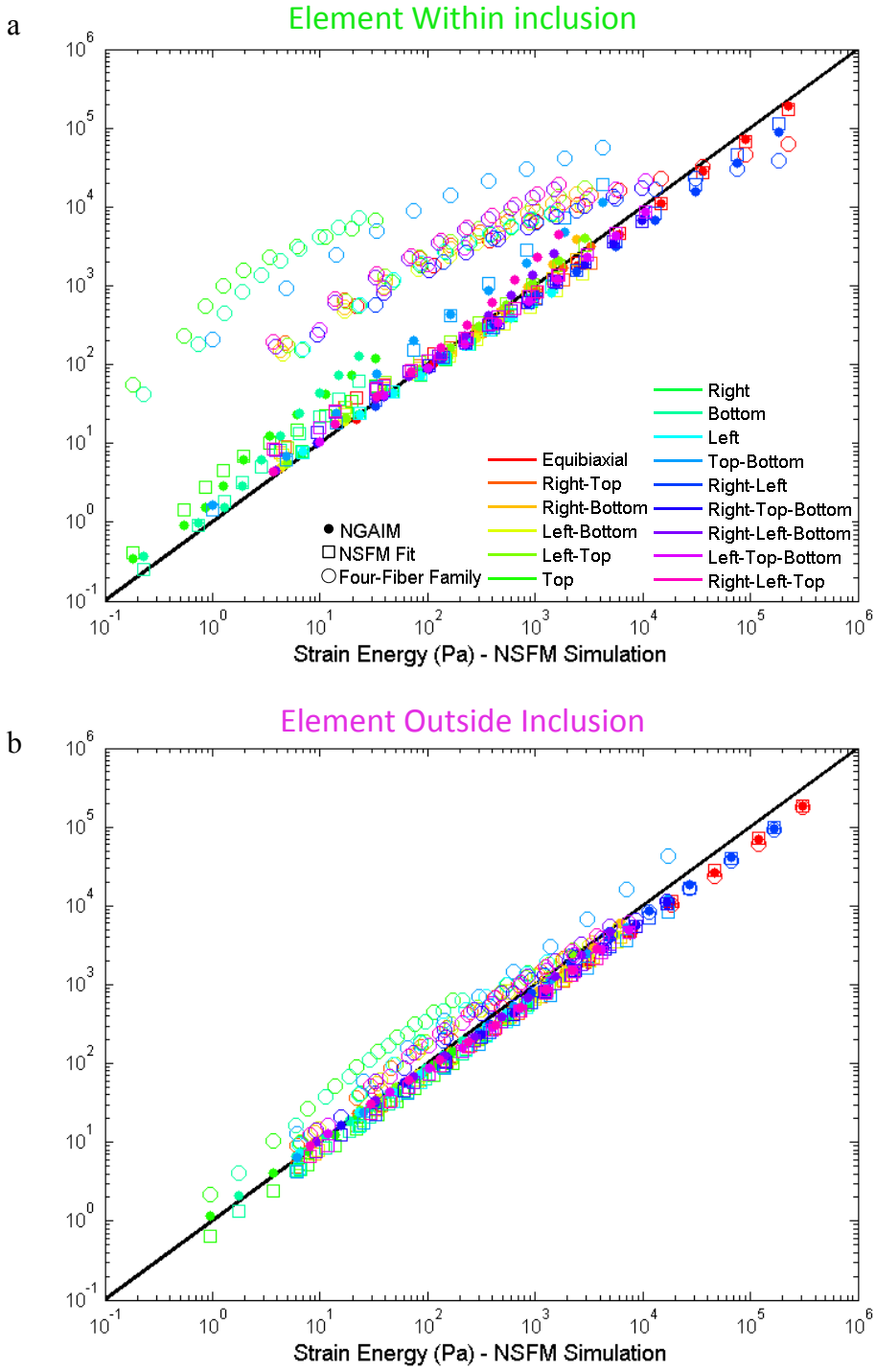

Figure D.19: Strain energy determined using NGAIM (colored dots), the strain energy determined by the NSFM fit to the NGAIM results (colored squares), and the strain energy determined using the four-fiber family model (colored circles) vs. the strain energy generated by the NSFM simulation with prescribed strength of alignment for all biaxial extensions for the element within the inclusion (a) and the element just outside of the inclusion (b). The diagonal black line indicates a perfect prediction.

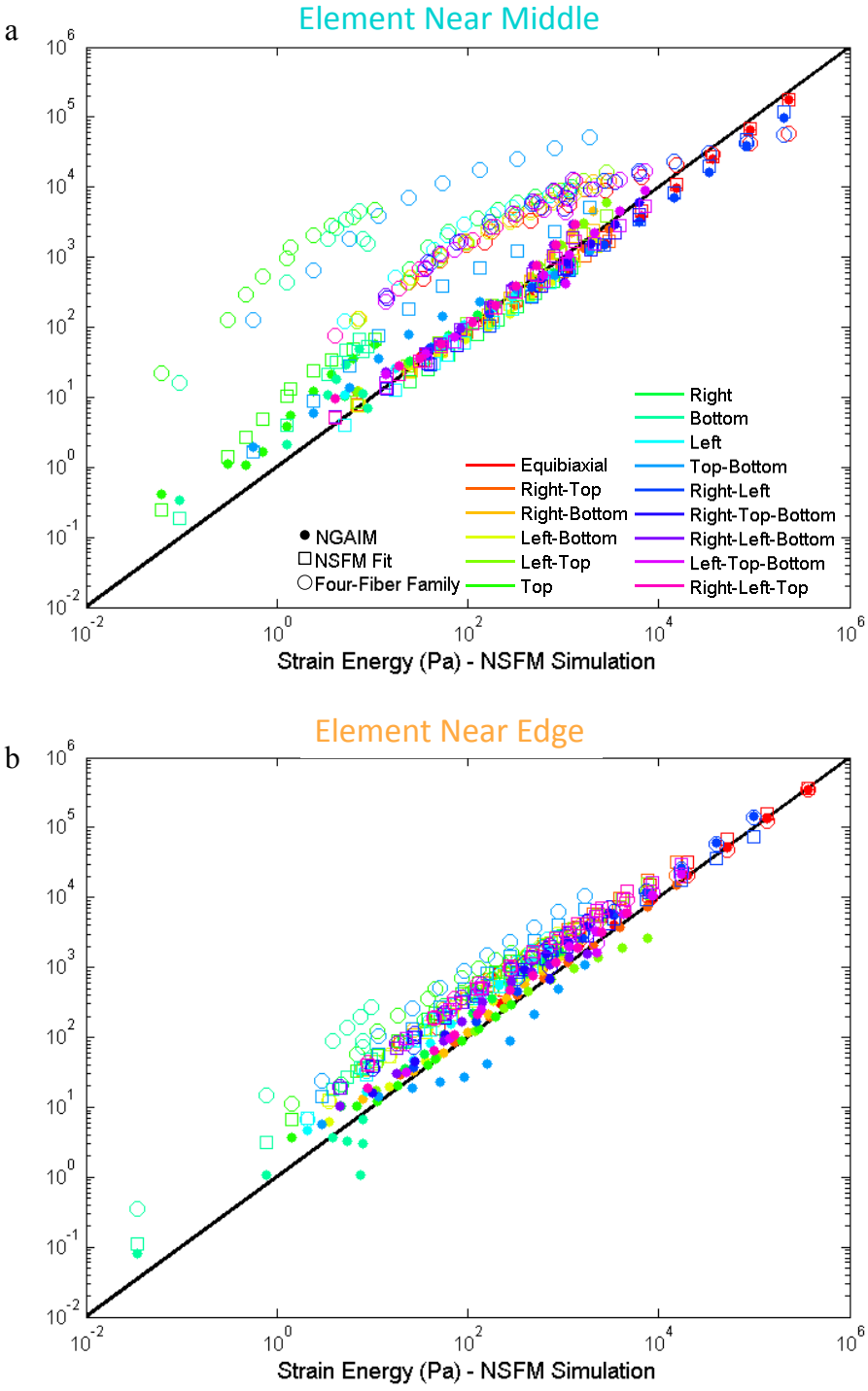

Figure D.20: Strain energy determined using NGAIM (colored dots), the strain energy determined by the NSFM fit to the NGAIM results (colored squares), and the strain energy determined using the four-fiber family model (colored circles) vs. the strain energy generated by the NSFM simulation with prescribed strength of alignment for the element near the center (a) and an element near the edge (b) of the radially symmetric simulation. The diagonal black line indicates a perfect prediction.

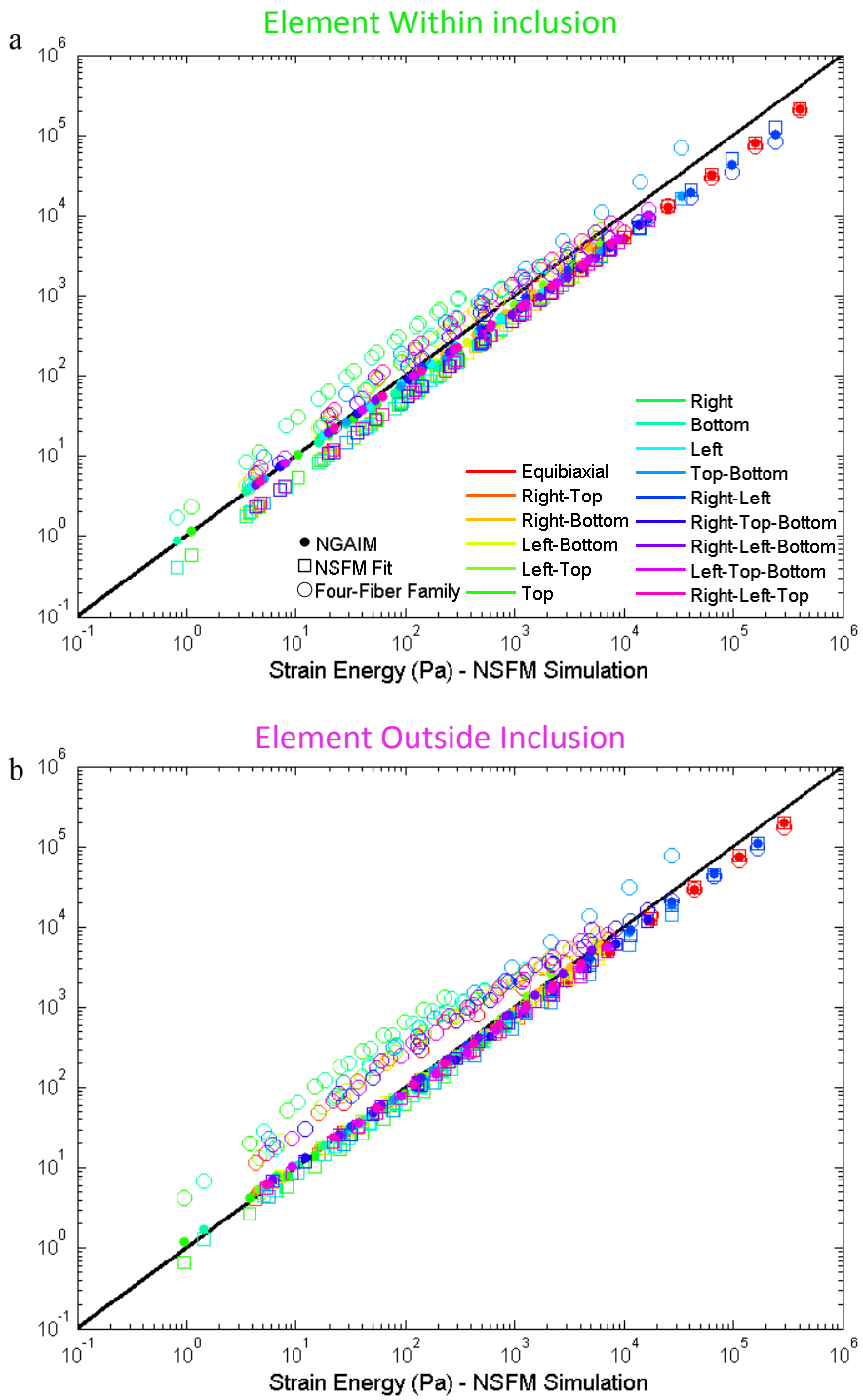

Figure D.21: Strain energy determined using NGAIM (colored dots), the strain energy determined by the NSFM fit to the NGAIM results (colored squares), and the strain energy determined using the four-fiber family model (colored circles) vs. the strain energy generated by the NSFM simulation with prescribed fiber stiffness for all biaxial extensions for the element within the inclusion (a) and the element just outside of the inclusion (b). The diagonal black line indicates a perfect prediction.

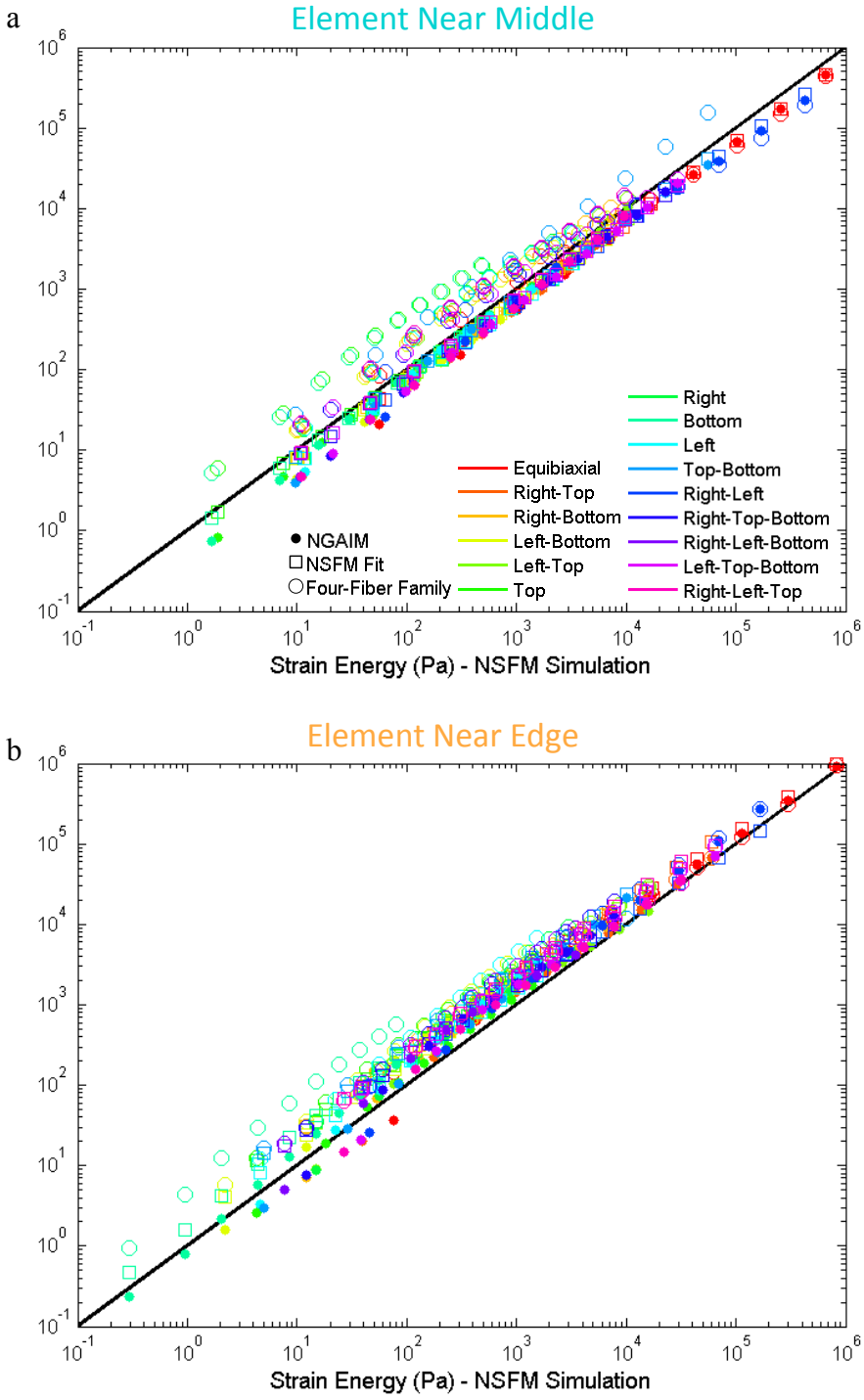

Figure D.22: Strain energy determined using NGAIM (colored dots), the strain energy determined by the NSFM fit to the NGAIM results (colored squares), and the strain energy determined using the four-fiber family model (colored circles) vs. the strain energy generated by the NSFM simulation with prescribed fiber stiffness for the element near the center (a) and an element near the edge (b) of the radially symmetric simulation. The diagonal black line indicates a perfect prediction

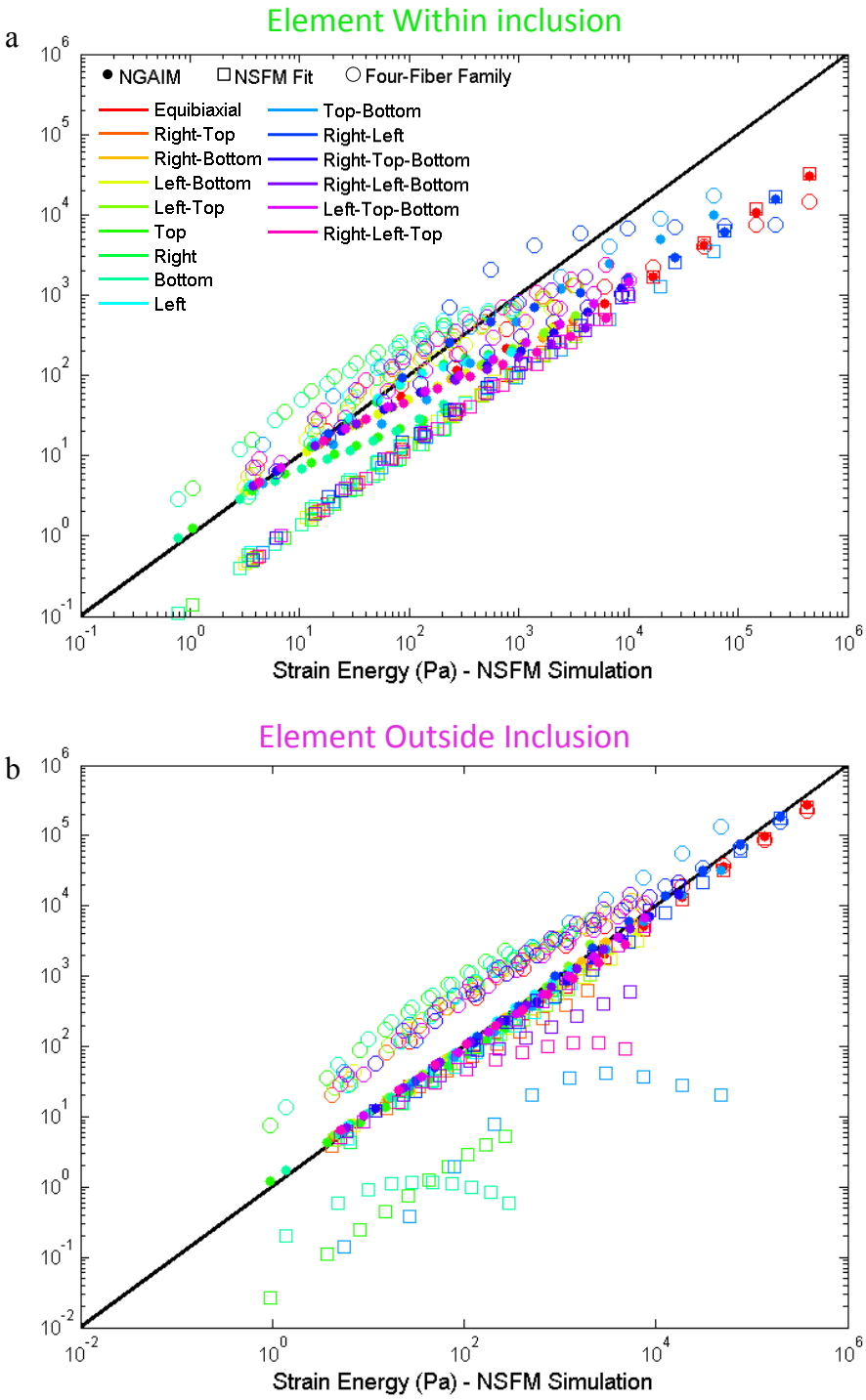

Figure D.23: Strain energy determined using NGAIM (colored dots), the strain energy determined by the NSFM fit to the NGAIM results (colored squares), and the strain energy determined using the four-fiber family model (colored circles) vs. the strain energy generated by the NSFM simulation with prescribed fiber nonlinearity for all biaxial extensions for the element within the inclusion (a) and the element just outside of the inclusion (b). The diagonal black line indicates a perfect prediction.

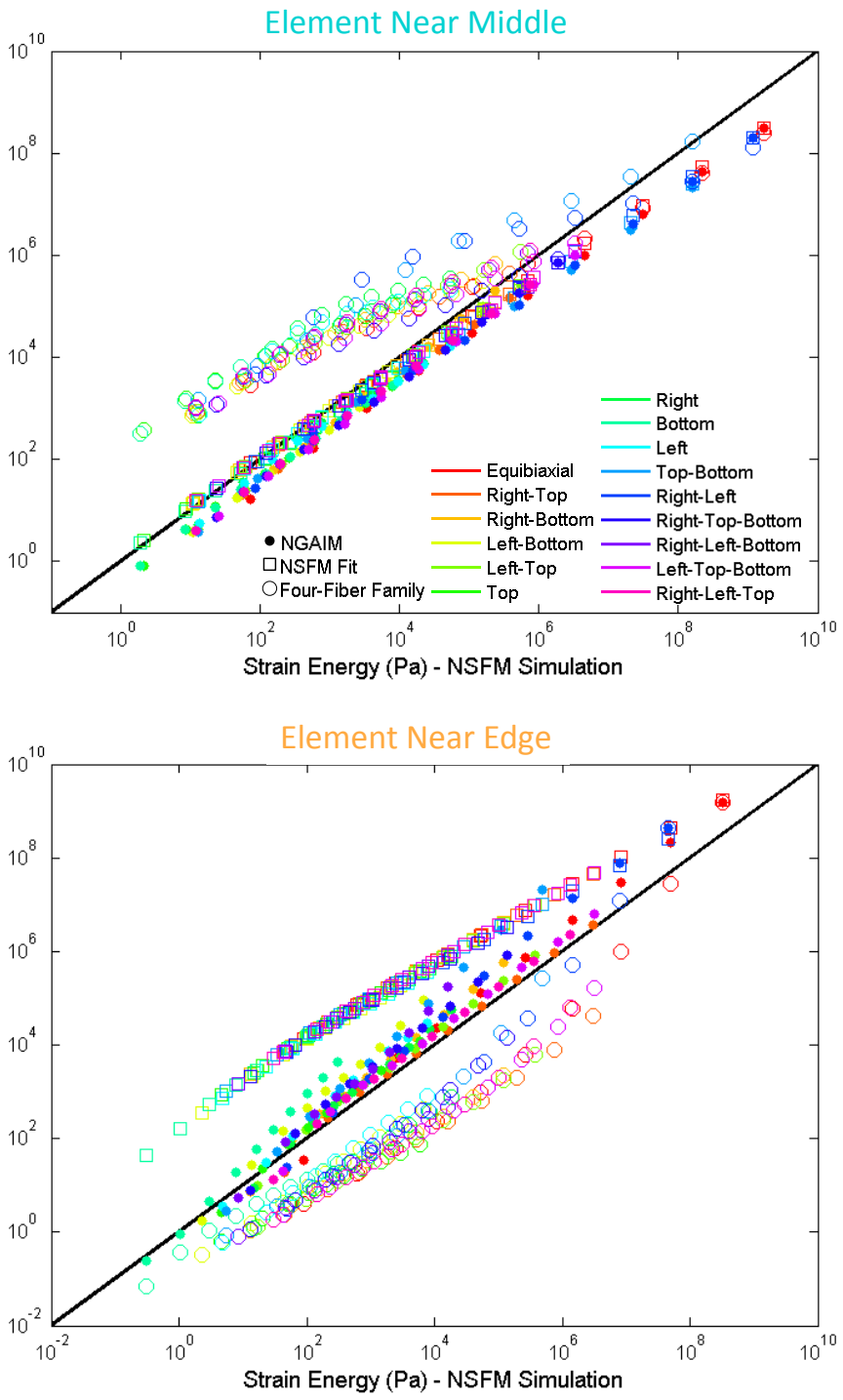

Figure D.24: Strain energy determined using NGAIM (colored dots), the strain energy determined by the NSFM fit to the NGAIM results (colored squares), and the strain energy determined using the four-fiber family model (colored circles) vs. the strain energy generated by the NSFM simulation with prescribed fiber nonlinearity for the element near the center (a) and an element near the edge (b) of the radially symmetric simulation. The diagonal black line indicates a perfect prediction

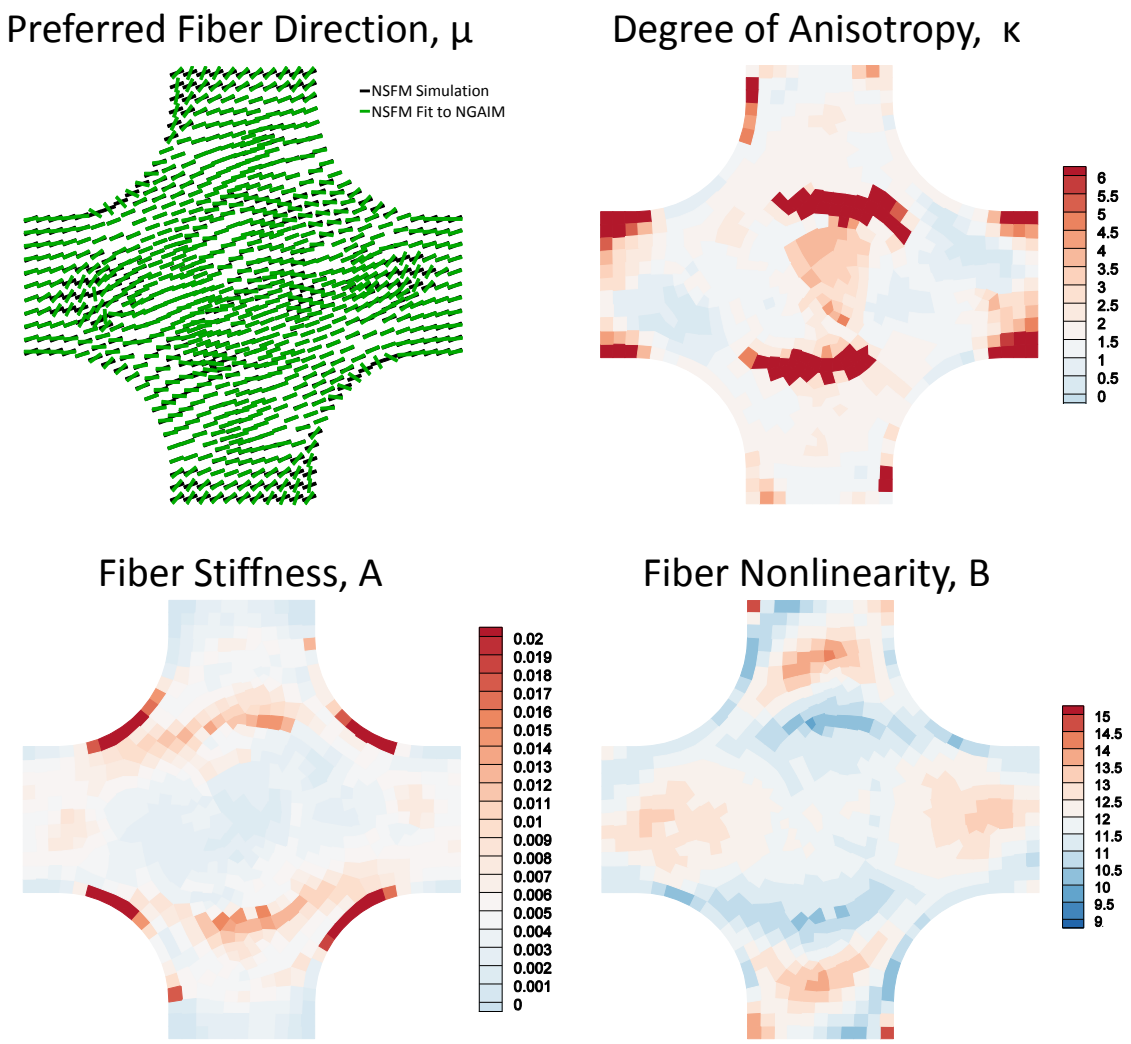

Figure D.25: NSFM parameters determined by fitting the stress-stain behavior predicted by the stepwise GAIM method compared with the NSFM parameters used to generate the simulated sample with the inclusion with prescribed anisotropy strength. The preferred fiber direction prescribed for NSFM is in black and the one recovered by the stepwise application of GAIM is in green. The prescribed anisotropy strength was 6.0 in the inclusion and 1.5 in the sample bulk. All other parameters are shown on scales which place the original values at the center.

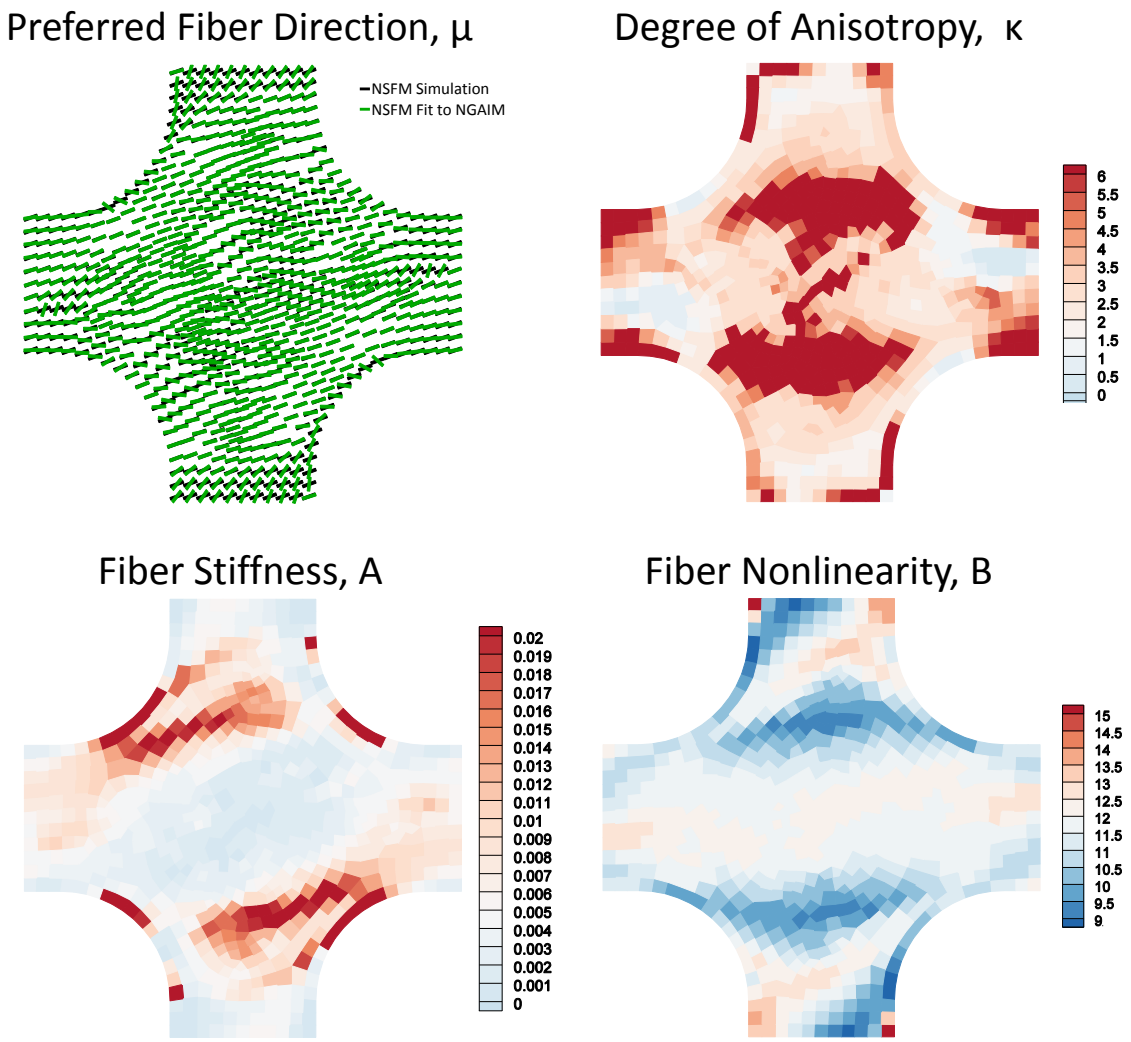

Figure D.26: NSFM parameters determined by fitting the stress-stain behavior predicted by the stepwise GAIM method compared with the NSFM parameters used to generate the simulated sample with radial symmetry with prescribed anisotropy strength. The preferred fiber direction prescribed for NSFM is in black and the one recovered by the stepwise application of GAIM is in green. The prescribed anisotropy strength was 6.0 at the sample center and 1.5 at the sample edge. All other parameters are shown on scales which place the original values at the center.

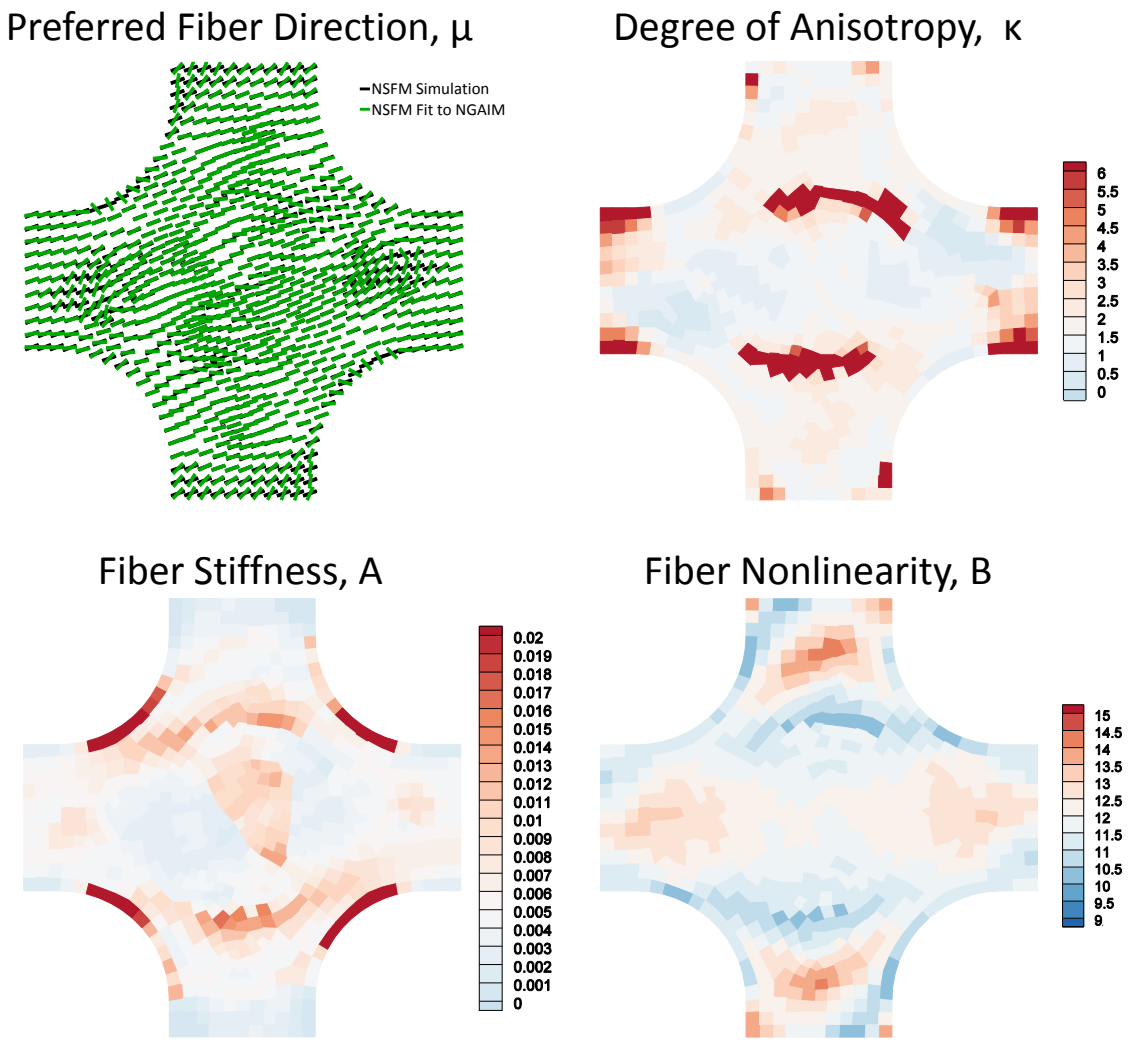

Figure D.27: NSFM parameters determined by fitting the stress-stain behavior predicted by the stepwise GAIM method compared with the NSFM parameters used to generate the simulated sample with the inclusion with prescribed fiber stiffness. The preferred fiber direction prescribed for NSFM is in black and the one recovered by the stepwise application of GAIM is in green. The prescribed fiber stiffness was 20.0 kPa in the inclusion and 5.0 kPa in the sample bulk. All other parameters are shown on scales which place the original values at the center.

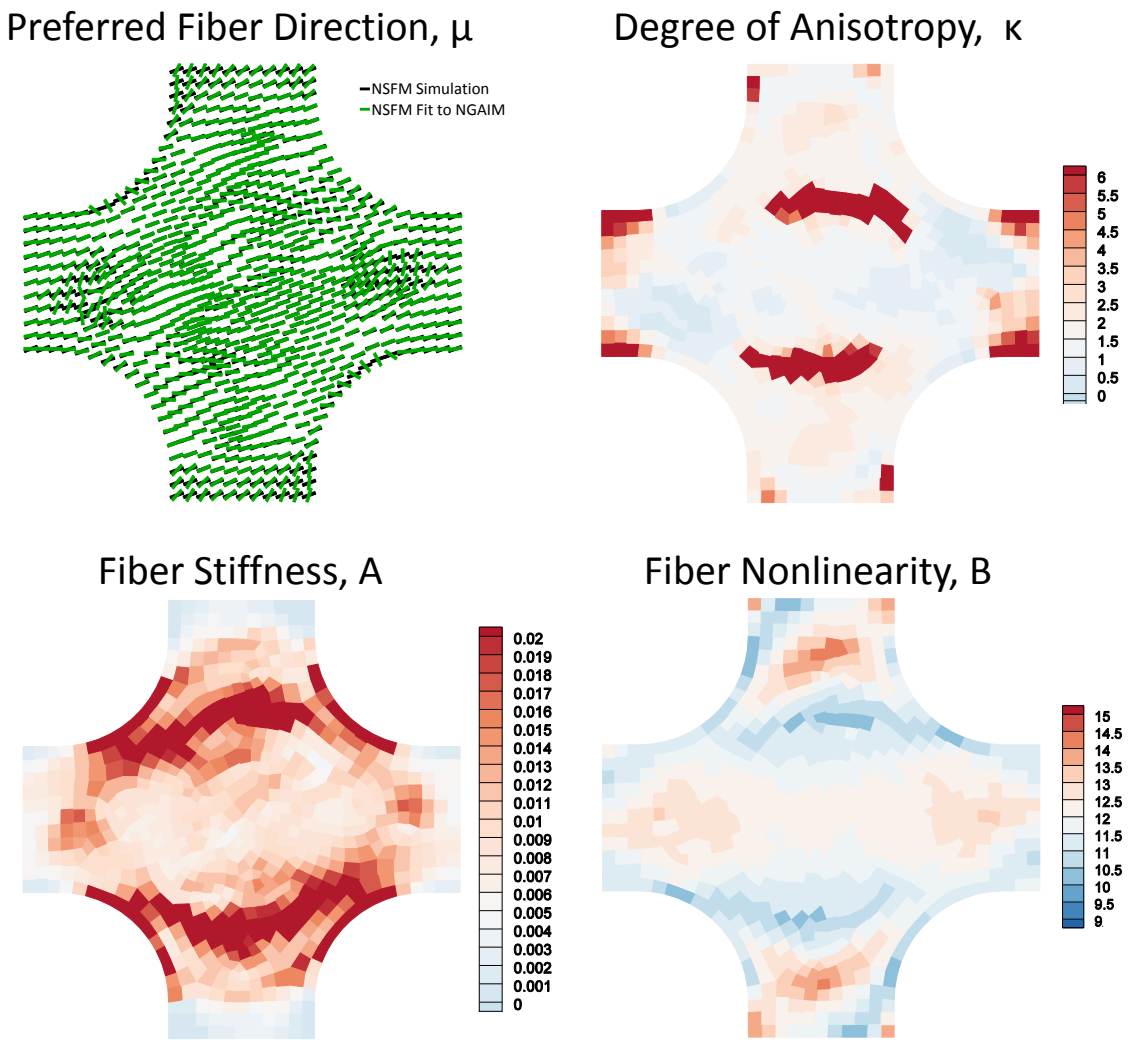

Figure D.28: NSFM parameters determined by fitting the stress-stain behavior predicted by the stepwise GAIM method compared with the NSFM parameters used to generate the simulated sample with radial symmetry with prescribed anisotropy strength. The preferred fiber direction prescribed for NSFM is in black and the one recovered by the stepwise application of GAIM is in green. The prescribed fiber stiffness was 20.0 kPa at the sample center and 5.0 kPa at the sample edge. All other parameters are shown on scales which place the original values at the center.

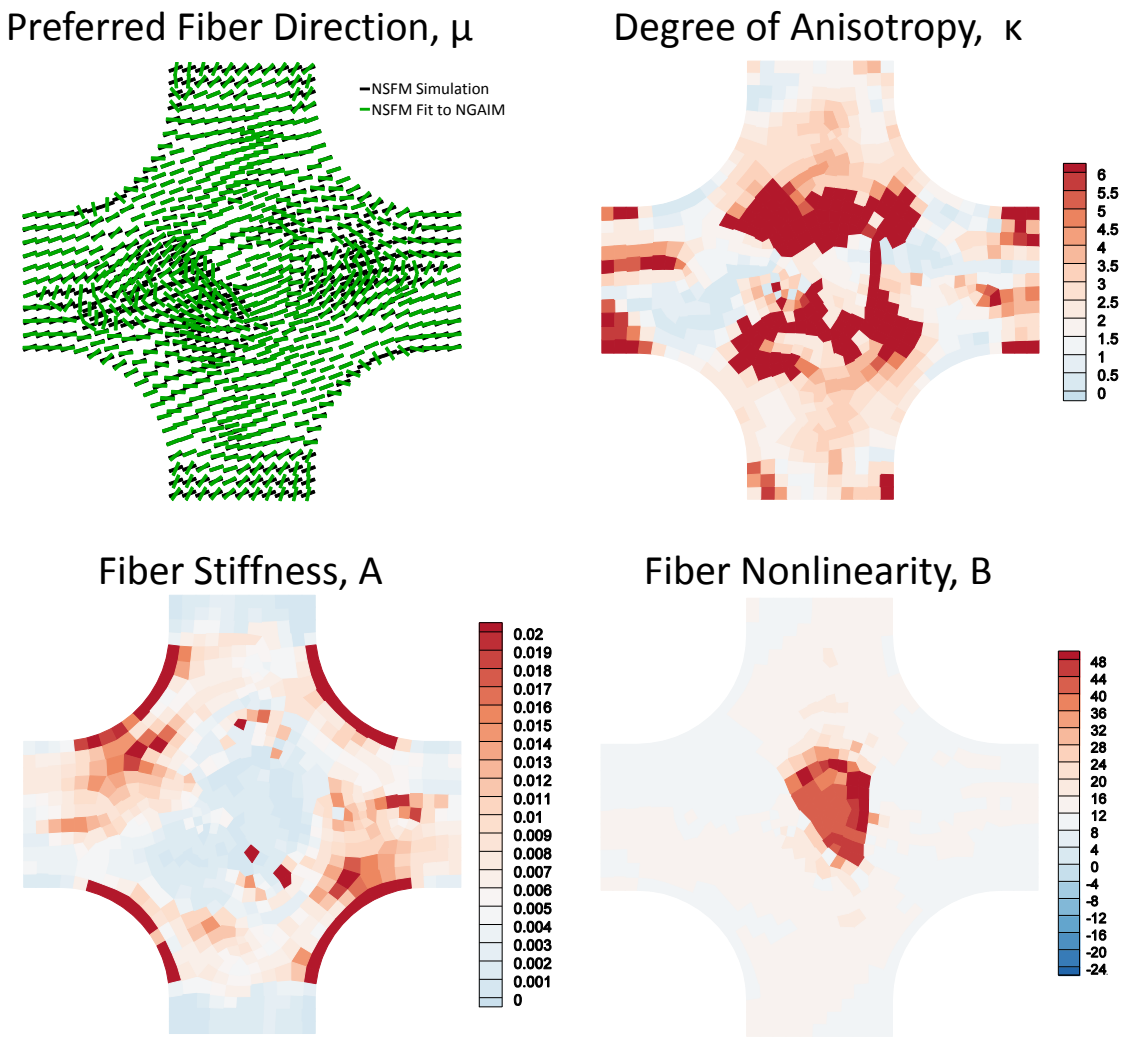

Figure D.29: NSFM parameters determined by fitting the stress-stain behavior predicted by the stepwise GAIM method compared with the NSFM parameters used to generate the simulated sample with the inclusion with prescribed fiber stiffness. The preferred fiber direction prescribed for NSFM is in black and the one recovered by the stepwise application of GAIM is in green. The prescribed fiber nonlinearity was 48.0 in the inclusion and 12.0 in the sample bulk. All other parameters are shown on scales which place the original values at the center.

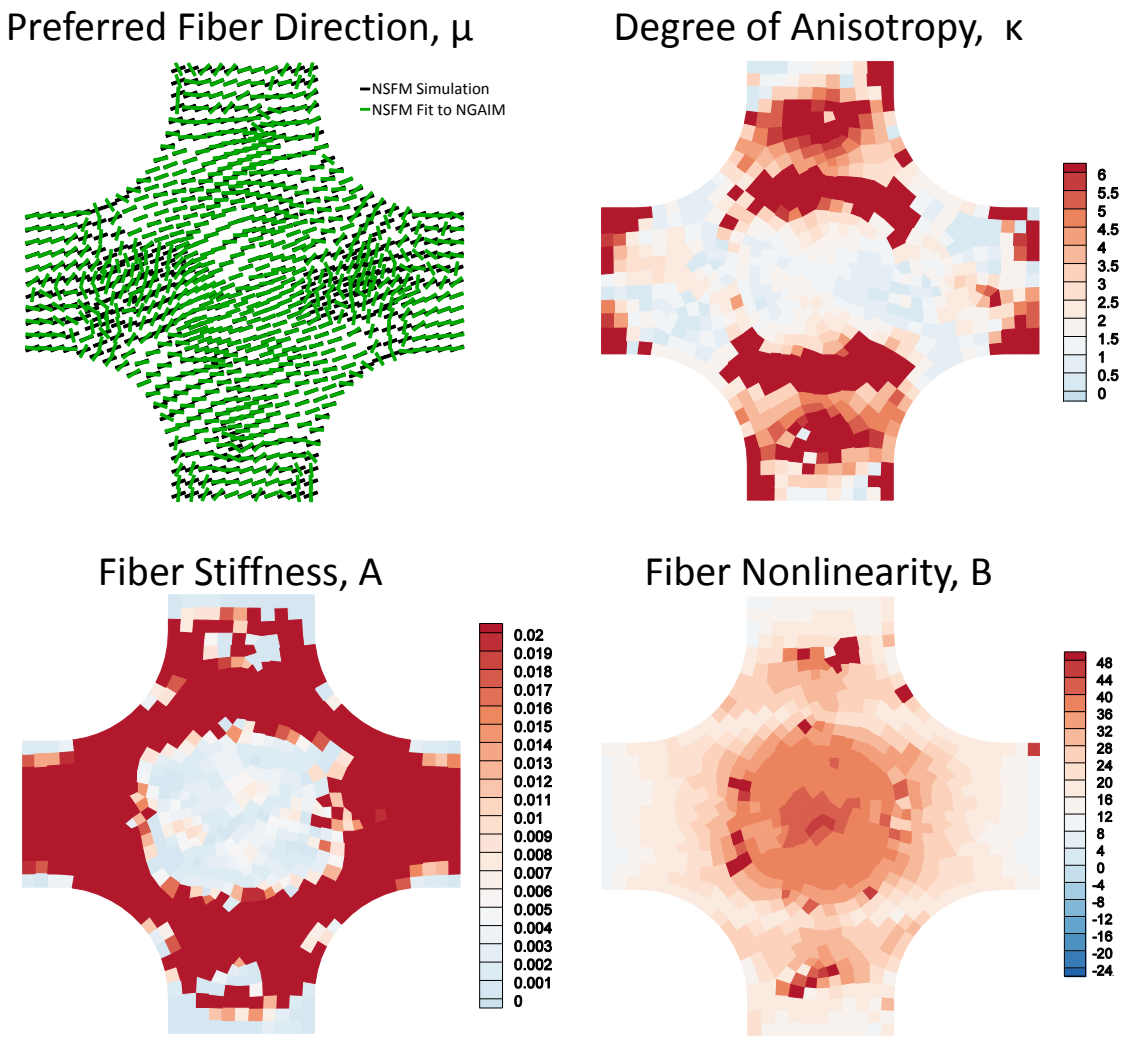

Figure D.30: NSFM parameters determined by fitting the stress-stain behavior predicted by the stepwise GAIM method compared with the NSFM parameters used to generate the simulated sample with radial symmetry with prescribed anisotropy strength. The preferred fiber direction prescribed for NSFM is in black and the one recovered by the stepwise application of GAIM is in green. The prescribed fiber nonlinearity was 48.0 at the sample center and 12.0 at the sample edge. All other parameters are shown on scales which place the original values at the center.

D.4 Four-Fiber Family Model Fitting of NGAIM Results

Table D.1: Best-fit four-fiber family model parameters for the elements of interest for both the simulation with the inclusion in which the prescribed alignment varied and the simulation with radial alignment.

Element of Interest	c	c_1	c_2	α
Element Within Inclusion, Simulation with Inclusion	2.08e-11 kPa	17.5 kPa	6.70e-3 kPa	28.1°
Element Outside Inclusion, Simulation with Inclusion	1.24e-7 kPa	16.6 kPa	9.55e-3 kPa	21.8°
Element Near Middle, Radially Aligned Simulation	2.32e-7 kPa	46.1 kPa	5.13e-3 kPa	61.7 °
Element Near Edge, Radially Aligned Simulation	1.50 e-15 kPa	29.2 kPa	7.82e-3 kPa	13.9 °